Spring 5-7-2011

The Self-Calibration Method for Multiple Systems at the CHARA Array

David P. O'Brien
Georgia State University

THE SELF-CALIBRATION METHOD FOR MULTIPLE SYSTEMS AT THE CHARA ARRAY

by

DAVID O'BRIEN

Under the Direction of Harold A. McAlister

ABSTRACT

The self-calibration method, a new interferometric technique using measurements in the K'-band (2.1 μm) at the CHARA Array, has been used to derive orbits for several spectroscopic binaries. This method uses the wide component of a hierarchical triple system to calibrate visibility measurements of the triple's close binary system through quasi-simultaneous observations of the separated fringe packets of both. Prior to the onset of this project, the reduction of separated fringe packet data had never included the goal of deriving visibilities for both fringe packets, so new data reduction software has been written. Visibilities obtained with separated fringe packet data for the target close binary are run through both Monte Carlo simulations and grid search programs in order to determine the best-fit orbital elements of the close binary.

Several targets, with spectral types ranging from O to G and luminosity classes from III to V, have been observed in this fashion, and orbits have been derived for the close binaries of eight targets (V819 Her B, κ Peg B, η Vir A, η Ori Aab, 55 UMa A, 13 Ceti A, CHARA 96 Ab, HD 129132 Aa). The derivation of an orbit has allowed for the calculation of the masses of the components in these systems. The magnitude differences between the components can also be derived, provided that the components of the close binary have a magnitude difference of $\Delta K < 2.5$ (CHARA's limit). Derivation of the orbit also allows for the calculation of the mutual inclination (Φ), which is the angle between the planes of the wide and close orbits. According to data from the Multiple Star Catalog, there are 34 triple systems other than the 8 studied here for which the wide and close systems both have visual orbits. Early formation scenarios for multiple systems predict coplanarity ($\Phi < 15°$), but only 6 of these 42 systems are possibly coplanar. This tendency against coplanarity may suggest that the capture method of multiple system formation is more important than previously believed.

INDEX WORDS: Long-baseline interferometry, Self calibration, Separated fringe packets, Triple systems, Close binaries, Multiple systems, Orbital parameters, Near-infrared interferometry

THE SELF-CALIBRATION METHOD FOR MULTIPLE SYSTEMS AT THE CHARA ARRAY

by

DAVID O'BRIEN

A Dissertation Presented in Partial Fulfillment of Requirements for the Degree of

Doctor of Philosophy

in the College of Arts and Sciences

Georgia State University

2011

THE SELF-CALIBRATION METHOD FOR MULTIPLE SYSTEMS AT THE CHARA ARRAY

by

DAVID O'BRIEN

Major Professor:	Harold A. McAlister
Committee:	Nikolaus Dietz
	Douglas Gies
	Todd Henry
	Russel White

Electronic Version Approved:

Office of Graduate Studies

College of Arts & Sciences

Georgia State University

May 2011

Dedication

To my parents, Daniel and Janet O'Brien, I am proud to be your son.

Acknowledgments

I would like to thank my family for their constant support and trust, without which this dissertation would not have been possible. Special thanks to my adviser, Dr. Harold McAlister, for guiding me through several difficult years of working on this project. To Dr. Douglas Gies and Dr. Theo ten Brummelaar, thank you for all the tips and suggestions as to how to improve this project. To the other CHARA graduate students, especially Dr. Deepak Raghavan and Dr. Tabetha Boyajian, thanks for helping me learn how to observe with CHARA and work with CHARA data. To the other members of my committee, thank you for giving me tips on how to improve the quality of my document and taking the time out of your busy schedules to make sure that I am worthy of this honor. Thanks to Rajesh Deo and Justin Cantrell for helping me out with my numerous computer problems over the years. Thanks to Saida Caballero-Nieves and Stephen Williams for always helping me out with coding and formatting and various other issues I have run into. Finally, to Misty Brown, I thank you for always being there for me.

Table of Contents

Tables

Figures

Abbreviations and Acronyms

AROC	Arrington Remote Operations Center
AU	Astronomical Units
BCL	Beam Combining Laboratory
BY	Besselian Year
CHARA	Center for High Angular Resolution Astronomy
HAFP	Higher-amplitude fringe packet
IDL	Interactive Data Language
IR	infrared
LAFP	Lower-amplitude fringe packet
mas	milliarcseconds
ms	milliseconds
MSC	Multiple Star Catalog
OPLE	Optical Path-Length Equalization
pc	parsecs
SCAM	Self-Calibration Method
SCAMS	Self-Calibrating Multiple System
SFPs	Separated Fringe Packets
SSFPs	Semi-Separated Fringe Packets

– 1 –
Introduction

For over a century, binary systems have provided a wealth of information about the fundamental properties of stars. The gravitational interaction between the two components of a binary allows us to derive stellar masses directly using a combination of visual and spectroscopic techniques. Mass is generally considered to be the most important fundamental stellar parameter because of its correlation to the evolution of the star.

Hierarchical multiple systems offer the opportunity for further insight into these gravitational configurations. A hierarchical triple system involves a binary with a relatively small separation gravitationally bound to a wide component. The mutual inclination, or the orientation of the angular momentum vector of the close orbit relative to the wide orbit, can give insight into the conditions under which multiple systems form (Sterzik & Tokovinin 2002). Current theories about binary and multiple system formation fall into two major categories: fragmentation and capture. Fragmentation involves the collapse of a gas cloud into a few individual gravitationally bound sub-condensations (Bodenheimer (1978), Bonnell & Bate (1994)). Multiple systems formed by fragmentation are expected to be coplanar (small mutual inclination) (Bodenheimer (1978), Bonnell & Bate (1994)). The capture scenario for binary stars involves two single stars becoming gravitationally bound after losing a substantial amount of their energies of relative motion (Clarke 1995). Multiple systems formed by the capture method are not expected to be coplanar (Sterzik & Tokovinin 2002).

A new interferometric technique employed at the Center for High Angular Resolution Astronomy (CHARA) Array has allowed for the probing of several of these systems. I was able to determine the orbital elements of eight close binaries in the systems I examined, thus allowing me to use Kepler's Third law to determine the masses of the two components of the close binary. All of these systems already had wide orbits from speckle interferometry observations, and comparison of the wide and close orbits in the systems has allowed me to determine the mutual inclinations.

This new technique has been named the "self-calibration method" (SCAM). It involves deriving visibilities from separated fringe packet (SFP) observations at the CHARA Array and using the wide component in a hierarchical triple system as a calibrator for visibility measurements of the close binary. Two objects with a sky separation within a certain acceptable range (∼10 - 80 milliarcsec (mas)) will produce two non-overlapping fringe packets that can be observed in the same fringe scan with the CHARA Array. The length and position angle of the baseline, along with the magnitude difference between the two components, also determine whether two separate fringe packets will appear. When separated fringe packets do appear, it is possible to use the visibility of the wide component to calibrate the visibility of the binary star. Since Dyck et al. (1995), separated fringe packets have been observed for astrometric purposes. Simultaneous observation and calibration of visibilities has not been attempted yet.

All astronomical observations from the ground are affected by atmospheric distortion of the wavefront of incoming light. The interferometric method of correcting this distortion involves observing a calibrator star along with the target system. Ideal calibrators have both a high visibility (unresolved stars) and a constant visibility (single, non-variable stars) for a given baseline. However, in many cases ideal calibrators can only be found at a relatively large angular distance away from the target on the sky. The configuration of V819 Her and other similar systems allows for a more accurate way to account for atmospheric distortion. For the target system V819 Her B, wide component A is a good calibrator. A is located only 75 mas away from B. On average, calibrators used in interferometric observations with the CHARA Array are located a few degrees away from their respective targets. Thus, the separation between target and calibrator in V819 Her is on the order of 10^5 times smaller than the separation in the average interferometric observation.

As first described by Dyck et al. (1995), the angular separation of the components of a binary star may be sufficiently wide to reveal non-overlapping or separated fringe packets when observed in a fringe-scanning mode by a long-baseline interferometer. In certain triple star systems, the orbital geometry of the three components may be such that one of the separated fringe packet pair corresponds to the wide component whereas the other packet is associated with the inner, short-period system whose resolution is targeted. This approach utilizes the observed visibility of the wide component to calibrate instrumental and atmospheric effects on the interferometric visibility of the close binary. Standard interferometric practice calls for the observation of a calibrator star, selected as close as possible to the target star, in a bracketed sequence before and after observations of the target. In triple systems where the angular separation between the close binary and the wide component is relatively small (on the order of 80 mas), all components can be observed nearly simultaneously during a single scan through interferometric delay. This reduces the offset in time between target and calibrator from minutes to a few tenths of a second and in position from degrees to a few tens of mas. In principle, this provides for a more accurate calibration than the standard method. The calibrated visibilities of the inner orbit can then be used to determine the visual orbital elements of the close binary system.

Observing triple systems this way can offer several obvious scientific advantages. The main consideration when observing the target and calibrator separately is the instrument configuration. Moving the telescope to a new position to observe a star in the different part of the sky effectively changes the instrument. The target and calibrator will be observed by different projected baselines with different baseline position angles. In a self-calibrating system, the discrepancy between baselines and position angles is essentially non-existant. The same exact instrument is being used to observe both the target and calibrator. In a spatial sense, the atmosphere should be more homogeneous over a smaller piece of the sky than a larger one. Thus, on a scale of a few milliarcseconds, the spatial atmospheric distortion in the direction of the calibrator will be relatively similar to that of the target, whereas over a range of several degrees, the atmosphere could be very different in comparison. In a temporal sense, the atmosphere is always changing. During the time that the telescope has to slew from the target to the calibrator, the atmosphere can undergo significant changes. If such occurrences affect only one of the components, significant error could be introduced into the visibility measurements. With self-calibrating systems, because we are observing both components concurrently, any temporal changes to the atmosphere should affect the target and calibrator equally and simultaneously. It should be noted that because of the time it takes for the fringe-scanning mirror to move through one scan of delay ($\sim$1 sec), observations of the two components are quasi-simultaneous rather than simultaneous.

In addition to the scientific advantages offered by observing self-calibrating systems, a few procedural advantages also exist. A significant amount of observing time is lost when the telescopes are slewing from one object to another. In addition, after the slewing procedure is complete, the telescopes must acquire the target. With fainter targets, this can be a time-consuming process, as the telescope(s) may fail to lock onto a target with fewer photons. The telescopes must slew between target and calibrator several times, thus increasing the number of chances that the telescope can "miss the target," thus further increasing the amount of time between observations. In practice, observers have been able to get many more observations of these separated fringe packet systems in a given time period than would be possible using bracketed observations. A related procedural advantage is the ability to "sit" on a specific target for as long as desired by the observer. Theoretically, a target can be observed continuously from its rising to its setting. The major limiting factor in "sitting" on a target is the computing power required to analyze the data derived from longer observation intervals. An observation of thirty minutes produces a data file of nearly 25 megabytes. A significant amount of time is needed to reduce such large data files with low computing power. For this reason, observation intervals are limited to roughly 5 minutes each.

We have identified roughly 30 triple systems appropriate to this approach. These objects typically consist of a long-period system whose visual orbital elements have been measured by speckle interferometry and a short-period system possessing a spectroscopic orbit. Once the visual orbit of the short-period system is determined from long-baseline interferometry, the mutual inclination of the two orbits comprising the triple system can be calculated. A resolved spectroscopic binary provides the angular semi-major axis, the orbital inclination, and the nodal longitude to the standard set of spectroscopic elements. However, the longitude of the node possesses a 180° ambiguity. In general, visual orbits for both the long-period and short-period components in triple systems are rare (Fekel 1981). Triple systems with visual orbits for the close binary usually have wide orbits with periods too long for study. On the other hand, triple systems in which the wide orbit can be determined visually usually have unresolvable close orbits. Thus, the number of systems accessible to this approach is modest. However, the long baselines of the CHARA Array enable the determination of visual orbits for the close binaries of triple systems with existing visual orbits for the wide component.

1.1 Basic Interferometry

This dissertation is only possible because of the incredible resolving ability of long-baseline interferometry. For a single aperture, the diffraction-limited resolution of a telescope is given by the Rayleigh Criterion:

$$\theta = 1.22\frac{\lambda}{D} \tag{1.1}$$

where λ is the wavelength of observations and D is the diameter of the aperture. When observing with an interferometer, the resolution is improved immensely because it is no longer dependent on the aperture of the telescopes, but on the distance between them, known as the baseline. The resolution of a two-telescope interferometer is:

$$\theta = \frac{\lambda}{2B} \tag{1.2}$$

where B is the baseline of observation. As an example, the K'-band (2.1 μm) resolution of an individual CHARA telescope is 537 mas, while the resolution of CHARA's longest baseline is 0.67 mas.

Interferometry is based on the principle of combining beams of light to obtain an interference pattern, as first shown in Young's double-slit experiment in the early 1800's. As displayed in Figure 1.1, when light of wavelength λ is shined through two slits separated by a distance d onto a screen a distance D away, the resulting intensity pattern displays alternating light and dark "fringes" due to the amount of constructive and destructive interference at certain points on the screen. This intensity pattern is:

$$I(x) = 4A^2 \cos^2(\frac{2\pi}{\lambda}\frac{xd}{D}) \tag{1.3}$$

where A is the amplitude of the fringes and $D >> d$. The maxima of the $I(x)$ occur at multiples of the wavelength $(0,\ \lambda,\ 2\lambda,\ 3\lambda,\ ...)$ where 0 marks the location of the central maximum. Successive peaks are separated by an angular spacing of:

$$\alpha = \frac{x}{D} = \frac{\lambda}{d}. \tag{1.4}$$

The A given in equation 1.3 is only constant in the case of monochromatic light. Real interferometric observations are always going to be polychromatic. The intensity patterns of different wavelengths will have different angular spacings between the fringes (equation 1.4). When the intensity patterns of interferometric observations at several different wavelengths are combined, the resulting total intensity pattern is that of a central "fringe packet" with "side-lobes" extending outward on either side. This is shown in Figure 1.2. The characterization of this fringe packet can be used to derive fundamental information about the object producing it.

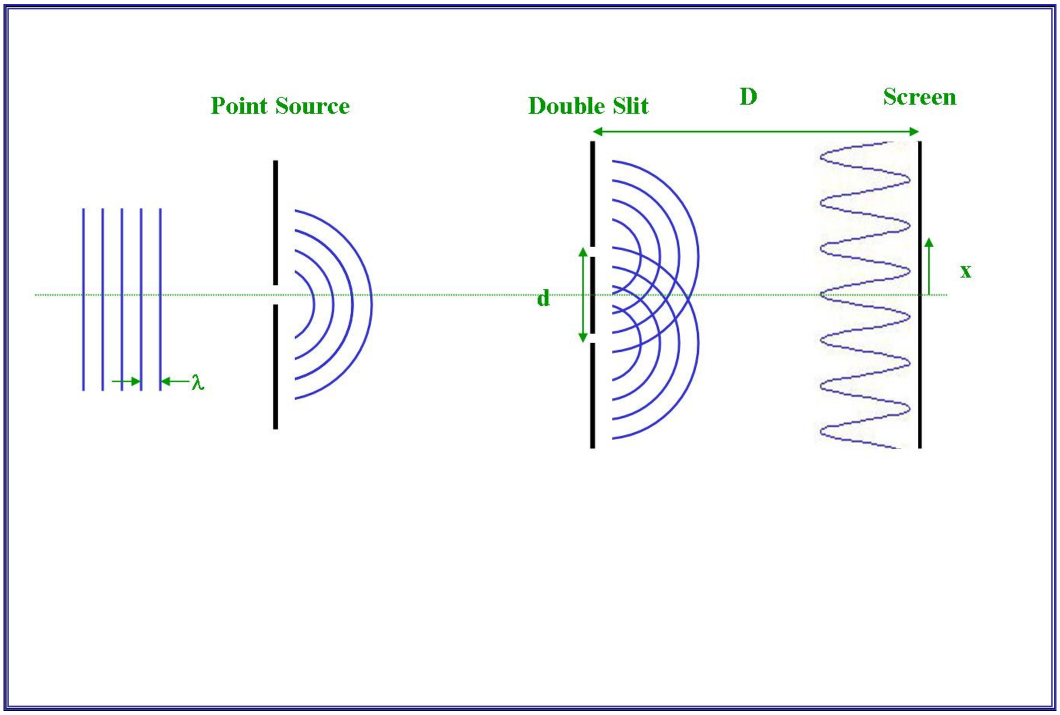

Figure. 1.1: Young's Double-Slit Experiment. Adapted from a figure by H.A. McAlister

The observable quantity of an interferometer is the "visibility" of a fringe packet, defined by Michelson (1920) as:

$$V = \frac{I_{\rm max} - I_{\rm min}}{I_{\rm max} + I_{\rm min}} \tag{1.5}$$

where $I_{\rm max}$ and $I_{\rm min}$ are the maximum and minimum intensity of the interference pattern, respectively. The visibility derived by an interferometer can be used to determine several parameters of the target system. For single stars, the visibility is dependent on the star's angular diameter. For binary systems, the visibility is depend on the angular diameters of the two stars, the separation between them, and the magnitude difference between them. The formulae governing those dependences

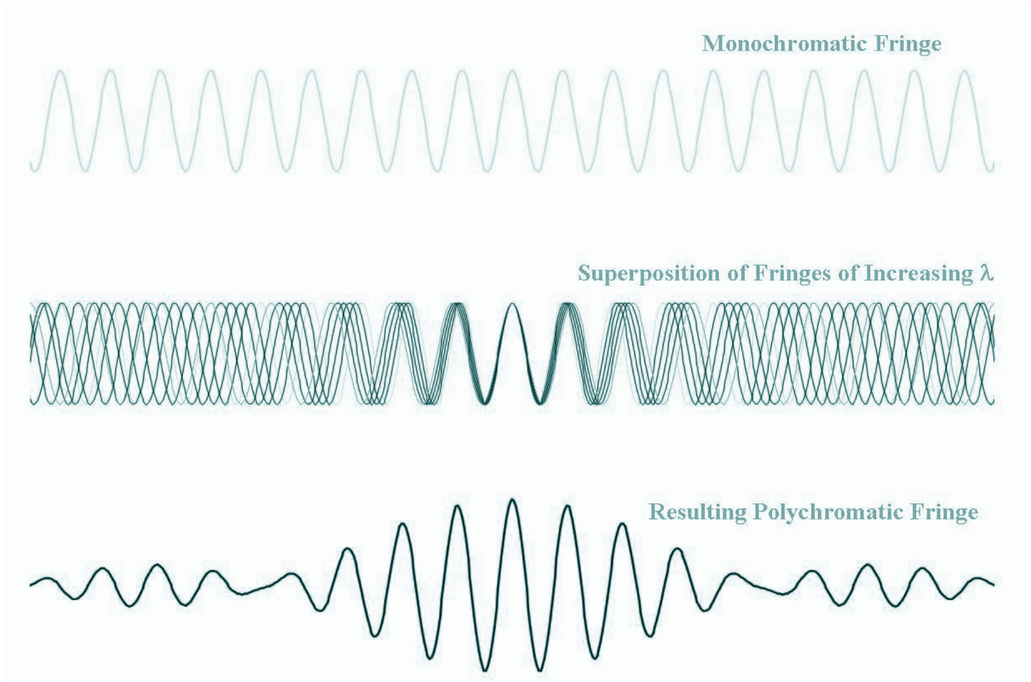

Figure. 1.2: Polychromatic Fringes. These plots show the effects of polychromatic observation. Adapted from a figure by H.A. McAlister

will be discussed later, but depictions of the dependences are shown in Figures 1.3, 1.4, and 1.5. These figures represent the ideal case of monochromatic observation. Since all observations are polychromatic, the real visibility curves will be affected by the bandwidth of observation. The resulting curves are the sum of all monochromatic curves within the range of the observation bandwidth. This effect, known as "bandwidth smearing," causes the minima of the curve to lift off of zero visibility.

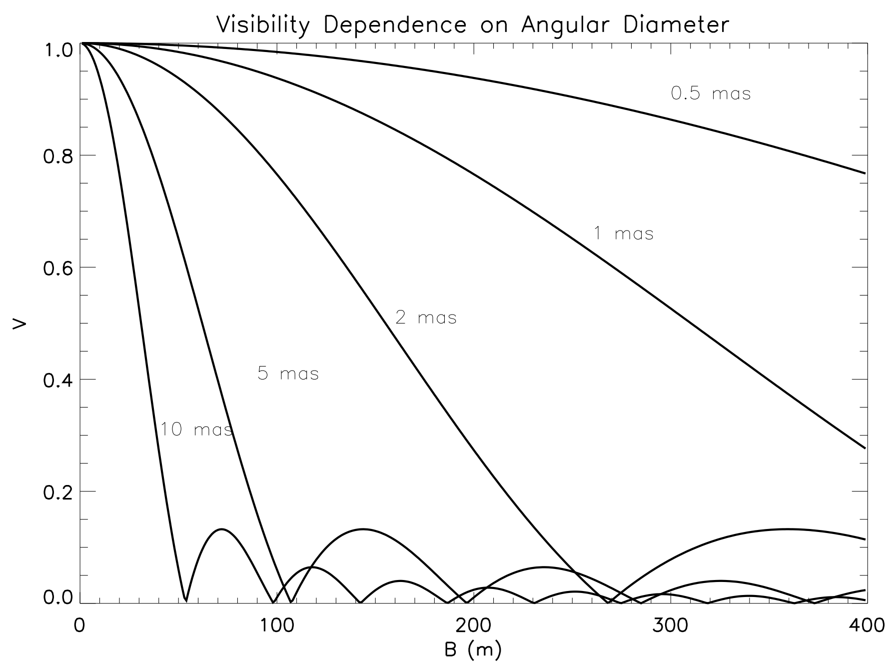

Figure. 1.3: Visibility Dependence on Angular Diameter. These curves show the visibility dependence on angular diameter for a single star.

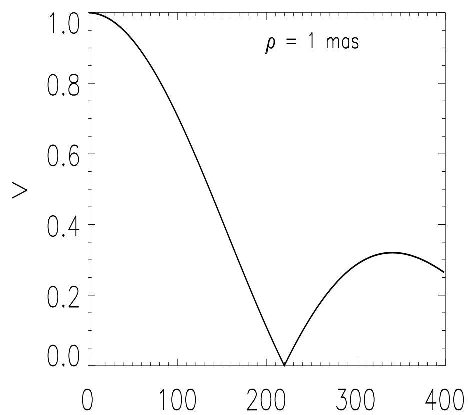

(a)

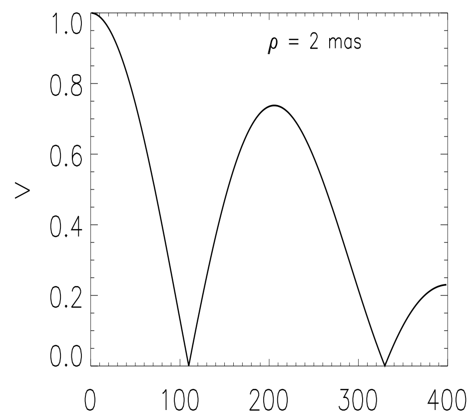

(b)

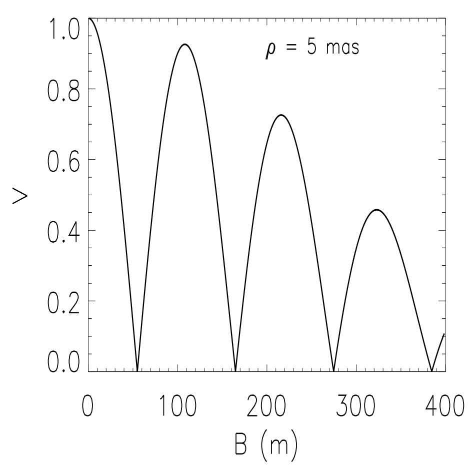

(c)

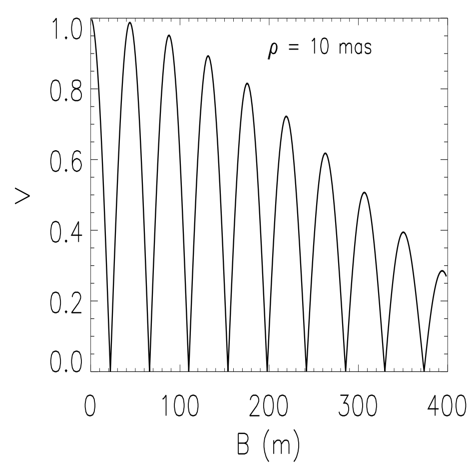

(d)

Figure. 1.4: Visibility Dependence on Separation. These curves show the visibility dependence on separation for a binary star. For each plot, the angular diameters of the two stars are set to 1.0 mas and the magnitude difference (Δm) is set to zero.

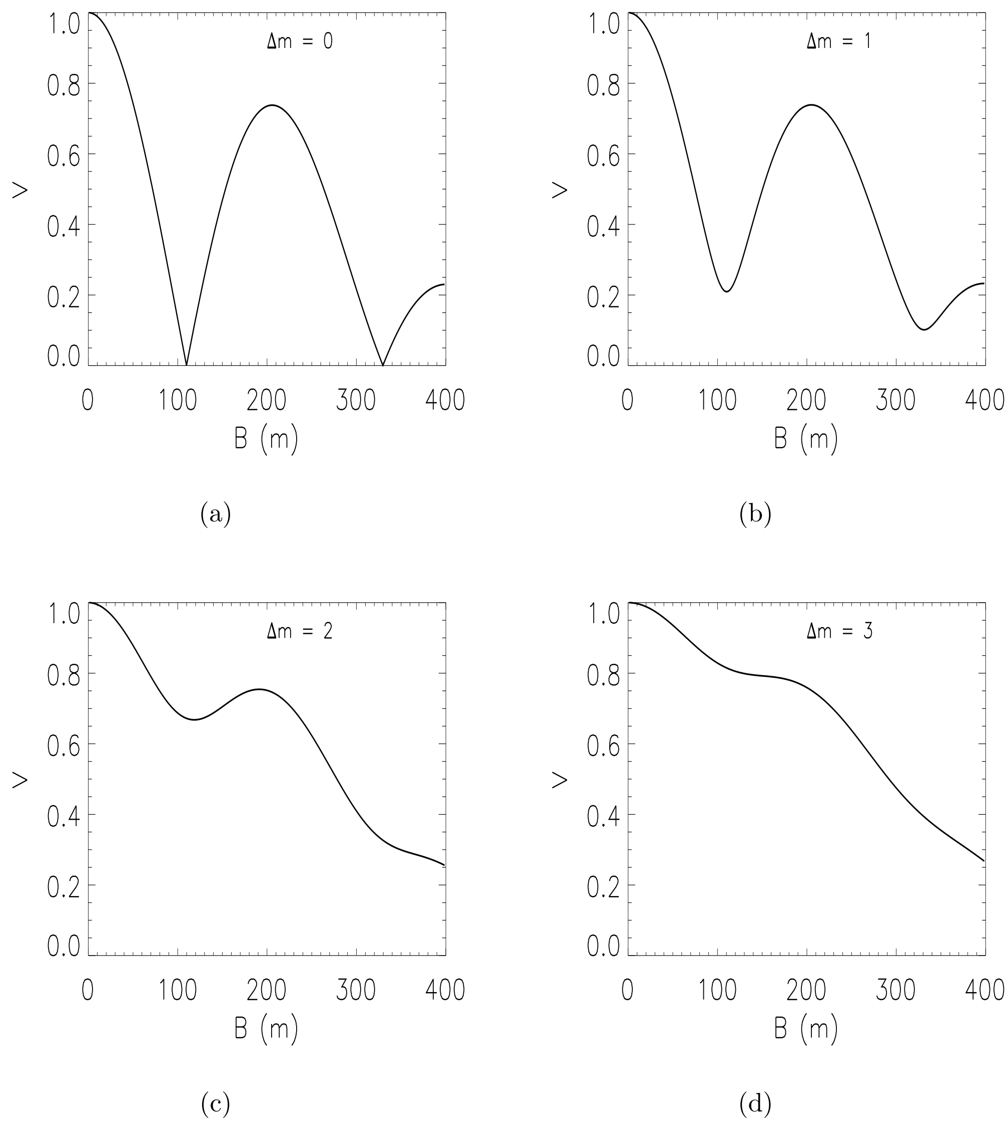

Figure. 1.5: Visibility Dependence on Magnitude Difference. These curves show the visibility dependence on the magnitude difference between the two components for a binary star. For each plot, the angular diameters of the two stars are set to 1.0 mas and the separation (ρ) is set to 2.0 mas.

1.2 The CHARA Array

The sole observation instrument for this project was Georgia State University's CHARA Array, located in California on the summit of Mount Wilson. The complete details of the instrument are given in ten Brummelaar et al. (2005). Six 1-meter telescopes are spread out on the CHARA grounds in a Y-shaped configuration, producing 15 baselines from 34 to 331 meters. The telescopes are named for their geographic location relative to the CHARA's Beam Combining Laboratory (BCL). The layout of the telescopes gives six different general baseline orientations (S-E, S-W, E-W, S1-S2, W1-W2, and E1-E2). The various orientations are of paramount importance to this project because of their role in SFP observations. The layout of CHARA is presented in Figure 1.6.

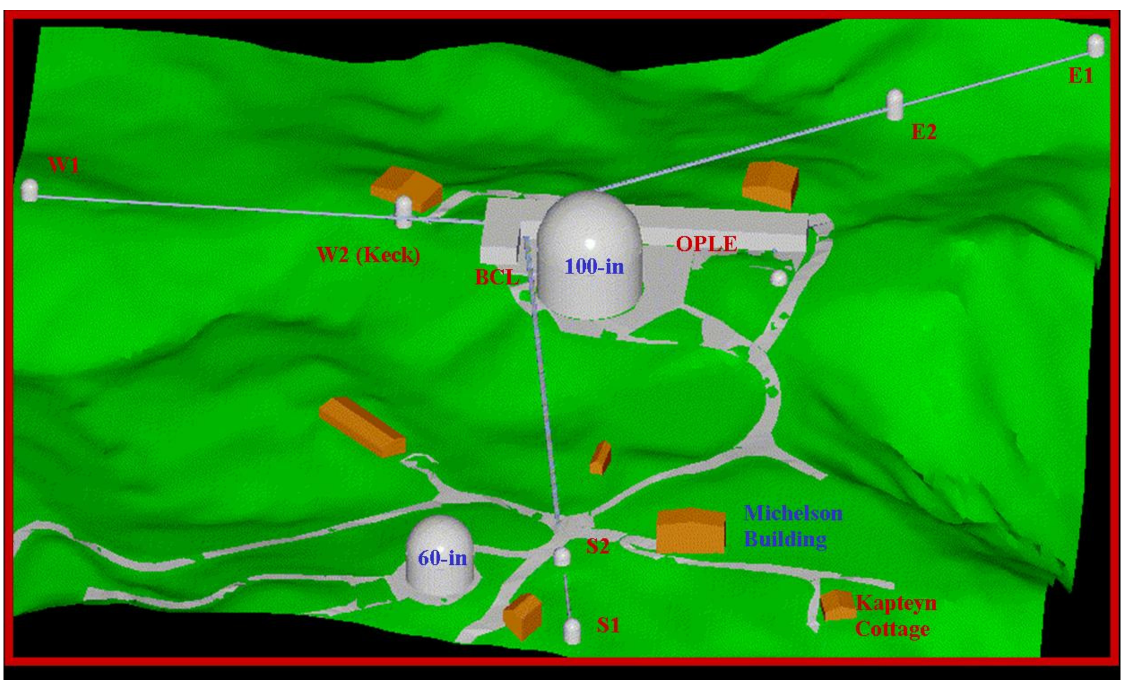

Figure. 1.6: The CHARA Array. Adapted from a figure by H.A. McAlister

Light from each telescope is transported as a 12.5-cm diameter collimated beam through 20-cm diameter evacuated light pipes to the BCL for Optical Path-Length Equalization (OPLE). The first stage of OPLE involves six parallel tube systems, referred to as the “Pipes of Pan” (PoPs) that introduce fixed amounts of delay into the beam (0, 36.6, 73.2, 109.7, and 143.1 meters). Down each PoP line are mirrors that can be moved into the beam to add or remove fixed amounts of delay. Then, a variable component of delay must be considered to account for a star’s movement across the sky during observation. This is achieved by six mobile OPLE carts that ride on steel rails 46 m in length and provide 92 m of path length compensation.

After the path lengths are equalized, the beams are reduced in size to 1.9 cm in diameter and split into separate visibile and infrared (IR) wave bands. The visible part is sent to the tip/tilt system to track the star, while the IR part is sent to the “Classic” beam combiner for analysis. The layout of CHARA Classic, shown in Figure 1.7, is that of a pupil-plane beam combiner where the two outputs from the beam splitter are separately imaged onto the Near Infrared Observer (NIRO) camera after passing through a filter. A filter wheel can be manually rotated through six different filters, but all observations in this project are taken in K' (2.1329 μm). Fringes are detected by dithering a mirror mounted to a piezoelectric translation stage through a region of delay. The stage is driven with a symmetric sawtooth signal at a data acquisition rate of 5 samples per fringe for four possible values of the fringe frequency (1000:200 Hz, 750:150 Hz, 500:100 Hz, 250:50 Hz). Almost all data for this project

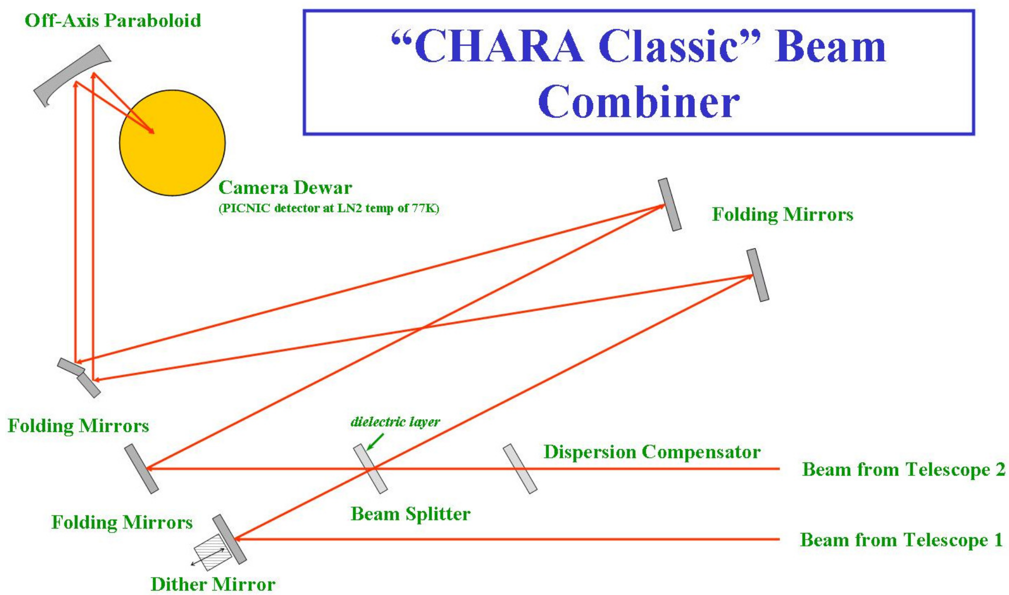

Figure. 1.7: CHARA Classic. This shows the layout of the CHARA Classic Beam Combiner. Adapted from a figure by H.A. McAlister.

were collected at a rate of 750 Hz for a fringe frequency of 150 Hz.

Almost all observations for this project were conducted using CHARA's remote observation facility, the Arrington Remote Operations Center (AROC), located on the Georgia State University campus in Atlanta. AROC's computers are connected to those at CHARA's Mount Wilson facility through the use of a Virtual Private Network (VPN), which allows observers to remotely control CHARA's computers. From AROC, observers are able to slew telescopes, acquire targets, and initiate the data collection sequence. With support from the on-site staff at Mount Wilson, AROC is a fully functional observation facility.

– 2 –

Target List

2.1 Observing Criteria

The goal of the observations for this project is the quasi-simultaneous observation of a target close binary and a calibrator star. The angular separation of the target and calibrator must fall within a certain range in order to achieve this goal. If the separation is too large, the two fringe packets will not appear in the same scan over interferometric delay. If the separation is too small, the two fringe packets could be overlapping or even unresolved.

The upper limit on the acceptable range of separations is determined by the specifications of the instrument of observation. Data are recorded with a dither mirror that oscillates back and forth over a certain range of delay space. The CHARA Array observation protocol allows the observer to select either a long, medium, or short-scanning mode. These modes differ in the amount of delay space that is recorded and the amount of time needed to record each data scan. For the purposes of this project, the long-scanning mode is the preferred observation mode because it allows the simultaneous observation of SFPs with larger projected separations. The range of delay space was 185.62 μm for all data recorded before 2008.

To determine how the separation between two fringe packets in delay space relates to the angular separation, a scaling equation is used:

$$\rho_{\mathrm{mas}} = \frac{206.265 \ \ \rho_{\mu\mathrm{m}}}{B_{\mathrm{m}}} \tag{2.1}$$

where B_{m} is the baseline of the observation in meters, $\rho_{\mu\mathrm{m}}$ is the separation between two fringe packets in delay space in μm, and ρ_{mas} is the angular separation between the two packets in mas. The scale depends on which of CHARA's 15 observation baselines are being used. For example, using the longest CHARA baseline (S1-E1: 330.67 m), 185.62 μm of delay space equates to 115.79 mas of sky separation. In 2008 January, the range of delay space covered by the dither mirror in long-scan mode was changed from 185.62 to 142.0 μm for operational reasons unrelated to this project. This new scan range results in an angular distance of 88.6 mas. Conversely, for the shortest CHARA baseline (S1-S2: 34.08 m) the scan ranges equate to a much larger portion of the sky: 1123.4 mas pre-2008 and 859.4 mas post-2008. Although the shorter baseline allows the observer to search a larger portion of the sky, the resolving ability is much lower, so when creating a target list, the focus is placed on the scan range available to larger baselines.

When compiling a target list, I looked for targets with a wide orbit semi-major axis of less than 250 mas. For such targets, an observation baseline can be chosen such that the projected angular separation is below the upper limit calculated above on a given night. To accomplish this task, information is needed about both the target system and the possible baselines of observation. This is explained in detail in the next section.

There are a few other considerations taken into account when creating the target list for this project. CHARA's sky coverage is a factor, such that the southerly declination limit for objects is -15°. Magnitude is a very important factor in a few different ways. The limiting magnitude of the CHARA Array in K' band is about 7.5 for the CHARA Classic beam combiner, so only bright targets are available for observation. Also, two magnitude differences must be taken into account. The magnitude difference between the target close binary and the calibrator wide component ($\Delta K_{\rm wide}$) affects the amplitude of the fringe packets. If $\Delta K_{\rm wide}$ is too large, the packet corresponding to the fainter component will not appear at all. Analysis of this phenomenon will be discussed explicitly in a later section. The other magnitude difference to consider is between the two stars in the target binary ($\Delta K_{\rm close}$). If $\Delta K_{\rm close}$ is too large, the fringe packet representing the binary will show little to no modulation in visibility and thus will resemble a single star. The modulation of the visibility is vital in determining the orbit of the close binary, so a large $\Delta K_{\rm close}$ disqualifies an object from being a candidate. A final consideration when choosing a target is the size of the calibrator. An ideal calibrator is unresolved even on CHARA's longest baseline. In general, an angular diameter of 0.5 mas is the cutoff between resolved and unresolved at CHARA. A collection of the criteria for SCAM targets is given in Table 2.1.

To find objects suitable for this project, three main sources were consulted: The Fourth Catalog of Interferometric Measurements of Binary Stars, The 9th Catalog of Spectroscopic Binary Orbits, and The Multiple Star Catalog.

Table 2.1. Criteria for Target List

Parameter	Limit
Dec.	$\geq$ -15°
$\alpha_{\rm wide}$ (mas)	$\leq$ 250
K	$\leq$ 7.5
$\Delta K_{\rm wide}$	$\leq$ 3.0
$\Delta K_{\rm close}$	$\leq$ 2.5
$\Theta_{\rm cal}$ (mas)	$\leq$ 5.0

2.1.1 The Fourth Catalog of Interferometric Measurements of Binary Stars

The Fourth Catalog of Interferometric Measurements of Binary Stars (Hartkopf et al. 2001) began in 1982 at CHARA by recording all speckle interferometry measurements taken by the facility's speckle camera. Later, the catalog expanded to include not only CHARA's speckle measurements, but all published speckle, astrometric, and photometric measurements obtained by high angular resolution techniques. With this wealth of information, the catalog is a useful resource.

To find possible targets, the entire catalog was searched for any objects with an angular separation of less than 250 mas at any observation epoch. Unfortunately, this catalog does not contain explicit multiplicity information (save for a few footnotes), so the list of possible candidates obtained here was populated by mostly binaries, rather than multiple systems.

2.1.2 The 9th Catalogue of Spectroscopic Binary Orbits

One useful source in determining the multiplicity of the targets found in the above catalog is the 9th Catalogue of Spectroscopic Binary Orbits (Pourbaix et al. 2004). For the candidate systems, this source was consulted to ensure that there existed two separate spectroscopic solutions: one corresponding to the wide orbit, the other corresponding to the close orbit. A certain case could occur in which the close orbit in the multiple system is the one identified in the above catalog as having an angular separation less than 250 mas, while the wide orbit's angular separation is much larger. These objects are of no interest for the purposes of this project, and this ambiguity can be resolved by consulting Pourbaix et al. (2004). The spectroscopic orbits contained within this catalogue are also useful in orbit fitting, which will be discussed in greater detail later.

2.1.3 The Multiple Star Catalog

The Multiple Star Catalog (MSC) (Tokovinin 1997) is a nearly perfect resource tool for this project. It is a collection of all known information on hundreds of multiple systems. All published visual and spectroscopic orbits are presented along with references for each. Included with each object is a hierarchical diagram showing the structure of the multiple system along with the standard naming convention for each component. Also given are all known magnitudes of the individual components as well as the collective magnitude of binary and multiple components. A "separation" value is given for the angular distance between two components in an orbit. This value is somewhat vague, as the author(s) of the catalog maintain that the exact meaning of the "separation" depends uniquely on the type of system. Although it is unclear whether this value refers to either an orbital semi-major axis for the system or some epoch-specific angular separation, this value does provide a good idea of the size of the system and whether or not a candidate can be eliminated based on this criterion. Finally, the spectral types of the individual components are given when known, as well as the composite spectral types of binary and multiple components.

This catalog contains all of the necessary information to create a target list of multiple systems. Unfortunately, this catalog was only discovered several months into this project, otherwise the need for the first two catalogs would have been minimal. All magnitudes in the MSC are given in V and must be converted to K, which is close to CHARA's K' observing band. K magnitudes are estimated using the spectral types of the individual components and $V-K$ values given in Cox (2000). Conversion to K gives the overall magnitude as well as ΔK_{wide} and $\Delta K_{\mathrm{close}}$, although missing individual magnitudes and spectral types complicate the process. Although unknown magnitudes can lead to uncertainty in ΔK_{wide} and $\Delta K_{\mathrm{close}}$, these objects are not rejected as targets. Observation of these objects will reveal whether these objects should be rejected based on ΔK_{wide} (absence of secondary fringe packet) or $\Delta K_{\mathrm{close}}$ (no visibility modulation in the target). The other determination that can be made using this catalog is the size of the potential calibrator in these systems. First, any references listed in the MSC are consulted in order to find radius measurements. If none are found, the size can be estimated using the spectral type and parallax given in the MSC and the radii for each spectral type given in Cox (2000). All tertiary components with an angular diameter greater than 0.5 mas are considered to be too resolved to serve as good calibrators.

Examination of these catalogs has produced the target list given in Table 2.2. All of the information given in Table 2.2 has been taken directly from the Multiple Star Catalog, except for the system K-magnitudes, which were taken from 2MASS (Skrutskie et al. 2006). Unfortunately, the table has many holes where information is unavailable. The list is separated into two groups: good targets and marginal targets, where good targets are loosely defined as those that satisfy most of the criteria described above, while marginal targets only satisfy some of the criteria.

Table. 2.2: Main Target List

Target(HD)	RA	Declination	"Separation"	K mag	V mag[1]						Sp. Type		
	J2000.0	J2000.0	(mas)	$P+S+T$	$P+S+T$	$P+S$	T	P	S	$P+S$	T	P	S
Good:													
3196	00 35 14.9	−03 35 34.2	241	3.90	5.20	5.60	6.30	⋯	⋯	F8V	G0V	⋯	⋯
23302	03 44 52.5	+24 06 48.0	62	3.92	3.70	3.70	5.70	⋯	⋯	B6III	⋯	⋯	⋯
35411	05 24 28.6	−02 23 49.7	44	3.90	3.64	4.24	5.65	4.50	5.90	B1V	B3V	B1V	B3V
37043	05 35 26.0	−05 54 35.6	140	3.75	2.77	2.82	6.12	⋯	⋯	O9III	B1III	⋯	⋯
41040	06 03 27.4	+19 41 26.0	53	5.36	5.14	5.14	6.67	5.92	6.66	B8III	B5V	B7III	B8III
58728	07 27 44.4	+21 26 42.9	74	4.14	5.25	5.58	6.58	6.11	6.61	F5V+	⋯	⋯	⋯
98353	11 19 07.9	+38 11 08.0	91	4.46	4.78	5.39	5.69	5.89	6.47	A1V	A1V	A1V	A2V
102928	11 51 02.2	−05 20 00.0	200	3.21	5.64	⋯	⋯	⋯	⋯	K0III	⋯	⋯	⋯
107259	12 19 54.4	−00 40 00.5	136	3.79	3.89	4.20	6.50	4.20	6.00	A2IV	⋯	⋯	⋯
129132	14 40 21.9	+21 58 33.1	74	5.07	6.10	⋯	⋯	⋯	⋯	G0III	⋯	⋯	⋯
157482	17 21 43.7	+39 58 28.4	75	3.84	5.51	6.82	6.11	6.82	8.27	F2V	G0III	F2V	F8V
173654	18 46 28.6	−00 57 41.6	219	5.60	5.90	⋯	⋯	⋯	⋯	A2Vm	⋯	⋯	⋯
176155	18 58 14.7	+17 21 39.3	161	3.53	5.38	⋯	⋯	⋯	⋯	F8Ib	⋯	⋯	⋯
183344	19 29 21.4	−07 02 38.7	74	3.98	6.61	⋯	⋯	⋯	⋯	F7I	⋯	F7I	A2
187949	19 53 06.4	−14 36 11.5	155	5.81	6.46	6.46	9.20	6.60	8.76	A2V+	F7V	A2V	G8IV
193322	20 18 07.0	+40 43 55.5	67	5.72	5.97	⋯	⋯	⋯	⋯	O9V	⋯	⋯	⋯
203156	21 14 28.8	+10 00 25.1	100	4.46	5.89	⋯	⋯	⋯	⋯	F1III	B7V	⋯	⋯
206901	21 44 38.7	+25 38 42.1	236	2.92	4.70	5.04	4.74	⋯	⋯	F6IV	F5IV	F6IV	K0V
216494	22 53 28.7	−11 36 59.5	79	5.93	5.80	6.33	6.83	6.89	7.31	B9III	⋯	⋯	⋯
Marginal:													
5408	00 56 47.0	+60 21 46.2	34	5.68	6.11	6.56	7.27	6.85	8.15	A0V	A1V	A0V	A4V
29763	04 42 14.7	+22 57 24.9	284	4.62	4.28	4.37	7.01	4.37	6.04	B3V	⋯	B3V	⋯
41116	06 04 07.2	+23 15 48.0	198	2.18	4.16	5.34	4.61	5.53	7.33	G8III	G7III	⋯	⋯
43358	06 15 54.0	+01 10 08.7	167	5.20	6.37	6.90	7.40	7.60	7.70	F6V	F5V	F6V	F6.5V
73712	08 40 20.1	+19 20 56.4	150	6.05	6.78	7.53	7.53	8.19	8.39	⋯	A9V	F0V?	⋯
85040	09 49 50.1	+21 10 45.9	208	5.47	6.09	6.55	7.24	7.30	7.30	A7IVn	A8IV	A7IVn	A7IV
86590	10 00 01.7	+24 33 09.9	220	5.44	8.45	8.57	10.87	9.32	8.32	K0V	⋯	K0V	⋯
103483	11 55 05.7	+46 28 36.6	225	6.36	6.54	6.70	8.50	7.40	7.40	A3Vn	⋯	A3Vn	A3Vn
115955	13 20 15.8	+17 45 57.0	119	5.90	7.14	7.63	8.23	⋯	⋯	F8	⋯	F8	⋯
135681	15 16 48.6	−13 02 21.1	155	6.54	7.25	7.25	⋯	7.10	7.60	A3IV	⋯	A3IV	A4V?
163151	17 54 14.2	+11 07 50.0	87	5.03	6.38	6.58	8.33	⋯	⋯	F5V	⋯	F3V	⋯
169985	18 27 12.5	+00 11 46.0	27	3.39	5.34	6.25	5.95	6.82	7.22	A6V	G0III	A6V	A7V
185936	19 41 05.5	+13 48 56.5	129	6.21	6.01	6.73	6.79	⋯	⋯	B5V	⋯	B5V	⋯
197226	20 41 00.4	+39 04 56.4	134	6.79	6.51	⋯	⋯	⋯	⋯	B6III	⋯	B6III	⋯
203345	21 21 21.6	+10 19 56.2	105	5.38	6.75	7.52	7.48	⋯	⋯	F7V	F7V	F7V	⋯

Table. 2.2 – Continued

Target(HD)	RA	Declination	“Separation”	K mag	V mag						Sp. Type		
	J2000.0	J2000.0	(mas)	$P+S+T$	$P+S+T$	$P+S$	T	P	S	$P+S$	T	P	S
206155	21 40 01.9	+09 11 05.1	30	6.65	6.90	···	7.50	···	···	A3m	F5V	A3m	···
206267	21 38 57.6	+57 29 20.5	100	5.22	5.62	5.84	7.45	6.26	7.06	O6.5V	B0V	O6.5V	O9V
216963	22 57 02.5	+24 40 56.0	182	6.92	8.76	9.24	9.88	···	···	K0V	···	K0V	···
217312	22 58 39.8	+63 04 37.7	240	6.52	7.44	7.54	10.11	···	···	B0IV	···	B0IV	···
219018	23 12 38.6	+02 41 10.4	204	6.18	7.72	8.33	8.63	8.33	12.73	G1V	G3V	G1V	M0V
219634	23 16 27.1	+61 57 46.6	120	5.97	6.53	6.63	9.22	···	···	B0V	···	B0V	···

[1]P = primary of the close binary, S = secondary of the close binary, and T = tertiary component. In some cases, the tertiary is the brighter component of the system and would be considered the “primary” component by standard definitions. However, the designations here are based only upon the geometry of the system.

2.2 Observation Planning

When observing SFPs, the separation between the packets is a projected separation along the particular baseline of observation rather than the intrinsic separation in the orbit. The projected angular separation ρ_{proj} is related to the intrinsic separation ρ by the following equation:

$$\rho_{\mathrm{proj}} = \rho \ \ cos(\theta - \psi) \tag{2.2}$$

where θ is the position angle of the wide orbit and ψ is the position angle of the observation baseline. With knowledge of the wide orbit in the triple system, a suitable baseline can be selected such that the projected angular separation is below the threshold determined above for a given epoch.

For the wide orbit, ρ and θ can be calculated for a given epoch using the seven standard orbital elements for a visual binary. The details of this method are presented in Appendix A. In addition, the details of the calculation of the baseline length B and baseline position angle ψ for a given epoch are found in Appendix A. This information can be plugged into equation 2.2 to obtain ρ_{proj} for the wide orbit in mas for the given epoch. That ρ_{proj} can be then plugged into equation 2.1 to determine the separation in delay space. This information can be used to establish favorable observing epochs and baselines for any target. As an example, Table 2.3 examines the projected separation for one target on a single night. The value of ρ_{proj} is given in μm for every hour of the night on every baseline. Because this night is post-2008, any value of ρ_{proj} larger than 142.0 μm will result in SFPs that cannot be observed simultaneously.

Table 2.3. Projected Separation Table (in μm) for HD 3196 on 2010 Dec 1

		Time (UT)											
Name	B_{m}	2:00	3:00	4:00	5:00	6:00	7:00	8:00	9:00	10:00	11:00	12:00	13:00
W2 S1	210.96	44.5	0.8	38.5	70.9	94.2	106.8	107.8	97.1	75.4	44.2	5.6	37.6
W2 S2	177.44	30.2	6.9	39.8	66.5	85.2	94.4	93.6	82.8	62.8	34.8	0.9	36.6
W2 E1	221.84	297.8	297.7	279.4	244.1	194.3	133.1	64.4	6.1	73.0	133.1	182.0	216.4
W2 E2	156.28	209.5	210.8	199.2	175.5	141.1	98.4	50.0	0.2	48.1	91.5	127.3	153.0
W2 W1	107.93	110.7	128.3	136.9	135.9	125.4	106.1	79.3	46.8	10.5	25.9	60.9	92.1
W1 S1	278.50	66.5	127.4	175.2	206.6	219.4	212.6	186.8	143.5	85.8	17.6	56.1	130.2
W1 S2	249.39	80.7	135.0	176.5	202.2	210.3	200.2	172.6	129.3	73.2	8.3	60.8	129.2
W1 E1	313.54	408.5	426.1	416.4	380.2	319.9	239.7	144.8	40.3	62.3	158.7	242.9	308.5
W1 E2	251.34	320.2	339.2	336.3	311.5	266.7	204.8	130.2	47.0	37.4	117.1	188.2	245.2
E2 S1	278.77	254.5	211.9	160.4	103.7	45.8	9.4	58.1	97.1	123.8	136.2	133.6	116.0
E2 S2	248.13	240.2	204.2	159.2	108.2	54.9	3.0	43.9	82.9	111.2	126.8	128.8	116.9
E2 E1	65.89	88.4	86.9	80.2	68.7	53.2	34.7	14.4	5.9	24.9	41.5	54.7	63.4
E1 S1	330.67	343.1	298.9	240.7	172.3	98.7	25.0	43.7	103.0	148.7	177.8	188.3	179.4
E1 S2	302.33	328.7	291.2	239.4	176.8	107.8	37.4	29.6	88.7	136.1	168.5	183.6	180.4
S2 S1	34.08	14.3	7.7	1.3	4.4	9.1	12.4	14.2	14.2	12.6	9.3	4.7	1.0

Although in theory, one could observe SFPs at any separation less than or equal to 142.0 μm, in practice, this is not the case. At the limit, the peaks of the two fringe packets will be separated by 142.0 μm, as shown in Figure 2.1. In order to reduce the data obtained on fringe packets, the entire packets must be visible. To accomplish this, the coherence length of the fringe packets must be taken into account. The coherence length is a measure of the length of a fringe packet in the direction of the motion of the dither mirror, as shown in Figure 2.2. It is determined solely by the parameters of the instrument and is given by

$$\Lambda_{\text{coh}} = \frac{\lambda^2}{\Delta\lambda} \tag{2.3}$$

where λ is the wavelength of observation and $\Delta\lambda$ is the observation bandwidth. Although λ is a well-known quantity at CHARA ($\lambda = 2.1329$ μm), $\Delta\lambda$ is not. Previously, a value of $\Delta\lambda = 0.250$ μm had been adopted, but recent estimates by Bowsher (2010) suggest that the value is closer to 0.350 μm. Using these values, the coherent length is $\Lambda_{\text{coh}} = 13.0$ μm. Taking into account the size of both fringe packets, the new maximum tolerable separation to observe SFPs is 142.0 - 26.0 = 116.0 μm. This separation can be viewed in Figure 2.3.

Drifting of the fringe packets must also be considered. Due to minor inconsistencies in the baseline solution of CHARA, the fringe packets will drift out of the scanning window over time. Although the cart upon which the dither mirror sits moves during observation to equalize the optical path length for the two telescopes,

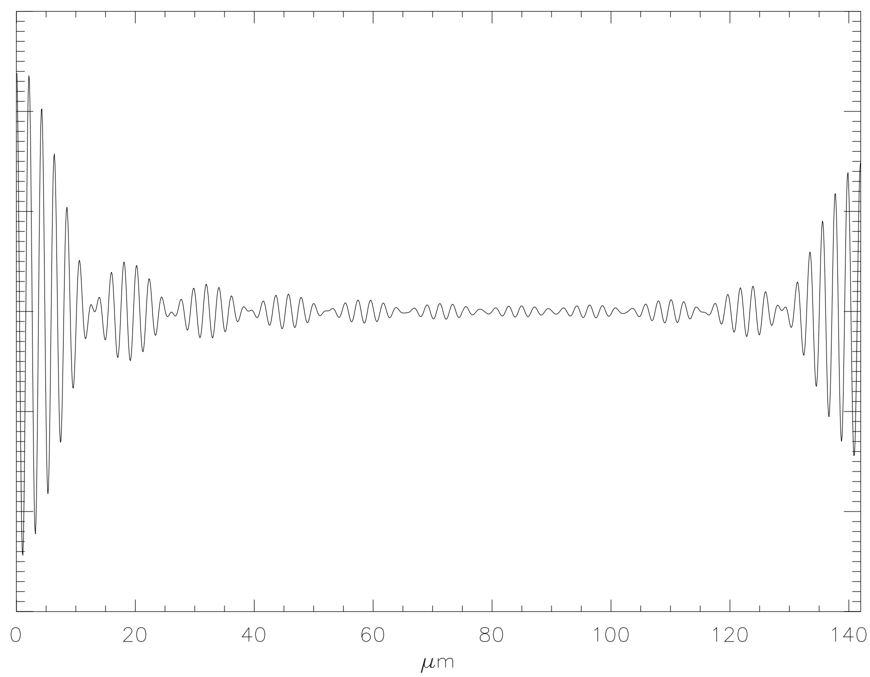

Figure. 2.1: Separated Fringe Packets at Threshold of Simultaneous Observation. These fringe packets are separated by 142.0 microns.

the minor inconsistencies can cause the fringe packets to drift by several hundred μm per hour. To account for this effect, CHARA's observation software includes the "SERVO" tool, which attempts to lock onto a target by finding the highest amplitude point in a scan, then shifting that position to the center of the scanning window. This tool is wonderful for observing single fringe packets, but has limited effectiveness for SFPs. The SERVO will lock onto the higher amplitude packet, moving it to the center and pushing the lower amplitude packet outside the window. The observer must manually move the window to keep the SFPs visible. When issuing the command to move the window, there is a slight time delay between the computer at AROC and the physical apparatus that moves the window. This can cause the observer to

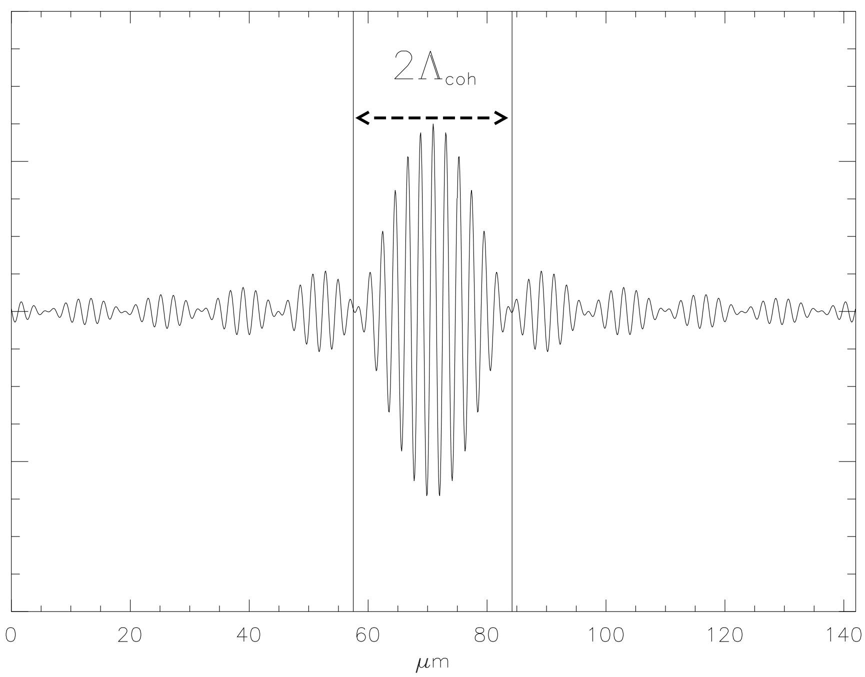

Figure. 2.2: Coherence Length. The distance between the vertical lines represent twice the coherence length of the fringe packet.

continually undershoot or overshoot the proper amount of movement, especially for fringe packets separated as widely as those in Figure 2.3. This effect can be compounded by poor seeing. Seeing-induced piston variations cause the fringe packets to oscillate back and forth around their rest position. This oscillation amounts to a few dozen μm in amplitude, making it nearly impossible to keep both widely separated fringe packets in the window. Poor seeing is defined as seeing that causes a standard deviation in the position of a fringe packet larger than 28 μm (20% of the 142 μm scanning range). Thus, although in theory it is possible to reduce data on fringe packets of separations near 116 μm, it is impratical to do so. A maximum separation of 100.0 μm is preferred.

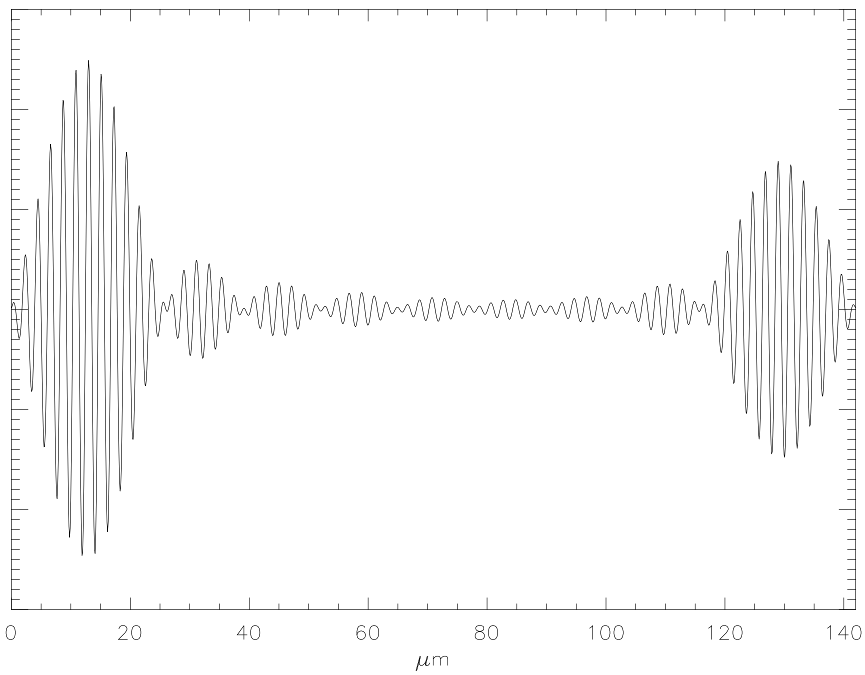

Figure. 2.3: Fully Visible Separated Fringe Packets. These fringe packets are separated by 116.0 microns.

All of the discussion so far has focused on finding the upper limit of separation. Of equal importance is the lower limit of separation. At a separation of zero, packets are blended together, and the individual fringes constructively interfere with each other. At small non-zero separations, the fringe packets are still blended together. For fringe packets of equal amplitude, the smallest separation at which the individual packets can be resolved is roughly 5.1 μm. This quantity increases with increasing amplitude ratio of the fringe packets.

At very small separations, the visibility of each fringe packet is corrupted by the side lobes of the other packet. The fringes in the side lobes of one packet will either constructively or destructively interfere with the fringes of the other packet, and vice versa, thus changing the amplitude (visibility) of the packet. The resulting visibility is not the true visibility of the system. An example of this effect is shown in Figure 2.4. Because the visibility is integral in determining the orbit of the system, observing SFPs that are close together is unacceptable. Extensive modeling of this "side-lobe interference" was conducted and is presented in Chapter 4. For now, this effect is only taken into account in terms of observation planning. The preference here is that during observations, each packet should lie fully outside of the other packet's second side lobe. The second side-lobe is selected as the cutoff point because at this point, the amplitude of side-lobe interference is roughly at the level of the scatter in the data in most cases. As with the coherence length, the location of the side lobes of a fringe packet is determined solely by the parameters of the instrument. The point between the second and third side-lobes lies at a distance of 32.0 μm from the peak of the central fringe packet for $\lambda = 2.1329$ μm and $\Delta\lambda = 0.350$ μm. Taking the coherence length into account, the fringe packets must be separated by 45.0 μm to achieve the desired separation, as shown in Figure 2.5.

An upper limit (100.0 μm) and lower limit (45.0 μm) have now been established for observation purposes. "Separation tables" like Table 2.3 are created for each target for the 1st and 15th day of each month during the observing season. The separation values are not substantially different on consecutive nights, so creating separation tables twice a month is sufficient. Analyzing all the separation tables generated for a particular date gives an idea of which baselines can produce good data for several

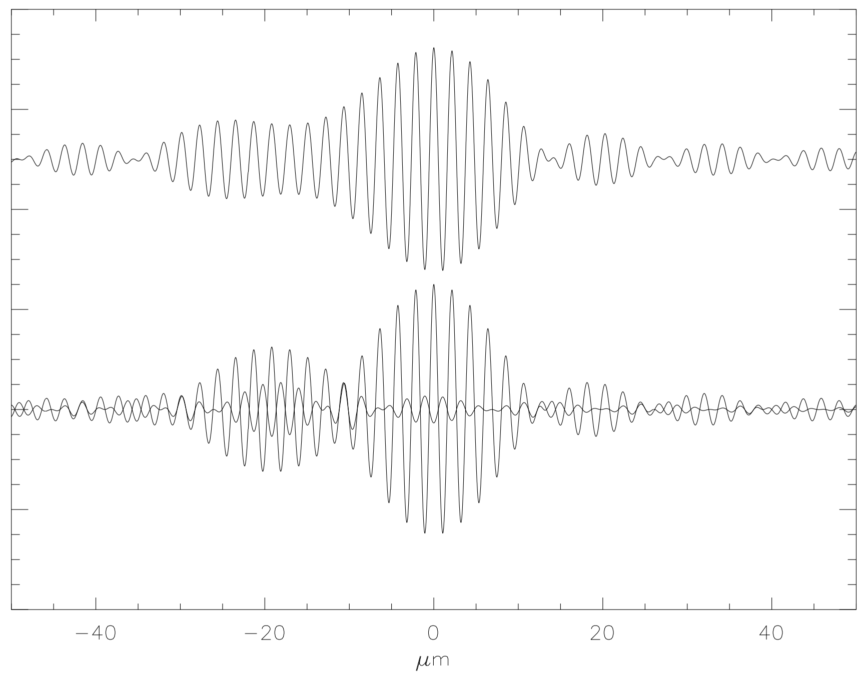

Figure. 2.4: Side-Lobe Interference. This is an example of side-lobe interference between two fringe packets. The bottom half of the plot shows two model fringe packets as single functions. The top half shows the addition of those two functions and how the visibility amplitudes change from their original value.

targets. In 2009, the decision was made to focus on the targets for which SFPs had already been observed, which amounted to seven objects (HDs 3196, 35411, 98353, 107259, 129132, 157482, 206901). Parameters of these seven targets, in addition to HD 193322 (an object observed by others and later added to this project), are presented in Table 2.4. Separation tables for these targets were consulted first when planning observations. Separations outside of the noted range were considered acceptable for other targets if the requirements for the main targets had been satisfied.

Most targets can only be observed for a few hours. Examination of Table 2.3 shows that the separation changes rapidly with time for certain baselines. This is due

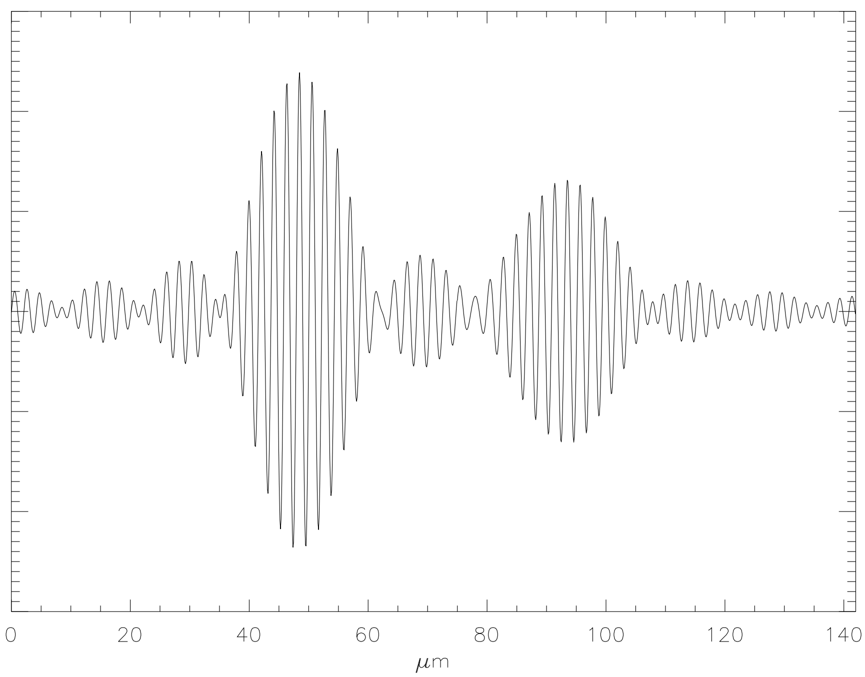

Figure. 2.5: Separated Fringe Packets at Lower Limit of Observation. These fringe packets are separated by 45.0 μm.

to the phenomenon known as baseline rotation, which is similar to aperture synthesis. As Earth rotates, the baseline's length and position angle change from the perspective of the target. Looking at equation 2.2, as ψ changes, ρ_{proj} also changes. The other variables in equation 2.2, ρ and θ, change during observation due to orbital movement. However, the wide orbits for all targets associated with this project are on the order of years, so the orbital motion during observation is minimal, and changes in ρ_{proj} are dominated by baseline rotation.

This observation scheme was first implemented in 2009 with great success. SFPs were always present when expected and were easily manageable despite the drifting fringe packets and changing separation, except in instances of poor seeing. The biggest

Table 2.4. Targets that produced separated fringe packets

HD No.	Name	π (mas)	V mag wide	V mag close	Sp. Type wide	Sp. Type close	$\alpha_{\rm wide}$ (mas) wide	$\alpha_{\rm wide}$ (mas) close	P (days) wide	P (days) close
3196	13 Ceti	47.51	6.30	5.60	G0V	F8V	241	1.73	2517	2.1
35411	η Ori	3.62	5.65	4.24	B3V	B1V	44	0.78	3449	8.0
98353	55 UMa	17.82	5.69	5.39	A1V	A1V	91	0.93	1873	2.6
107259	η Vir		6.50	4.20	···	A2IV	136	7.53	4792	71.8
129132	···		···	6.10	···	G0III	74	6.69	3385	101.6
157482	V819 Her	14.70	6.11	6.82	G0III	F2V	75	0.67	2019	2.2
193322	CHARA 96		···	5.97	O9V	O8III	67	3.90	11432	312.4
206901	κ Peg		4.74	5.04	F5IV	F6IV	236	2.81	4240	6.0

difficulty with this scheme is finding a baseline and night on which several targets can be observed, but for the 2009 and 2010 observing seasons, this was not a problem. There was concern that the inaccuracy of the published wide orbits might lead to a $\rho_{\rm proj}$ different than what was expected, but, at least for the main targets, this was not a problem either. Of the seven main targets mentioned earlier, only HD 107259 suffers from a lack of data. This was due to weather conditions and technical issues with the Array.

Because all pre-2009 data were taken before the observation scheme was put into effect, many observations during that time featured SFPs outside the necessary range in separation. These data fall into four categories. First, data in which the separation is nearly zero show no SFPs, and must be discarded. Second, data in which the separation is small, but still large enough to show SFPs, may be usable under certain conditions which will be discussed in Chapter 4. Third, data similar to Figure 2.1, in which SFPs are visible, but impossible to keep in the scanning window, must be discarded. Fourth, if the SFPs are separated by several scanning windows in length, it becomes possible to use the “bracketing” method to collect data. Bracketing involves separately observing the calibrator and target and alternating between the two.

– 3 –
Data Reduction

The objective in reducing SFP data is to obtain two instrumental visibilities, one for the target close binary and one for the calibrator wide component. Once these are obtained, the instrumental visibilities of the wide component can be used to calibrate the instrumental visilibities of the close binary. The calibrated visibilities of the close binary can then be used for orbit fitting. Although SFPs have been reduced extensively for multiplicity studies and determining separations, SFP data have never been reduced for the purposes of obtaining visibilities from both packets. The data reduction code used here is a modified form of the MathCAD program "VisUVCalc," written by H.A. McAlister and A. Jerkstrand and based on Benson et al. (1995). The original program directly fits the individual fringes in the packets, determining V, the visibility of the packet. VisUVCalc also calculates B and ψ for the epoch of observation.

3.1 Initial data processing

Data sets obtained are standard for observations with the "CHARA Classic" beam combiner. These files consist of roughly 200 scans of the dither mirror, which oscillates back and forth through 142.0 μm of delay at a frequency of 150 Hz in the region that the fringe packets are detected. The scan accumulation time is limited to about 5 minutes. In theory, objects could be observed for a longer period of time, but data sets obtained in this fashion have consistently crashed the data reduction code.

CHARA records data using two detector channels, the first of which records the transmissive component of the beam from one telescope and the reflective component of the beam from the other telescope, while the second records the opposite. CHARA's detectors record the photon count and the dither mirror position once per millisecond. The dither mirror positions can be used to break the data into individual scans by finding every instance in which the mirror changed direction. For the purposes of data reduction, the x-axis for all scans is left as time in ms, rather than converting to μm of delay space or mas of angular distance. The recording process is bookended by shutter sequences (visible in Figure 3.1 as the dips in the flux level) which help measure the noise levels and the flux ratio between the two telescopes. The first and third areas of the shutter sequence represent the flux levels of the individual telescopes. The shutter for one telescope is closed in the first region and the shutter for the other telescope is closed for the third region. The second region represents the dark noise scans, where the shutters for both telescopes are closed.

The first step in reducing these data is to account for the dark level, which is accomplished by calculating the average flux value from all dark noise scans in both the "before" and "after" noise scans and subtracting that value from all points in Figure 3.1. Data with the dark noise subtracted is presented in Figure 3.2. After breaking up the data into individual scans, a low-pass filter can be applied to normalize each scan, as shown in Figure 3.3. After obtaining the normalized functions of intensity with respect to time for both detectors, the visibility as a function of time can be

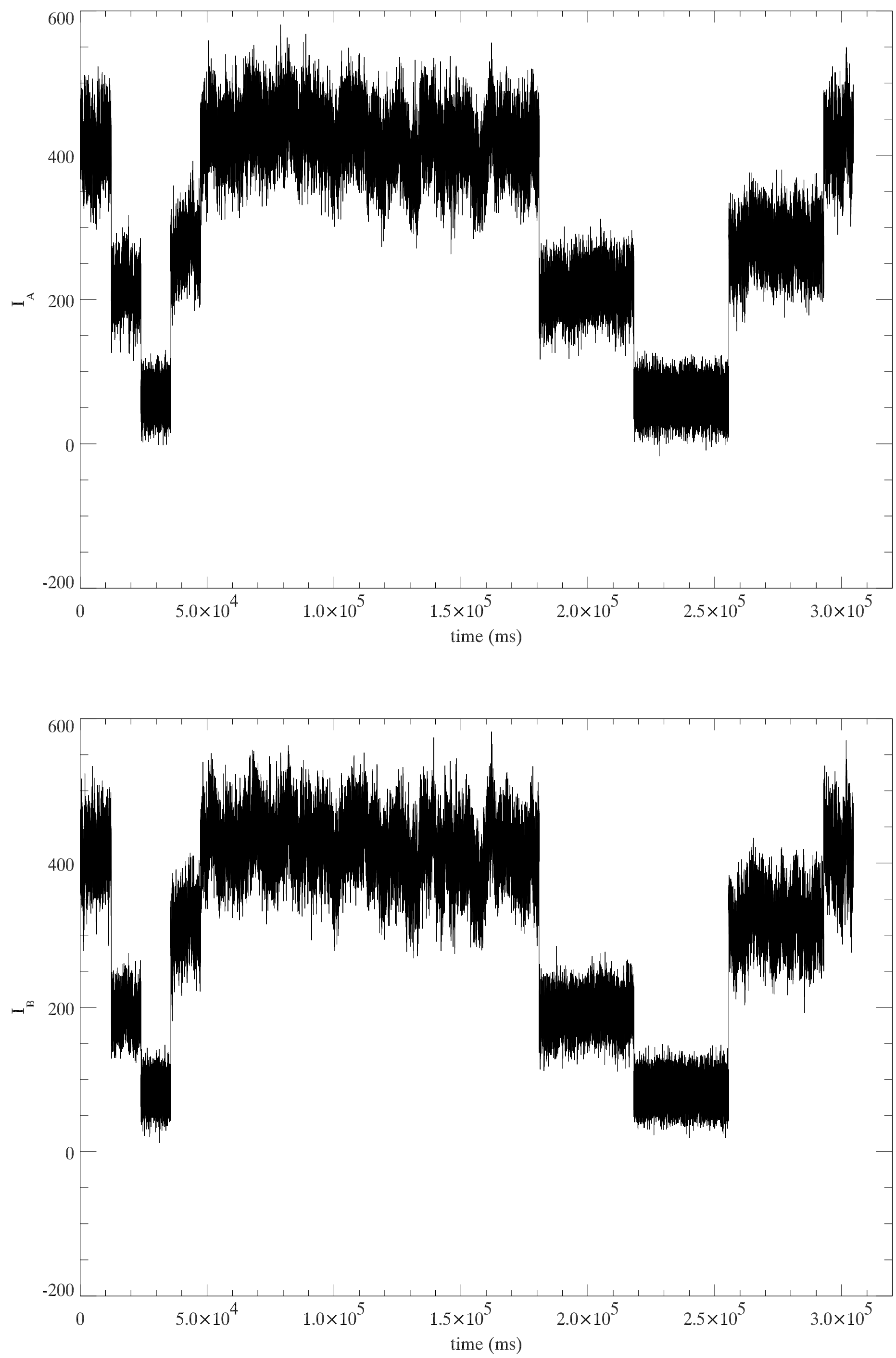

Figure. 3.1: Typical raw data from a single detector

determined. From Benson et al. (1995), the normalized intensities of both detectors are known:

$$I_{\mathrm{A,N}}(t) = 1 + \frac{2\sqrt{\alpha\beta}}{\alpha+\beta} V(t) \tag{3.1}$$

$$I_{\mathrm{B,N}}(t) = 1 - \frac{2\sqrt{\alpha\beta}}{1+\alpha\beta} V(t) \tag{3.2}$$

$$V(t) = V \frac{\sin(\pi\Delta\sigma v_{\mathrm{g}} t)}{(\pi\Delta\sigma v_{\mathrm{g}} t)} \cos(2\pi\sigma_0 v_{\mathrm{g}} t + \phi) \tag{3.3}$$

where $\alpha = I_2/I_1$, the intensity ratio between the two telescopes, $\beta = R/T$, the ratio between the reflectance and transmittance of the beam splitter, $V(t)$ is the visibility as a function of time, V is the visibility amplitude, $\Delta\sigma$ is the inverse of the coherence length ($\Lambda_{\mathrm{coh}}^{-1}$), v_{g} is the group velocity of the dither mirror, t is time, σ_0 is the wavenumber, and ϕ is the phase. By rearranging equations 3.1 and 3.2, the time-dependent visibility can be written as a function of the intensities of the two detectors:

$$V(t) = 0.5(\alpha\beta)^{-0.5}\left(\frac{1}{\alpha+\beta} + \frac{1}{1+\alpha\beta}\right)^{-1}(I_{\mathrm{A,N}}(t) - I_{\mathrm{B,N}}(t)). \tag{3.4}$$

The flux reaching the detectors during the shutter sequence allows for the determination of the quantities α and β. When shutter S_1 is closed, the flux reaching detector A, indicated as I_{AS1}, is $I_2 T$, while the flux reaching detector B (I_{BS1}) is $I_2 R$. Similarly, when shutter S_2 is closed, the fluxes reaching detector A and B are, respectively, $I_{\mathrm{AS2}} = I_1 R$ and $I_{\mathrm{BS2}} = I_1 T$. These four variables can be determined by the shutter sequences. For example, to determine the value of I_{AS1} for a particular data set, the average of all points in the designated regions in Figure 3.2 is calculated. From the aforementioned definition of α and β, the following can be derived:

$$\alpha = \frac{I_{\text{AS1}}}{I_{\text{BS2}}} = \frac{I_{\text{BS1}}}{I_{\text{AS2}}} \tag{3.5}$$

and

$$\beta = \frac{I_{\text{BS1}}}{I_{\text{AS1}}} = \frac{I_{\text{AS2}}}{I_{\text{BS2}}}. \tag{3.6}$$

Once the coefficients α and β have been determined, a "visibility scan" can finally be calculated from equation 3.4. Next, the scan is smoothed by isolating the fringe frequency in the scan's power spectrum. Taking the Fourier Transform of a scan gives the characterization of the fringe packets in the frequency domain. The peak of this power spectrum is ideally located at the frequency set during observation, which, for this project, is generally 150 Hz, but can occasionally be 100 Hz for fainter targets. After locating the peak, a bandpass filter of 60 Hz is applied to enhance the fringe signal relative to the noise present at other frequencies. Bandpass-filtering is equivalent to multiplying the power spectrum by a box function whose box width is 60 Hz. This enhanced signal is inverse Fourier Transformed to obtain the smoothed visibility scan. The power spectrum for an example scan has been presented in Figure 3.4 along with the boundaries for the bandpass-filtering. Figure 3.5 shows the results of bandpass-filtering, with the smoothed scan offset from the unsmoothed scan for

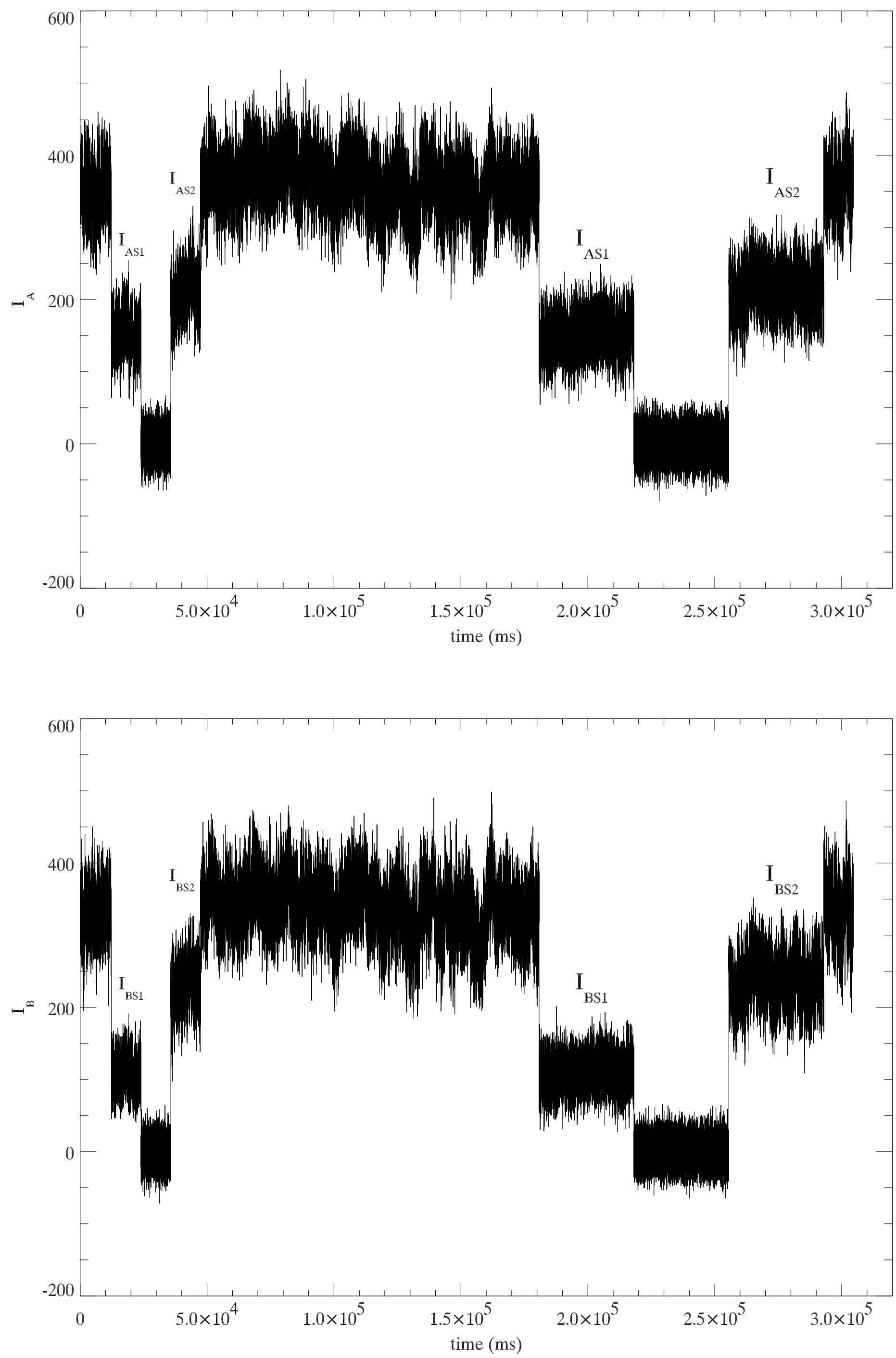

Figure. 3.2: Dark noise-subtracted data

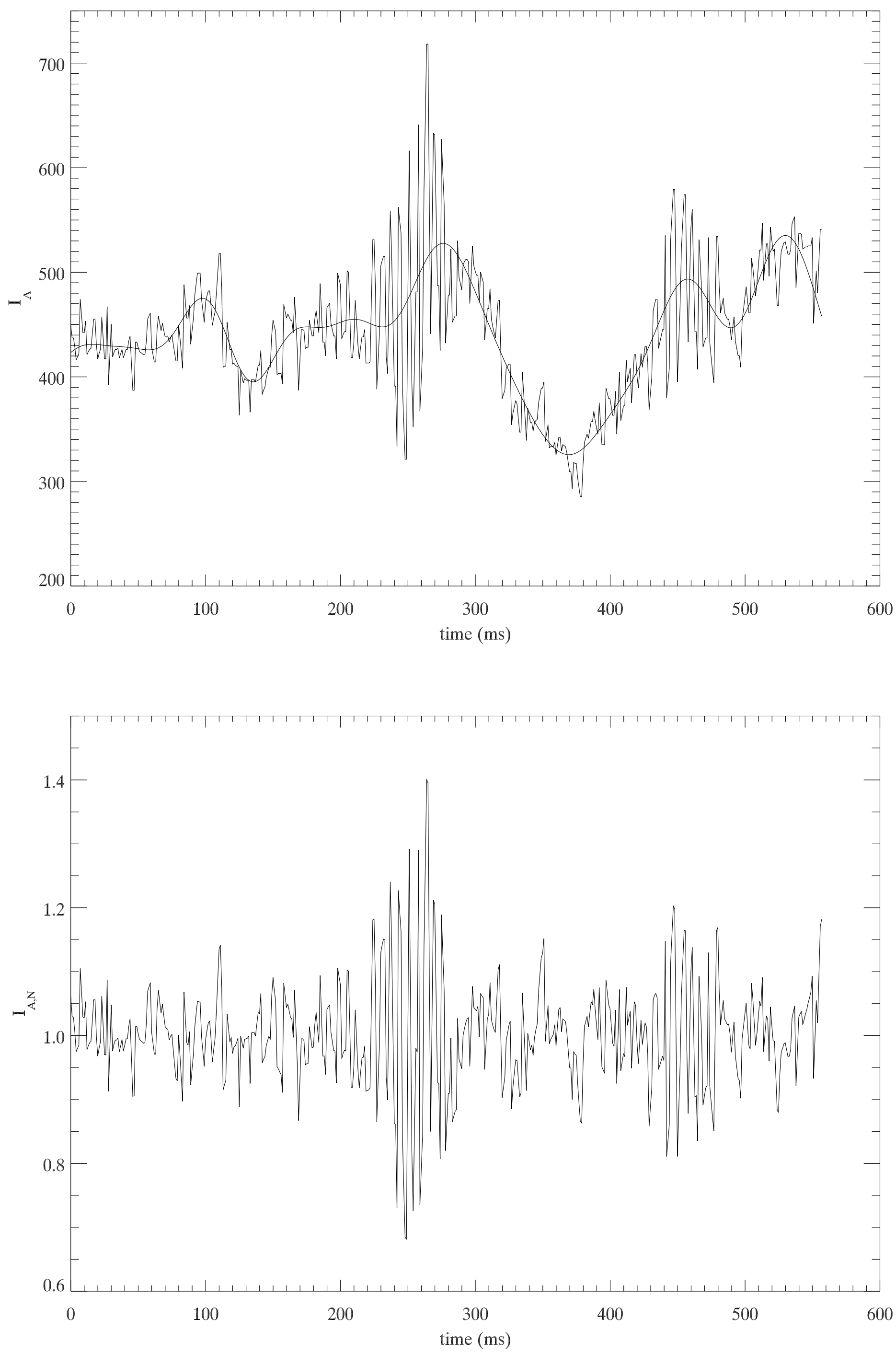

Figure. 3.3: Normalization. This shows the method of normalizing a CHARA data scan.

clarity. The bandpass-filtered scan is the final product that is now used to evaluate the presence of SFPs.

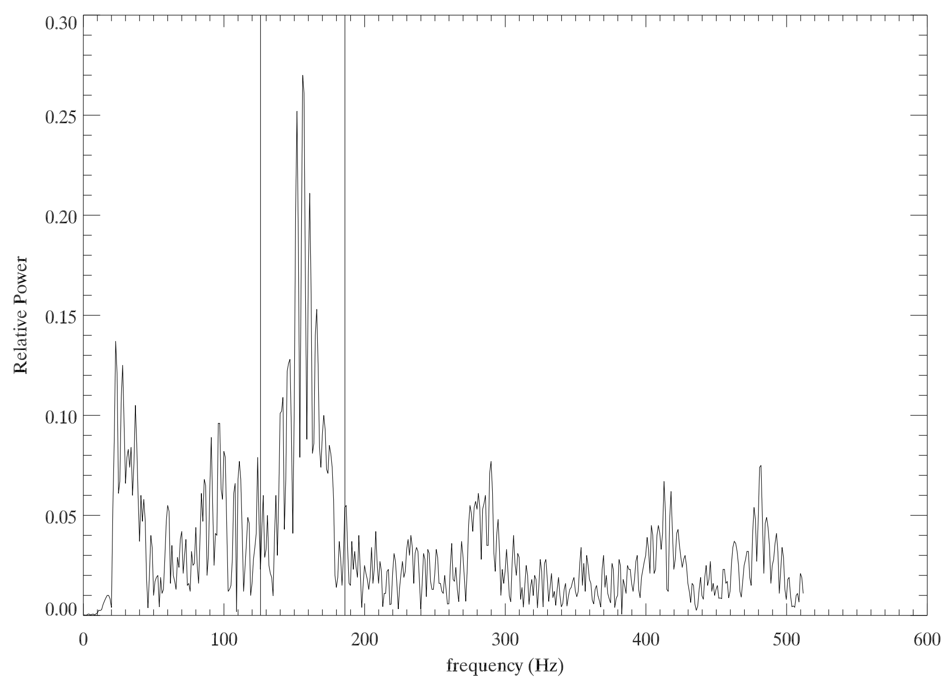

Figure. 3.4: Bandpass filtering. The vertical lines show the boundaries of bandpass filtering.

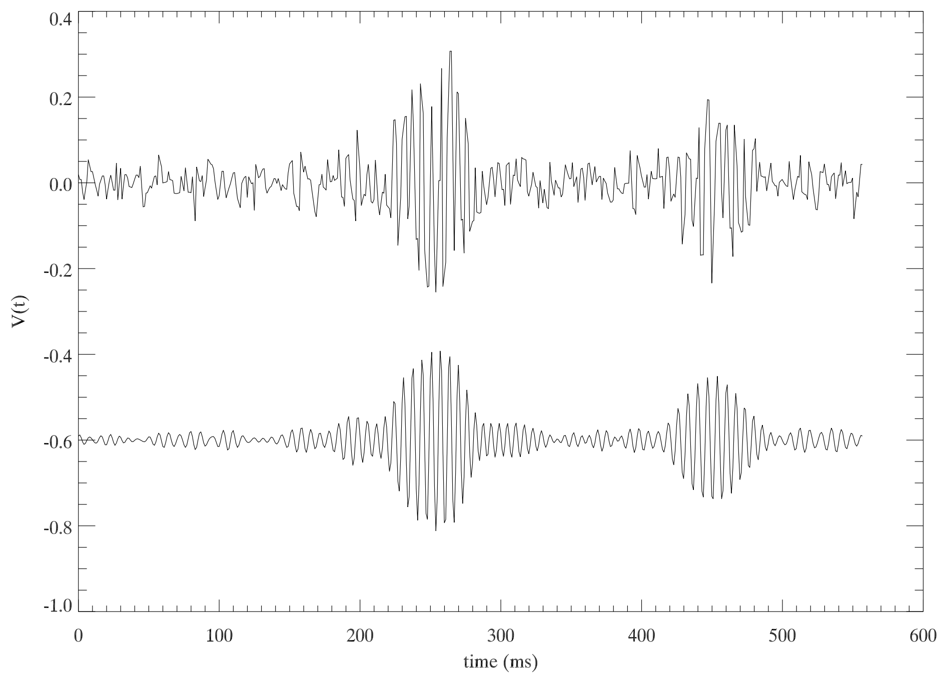

Figure. 3.5: Bandpass-filtered scan. The top half of the plot shows the normalized scan in the lower plot of Figure 3.3. After applying the 60-Hz bandpass filter shown in Figure 3.4, the result is the smoothed scan in the lower half of the plot.

3.2 Finding separated fringe packets

The next step is to actually search data for the presence of SFPs. A useful tool in this undertaking is the fringe envelope. The fringe envelope is obtained by performing a Hilbert Transform on the visibility scan, in which the negative frequencies are shifted by -180°, leaving only the positive frequencies (Farrington et al. 2010). The absolute value of the resulting inverse transformation is the envelope of the scan. The envelope of the smoothed scan in Figure 3.5 is shown in Figure 3.6. Shift-and-add co-addition of many scan envelopes very effectively smooths the atmospheric noise present in the individual scans, leaving any possible fringe packets clearly visible. The shift-and-

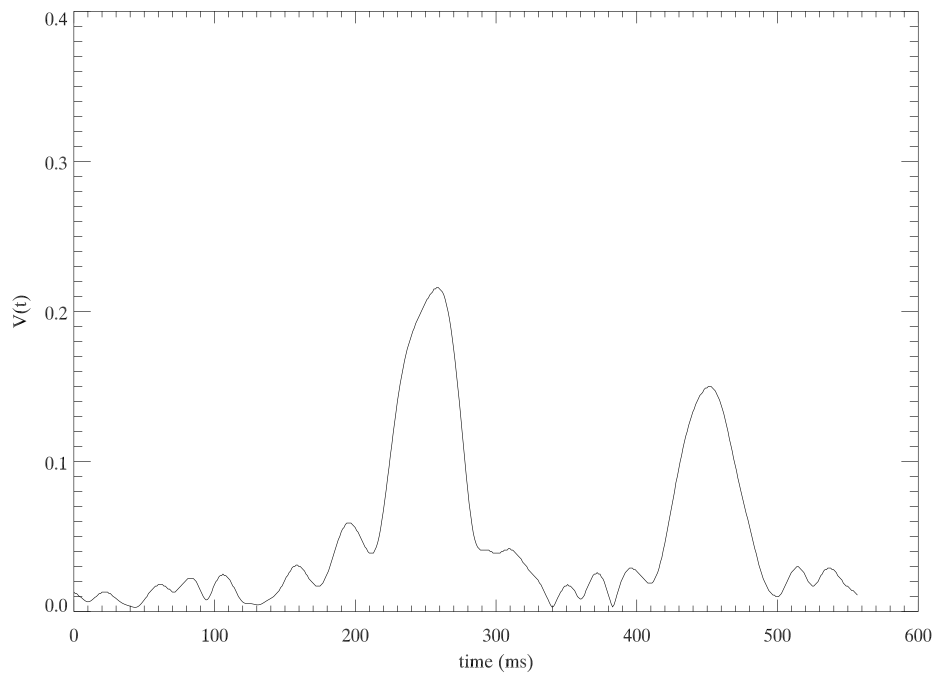

Figure. 3.6: Fringe envelope of a single scan

add procedure involves identifying the maximum of each scan's envelope, shifting all of them to the same position on the x-axis, and adding all the scans together. Instances of poor seeing can cause the secondary packet to move relative to the position of the primary packet from scan to scan, so that in the shift-and-added envelope, the secondary packet may be smeared out and not visible. Thus, data must be meticulously examined in order to confirm or deny the existence of the secondary packet. Fig. 3.7 shows a shift-and-added envelope for an entire data set. The primary packet is prominent, and the secondary packet is clearly visible to the right of the primary. In cases where the two fringe packets are of similar amplitude, the shift-and-add process may produce secondary packets on the left and right of the primary.

This is due to the possibility of the maximum of the scan switching between the fringe packets from scan to scan. However, this is not problematic, because the existence of these artifacts still confirms the presence of two fringe packets.

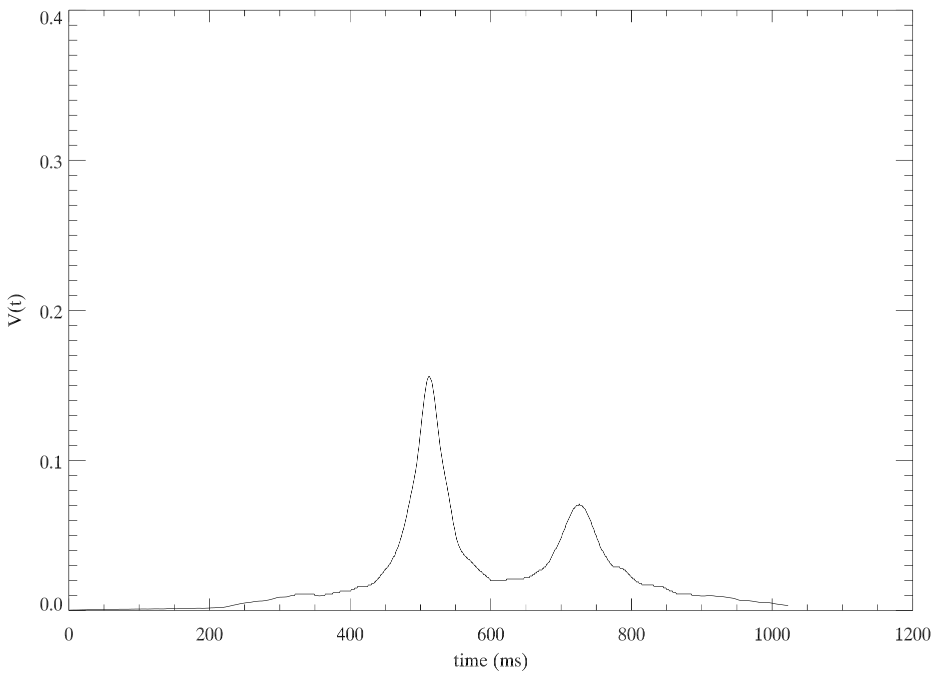

Figure. 3.7: Shift-and-added envelope. The shift-and-added envelope for all non-zero weighted scans in a data set. This envelope represents 86 individual scans.

When the existence of SFPs is confirmed, the next task is pinpointing their exact locations on the x-axis. The location of a fringe packet is defined as the position in time of the peak of the packet. Three different methods are used to determine the positions of the two fringe packets. The method used on a particular data set is dependent upon the nature of the separation of the fringe packets. The method is used on each of the scans in the data set. For widely separated packets, like those in Figure 2.3, a marker is placed at the center of the scan. Two searches are then performed, one on each side of the marker. The highest amplitude point on each side is recorded as the fringe packet location.

The second method of finding fringe packet locations is used for SFPs of intermediate separation. The higher-amplitude fringe packet (HAFP) is located by searching the entire scan for the highest point. All scans are then visually inspected to determine whether this higher amplitude packet is located on the left or right side of the lower amplitude packet. There is also a special case in which the fringe packets are of nearly equal amplitude, such that the higher amplitude packet could change between the left and right packets in successive scans. In any case, the next step is to subtract the HAFP and search the remaining portion of the scan. The subtraction involves placing a marker at about 100 ms away from the HAFP's peak in the direction of the lower amplitude fringe packet (LAFP). Everything on one side of the marker is set to zero, leaving only the LAFP. In the special case, markers are placed on each side of the HAFP at 100 ms, and everything between the markers is set to zero. This is to ensure that the LAFP is not subtracted out no matter which side it is on. The highest point remaining is considered to be the location of the LAFP. The location of the markers, 100 ms, is merely a starting point, and can be changed if the situation requires it.

The third and final method of finding fringe packet locations is used for very close and overlapping fringe packets, which will henceforth be known as semi-separated fringe packets (SSFP). At small separations, piston error becomes a large issue in locating the LAFP. In any observation of SFPs, the separation between the two packets is modified by atmospheric seeing variations such that the fringe packets move due to differing air path lengths Farrington et al. (2010). A quantitative estimate this phenomenon, known as piston error, at the CHARA Array is given in Farrington et al. (2010). The piston error at small separations changes the overall shape of the fringe packets and virtually ensures that choosing a single value for the location of the marker relative to the HAFP in every scan is insufficient. Instead of placing a marker a certain distance away from the HAFP, the location of the marker must be determined for each individual scan. The trough between the peaks of the two fringe packets in the scan envelope represents the ideal spot to place the marker. To find this exact position, the first derivative of the envelope is calculated and the first zero on the left or right of the peak of the higher amplitude packet is determined. The location of the first zero corresponds to the trough. The marker is placed here, the side with the HAFP is subtracted, and the highest point of the remaining portion of the scan is the location of the LAFP. An example of each type of fringe packet-locating methods is given in Figure 3.8.

Once the existence of the second packet in a data set has been established and the locations of each packet determined, each data scan must be examined, and criteria for the rejection of scans must be established. In order to avoid biasing the results with low signal-to-noise data, 40% of the scans in each data set are rejected based on their low signal-to-noise ratios. This rejection process was set at the onset of this

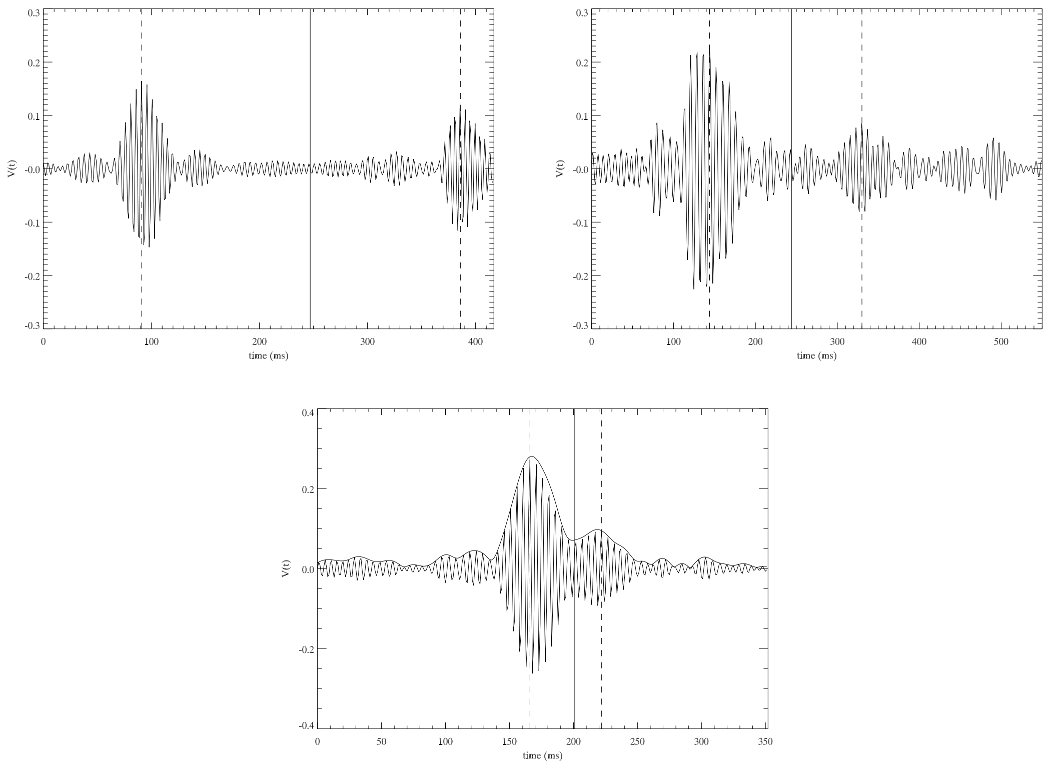

Figure. 3.8: Locating fringe packets. The three different methods of locating the second fringe packet in SFP observations. In the upper left plot, a marker (solid line) is placed in the middle of the scan and everything to the left of it is set to zero so that only the smaller packet remains. In the upper right plot, the marker is placed 100 ms to the right of the larger fringe packet, and everything to the left is set to zero. In the bottom plot, the marker is placed at a zero of the first derivative of the envelope of the scan. This is the first zero to the right of the larger fringe packet. Everything to the left of the marker is set to zero.

project by H. A. McAlister. A relative signal-to-noise ratio measurement is calculated for each scan by dividing the peak of a scan's power spectrum by the integrated area under the power spectrum from 300 to 325 Hz (a band outside the position of the fringe (150 Hz) in the frequency domain). The separation between the two fringe packets in each scan must also be considered. If the separation measurement for a particular scan is outside of 2σ of the mean of all scans in the set, then one or both of the fringe packets has been misidentified, most likely due to noise peaks. These scans are rejected. A related consideration is the position of the fringe packets. The positions of the packets should be relatively consistent between successive scans in a data set. To measure the level of consistency, the position of one fringe packet in a scan is compared to the mean of that packet's position in the two previous and the two successive scans. If the position differs from that mean by more than 100 ms, this fringe packet is considered to be misidentified, and the scan is rejected. This process is repeated for the other fringe packet. Finally, all scans are visually inspected to make sure that both fringe packets are still within the scan range. Due to either poor seeing or the general inconsistency in the optical path-length equalization, the fringe packets may drift out of the scan range during observation. Scans such as these must be rejected as well. Typically, after all rejection criteria have been satisfied, roughly 50% of the data scans remain.

3.3 Fringe fitting

Instrumental visibilities are obtained for a data set by determining the instrumental visibility of a packet in each individual scan, then averaging all of those values. It should be noted that because of the changing baseline and atmospheric effects, visibilities cannot be determined by coadding the individual fringe packets from each scan and deriving a visibility value from the coadded data (Benson et al. 1995). In order to obtain visibilities from each scan, fringe-fitting is performed on both packets.

Fringe-fitting is performed in one of two ways, depending on the separation between the packets. If the fringe packets are relatively far apart, the two packets should be fit separately. When the packets are close together, such that they are overlapping, the two packets should be fit simultaneously. In this section, only separately fitting the packets is discussed, as simultaneous fitting will be addressed in detail in Chapter 4.

When the fringe packets are fit separately, a five-parameter fit of equation 3.3 is applied to each packet with the goal being the derivation of the visibility amplitude, V, of each packet. The peak of the packet is considered the center, and the fit is performed on 50 total points, 25 on each side of the center. The five parameters of the fit are V, $\Delta\sigma$, v_{g}, σ_0, and ϕ. Although the values of λ and $\Delta\lambda$ are nominally known from the manufacturer's testing of CHARA's K-band filter, the parameter $\Delta\sigma$ is kept as a free parameter in the solution because of a small bias that is introduced by the transmissive and reflective properties of the atmosphere, mirror surfaces, and optical windows as well as the detector spectral response across the K passband. Previous attempts to determine $\Delta\lambda$ have produced varied results: $\Delta\lambda = 0.350$ μm from Bowsher (2010) vs. $\Delta\lambda = 0.622$ μm from Farrington et al. (2010). Also, the group velocity, v_{g} is not constant during a scan. The fringe scanning mirror is attached to a moving cart that acts to equalize the optical path length of the two telescopes as a target moves across the sky. The cart's movement introduces an acceleration term into the movement of the fringe scanning mirror, so the velocity must be treated as a free parameter as well.

The five-parameter fit is applied after initial "guess" values are assigned to the five parameters. The initial values of $\Delta\sigma$ (equation 2.3) and σ_0 ($= \frac{2\pi}{\lambda}$) are determined using the standard values of $\lambda = 2.1329\ \mu$m and $\Delta\lambda = 0.350\ \mu$m. The initial value of v_{g} is determined by taking the distance that the dither mirror traveled over one scan and dividing by the time taken to travel that distance. The phase parameter ϕ is always initially set to zero. Three different fringe fits, centered on the highest amplitude individual fringe in the packet and on its two nearest neighbors, are performed on each packet. The initial value of V is the peak of the individual fringe that is being used in the fit. The fit with the smallest standard deviation of its residuals is accepted as the best fringe fit. An example fringe fit is given in Figure 3.9.

In general, the standard deviations of the fitted values for both v_{g} and λ among all non-rejected scans in a data set are both less than 3%. The standard deviation of $\Delta\lambda$ is larger, at roughly 15%. This shows that even within a single data set, there is a large uncertainty in the value of $\Delta\lambda$. This is most likely due to atmospheric seeing changing the shape of the fringe packets. If the timescale for atmospheric seeing is smaller than the timescale of the scanning of a fringe packet (0.1 sec), the fringe packets can be stretched or compressed on the time axis. If seeing moves a fringe packet in the direction of the motion of the dither mirror, the fringe packet will be stretched. Similarly, if seeing moves the fringe packet opposite the direction of motion of the dither mirror, the fringe packet will be compressed.

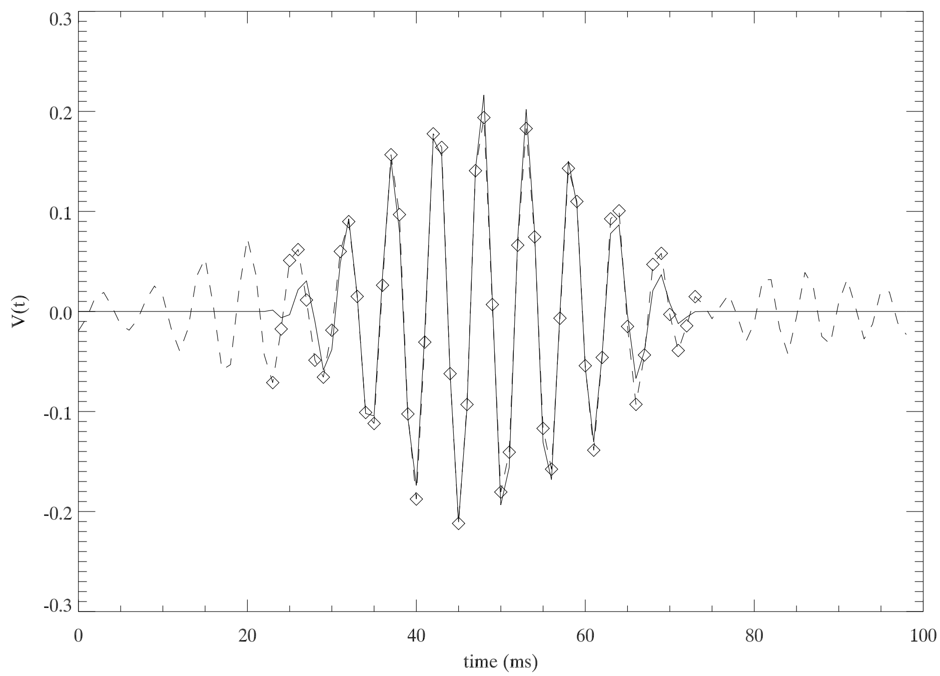

Figure. 3.9: Single packet fringe fit. The diamonds represent the data points while the dashed line just connects them, showing the general trend of the data. The solid line is the best-fit solution to the data.

The result of the fringe fitting is a pair of visibilities for each data scan. The locations of the packets on the time axis allows the designation of each packet as either the "left" or "right" packet. The final two visibilities derived for each data set are the average of the left-packet visibilities and the average of the right-packet visibilites for all scans that are not weighted zero. All of the scans not weighted zero are weighted equally in the average. These averaged results represent the observed instrumental visibilities of the target and calibrator for a single data set and will now be designated as $V_{\rm obs}$. These values must undergo a few additional corrections before the true visibility of the target can be obtained.

3.4 Identifying the fringe packets

At this point, visibilities for two fringe packets have been obtained, but which visibility represents the target and which represents the calibrator is still unknown. The magnitudes of these two components of the system are helpful in resolving this discrepancy. Any two fringe packets within the field of view of the CHARA Array (1 arcsecond) will have an effect on each other's visibility due to the magnitude difference between the two objects, even if the two objects are not observed within the same delay scan (ten Brummelaar, private comm.). The ratio of the visibilities between two objects is affected as follows:

$$\frac{V_{1,\mathrm{corr}}}{V_{2,\mathrm{corr}}} = \beta \frac{V_{1,\mathrm{obs}}}{V_{2,\mathrm{obs}}} \tag{3.7}$$

$$\beta_{\mathrm{wide}} = 10^{0.4 \Delta K_{\mathrm{wide}}} \tag{3.8}$$

$$\Delta K_{\mathrm{wide}} = K_1 - K_2 \tag{3.9}$$

where $V_{1,\mathrm{corr}}$ and $V_{2,\mathrm{corr}}$ are the corrected visibilities of the brighter and fainter components of the wide orbit, respectively, $V_{1,\mathrm{obs}}$ and $V_{2,\mathrm{obs}}$ are the observed visibilities that were derived above from fringe-fitting, and K_1 and K_2 are the magnitudes of the components. Further details on the derivation of Equation 3.7 are given in Appendix A. From these equations, it can be deduced that the larger the magnitude difference between the components, the larger the visibility ratio between the bright and faint components. For this reason, the larger packet is generally assumed to be the brighter component. The MSC is consulted to determine whether the brighter component is the target or the calibrator. The MSC presents only V-magnitudes for the individual components, so spectral types and $V - K$ values from Cox (2000) are used to convert these to K-magnitudes. If spectral types are not available for all components, the V magnitudes are used to determine whether the calibrator or target is brighter. Generally, the spectral types of the stars in a given system are not so different that one component would be brighter than the other in V but dimmer in K. In cases where the magnitudes appear to be roughly equal in K according to the MSC, two separate sets of data are produced, one for each of the two scenarios. Orbit fits, which will be discussed in detail later, are performed on both sets of data.

In theory, one could use the wide orbit's position angle along with the baseline orientation to determine the relative identities of the fringe packets on a given night. Consider the configurations in Figure 3.10. The middle baseline position is completely perpendicular to the position angle of the binary. According to equation 2.2, this will produce a separation of zero between the two fringe packets. Two other baselines positions are displayed, one on either side of the perpendicular position. Both of these baselines will produce a non-zero separation between the fringe packets, but the orientations of the packets on the delay scan will be opposite. In other words, the baseline for which the angle T1OI (where O is the origin) is acute produces a fringe packet for component I at a position of higher delay than the fringe packet for component II. The baseline for which angle T1OI is obtuse will then produce a fringe packet for component I at a position of lower delay than the fringe packets for component II. Because the CHARA Array records the position of the dither mirror for all data points, it would be obvious in the data reduction process which fringe packet is located at higher delay and which one is located at lower delay. It should be noted that this method only gives the relative identities (I and II) of the packets, not the absolute identities (target and calibrator). If the same system was observed on a different night, where the binary position angle and baseline orientation have completely changed, it would be theoretically possible to determine which packet in the new configuration would correspond to I and which would correspond to II. It would not, however, be possible to determine whether I represented the target or the calibrator. One would have to try both possible scenarios.

A method of using the baseline orientations and binary position angles has been developed by ten Brummelaar (private comm.). For every epoch of observation, the difference in the angles, $\delta = \theta - \psi$, is calculated. Then, because the baseline orientation angle is only defined between 0° and 180°, 2π is added to any value of δ less than $-180°$ and subtracted from any value greater than 180°. Then, all values of $|\delta| < 90°$ are considered to have one orientation of the fringe packets, and all values of $|\delta| > 90°$ have the opposite. This method was tested on the system V819 Her, an object in which the packet identities are obvious due to the large magnitude difference between the target and calibrator. Unfortunately, this method did not produce the expected results for V819 Her. This may be due to some inherent difference in the

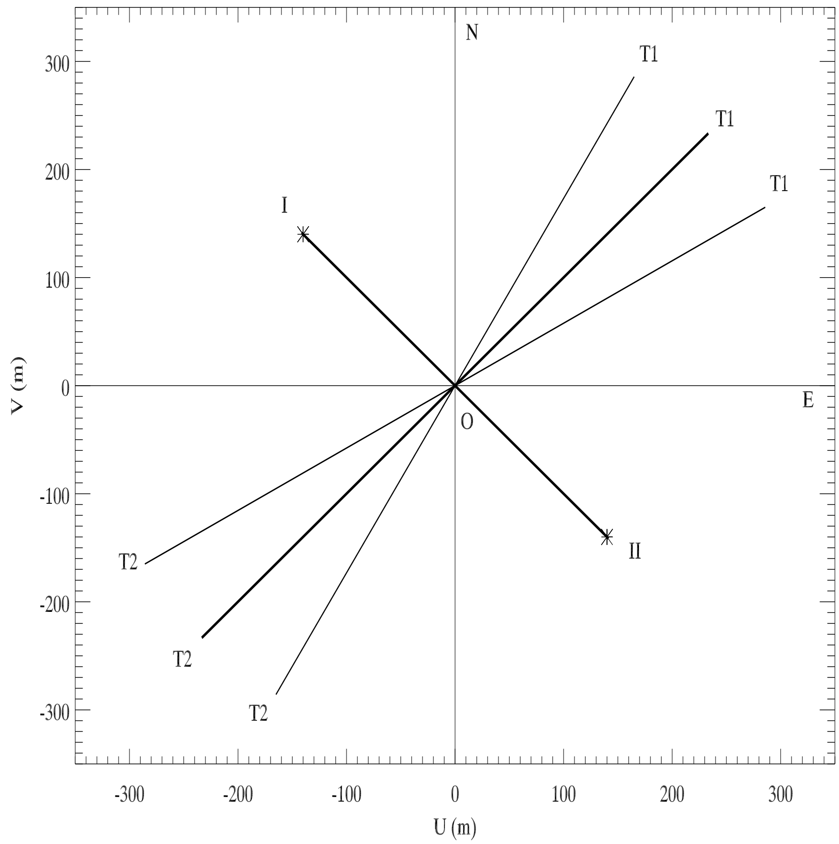

Figure. 3.10: Identifying fringe packets. I and II represent two stars in a binary system with a certain position angle measured from North to East. Three different baselines are plotted against the binary. The middle baseline position angle is perpendicular to the binary position angle, while the other two baselines are slightly displaced from the middle one.

way data are processed between CHARA's three general sets of baselines (S-E, S-W, E-W), especially in regard to how positions of higher delay relate to the positions of the components on the sky. Because the use of baseline orientations failed to produce consistent results, the method of assigning the larger fringe packet to the higher flux component is always used.

3.5 Calibration

Calibration is the final step in obtaining the binary star visibilities that will be used in orbit fitting. When observing an object with an interferometer, the visibility returned by the instrument is always diminished from the intrinsic visibility of the object due to the effects of the atmosphere, instrumental vibrations, optical aberrations, etc. McAlister (2005). The standard method of compensating for these effects is observation of a calibrator star. An ideal calibrator is an unresolved, non-variable, single star. The standard form of linear calibration is given by Boden (2007):

$$\frac{V_{\mathrm{tgt}}}{V_{\mathrm{cal}}} = \frac{V_{\mathrm{tgt,corr}}}{V_{\mathrm{cal,corr}}} \tag{3.10}$$

where V_{tgt} and V_{cal} are the respective intrinsic visibilities of the target and calibrator and $V_{\mathrm{tgt,corr}}$ and $V_{\mathrm{cal,corr}}$ are defined in equation 3.7. The intrinsic visibility of the calibrator is calculated by the visibility equation for a single star:

$$V_{\mathrm{cal}} = \frac{2J1(\frac{\pi\Theta_{\mathrm{cal}}B}{\lambda})}{\frac{\pi\Theta_{\mathrm{cal}}B}{\lambda}} \tag{3.11}$$

where $J1$ is the first-order Bessel function, Θ_{cal} is the angular diameter of the calibrator, and B and λ are the baseline and wavelength of observation. Finally, the value of highest interest, the intrinsic visibility of the target, can be calculated using equations 3.7, 3.10, and 3.11. Before 3.7 can be substituted into 3.10, the components of the system must be designated as either brighter or dimmer. This leads to two possible outcomes: the target is brighter or the calibrator is brighter. In the case of the target being brighter than the calibrator, the intrinsic visibility of the target is given by:

$$V_{\mathrm{tgt}} = V_{\mathrm{cal}} \frac{\beta V_{\mathrm{tgt,obs}}}{V_{\mathrm{cal,obs}}}. \tag{3.12}$$

In the case of the calibrator begin brighter, the intrinsic visibility of the target is given by:

$$V_{\mathrm{tgt}} = V_{\mathrm{cal}} \frac{V_{\mathrm{tgt,obs}}}{\beta V_{\mathrm{cal,obs}}}. \tag{3.13}$$

V_{tgt} can now be used in orbit fitting to determine the orbital elements of a binary system.

– 4 –
Side-Lobe Interference

In Chapter 2, it was mentioned that it is preferable to observe SFPs when they are well-separated. In Chapter 3, it was stated that for SFPs with very small separations, the fringe-fitting to individual packets is insufficient in determining the visibilities of the components. The reason for both of these is the existence of side-lobes. Polychromatic interferometric observations produce both a central fringe packet and side-lobes extending out infinitely on either side. When observing SFPs, each central fringe packet from which we derive a visibility will interact with the side-lobes of the other packet, leading to a distortion of the intrinsic visibility of the packet. The interaction manifests itself as either constructive or destructive "interference", leading to an enhancement or diminution of the amplitude of the packet. A qualitative example of this effect is shown in Figure 4.1. Because this project depends on the accurate calculation of the visibilities of two fringe packets, it is imperative that the effect of "side-lobe interference" is taken into account.

Extensive modeling has been conducted to calculate the quantitative effect of side-lobe interference and determine ways to correct for its effect. Two of the main effects that are evident in modeling are the change in amplitude and change in position of the packets. The change in amplitude should be obvious from Figure 4.1. The position change is less intuitive, but can occur if, for example, the central fringe of the LAFP lies on the null between the first and second side-lobes of the HAFP while the third

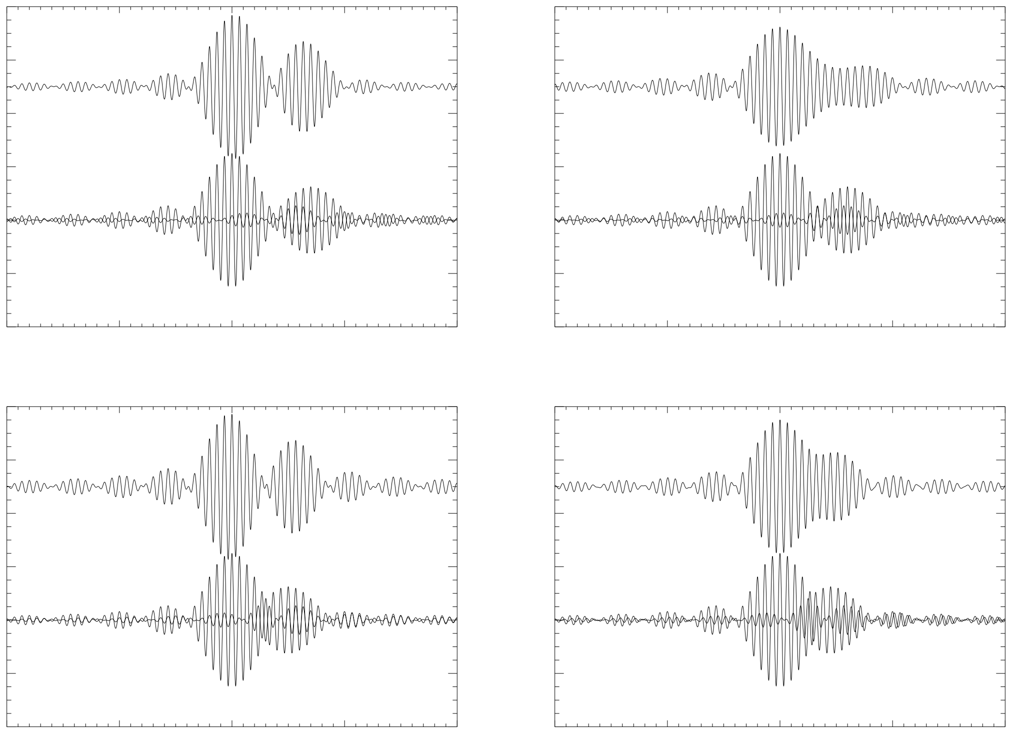

Figure. 4.1: Side-Lobe Interference Effect. This is a qualitative look at how side-lobes affect the amplitudes of the fringe packets. On each of the plots, two individual fringe packets, the larger of which is twice the amplitude of the smaller, are plotted on the bottom half. From left to right, the separation between these individual packets is decreased. The top half of each plot shows the combined interferogram of the individual packets below. It can clearly be seen that the amplitude of the LAFP changes significantly with varying values of separation.

fringe of the LAFP's central packet lies on the peak of the HAFP's first side-lobe. In that case, the peak of the LAFP would be identified at the position of the third fringe of the LAFP, rather than its actual position at the central fringe. Because the position of the fringe packets can change, the separation between them will also change from its intrinsic value. The percent error in the visibilities of both packets and the separation between them is calculated as a function of intrinsic separation.

The modeling was conducted for SFPs with intrinsic visibility ratios of 1, 1.5, 2, and 3 and is presented in Figures 4.2, 4.3, 4.4, and 4.5. All models are calculated using $\lambda = 2.1329$ μm and $\Delta\lambda = 0.350$ μm. As expected, the error in each case is substantial at small true separations between the packets. At small values of intrinsic separation, the secondary packet is interfering with either the central packet or the first (and largest) side-lobe of the primary packet, so the error should be large. Also, the errors in the separation and the visibility of the LAFP increase substantially with increasing ratio. For a ratio of 3, the error in V_{LAFP} can exceed 60%, while the error in separation can reach almost 40%. Even the best case scenario ($\frac{V_{\mathrm{HAFP}}}{V_{\mathrm{LAFP}}} = 1$) results in an error of up to 10% in separation and up to 20% in V_{HAFP} and V_{LAFP}. More important, however, than the individual visibilities is the ratio between them ($V_{\mathrm{Ratio}} = \frac{V_{\mathrm{HAFP}}}{V_{\mathrm{LAFP}}}$). Looking at equations 3.12 and 3.13, only the ratio of the observed visibilities is needed to calculate the calibrated visibility of the target. Therefore, if a correction can be applied to the visibility ratio, the errors on the individual visibilities can be ignored. The change in the ratio as a function of separation is given in Figures 4.6 and 4.7 for intrinsic ratios of 1, 1.5, 2, and 3. For a ratio of 1, the two fringe packets' side-lobes affect each other equally, so the ratio never deviates from 1. As the intrinsic ratio increases, the side-lobes of the HAFP become larger in size relative to the LAFP while the side-lobes of the LAFP become smaller relative to the HAFP. This leads to the ratio oscillating sinusoidally about the intrinsic ratio as a function of separation.

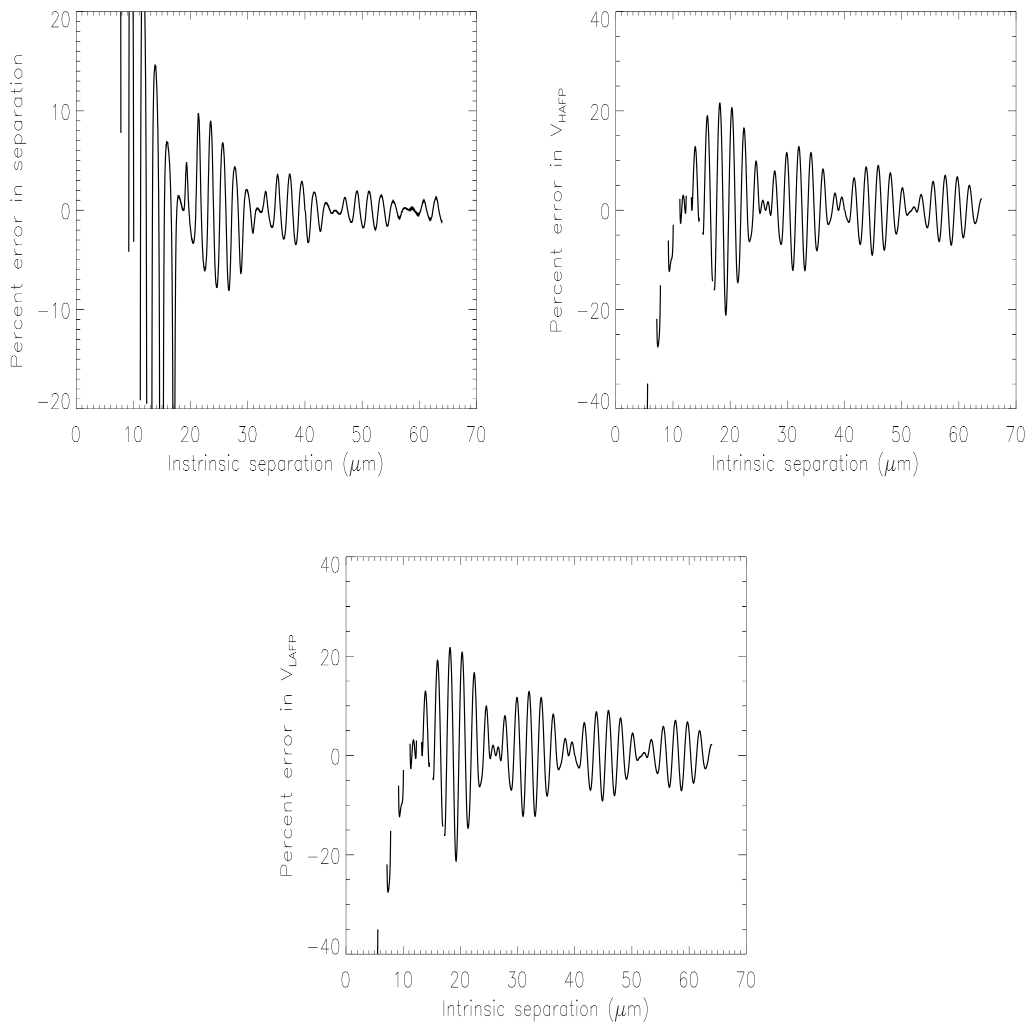

Figure. 4.2: Side-lobe Interference Modeling for a Visibility Ratio of 1. These plots are constructed by comparing the parameters of the two individual fringe functions to the parameters of the combined fringe function. The upper left plot shows the percent error in the separation as a function of the intrinsic separation of the fringe packets. The upper right plot shows the percent error of the visibility of the HAFP, while the lower plot shows the same for the LAFP.

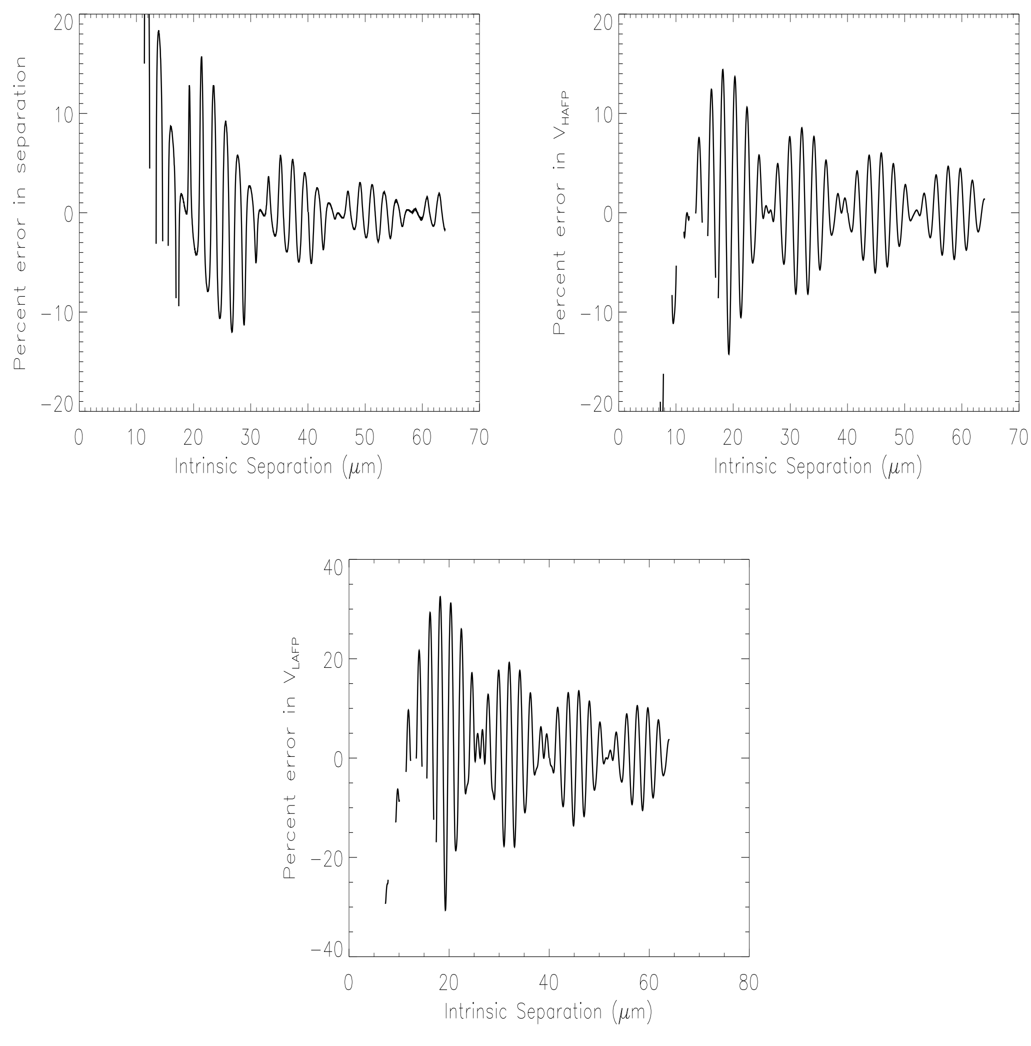

Figure. 4.3: Side-lobe Interference Modeling for a Visibility Ratio of 1.5. For more information, see Figure 4.2.

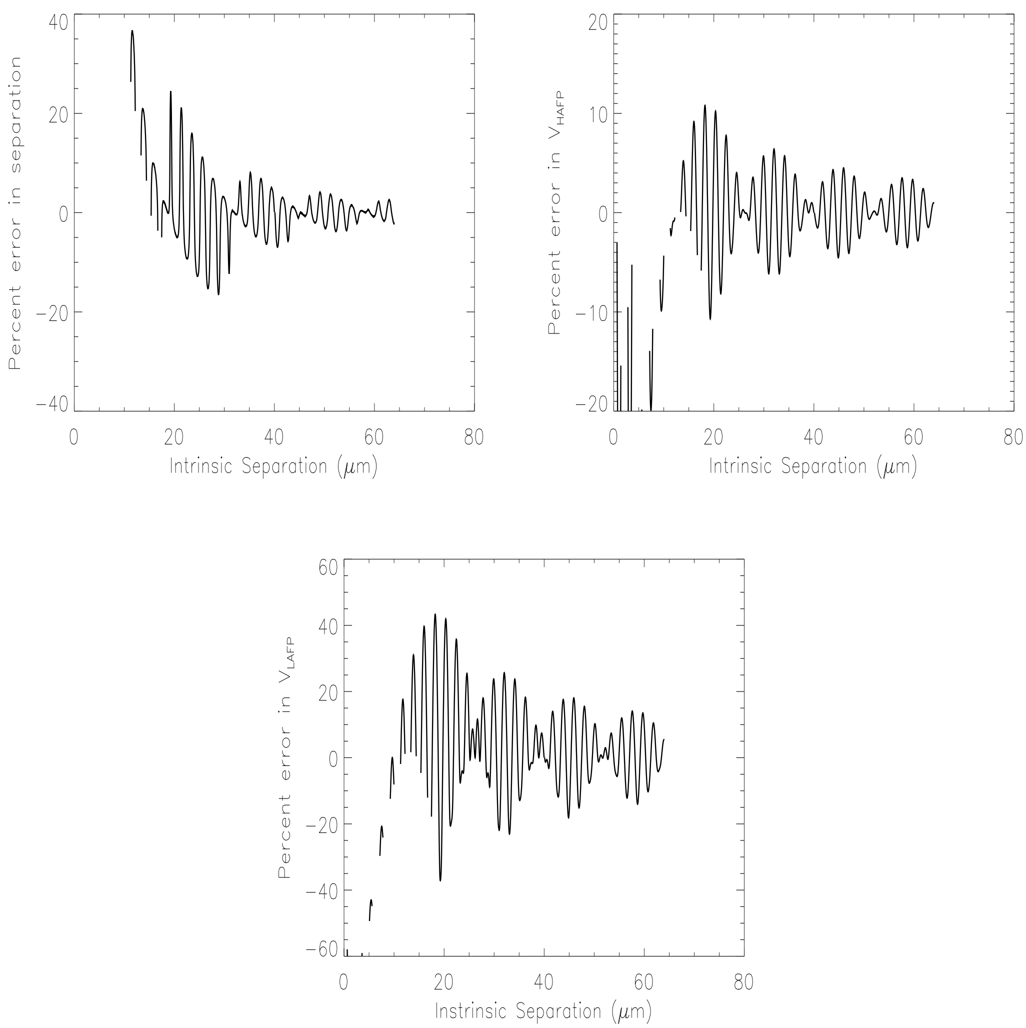

Figure. 4.4: Side-lobe Interference Modeling for a Visibility Ratio of 2. For more information, see Figure 4.2.

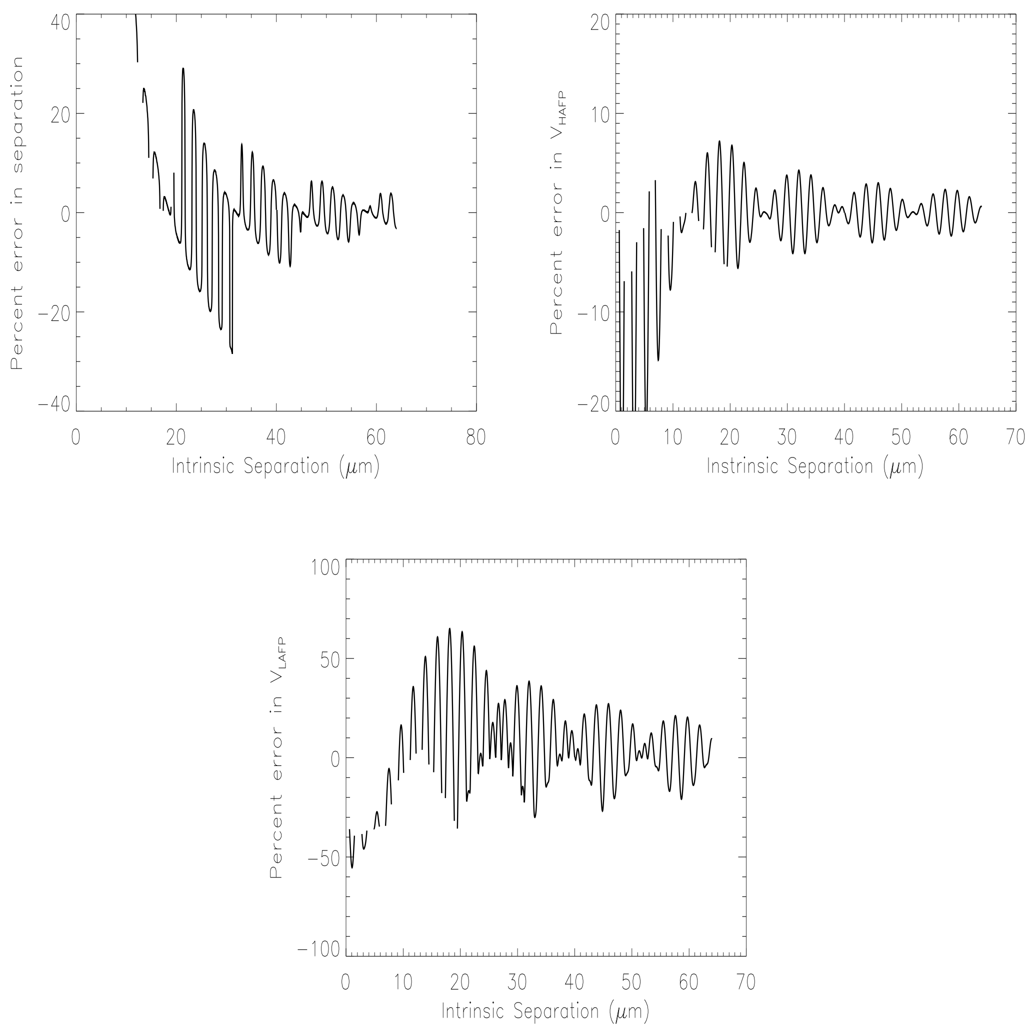

Figure. 4.5: Side-lobe Interference Modeling for a Visibility Ratio of 3. For more information, see Figure 4.2.

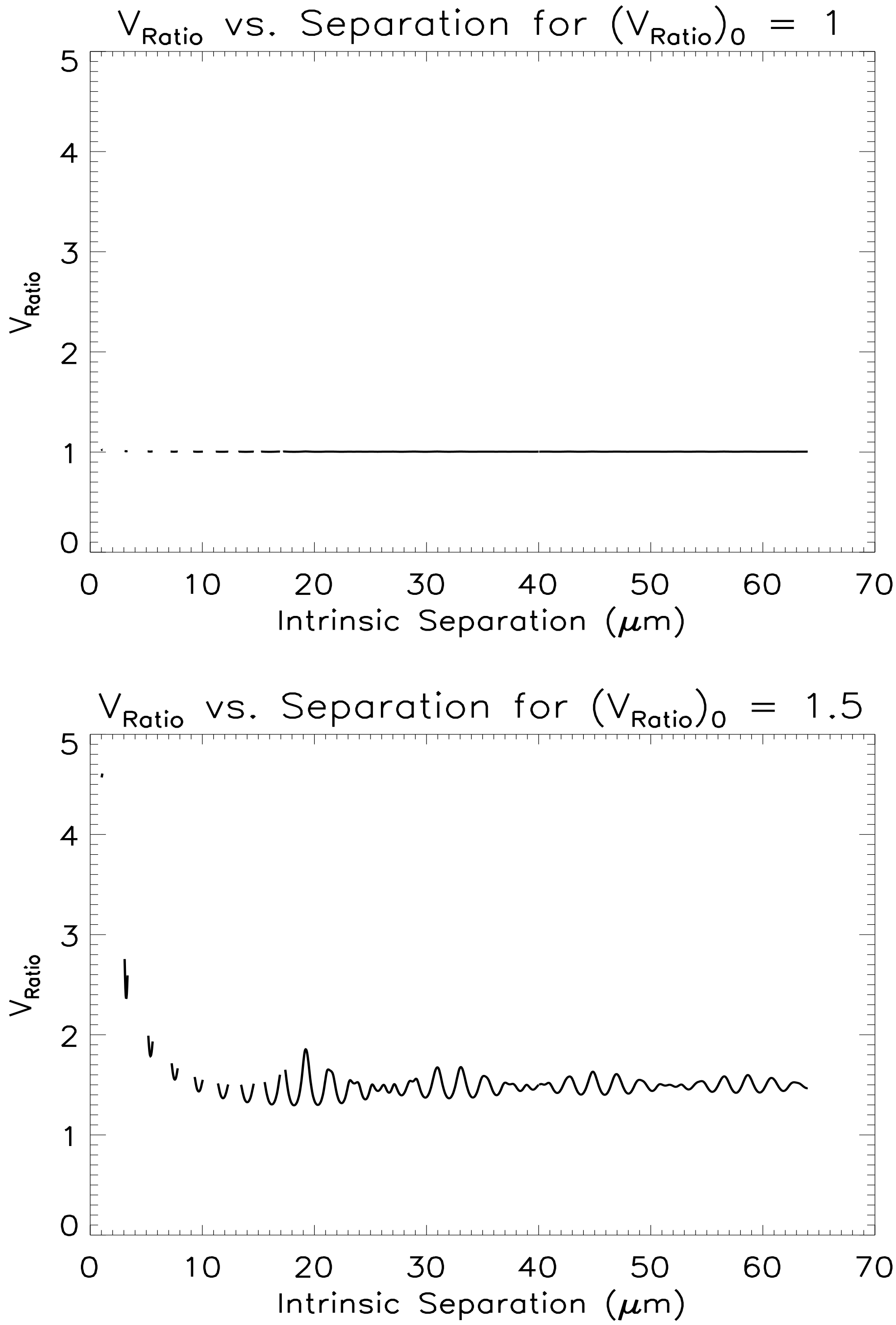

Figure. 4.6: Visibility ratio as a function of separation. The top plot represents a ratio of 1, while the bottom represents a ratio of 1.5.

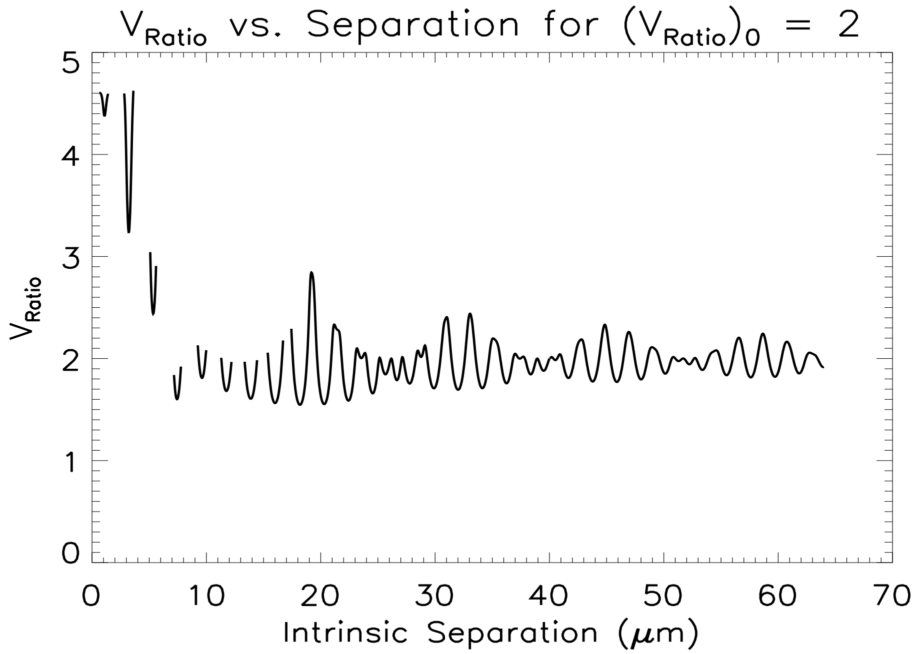

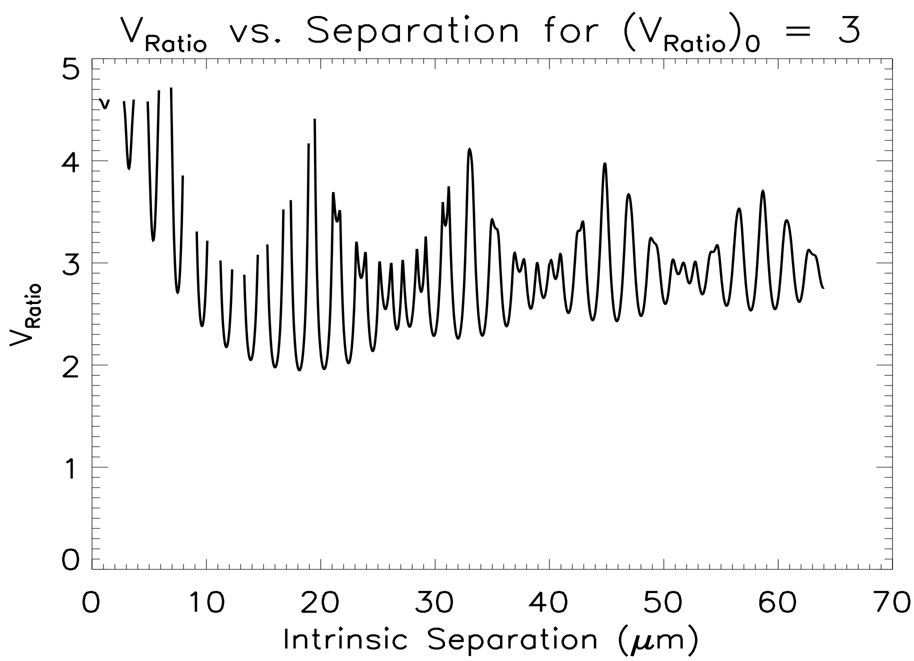

Figure. 4.7: Visibility ratio as a function of separation (cont'd). The top plot represents a ratio of 2, while the bottom represents a ratio of 3.

4.1 Deconstructing the semi-separated fringe packets

A first attempt at correcting for the effect of the side-lobes involves deconstructing the overall SSFP into its individual components. This process involves modeling two individual fringe packets that will produce the overall SSFP that is observed. The three parameters considered in these correction attempts are the separation between the packets and the visibility amplitude of each packet. Attempts are made to find packets that combine to match the values of $V_{\mathrm{tgt,obs}}$, $V_{\mathrm{cal,obs}}$, and separation for a particular data set.

In the first generation of this method, the separation of the modeled packets was governed by the published wide orbit for the system. The projected separation is calculated for the observation epoch of the data set using the formulae in Appendix A and equation 2.2. The separation gives the positions of the fringe packets relative to one another, thus giving an idea of the nature of the interference (constructive, destructive, or somewhere in between) between the central packets and side-lobes. For this separation, many different values of the visibility amplitudes are input into the program. The pair of amplitudes that form the combined SSFP that best matches the SSFP from data reduction are adopted as the corrected values. For example, based on data reduction, the values of V_{obs} are derived to be 0.181 and 0.069 for the two fringe packets recorded for HD 35411 at an epoch of 54721.46828 Modified Julian Date (MJD). It should be noted that due to the proximity of the packets the fitting method described in Chapter 3 could not be performed. The values of V_{obs} in this case are simply the peak values of the fringe packets. According to the wide orbit, the separation between the packets should be 16.3 μm. At this separation, corrected values of 0.176 and 0.039 would combine to give the observed values of 0.181 and 0.069. Thus, the visibility ratio would be corrected from 2.63 to 4.51. A graphical representation of this situation is given in Figure 4.8.

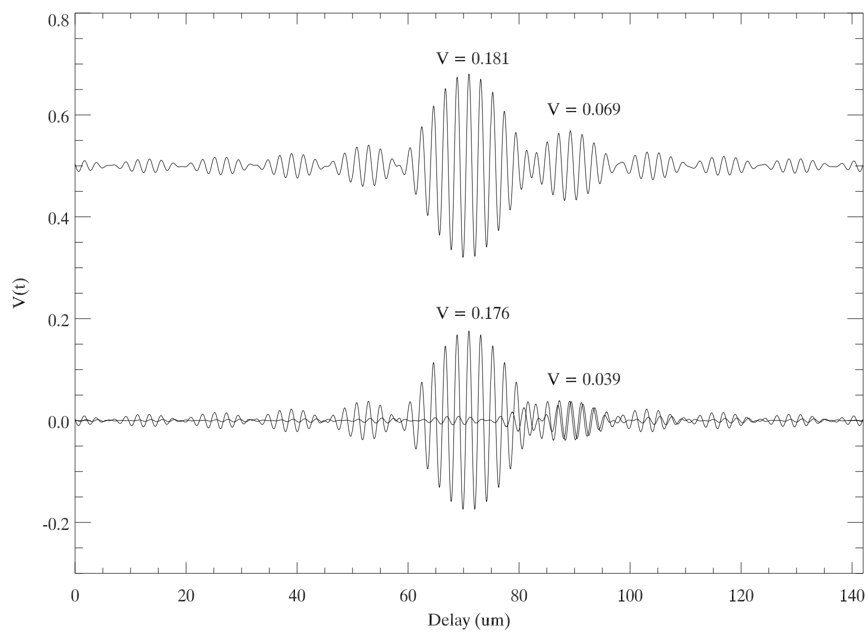

Figure. 4.8: Deconstructing the SSFPs. This is an attempt to deconstruct the overall SSFPs into the component parts

This method did not work as well as hoped. In Table 4.1, the original and corrected values of the visibilities and their ratio are given for data taken for HD 35411 on 2008 September 12. This is a rather simple example of the sinusoidal behavior of the visibility ratio. From the information in Table 4.1, one would expect the corrected ratios to all be around 2.6. However, the corrected ratios are far different. Not only did

Table 4.1. Original and corrected visibility ratios for HD 35411 on 2008 September 12

		Original			Corrected		
Epoch (MJD)	$\rho_{\mu m}$	V_{HAFP}	V_{LAFP}	V_{Ratio}	V_{HAFP}	V_{LAFP}	V_{Ratio}
54721.46828	16.3	0.181	0.068	2.64	0.176	0.039	4.51
54721.47467	16.0	0.191	0.061	3.15	0.186	0.029	6.41
54721.48104	15.7	0.184	0.057	3.19	0.180	0.038	4.74
54721.48662	15.4	0.188	0.064	2.91	0.189	0.068	2.78
54721.49233	15.1	0.190	0.077	2.47			
54721.49820	14.7	0.191	0.085	2.24			
54721.50391	14.3	0.192	0.083	2.33	0.191	0.063	3.03

this method not solve for the sinusoidal behavior, but it actually made the situation worse. For two of the seven epochs, a corrected value could not be calculated because the packets were blended together at the given separation value. Similar results for other epochs and other targets have led to the determination that this method is incorrectly solving for the behavior of the visibility ratio.

A second attempt was made to deconstruct the SSFPs using a modified form of the above program. It was thought that the published wide orbits were not of sufficient accuracy. The distance between individual fringes in delay space is around 2 μm, so minor inaccuracies in the orbital elements can be the difference between constructive and destructive interference. To correct for this, it was decided that the separation should be a fitted parameter along with V_{HAFP} and V_{LAFP}. Now, with three variable parameters, a grid search was employed to find the best fit to the observed visibilities and separation from the data reduction. Unfortunately, the grid search did not produce the expected results either. It was hoped that the best fit parameters could reproduce the observed separation to within 0.1 μm. This would ensure that the modeling incorporated the correct level of constructive or destructive interference. Unfortunately, in most cases, the fit would settle on a separation for which the packets were blended, and a side-lobe several μm away would be falsely identified as the LAFP. In a few other cases, the fit seemed to settle on a separation that gave a state of null interference. In other words, the maxima of a central fringe packet lie on the zero points of the side-lobes of the other packet, so there is virtually no change between the separate interferograms of the best fit parameters and the combined interferogram. The failure of these methods to produce consistent and believable results argues that there is no simple way to descontruct SSFPs into component parts.

4.2 Simultaneous fitting

Another way in which it is theoretically possible to correct for side-lobe interference is by employing simultaneous fitting of the two fringe packets for every data scan. In Chapter 3, it is explained that the single-packet method of fringe-fitting is applied to each packet individually to derive a value of $V_{\rm obs}$ for each. The method of simultaneous fitting alters the fringe-fitting by adding another term into equation 3.3 to represent a second packet. Thus, the equation for simultaneous fitting of the packets is a seven-parameter fit:

$$V(t) = V_{\mathrm{L}} \frac{\sin(\pi \Delta\sigma v_{\mathrm{g}} t)}{(\pi \Delta\sigma v_{\mathrm{g}} t)} \cos(2\pi\sigma_0 v_{\mathrm{g}} t + \phi) + V_{\mathrm{R}} \frac{\sin(\pi \Delta\sigma v_{\mathrm{g}} (t - t_0))}{(\pi \Delta\sigma v_{\mathrm{g}} (t - t_0))} \cos(2\pi\sigma_0 v_{\mathrm{g}} (t - t_0) + \phi) \tag{4.1}$$

where V_{L} and V_{R} represent the respective visibility amplitudes for the packets on the left and right side of the scan, t_0 represents the separation between the packets in the time domain, and all other parameters are the same as in equation 3.3. Before the fit is applied, the initial values of V_{L} and V_{R} are the peaks of the respective packets, while the initial value for t_0 is the separation of those peaks in the time domain. Two markers are placed on each scan, one 25 points to the left of the left fringe packet's peak and the other 25 points to the right of the right fringe packet's peak, and the fit is performed on every point between these two markers.

The overall quality of the resulting simultaneous fits is a mixed bag. About half of the fitting attempts fit the data reasonably well, while the other half are very poor. Examples of both types are shown in Figure 4.9. The main concern with the poor fits is that they do not fit the separation very well. In these fits, the position of the HAFP is generally consistent with the data, but the position of the LAFP is very different. Again, the separation is a crucial parameter in these fits because it determines the nature of the interference between the central packets and the side-lobes.

Another way to examine the effectiveness of this method is to compare the original visibility ratio from data reduction to the ratio obtained from the best-fit parameters. Given in Table 4.2 is the comparison for two different targets on one night each. From

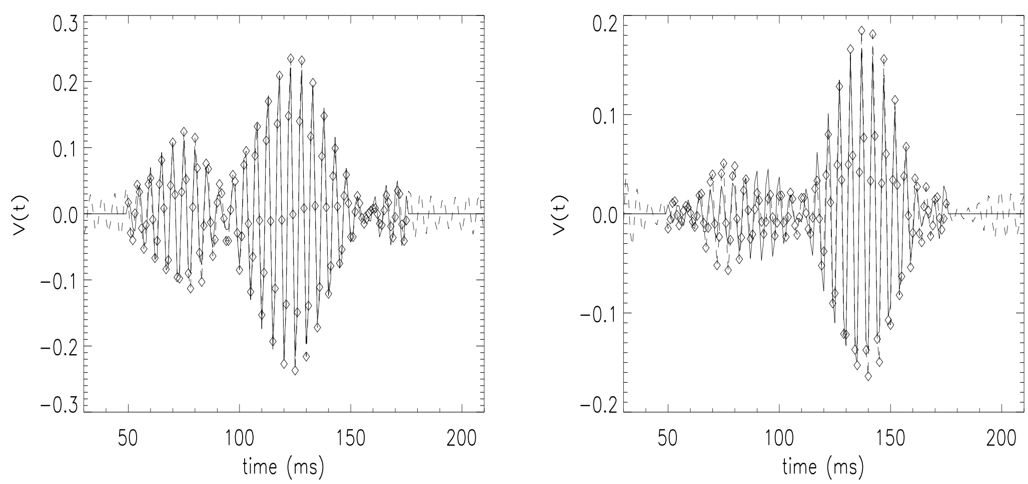

Figure. 4.9: Example simultaneous fits. These fits are performed on individual data scans for HD 157482. Diamonds represent the individual data points, the solid line represents the fit, and the dashed line represents the general trend of the data. The left plot is an example of a good fit, where the peak of the lower amplitude fringe packet in the scan matches the peak from the fit. The right plot is an example of a bad fit, where the peak of the LAFP lies at 95 ms in the data, but at 75 ms from the fit.

the information in this table, the ratio is increased in every case by the simultaneous fitting. It was hoped that the ratio would decrease at the peak of the sinusoidal variation and increase at the trough. Thus, the simultaneous fitting method seems to shift the sinusoidal variation caused by the side-lobe, rather than solving it. Figure 4.10 shows the comparison of the the original and corrected ratios for two nights. It looks like the fitting routine settles on a state of destructive interference in every case, such that the individual visibilities of the fits are almost always lower than their original values.

Piston error may be another factor that contributes to the unexpected results seen with simultaneous fitting. The fitting method works with individual data scans

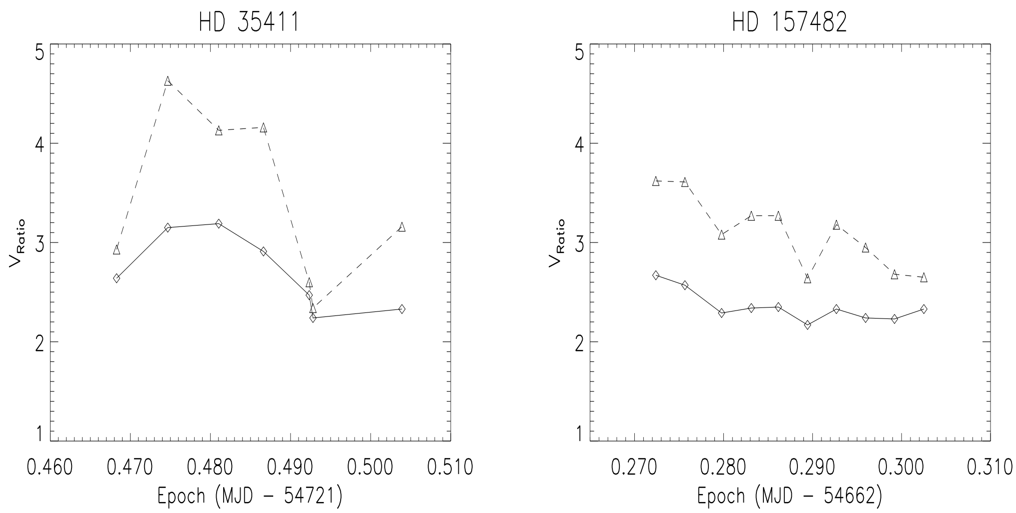

Figure. 4.10: Original vs. corrected visibility ratio for simultaneous fitting. The diamonds/solid line represents the original ratio and the triangles/dotted line represents the corrected ratio. For two different targets, it seems that simultaneous fitting is not solving for the sinusoidal variation, but rather just shifting it.

rather than the resulting average values for a data set of a few hundred scans. Piston error causes one of the packets to move relative to the other between successive scans. At very small separations, the shapes of the fringe packets can change significantly from this effect, even in high signal-to-noise data. The shapes may change such that the two packets blend together in some scans but are both visible in others. This can essentially fool the fitting program into identifying a false LAFP.

The combination of poor fits, a lack of solving for the sinusoidal variation in the visibility ratio, and the strong possibly that piston error corrupts the results have lead to the conclusion that simultaneous fitting is not a favorable way to reduce data on SSFPs.

Table 4.2. Original and corrected visibilities and ratios from simultaneous fitting for HD 35411 and HD 157482

Epoch (MJD)	Original $\rho_{\mu\mathrm{m}}$	Original V_{HAFP}	Original V_{LAFP}	Original V_{Ratio}	Corrected $\rho_{\mu\mathrm{m}}$	Corrected V_{HAFP}	Corrected V_{LAFP}	Corrected V_{Ratio}
HD 35411								
54721.46828	13.2	0.181	0.068	2.64	13.3	0.173	0.059	2.93
54721.47467	16.2	0.191	0.061	3.15	16.7	0.190	0.041	4.63
54721.48104	23.8	0.184	0.057	3.19	21.4	0.178	0.043	4.13
54721.48662	19.0	0.188	0.064	2.91	19.0	0.179	0.043	4.16
54721.49233	15.7	0.190	0.077	2.47	15.4	0.169	0.065	2.60
54721.49820	15.1	0.191	0.085	2.24	14.9	0.164	0.070	2.34
54721.50391	15.7	0.192	0.083	2.33	15.7	0.187	0.059	3.16
HD 157482								
54662.27239	24.7	0.163	0.061	2.67	24.9	0.163	0.045	3.62
54662.27566	22.5	0.152	0.059	2.57	22.7	0.148	0.041	3.61
54662.27978	22.0	0.149	0.065	2.29	22.0	0.148	0.048	3.08
54662.28312	23.2	0.164	0.070	2.34	23.0	0.160	0.049	3.27
54662.28616	21.2	0.153	0.065	2.35	21.1	0.147	0.045	3.27
54662.28944	19.2	0.163	0.075	2.17	19.0	0.161	0.061	2.64
54662.29268	17.2	0.163	0.070	2.33	17.0	0.162	0.051	3.18
54662.29596	17.7	0.161	0.072	2.24	17.5	0.162	0.055	2.95
54662.29921	16.8	0.147	0.066	2.23	16.4	0.142	0.053	2.68
54662.30251	17.1	0.154	0.066	2.33	16.9	0.151	0.057	2.65

4.3 Sinusoid fitting of visibility ratio

The final method discussed in the attempts to solve for side-lobe interference is sinusoid fitting of the visibility ratios. This method is similar to the method used by Bagnuolo et al. (2006) in correcting the separation of 12 Persei. Although a global function for the visibility ratio as a function of separation could not be derived to decribe the behavior seen in Figures 4.6 and 4.7, a generalized sinusoidal function can be used to approximate this behavior:

$$V_{\mathrm{Ratio}} = C_0 \sin(C_1 x + C_2) + C_3 x + C_4 \tag{4.2}$$

where x is a variable that represents the separation of the fringe packets and is determined to be $x = \cos(\theta - \psi)$, where θ and ψ are the respective position angle of the wide orbit and the observation baseline. This quantity is used because it is directly proportional to the projected separation of the fringe packets according to equation 2.2. The change in θ is insignificant, so this parameter is considered to be a constant, while the change in ψ is significant and can be calculated in Appendix A. A five-parameter fit is applied to the above equation to find the best-fit C-parameters. C_0 represents the amplitude of the sinusoidal variation, C_1 is the wavenumber, C_2 is the phase, C_3 is the slope of the function, and C_4 is the y-intercept of the function. The final two terms of equation 4.2 are included in case there is any general trend upward or downward separate from the sinusoidal variation. This would represent a change in V_{Ratio} that is dependent only upon the changes in the orbit of the close binary, so it must be taken into account. To determine V_{Ratio} for a data scan, the single-packets visibilities are assumed to be the highest amplitude point of each fringe packet. Single-packet fringe-fitting, as described in Chapter 3, will not work because the packets may be overlapping.

There are a few drawbacks with this method. For one, the object of interest needs to be observed long enough to get good "phase coverage" of the variation in V_{Ratio}. To facilitate this, the baseline of observation must be chosen carefully. The baseline's position angle must change enough over the course of observation that the variation in the ratio can be observed. However, if the baseline changes too quickly, there will be poor sampling of the curve, and the variation may not be observed at all. Also, this method is limited in how much of the curve it can fit. Notice from Figures 4.6 and 4.7 that the amplitude of the sinusoidal variation can change with separation. Equation 4.2 only accounts for one amplitude (C_0), and it is unclear as to how to incorporate more. In the case that multiple peaks with different amplitudes are seen, two fits are performed. Similarly, if the general trend of the data changes, two fits are performed. The results of seven nights on which the method was performed are presented in Figures 4.11 and 4.12. For the nights with two fits performed, the corrected ratio for any overlapping points is the average of the values from each fit.

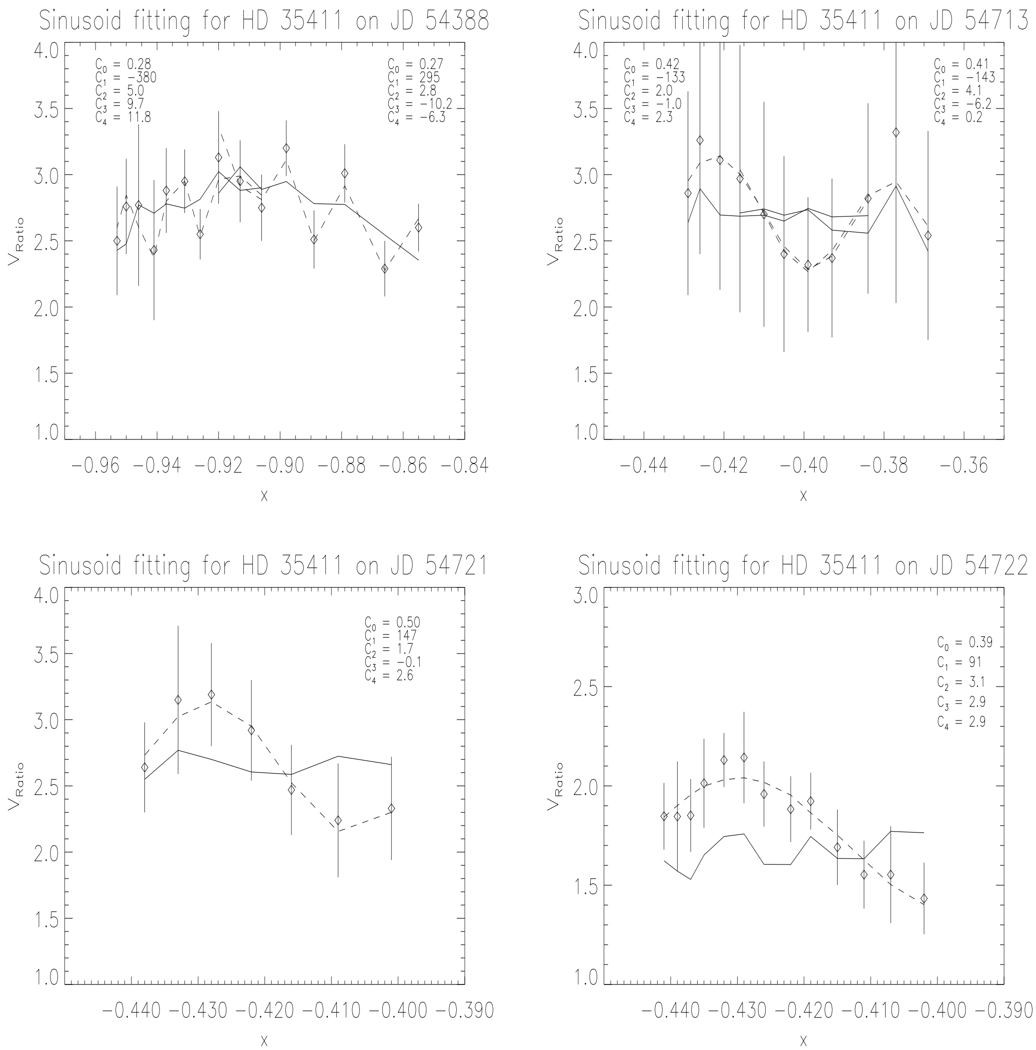

Figure. 4.11: Sinusoid fitting on four nights of HD 35411 data. For each night, V_{Ratio} is plotted against $x = \cos(\theta - \psi)$. The visibility ratio derived, along with error bars, from data reduction is represented by diamonds. The dashed line is the best fit sinusoid. The solid line represents the corrected ratio, which is the sinusoid subtracted out from the data. The plots for JD 54388, JD 54713, and JD 54723 have two corrected ratios used for the two different amplitude peaks. The change in V_{Ratio} between nights is due to changes in the orbit of the close binary.

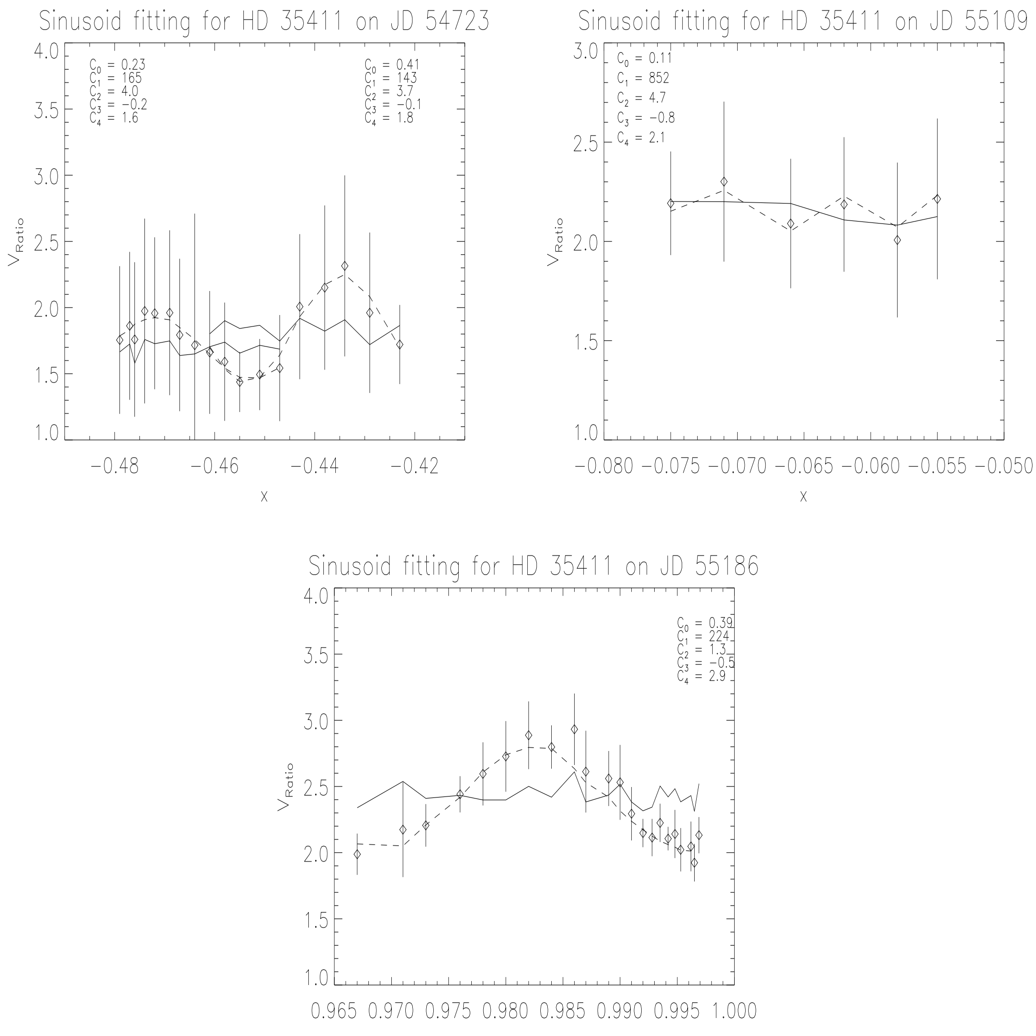

Figure. 4.12: Sinusoid fitting on three more nights of HD 35411 data.

4.4 Adopted correction method

The sinusoid-fitting method of correcting for side-lobe interference has been deemed successful, while deconstructing the fringe packets and simultaneously fitting the packets have been deemed unsuccessful, so sinusoid-fitting has been adopted as the general method of correcting for this effect. The corrected data using sinusoid-fitting for HD 35411 have been used in orbit fitting. Unfortunately, data for SSFPs on other targets could not be corrected by this method. Either targets were not observed long enough to see the sinusoidal variation or the configuration of the instrument on that night did not change the projected separation of the packets enough over the course of observation. By 2009 January, it had become clear that SSFPs were going to produce problematic data, so most observations afterwards were planned for with the intent to get well-separated fringe packets. The tools mentioned in Chapter 2 were used to make sure that this could be accomplished.

– 5 –
Results

5.1 Orbit fitting procedure

Calibrated visibilities obtained for a binary star by single-baseline observations unfortunately cannot be broken down into the instantaneous angular separation ($\rho_{\rm close}$) and binary position angle ($\theta_{\rm close}$). The equation for a binary star visibility is:

$$V_{\rm tgt} = (1+\beta_{\rm close})^{-1}[V_{\rm P}^2 + \beta_{\rm close}^2 V_{\rm S}^2 + 2V_{\rm P}V_{\rm S}\beta_{\rm close}\cos(\frac{2\pi\rho_{\rm close}B}{\lambda}\cos(\theta_{\rm close}-\psi))]^{0.5} \quad (5.1)$$

where $V_{\rm P}$ and $V_{\rm S}$ are the respective single star visibilities of the primary and secondary components of the binary, $\beta_{\rm close}$ is the luminosity ratio between the two components of the close binary, B is the baseline of observation, λ is the wavelength of observation, and ψ is the position angle of the baseline of observation projected onto the sky. For a single value of $V_{\rm tgt}$, there is an infinite number of combinations of the unknown values $\rho_{\rm close}$, $\theta_{\rm close}$, and $\beta_{\rm close}$ that will satisfy equation 5.1. Therefore, the orbit fitting program used to produce an orbit is based on a χ^2 fit of the target's visibilities to equation 5.1.

The orbit fitting code is a slightly modified version of that of Raghavan et al. (2009). Each line of data is comprised of the following information: the epoch t, baseline B, and wavelength λ of observation, the baseline position angle ψ, and the visibility information, $V_{\rm tgt,obs}$, $\sigma V_{\rm tgt,obs}$, $V_{\rm cal,obs}$, and $\sigma V_{\rm cal,obs}$. The diameters of the three components of a system are determined by consulting previously published results. Sources will generally quote a spectral type for each component seen in the overall spectrum and a proposed spectral type for each component not seen in the spectrum. Cox (2000) is then consulted to estimate a diameter for these spectral types. The error on the classification of these stars is considered to be one spectral type, so the angular diameters of stars one spectral type higher and one spectral type lower are calculated from Cox (2000) to get the error on the angular diameter. These diameters are then input into equation 3.11, along with B and λ, to determine V_{P}, V_{S}, and V_{cal} for each observation epoch.

Nine total orbital parameters are needed to perform the χ^2 fit. The seven classical binary orbital elements (P, T, a, e, i, ω, Ω) describe the motion, size, shape, and orientation of the orbit. The other two parameters are related to the flux ratio between components: 1) $\Delta K_{\mathrm{close}}$ is the magnitude difference between the two components of the close binary, and 2) ΔK_{wide} is the magnitude difference between the close binary and the wide component.

Monte Carlo simulations are first run to explore possible solutions within reasonable lower and upper limits to the orbital parameters. These simulations generally consist of several million randomly selected sets of orbital parameters. In each iteration of the fit, to calculate the data point V_{tgt}, the randomly selected value of ΔK_{wide} is plugged into equation 3.8, then into 3.12 or 3.13, along with V_{cal}, $V_{\mathrm{tgt,obs}}$, and $V_{\mathrm{cal,obs}}$ for each observation epoch. Literature is consulted as to which component, target or calibrator, is brighter and thus which equation should be used.

To calculate a model $V_{\rm tgt}$ to which this data point will be compared, the remaining eight elements are used. For each iteration of the fit, the randomly selected values of the seven classical orbital elements are used to determine ρ_{close} and $\theta_{\rm close}$ by the Thiele-Innes method described in Appendix A. $\Delta K_{\rm close}$ is used to determine $\beta_{\rm close}$ by equation 3.8. Now, all of the variables in equation 5.1 have been determined and a model $V_{\rm tgt}$ can be calculated for each epoch. The residuals of the fit are compared to the errors on the data points to derive χ^2.

The Raghavan et al. (2009) method of determining uncertainties on the orbital parameters is adopted here. Using the χ^2 value for each Monte Carlo iteration, a multi-dimensional χ^2 volume is created. When this volume is projected onto an individual parameter axis, a plot such as those in Figure 5.2 is created, where each point represents the χ^2 value of one iteration of the orbit fit. These points are plotted on the x-axis at the position of the parameter that represents the randomly selected value for that particular iteration of the fit. The levels above the minimum χ^2 that mark the 1σ, 2σ, and 3σ confidence levels can be determined by the table on p. 555 of Press et al. (1986). According to that source, those confidence levels are located at 1.00, 4.00, and 9.00 above the minimum χ^2 when all parameters are varied simultaneously. The horizontal dashed lines in Figure 5.2 represent those confidence levels. The uncertainties on the orbital parameters are determined by the intersection of the 1σ dashed line with the outer edges of the collection of points. These figures are also vital in narrowing down the search space. Once this has been accomplished, a higher-resolution grid search of the parameter space converges on the final solution.

There is a question as to which of the orbital parameters should be fixed and which should be variable in the fitting routine. In every case, the period of the orbit is fixed based on previously published spectroscopic and eclipsing (if available) orbits. This quantity is considered to be well-known such that fitting this parameter is unnecessary. The period also serves as a basis for getting adequate phase coverage on a system. In cases for which the orbit has been deemed circular by spectroscopic observations, the eccentricity and longitude of periastron are fixed at zero. All other parameters are left as variable in the orbit fitting on the first attempt at deriving the orbital parameters.

If the orbital elements derived on the first attempt suggest non-physical masses, further attempts may fix other selected orbital parameters. The main parameter scrutinized when judging if results are non-physical is the semi-major axis. The semi-major axis can be used to derive the total mass of the system and, if the system is a spectroscopic double-lined binary, the individual masses by Newton's version of Kepler's 3rd law:

$$M_{1+2} = \frac{a^3}{P^2} \tag{5.2}$$

combined with the mass ratio:

$$q = \frac{M_2}{M_1} = \frac{K_1}{K_2} \tag{5.3}$$

where $M_{1,2}$ are the masses and $K_{1,2}$ are the radial velocities of the more massive and less massive stars, respectively. Because of the cubic dependence of the mass sum on the semi-major axis, any small change in a leads to a large change in M_{sum}. If orbit-fitting returns a best-fit semi-major axis that is slightly different than expected, the mass derived for the binary will be unreasonable for the spectral types of the stars. A mass estimate is considered unreasonable if it falls outside of 20% of the value given by Cox (2000) for the spectral type of the star.

In addition to comparing the masses derived with the spectral types of the stars, the masses can also be compared to the "expected" masses that can be calculated from the wide orbit. Triple systems offer unique insight into the expected masses of the close binary. If the wide orbit of the system is a double-lined spectroscopic system, then the mass ratio obtained can be combined with the mass sum of the triple system from the speckle orbit to derive the individual masses of the components of the wide system. One of these masses is the mass of the close binary. This value can be combined with the period of the orbit to get an expected value for the semi-major axis. Again, a 20% range is used to determine if the masses derived are unreasonable compared to the expected masses. In most cases, this is a problem. The semi-major axes derived by orbit-fitting are slightly different from the expected values, which leads to unreasonable mass estimates. The results for all systems will be discussed in

Section 6.2.

There are a few other ways to judge whether derived orbital parameters make sense. The epoch of periastron and, in non-circular systems, the eccentricity and longitude of periastron, should be comparable with those derived from the spectroscopic orbit. In eclipsing systems, the inclination should be close to 90°. The magnitudes differences (derived in K) should be consistent with the spectral types and magnitude differences in V. If a measurement for the overall K-magnitude of the triple system is available from 2MASS (Skrutskie et al. 2006) or elsewhere, the individual K-magnitudes can be calculated and compared with the individual V-magnitudes. If the close binary is spectroscopically single-lined, no magnitude estimate is given in the MSC. This suggests that the magnitude difference in the close binary should be relatively large.

5.2 Orbits

5.2.1 V819 Her (HD 157482)

HD 157482 is the first object for which the self-calibration method produced an orbit for the close binary system. It is also one of three targets for which there is a previously published orbit for the close binary. Targets like these provide the opportunity to compare results of the self-calibration method with other methods.

This object consists of an evolved star (G8 III) orbiting a pair of F dwarfs (F2V + F8V). The wide component's orbit is eccentric (e = 0.673), with a period of 5.5

years and a semi-major axis of 75 mas, while the close binary orbit is circular, with a period of 2.2296334 days (Scarfe et al. 1994). The evolved star is the brightest component of the system, so it is designated as A, while the close binary components are designated as Ba and Bb, with Ba being the brighter of the two F stars. The close binary is a single-lined spectroscopic binary, with the fainter component undetected in the spectrum. However, it is also an eclipsing system, so Bb has been characterized by its affect on the light curve (van Hamme et al. 1994). The orbital parallax of Scarfe et al. (1994), 14.7 ± 0.2 mas, is adopted as the parallax of the system.

This system has been well-studied through the years. Consistent orbital solutions have been derived for the wide orbit through speckle interferometry (Scarfe et al. 1994) and differential astrometry (Muterspaugh et al. 2006a). Examination of the light curve of the close binary has resulted in eclipsing orbits (van Hamme et al. (1994); Wasson et al. (1994)). An orbital solution for the close binary has also been derived by Muterspaugh et al. (2006a) using differential astrometry obtained from long-baseline interferometry. Minor corrections to this orbit were presented in Muterspaugh et al. (2008). V-magnitudes and diameters for each component are given in Scarfe et al. (1994). The diameters, given in solar radii, are combined with parallax to calculate angular diameters of $\Theta_{\rm A} = 0.394$ mas $\pm$ 0.081, $\Theta_{\rm Ba} = 0.126 \pm 0.008$ mas, and $\Theta_{\rm Bb} = 0.085 \pm 0.007$ mas.

Using both the visual and spectroscopic solutions for the wide orbit, an estimate of the semi-major axis of the close binary can be made. The period and semi-major axis of the wide orbit give a mass total for the triple system of $M_{\mathrm{AB}} = 4.35\ M_{\odot}$. The spectroscopic elements of $K_{\mathrm{A}} = 18.3$ km/s and $K_{\mathrm{Bab}} = 12.9$ km/s (Scarfe et al. 1994) give a mass ratio of 1.42. This leads to component masses of $M_{\mathrm{A}} = 1.80\ M_{\odot}$ and $M_{\mathrm{Bab}} = 2.55\ M_{\odot}$. M_{B}, combined with the aforementioned period and parallax, gives a semi-major axis of $\alpha = 0.671$ mas. When performing orbit-fitting, it is expected that the best-fit value of α should be similar to this value. An eclipsing orbit is also available for this system, giving the inclination $i = 81.00 \pm 0.36$ (van Hamme et al. 1994). Orbit-fitting should also produce an inclination similar to this value.

This system has been observed extensively at the CHARA Array. The first orbit-fitting attempt encompassed data taken on 25 different nights between 2005 June to 2009 April. In the early days of observing, the separation of the packets was not accounted for when planning observations. This turned out to be a big problem in the long run, because on most of the epochs, SFPs were not visible. When checked later against the observation planning scheme, the projected separations on these epochs were very low, so the absence of SFPs could be explained. Thirteen nights of data on this target were thrown out as a result. Four more nights of data were found to be taken during the eclipse of the close binary when compared with the eclipse timings of van Hamme et al. (1994). During an eclipse, the full amount of light from both components of the close binary is not visible, so the model fit would be invalid for those data. This left eight nights of data, presented in Table 5.1. In order to reduce computing time and scatter in the data, several sets (roughly five minutes each) of data have been averaged together. The epoch listed is the mid-observation epoch of all data sets represented by that point. The final column indicates the number of data sets included in each point.

In the fitting routine, the eccentricity (e) and longitude of periastron (ω) can be fixed at zero based on the deduction of a circular orbit (Scarfe et al. 1994). The period (P) of the close binary has been established by several sources (Scarfe et al. (1994); van Hamme et al. (1994); Wasson et al. (1994); Muterspaugh et al. (2006a)) and is fixed at $P = 2.2296334$ days. The earliest attempts to fit an orbit to these data resulted in a semi-major axis of $\alpha = 0.934$ mas, about 40% larger than expected, leading to an unreasonable mass sum of 6.9 $M_{\odot}$ for a pair of F dwarfs. For this reason, it was decided that the value α sin i (Scarfe et al. 1994) should be fixed ($\alpha \sin i =$ 0.6625 mas) as well.

The orbit solution is given in Table 5.2, and the data points are plotted against the model visiblities for this solution in Figure 5.1. As seen from the table, these results are based on a fit with 6 free parameters and 6 constraints. The errors on the visibilities led to an overestimation of the errors on the orbital parameters. The visibility errors were scaled downwards until a reduced χ^2 of 1.00 was achieved. The χ^2 plots from which the errors on the orbital parameters are estimated are shown in Figure 5.2. These results are in very good agreement with previously published information, specifically the orbit derived by Muterspaugh et al. (2008), which is also presented in the Table 5.2. Most of the orbital elements are within the 1σ error bars of Muterspaugh et al. (2008). The exception is the inclination, for which there is a 1.3-σ deviation from the value of Muterspaugh et al. (2008).

Table. 5.1: V819 Her Data

t (MJD)	B (m)	ψ (degrees)	$V_{\mathrm{A,obs}}$	$\sigma V_{\mathrm{A,obs}}$	$V_{\mathrm{B,obs}}$	$\sigma V_{\mathrm{B,obs}}$	N
53948.357	330.5	163.8	0.2185	0.0146	0.0750	0.0040	3
53948.369	330.3	161.1	0.2291	0.0154	0.0782	0.0055	2
54288.219	245.3	25.7	0.2310	0.0111	0.0836	0.0043	3
54605.383	278.5	143.0	0.3022	0.0171	0.0846	0.0039	1
54650.294	330.5	16.9	0.1903	0.0107	0.0683	0.0038	4
54650.307	330.6	14.0	0.1965	0.0058	0.0673	0.0025	4
54650.320	330.7	11.1	0.1998	0.0076	0.0655	0.0040	4
54650.333	330.7	8.2	0.1895	0.0088	0.0602	0.0040	4
54650.346	330.6	5.1	0.1650	0.0090	0.0532	0.0041	4
54651.289	330.4	17.6	0.2619	0.0076	0.0967	0.0067	3
54651.307	330.6	13.5	0.2702	0.0077	0.0943	0.0051	4
54651.325	330.7	9.2	0.2422	0.0114	0.0733	0.0061	3
54651.337	330.6	6.6	0.2417	0.0071	0.0588	0.0037	4
54651.348	330.6	3.8	0.2341	0.0098	0.0583	0.0031	3
54651.359	330.6	1.2	0.2300	0.0054	0.0626	0.0028	4
54662.297	330.7	8.9	0.1777	0.0082	0.0636	0.0058	3
54662.309	330.6	6.1	0.1829	0.0100	0.0674	0.0047	3
54662.330	330.6	0.9	0.1516	0.0089	0.0444	0.0043	2
54662.339	330.6	178.9	0.1446	0.0081	0.0429	0.0042	3
54663.276	330.6	13.0	0.1472	0.0086	0.0516	0.0026	3
54663.286	330.7	10.7	0.1481	0.0156	0.0554	0.0046	3
54663.298	330.7	8.0	0.1509	0.0107	0.0579	0.0039	4
54933.510	277.1	136.9	0.3897	0.0121	0.0899	0.0036	3

Table 5.2. Orbital Elements for V819 Her B derived from minimum χ^2 fit

Element	Value	Muterspaugh et al. (2008)
Fixed Elements:		
P (days)	$2.2296334 \pm 1.6 \times 10^{-6}$	$2.2296330 \pm 1.9 \times 10^{-6}$
$\alpha \sin i$ (mas)	0.6625 ± 0.0230	
e	0	0.0041 ± 0.0033
ω	0	$227° \pm 47°$
$\Theta_{\rm Ba}$ (mas)	0.126 ± 0.008	
$\Theta_{\rm Bb}$ (mas)	0.085 ± 0.007	
Varied elements:		
$T_{\rm node}$ (MJD)	52626.872 ± 0.054	52627.17 ± 0.29
α (mas)	0.6631 ± 0.0221	0.6657 ± 0.0058
i	$87.6° \pm 9.7°$	$80.70° \pm 0.38°$
Ω	$131.3° \pm 4.0°$	$131.1° \pm 4.1°$
$\Delta K_{\rm close}$	1.24 ± 0.21	1.38 ± 0.14
$\Delta K_{\rm wide}$	1.128 ± 0.050	
Reduced χ^2	1.00	
Wide Orbit:		
$P_{\rm wide}$ (days)	2018.8 ± 0.7	
$T_{\rm wide}$ (MJD)	46564.1 ± 1.0	
$e_{\rm wide}$	0.672 ± 0.002	
$\omega_{\rm wide}$	$40.6° \pm 0.3°$	
$\alpha_{\rm wide}$ (mas)	75.0 ± 0.5	
$i_{\rm wide}$	$56.2° \pm 0.4°$	
$\Omega_{\rm wide}$	$143.7° \pm 0.3°$	

Note. — Muterspaugh et al. (2008) orbital elements are presented for comparison. Wide orbit taken from Scarfe et al. (1994).

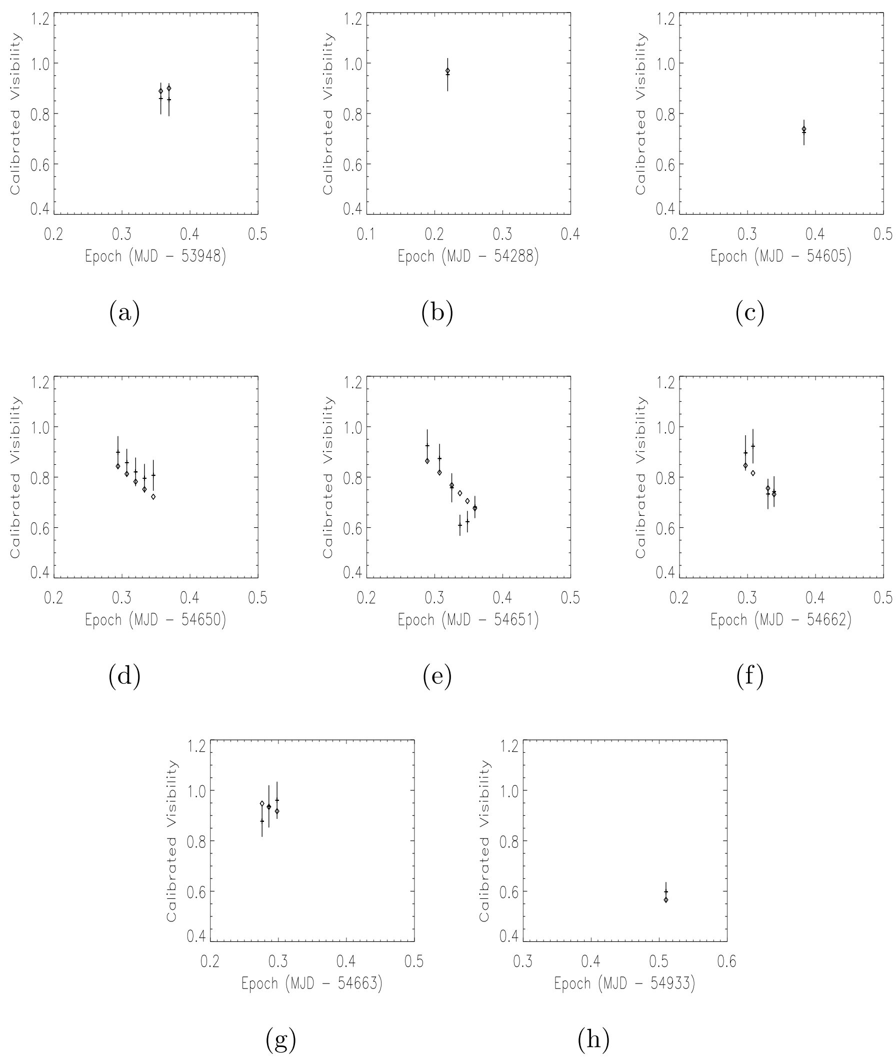

Figure. 5.1: Optimal orbit fit of visibilities for V819 Her B. This is a plot of calibrated visibility of the binary versus the epoch of observation. Each plot represents a different night of data. The crosses represent the data points while the diamonds represent the model.

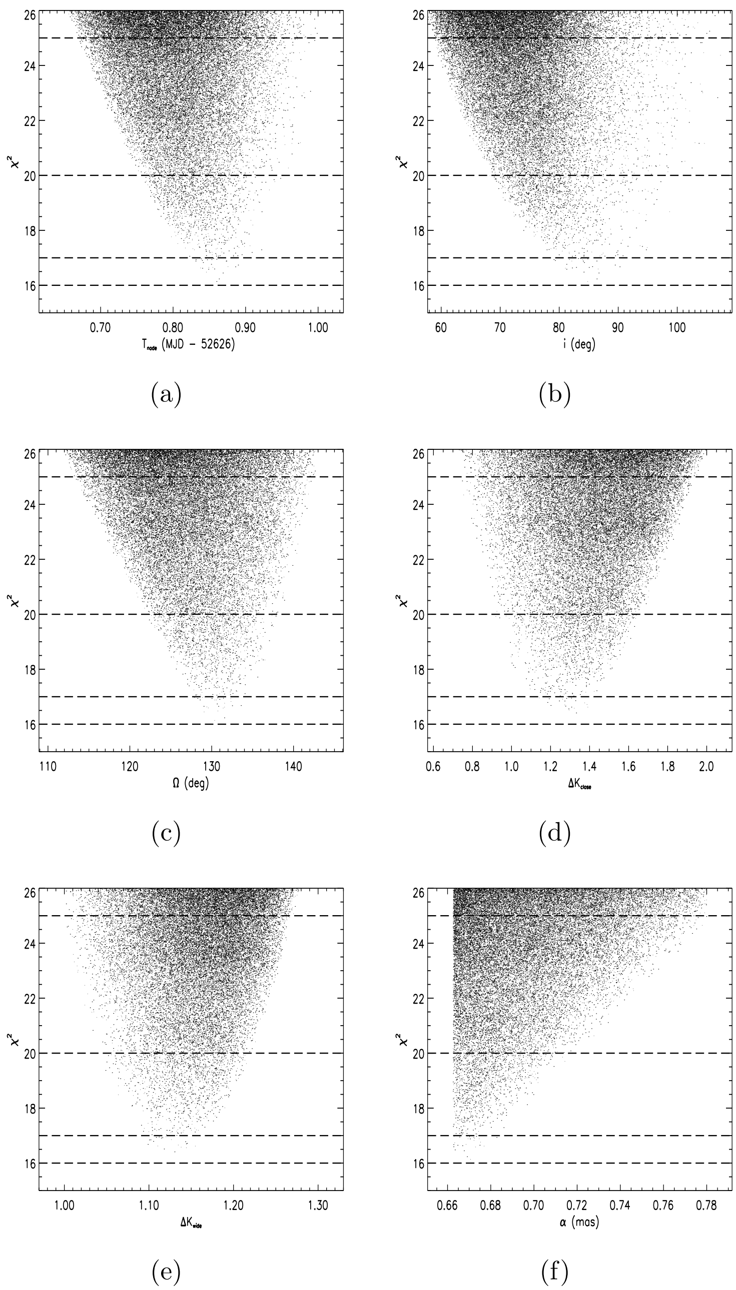

Figure. 5.2: χ^2 plots for V819 Her B. The “wall” at on the left side of the x-axis in the plot for α is due to the fact that α sin i is fixed in the orbit fitting. The inclination is thus dependent on the randomly chosen semi-major axis. At values of $\alpha < \alpha \sin i$, the calculation of i will lead to an arcsine of a value greater than 1, giving a non-physical result. This is a circular orbit, so $e = 0$ and $\omega = 0$.

Further details of the orbit are given in O'Brien et al. (2011). Although this solution is very good, there were still reservations about it. Five of the eight nights upon which the orbit is based possess SSFPs. These data were corrected in 2008 with the simultaneous fitting method, which was later deemed to be ineffective at solving for side-lobe interference. To obtain an orbit free of this interference, this object was observed on six more nights over 2009 and 2010. The goal of getting widely-separated fringe packets was achieved in these cases. One of the 2010 nights was corrupted by a faulty shutter sequence and had to be dropped. The five new nights were added to the data and the five problematic nights from the previous fit were dropped. The new data are given in Table 5.3.

The revised solution is presented in Table 5.4. In order to examine the orbit more thoroughly here, none of the data points have been averaged together. The results are much the same as the previous solution and still close to Muterspaugh et al. (2008), so there is high degree of confidence in this orbit, even if the errors on the orbital parameters are a bit larger. The errors on the parameters are larger probably because a higher percentage of the data points in the revised fit are at larger visibilities, suggesting that it is unresolved on those nights. The data points versus model visibilities are shown in Figure 5.3. With the new derived value of ΔK_{wide}, some of the data points now have a visibility larger than 1 (a theoretically impossible situation). This suggests that the value of ΔK_{wide} is being overestimated. One possible solution is to fix the ΔK_{wide} such that the highest visibility point is at

1 and conducting a new orbit fit. Still, the model fits the data pretty well in general. The χ^2 plots are shown in Figure 5.4. An alternative way to examine the fit of the visibilities is plot the visibility curve versus baseline for each data point. At any epoch, ρ and θ of the close binary can be calcated from the derived orbital elements, then combined with $\Delta K_{\rm close}$ to get a curve of visibility versus baseline. These plots are given for V819 Her B, as well as the other targets in this study, in Appendix B. Also, plots of the orbit on the sky for all targets are given in Appendix C. The observation epochs are plotted on these orbits to show the phase coverage for each target.

Several fundamental parameters of this system can be derived from the results presented here. The most important result from this study is the mutual inclination (Φ) that has been calculated from the orientations of the wide and close orbits. The mutual inclination in a triple system is the angle between the planes of the wide orbit and the close orbit, given by (Fekel 1981):

$$\cos\Phi = \cos i_{\rm wide}\cos i_{\rm close} + \sin i_{\rm wide}\sin i_{\rm close}\cos(\Omega_{\rm wide} - \Omega_{\rm close}) \tag{5.4}$$

where $i_{\rm wide}$ and $i_{\rm close}$ are the inclinations and $\Omega_{\rm wide}$ and $\Omega_{\rm close}$ are the nodal position angles of the wide and close orbits. The quantity Φ has long been an item of astronomical interest because of its relation to the conditions under which triple systems form (Sterzik & Tokovinin 2002). A more detailed examination of this parameter will be given in Chapter 6. For this system, the mutual inclination is derived to be

Φ = 32.2 $\pm$ 11.0 degrees. This uncertainty is large, due to the large uncertainties in i_{close} and Ω_{close}. The derivation of a visual orbit through interferometry always results in an 180° ambiguity in Ω_{close} because of the inability to differentiate between the ascending and descending nodes of the bright component. Therefore, there are two possible values of the mutual inclination for all orbits in this project. Differential astrometry provided by Muterspaugh et al. (2008) can resolve this ambiguity with support data if it is available. Muterspaugh et al. (2008) derives a center-of-light astrometric orbit in which the ascending node is degenerate with the luminosity ratio (one possible luminosity ratio is less than 1, the other greater than 1). The eclipsing orbit of the system suggests that the luminosity ratio is less than 1, thus the degeneracy is resolved. According to Muterspaugh et al. (2008), the correct value of Ω_{close} is less than 180°, which suggests that in this work, the correct values are $\Omega_{\mathrm{close}} = 130.4°$ and $\Phi = 32.2°$. All parameters needed for the calculation of Φ are given in Table 5.5.

The derivation of the semi-major axis of V819 Her B, when combined with the mass ratio given by the spectroscopy of Scarfe et al. (1994), allows for the calculation of the individual masses of the system. Those masses, along with all values needed to calculate them, are given in Table 5.6. The results are reasonable for the spectral types of these stars, and are in very good agreement with the masses derived by Muterspaugh et al. (2008) and Scarfe et al. (1994).

Due to the presence of the evolved component (V819 Her A), it is possible to estimate the age of V819 Her. Combining the overall K magnitude (K_{AB}) of the system with V magnitudes from Scarfe et al. (1994) and the derived values of $\Delta K_{\rm close}$ and $\Delta K_{\rm wide}$, the three components of the system can be plotted on an H-R diagram. The 2MASS value of the overall K magnitude ($K_{\rm AB} = 3.839 \pm 0.368$ is adopted for the system (Skrutskie et al. 2006). Table 5.7 shows the derived K-magnitudes for each of the components.

Figure 5.5 shows the components plotted against Yonsei-Yale isochrones (Demarque et al. 2004) for solar mixtures. Component A lies on the 1.6-Gyr isochrone, while component Ba lies roughly at 2.0 Gyr. Component Bb is not considered in the age determination, as its proximity to the main sequence causes decent agreement with virtually all of the plotted isochrones. Based on this information, along with the large uncertainties in the K magnitudes, the estimated age of this system is 1.8 ± 0.7 Gyr. Although very rough, this value is near the age of 1.5 ± 0.3 Gyr given by Scarfe et al. (1994).

Table. 5.3: V819 Her Data Revised

t (MJD)	B (m)	ψ (degrees)	$V_{\mathrm{A,obs}}$	$\sigma V_{\mathrm{A,obs}}$	$V_{\mathrm{B,obs}}$	$\sigma V_{\mathrm{B,obs}}$
53948.35303	330.5578	164.7310	0.2058	0.0219	0.0711	0.0071
53948.35706	330.5058	163.7626	0.2121	0.0261	0.0703	0.0081
53948.36143	330.4426	162.8346	0.2377	0.0277	0.0835	0.0052
53948.36562	330.3616	161.8918	0.2451	0.0245	0.0818	0.0057
53948.37290	330.1792	160.2861	0.2131	0.0188	0.0746	0.0095
53948.37727	330.0281	159.2645	0.2050	0.0272	0.0813	0.0132
53948.38235	329.8441	158.2249	0.1990	0.0203	0.0807	0.0093
54288.20821	244.3511	27.8184	0.2655	0.0223	0.0975	0.0074
54288.22157	245.4974	25.2397	0.2222	0.0128	0.0808	0.0092
54288.22809	245.9525	23.9440	0.2053	0.0213	0.0724	0.0053
54288.35370	248.0672	176.6238	0.3078	0.0161	0.0926	0.0031
54288.40191	247.7160	165.9277	0.3451	0.0205	0.0942	0.0087
54933.50672	277.4504	137.7036	0.3886	0.0239	0.0854	0.0074
54933.51026	277.1473	136.9389	0.3988	0.0198	0.0839	0.0062
54933.51824	276.3142	135.2640	0.3743	0.0129	0.0926	0.0032
55106.12429	254.9679	121.0614	0.3060	0.0289	0.0652	0.0058
55106.13872	247.7424	118.6614	0.3179	0.0351	0.0692	0.0083
55106.14342	245.1174	117.8855	0.3476	0.0239	0.0727	0.0092
55106.14761	242.7280	117.2152	0.3421	0.0380	0.0764	0.0069
55106.12815	253.1317	120.4080	0.3364	0.0279	0.0642	0.0064
55106.11281	259.9356	123.0249	0.3571	0.0333	0.0735	0.0099
55106.13304	250.7235	119.5991	0.3437	0.0374	0.0740	0.0063
55310.45721	247.1549	18.8919	0.2706	0.0218	0.0728	0.0043
55310.46187	247.3032	17.9250	0.2398	0.0315	0.0798	0.0115
55310.46588	247.4173	17.0741	0.2030	0.0162	0.0671	0.0093
55310.47000	247.5200	16.2004	0.2597	0.0199	0.0745	0.0042
55310.47382	247.6049	15.3751	0.2320	0.0203	0.0700	0.0083
55310.47745	247.6751	14.5979	0.2536	0.0161	0.0695	0.0057
55310.48129	247.7404	13.7700	0.2104	0.0264	0.0577	0.0064
55310.48555	247.8025	12.8542	0.2218	0.0113	0.0742	0.0066
55311.44761	246.8938	20.3230	0.1573	0.0207	0.0553	0.0053
55311.45531	247.1828	18.7203	0.1846	0.0214	0.0682	0.0068
55311.45917	247.3049	17.9138	0.2014	0.0140	0.0647	0.0063
55353.41001	172.4150	146.3587	0.3635	0.0136	0.0864	0.0055
55353.41367	171.9913	145.7172	0.3599	0.0112	0.1035	0.0072
55353.41736	171.5425	145.0817	0.3645	0.0216	0.1030	0.0048
55353.42553	170.4529	143.6938	0.3313	0.0165	0.0726	0.0035
55353.42920	169.9220	143.0832	0.3282	0.0185	0.0924	0.0078
55353.43349	169.2670	142.3787	0.3505	0.0206	0.0935	0.0070
55354.40604	172.5592	146.5878	0.3212	0.0306	0.0778	0.0075
55354.41013	172.0905	145.8637	0.3247	0.0446	0.0900	0.0086
55354.41394	171.6324	145.2057	0.3156	0.0353	0.0879	0.0130
55354.41809	171.0998	144.4940	0.2838	0.0385	0.0716	0.0033
55354.42212	170.5508	143.8110	0.2886	0.0426	0.0828	0.0051
55354.42663	169.9046	143.0639	0.3240	0.0233	0.0894	0.0111
55354.43436	168.6922	141.7993	0.3098	0.0286	0.0785	0.0061

Table 5.4. Revised Orbital Elements for V819 Her B derived from minimum χ^2 fit

Element	Value	Muterspaugh et al. (2008)
Fixed Elements:		
P (days)	$2.2296334 \pm 1.6 \times 10^{-6}$	$2.2296330 \pm 1.9 \times 10^{-6}$
$\alpha \sin i$ (mas)	0.6625 ± 0.0230	
e	0	0.0041 ± 0.0033
ω	0	$227° \pm 47°$
$\Theta_{\rm Ba}$ (mas)	0.126 ± 0.008	
$\Theta_{\rm Bb}$ (mas)	0.085 ± 0.007	
Varied elements:		
$T_{\rm node}$ (MJD)	52626.707 ± 0.040	52627.17 ± 0.29
α (mas)	0.6642 ± 0.0233	0.6657 ± 0.0058
i	$85.9° \pm 10.9°$	$80.70° \pm 0.38°$
Ω	$130.4° \pm 11.9°$	$131.1° \pm 4.1°$
$\Delta K_{\rm close}$	1.34 ± 0.17	1.38 ± 0.14
$\Delta K_{\rm wide}$	1.306 ± 0.032	
Reduced χ^2	1.00	

Note. — Muterspaugh et al. (2008) orbital elements are presented for comparison.

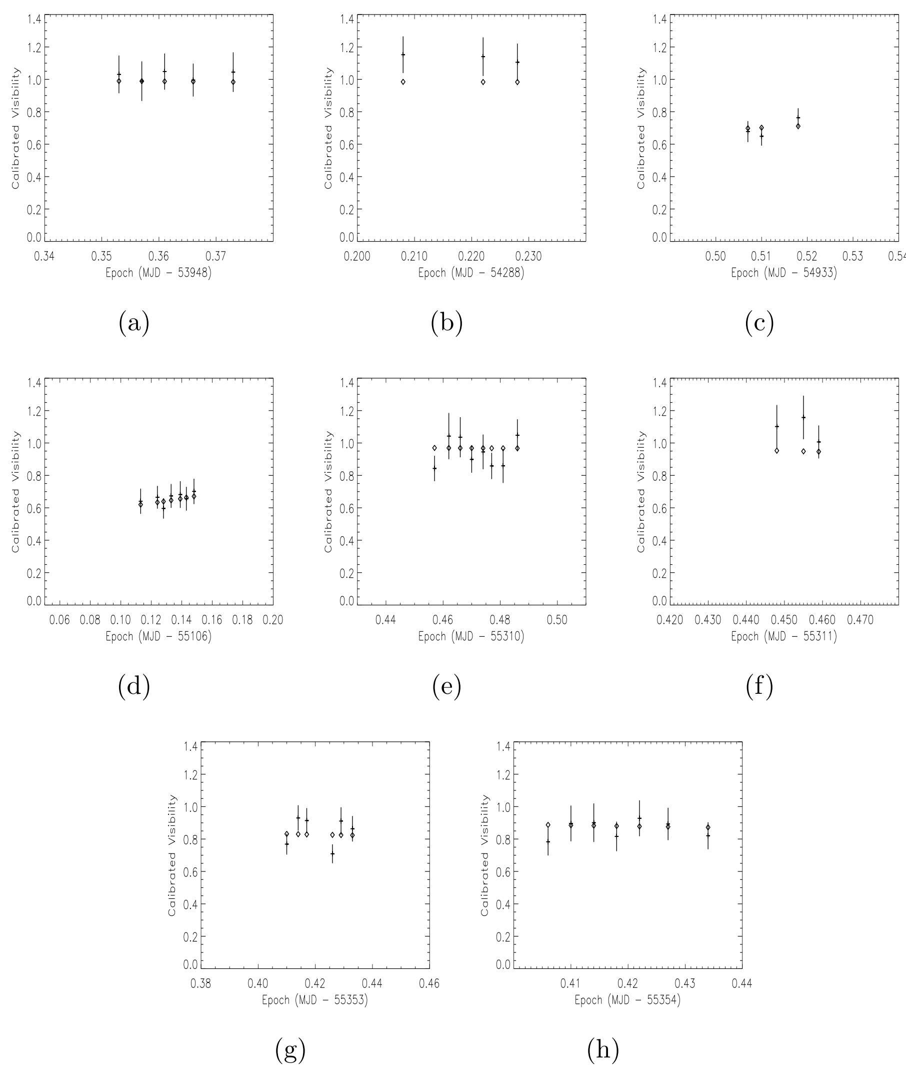

Figure. 5.3: Revised optimal orbit fit for V819 Her B

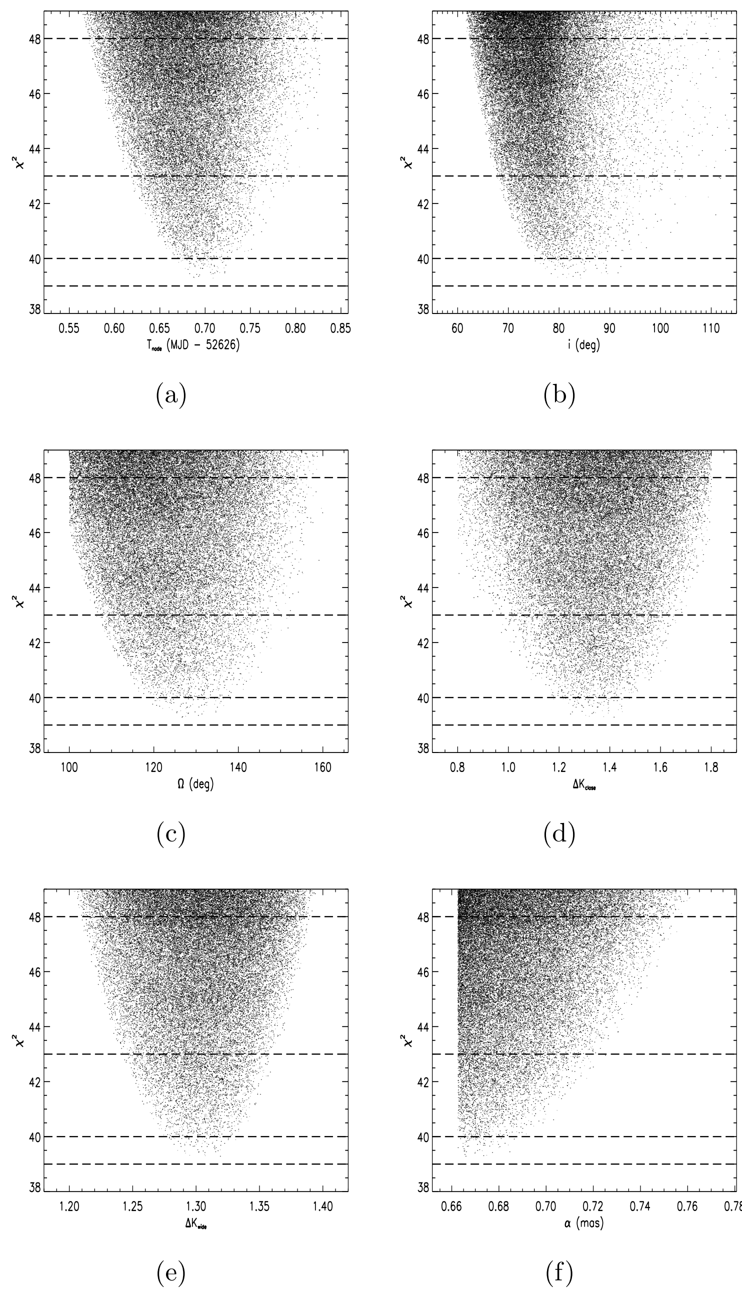

Figure. 5.4: Revised χ^2 plots for V819 Her B

Table 5.5. V819 Her Mutual Inclination

Element	Value (degrees)	
$i_{\rm wide}$	56.2 ± 0.4	
$i_{\rm close}$	85.9 ± 10.9	
$\Omega_{\rm wide}$	143.7 ± 0.3	
Ambiguous values:		
$\Omega_{\rm close}$	130.4 ± 11.9	310.4 ± 11.9
Φ	32.2 ± 11.0	140.1 ± 11.0

Table 5.6. V819 Her Masses

Element	Value	Muterspaugh et al. (2008)
π (mas)	14.7 ± 0.2	14.57 ± 0.19
α (mas)	0.6642 ± 0.0233	0.6657 ± 0.0058
a (AU)	0.04573 ± 0.00163	0.04569 ± 0.00040
P (days)	$2.2296334 \pm 1.6 \times 10^{-6}$	$2.2296330 \pm 1.9 \times 10^{-6}$
q	0.725 ± 0.010	0.742 ± 0.012
$M_{\rm B}$ ($M_\odot$)	2.566 ± 0.274	2.560 ± 0.067
$M_{\rm Ba}$ ($M_\odot$)	1.488 ± 0.181	1.469 ± 0.040
$M_{\rm Bb}$ ($M_\odot$)	1.079 ± 0.148	1.090 ± 0.030

Table 5.7. Magnitudes of V819 Her components

	AB	B	A	Ba	Bb
V			6.11 ± 0.05	6.82 ± 0.08	8.27 ± 0.16
K	3.839 ± 0.368	5.43 ± 0.37	4.12 ± 0.37	5.71 ± 0.37	7.05 ± 0.41
$V - K$			1.99 ± 0.37	1.11 ± 0.38	1.22 ± 0.44
$M_{\rm V}$			1.92 ± 0.04	2.63 ± 0.07	4.08 ± 0.16

Note. — V magnitudes are taken from Scarfe et al. (1994)

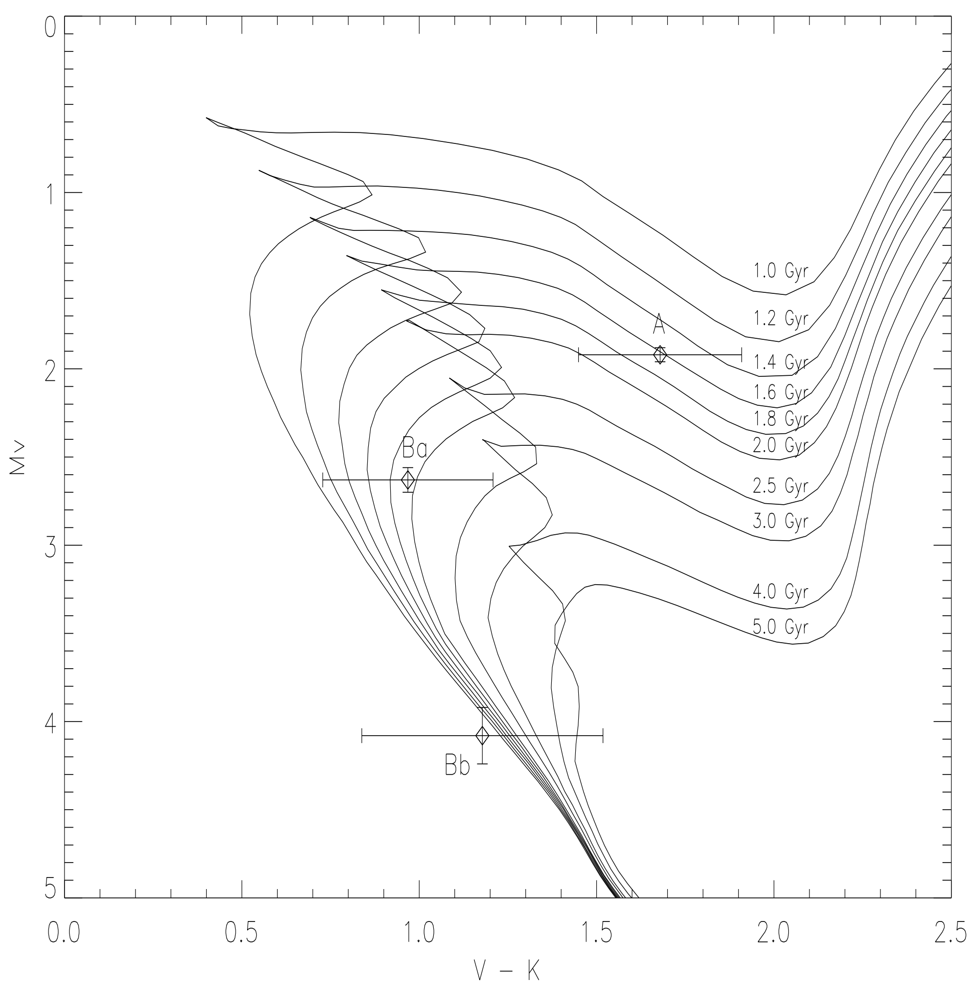

Figure. 5.5: V819 Her Age. $M_{\rm V}$ vs. $V-K$ for V819 Her components are plotted along with $\rm Y^2$ isochrones for $K_{\rm AB}=3.839$

5.2.2 κ Peg (HD 206901)

κ Pegasi is the second target for which an orbit has been already published. This system was first identified as a triple by Campbell & Wright (1900). Speckle interferometry by Hartkopf et al. (1989) has produced the visual 11.6-year, 236-mas wide orbit of the system while spectroscopy by Mayor & Mazeh (1987) has given the spectroscopic orbit of the 5.97-day close binary. Later, Muterspaugh et al. (2008) derived the visual orbit of the close binary by the same differential astrometry method used on V819 Her B. Visual components A and B of the system both show F subgiant spectra, with the component A classified as F5IV and component Ba, which dominates the spectrum of the close binary, classified as F6IV. The third component, Bb, is only weakly visible in the spectrum in favorable conditions, but may be anywhere from a main sequence F (Beardsley & King 1976) to K0 (Tokovinin 1997) spectral type. A very wide component C exists as well, but at 14 arcseconds away, it has no affect on the measurements taken here.

This system has been observed on 18 nights from 2006 July to 2010 April. On half of those nights, the opposite problem of V819 Her occurred. Instead of the SFPs being too close, they were too far apart to be observed simultaneously. For these nine nights, observations reverted to the normal method of CHARA bracketing, where the target and calibrator are alternately observed for about five minutes apiece. However, instead of moving the telescope between the objects, all that was required was to move the dither mirror to a different position in delay space. The fringe packets were far enough apart that there was no problem confusing the two. Although this is not the optimal observing strategy, these data are still valid. Data for this object are presented in Table 5.8.

Parameters fixed in the close orbit fitting are the period (P = 5.9714971 days) and the circular orbit parameters ($e = \omega = 0$). The angular diameters have been estimated based on the spectral types and a HIPPARCOS parallax of 28.34 ± 0.88 mas. All parallax values from this point on are taken from the original reduction by Perryman et al. (1997). The diameters are $\Theta_{\rm A} = 0.475 \pm 0.060$ mas, $\Theta_{\rm Ba} = 0.475 \pm 0.060$ mas, and $\Theta_{\rm Bb} = 0.114 \pm 0.016$ mas).

The orbital parameters of the minimum χ^2 fit are given in Table 5.9 along with the previously published solution by Muterspaugh et al. (2008). The plot of data vs. model visibilities is shown in Figures 5.6 and 5.7, with χ^2 plots given in Figure 5.8. The only errant night in the fit is JD 54706, in which the single data point lies far from the model. Since observations were limited to only one point that night, it is probably just an errant point, and if further observations had been conducted on that night, the rest of the data would have fit better. The fit is in decent agreement with the Muterspaugh orbit, with the only possible trouble spot being Ω, which is about 15° greater. This may be related to the large magnitude difference between the components of the close binary. The larger the magnitude difference in the binary, the more the system resembles a single star. Muterspaugh et al. (2006b) note the large difference in magnitude as a warning for validity of that orbit and find a luminosity ratio that suggests that the duplicity would not be visible with CHARA. It is contested here that CHARA is detecting the duplicity of this system because the model fits the data so well and the orbit derived in this work is so similar to what is found in Muterspaugh et al. (2008).

The mutual inclination of the system could be either $\Phi = 30.9°$ or $\Phi = 119.3°$ based on the ambiguous value of $\Omega_{\rm close}$. The method of Muterspaugh et al. (2008), after resolving the ambiguity, suggests that the former value is the correct one. Relevant information is presented in Table 5.10.

For this single-lined spectroscopic binary, the mass of the less massive component, $M_{\rm Bb}$, can be calculated by the mass function:

$$f(M) = \frac{M_{\rm Bb}^3 \sin^3 i}{(M_{\rm Ba} + M_{\rm Bb})^2} = 1.036 \times 10^{-7}(1 - e^2)^{1.5} K_{\rm Ba}^3 P \tag{5.5}$$

where the inclination i and the total mass of the two stars are known from the orbit given in Table 5.9. The masses calculated from this method are $M_{\rm Ba} = 2.62\ M_\odot$ and $M_{\rm Bb} = 1.04\ M_\odot$. These are slightly larger than one would expect for stars of these spectral types. The expected mass sum of the binary from the wide orbit is $M_\odot = 2.63\ M_\odot$, about 1 solar mass lower than what is derived here. This stems from a semi-major axis of 2.812 mas, about 0.3 mas larger than what is expected. Information on the masses is given in Table 5.11.

The magnitudes of the system are presented in Table 5.12. The overall magnitude is taken from the 2MASS Catalog (Skrutskie et al. 2006). With two subgiants, an age determination can be made for this system as well. The V magnitudes are taken from the Multiple Star Catalog. No errors accompany these measurements, so the error is estimated as $\sigma V = 0.18$ based on Beardsley & King (1977). This is the only source that contains any error estimates on the magnitudes of this system, so it is the only chance to get a reasonable error estimate on $V - K$. No individual magnitude is given for the faintest component of the system, so it has been left out of the age determination. An H-R diagram with isochrones is shown in Figure 5.9. The age of this system is determined to be 1.9 ± 0.5 Gyr.

Table. 5.8: κ Peg Data

t (MJD)	B (m)	ψ (degrees)	$V_{\mathrm{A,obs}}$	$\sigma V_{\mathrm{A,obs}}$	$V_{\mathrm{B,obs}}$	$\sigma V_{\mathrm{B,obs}}$
53944.33094	330.5916	57.9032	0.1512	0.0181	0.1301	0.0145
53944.33409	330.5148	58.4168	0.1639	0.0093	0.1279	0.0128
53944.33773	330.3754	59.0843	0.1317	0.0129	0.1150	0.0209
53944.34165	330.2181	59.6896	0.1244	0.0218	0.1103	0.0096
53944.34677	329.9388	60.5692	0.1328	0.0085	0.1057	0.0055
53944.34999	329.7296	61.1421	0.1227	0.0215	0.1221	0.0077
53944.35417	329.4253	61.8987	0.1384	0.0230	0.1113	0.0083
53944.35791	329.1333	62.5682	0.1333	0.0208	0.1179	0.0126
54387.35121	165.3590	61.1687	0.1434	0.0196	0.0984	0.0100
54649.41878	329.8860	29.2797	0.0718	0.0071	0.0515	0.0028
54649.42200	329.6749	28.7149	0.0655	0.0073	0.0510	0.0078
54649.42528	329.4350	28.1232	0.0655	0.0080	0.0585	0.0061
54649.42850	329.1786	27.5320	0.0624	0.0039	0.0579	0.0037
54649.43609	328.5114	26.1211	0.0571	0.0058	0.0528	0.0045
54649.43931	328.1989	25.5012	0.0644	0.0036	0.0600	0.0034
54649.44250	327.8788	24.8839	0.0661	0.0062	0.0542	0.0049
54649.44576	327.5418	24.2487	0.0588	0.0045	0.0506	0.0037
54649.44909	327.1849	23.5876	0.0581	0.0024	0.0426	0.0036
54649.45242	326.8189	22.9181	0.0549	0.0063	0.0401	0.0032
54649.45603	326.4207	22.1955	0.0515	0.0063	0.0472	0.0047
54649.45935	326.0423	21.5109	0.0439	0.0035	0.0441	0.0073
54649.46372	325.5411	20.6027	0.0455	0.0093	0.0446	0.0054
54649.46856	324.9766	19.5706	0.0484	0.0071	0.0453	0.0034
54649.47228	324.5432	18.7666	0.0534	0.0066	0.0465	0.0043
54649.47740	323.9596	17.6597	0.0644	0.0068	0.0517	0.0060
54649.48168	323.4748	16.7124	0.0636	0.0094	0.0448	0.0069
54649.48601	322.9998	15.7517	0.0683	0.0120	0.0451	0.0074
54650.41623	329.8752	29.2497	0.0489	0.0059	0.0483	0.0051
54650.41968	329.6451	28.6390	0.0533	0.0080	0.0482	0.0027
54650.42296	329.4044	28.0506	0.0516	0.0043	0.0449	0.0052
54650.42662	329.1110	27.3819	0.0560	0.0073	0.0454	0.0042
54650.43008	328.8121	26.7392	0.0532	0.0036	0.0419	0.0051
54650.43334	328.5130	26.1241	0.0567	0.0046	0.0421	0.0036
54650.43663	328.1959	25.4952	0.0574	0.0032	0.0385	0.0022
54650.44000	327.8571	24.8427	0.0632	0.0052	0.0402	0.0012
54650.44333	327.5104	24.1902	0.0537	0.0064	0.0439	0.0037
54650.44684	327.1310	23.4885	0.0588	0.0050	0.0422	0.0044
54650.45042	326.7363	22.7677	0.0499	0.0065	0.0404	0.0042
54650.45369	326.3713	22.1061	0.0498	0.0040	0.0393	0.0043
54650.46091	325.5391	20.5991	0.0845	0.0062	0.0579	0.0036
54650.46412	325.1661	19.9188	0.0777	0.0098	0.0574	0.0045
54650.46731	324.7978	19.2406	0.0775	0.0099	0.0553	0.0092
54650.47070	324.4067	18.5107	0.0753	0.0140	0.0592	0.0036
54651.41237	329.9448	29.4468	0.0976	0.0097	0.0665	0.0046
54651.41598	329.7122	28.8115	0.1005	0.0109	0.0703	0.0032
54651.41961	329.4524	28.1652	0.0882	0.0115	0.0658	0.0097
54651.42254	329.2197	27.6246	0.0988	0.0068	0.0679	0.0072
54651.42593	328.9358	27.0012	0.0978	0.0085	0.0681	0.0047
54651.42923	328.6411	26.3846	0.0982	0.0127	0.0649	0.0066
54651.43304	328.2815	25.6631	0.0895	0.0100	0.0579	0.0052
54651.43655	327.9308	24.9832	0.0776	0.0084	0.0511	0.0048
54651.43998	327.5782	24.3168	0.0895	0.0068	0.0573	0.0062
54651.44341	327.2114	23.6364	0.0862	0.0078	0.0579	0.0039
54651.44692	326.8257	22.9305	0.0835	0.0077	0.0553	0.0074
54651.45042	326.4308	22.2138	0.0850	0.0071	0.0557	0.0051
54651.45392	326.0315	21.4914	0.0893	0.0055	0.0540	0.0042
54651.45732	325.6408	20.7839	0.0901	0.0055	0.0599	0.0033
54651.46120	325.1912	19.9649	0.0918	0.0095	0.0594	0.0055
54651.46531	324.7128	19.0829	0.0911	0.0096	0.0533	0.0054
54651.46896	324.2916	18.2935	0.1011	0.0091	0.0597	0.0076

Table. 5.8 – Continued

t (MJD)	B (m)	ψ (degrees)	$V_{\mathrm{A,obs}}$	$\sigma V_{\mathrm{A,obs}}$	$V_{\mathrm{B,obs}}$	$\sigma V_{\mathrm{B,obs}}$
54662.38281	329.9168	29.3666	0.0812	0.0096	0.0851	0.0123
54662.38596	329.7110	28.8083	0.0786	0.0052	0.0748	0.0053
54662.38919	329.4784	28.2272	0.0907	0.0117	0.0951	0.0094
54662.39232	329.2355	27.6604	0.1005	0.0167	0.0954	0.0145
54662.39547	328.9714	27.0775	0.0870	0.0106	0.0861	0.0092
54662.40150	328.4246	25.9469	0.0858	0.0096	0.0744	0.0069
54662.40529	328.0529	25.2178	0.1001	0.0051	0.0855	0.0110
54662.40849	327.7277	24.5976	0.0911	0.0056	0.0813	0.0059
54662.41171	327.3892	23.9648	0.0982	0.0153	0.0785	0.0094
54662.41464	327.0696	23.3758	0.1083	0.0087	0.0828	0.0085
54662.41784	326.7156	22.7301	0.0981	0.0101	0.0741	0.0123
54663.38022	329.9079	29.3416	0.0921	0.0066	0.0781	0.0107
54663.38347	329.6941	28.7645	0.0982	0.0081	0.0859	0.0065
54663.38664	329.4659	28.1971	0.0922	0.0111	0.0740	0.0074
54663.38978	329.2195	27.6242	0.0958	0.0032	0.0751	0.0069
54663.39289	328.9592	27.0514	0.1004	0.0077	0.0785	0.0092
54663.39604	328.6790	26.4625	0.0873	0.0063	0.0661	0.0086
54663.39920	328.3837	25.8653	0.0959	0.0035	0.0719	0.0072
54663.40269	328.0402	25.1933	0.0917	0.0090	0.0673	0.0081
54663.40726	327.5691	24.2998	0.0745	0.0093	0.0625	0.0058
54663.41059	327.2154	23.6437	0.0901	0.0118	0.0763	0.0127
54663.41388	326.8531	22.9804	0.0877	0.0118	0.0655	0.0089
54706.47102	245.7367	160.0056	0.1367	0.0061	0.0937	0.0076
54711.40280	242.4052	171.6978	0.1303	0.0117	0.1191	0.0086
54711.41235	242.8638	169.5504	0.1298	0.0132	0.1138	0.0091
54711.42217	243.4087	167.4046	0.1307	0.0128	0.1158	0.0116
54711.43158	244.0037	165.3370	0.1280	0.0115	0.1171	0.0081
54711.44181	244.6833	163.1740	0.1321	0.0115	0.1095	0.0054
54711.45174	245.3594	161.1299	0.1388	0.0095	0.1119	0.0041
54713.39732	319.2777	175.2732	0.1109	0.0102	0.1171	0.0091
54713.40661	319.7342	173.0276	0.1155	0.0144	0.1238	0.0070
54713.42173	320.8195	169.3933	0.1211	0.0124	0.1074	0.0072
54713.44091	322.6658	164.9464	0.1123	0.0069	0.1049	0.0078
54713.45104	323.7824	162.6827	0.1086	0.0086	0.0890	0.0066
54721.35249	318.9018	0.9549	0.1259	0.0172	0.1131	0.0130
54721.36857	319.0410	177.0335	0.1248	0.0100	0.1069	0.0100
54721.38071	319.5115	174.0207	0.1256	0.0092	0.1201	0.0095
54721.39831	320.6563	169.8657	0.1182	0.0093	0.1001	0.0160
54721.41204	321.9012	166.6444	0.1166	0.0088	0.0946	0.0111
54722.33441	319.2355	4.4661	0.1395	0.0104	0.1163	0.0035
54722.34133	319.0209	2.7758	0.1491	0.0122	0.1206	0.0094
54722.34816	318.9068	1.1081	0.1383	0.0106	0.1177	0.0072
54722.35502	318.8909	179.4253	0.1296	0.0093	0.1223	0.0143
54722.36148	318.9679	177.8312	0.1356	0.0096	0.1309	0.0128
54722.37072	319.2294	175.5736	0.1378	0.0096	0.1312	0.0118
54722.37774	319.5415	173.8768	0.1382	0.0094	0.1263	0.0096
54722.38543	319.9950	172.0126	0.1366	0.0098	0.1321	0.0088
54722.39225	320.4833	170.3828	0.1341	0.0092	0.1377	0.0076
54722.40767	321.8468	166.7696	0.1518	0.0109	0.1430	0.0047
54722.41462	322.5585	165.1758	0.1614	0.0132	0.1340	0.0073
54722.42153	323.3097	163.6168	0.1662	0.0124	0.1266	0.0063
54811.15548	320.9901	168.9219	0.1758	0.0101	0.1536	0.0136
54811.16305	321.6885	167.1453	0.1859	0.0096	0.1559	0.0086
54811.17131	322.5218	165.2551	0.1830	0.0112	0.1591	0.0120
54811.17901	323.3578	163.5207	0.1874	0.0122	0.1484	0.0110
54811.18701	324.2628	161.7613	0.2016	0.0129	0.1456	0.0084
55106.23798	278.4273	134.3723	0.1802	0.0164	0.2293	0.0307
55106.24484	278.4945	133.2825	0.1888	0.0136	0.1836	0.0111
55106.25173	278.3353	132.2363	0.1983	0.0208	0.1861	0.0172
55106.25864	277.9367	131.2302	0.2024	0.0220	0.1944	0.0145
55106.26577	277.2664	130.2400	0.1987	0.0143	0.1699	0.0051

Table. 5.8 – Continued

t (MJD)	B (m)	ψ (degrees)	$V_{\mathrm{A,obs}}$	$\sigma V_{\mathrm{A,obs}}$	$V_{\mathrm{B,obs}}$	$\sigma V_{\mathrm{B,obs}}$
55106.27261	276.3613	129.3264	0.1925	0.0112	0.1765	0.0161
55106.27965	275.1574	128.4297	0.1936	0.0153	0.1601	0.0109
55106.28673	273.6593	127.5701	0.1974	0.0199	0.1694	0.0175
55106.36380	237.4089	120.8595	0.2425	0.0243	0.1434	0.0099
55107.13016	292.6872	83.8645	0.1655	0.0148	0.1340	0.0085
55107.13812	297.4457	82.7262	0.1566	0.0159	0.1208	0.0139
55107.14593	301.5131	81.6121	0.1613	0.0168	0.1231	0.0119
55107.15330	304.7973	80.5612	0.1567	0.0149	0.1235	0.0160
55108.17899	312.5456	76.4116	0.1234	0.0134	0.1152	0.0100
55108.18688	313.3196	75.2113	0.1201	0.0151	0.1095	0.0126
55108.19492	313.4968	73.9686	0.1197	0.0143	0.1055	0.0114
55108.20343	313.0256	72.6011	0.1202	0.0140	0.1040	0.0107
55310.49438	238.8494	40.3024	0.2234	0.0206	0.1879	0.0161
55310.49817	239.7552	39.9702	0.1898	0.0185	0.1768	0.0123
55310.50208	240.6352	39.6141	0.1764	0.0115	0.1561	0.0169
55310.50590	241.4530	39.2485	0.1950	0.0139	0.1884	0.0161
55311.46739	231.7619	42.1299	0.1903	0.0069	0.1398	0.0199
55311.47176	233.2083	41.8399	0.1516	0.0186	0.1794	0.0167
55311.47528	234.3050	41.5965	0.2023	0.0240	0.1599	0.0109
55311.47889	235.3922	41.3326	0.1872	0.0251	0.1633	0.0226
55311.48253	236.4494	41.0514	0.1813	0.0149	0.1603	0.0079
55311.48626	237.4641	40.7554	0.2134	0.0140	0.1896	0.0188
55311.49005	238.4480	40.4401	0.1699	0.0083	0.1585	0.0158
55311.49381	239.3689	40.1158	0.1763	0.0155	0.1687	0.0153
55311.49746	240.2225	39.7854	0.1706	0.0172	0.1879	0.0137
55311.50098	240.9950	39.4579	0.1800	0.0103	0.1774	0.0199

Table 5.9. Orbital Elements for κ Peg B derived from minimum χ^2 fit

Element	Value	Muterspaugh et al. (2008)
Fixed Elements:		
P (days)	$5.97164 \pm 6 \times 10^{-5}$	$5.971497 \pm 1.3 \times 10^{-6}$
e	0	0.0073 ± 0.0013
ω	0	$179.0° \pm 6.0°$
$\Theta_{\rm Ba}$ (mas)	0.475 ± 0.060	
$\Theta_{\rm Bb}$ (mas)	0.114 ± 0.016	
Varied elements:		
$T_{\rm node}$ (MJD)	52402.586 ± 0.088	52402.22 ± 0.10
α (mas)	2.812 ± 0.082	2.520 ± 0.006
i	$124.9° \pm 3.7°$	$125.7° \pm 5.1°$
Ω	$258.2° \pm 2.8°$	$244.1° \pm 2.3°$
$\Delta K_{\rm close}$	2.39 ± 0.12	
$\Delta K_{\rm wide}$	0.132 ± 0.013	
Reduced χ^2	1.00	
Wide Orbit:		
$P_{\rm wide}$ (years)	11.60 ± 0.12	
$T_{\rm wide}$ (BY)	1979.207 ± 0.027	
$e_{\rm wide}$	0.313 ± 0.009	
$\omega_{\rm wide}$	$304.17° \pm 0.60°$	
$\alpha_{\rm wide}$ (mas)	236.2 ± 0.4	
$i_{\rm wide}$	$108.0° \pm 0.5°$	
$\Omega_{\rm wide}$	$288.8° \pm 0.6°$	

Note. — Muterspaugh et al. (2008) orbital elements are presented for comparison. Wide orbit taken from Hartkopf et al. (1989).

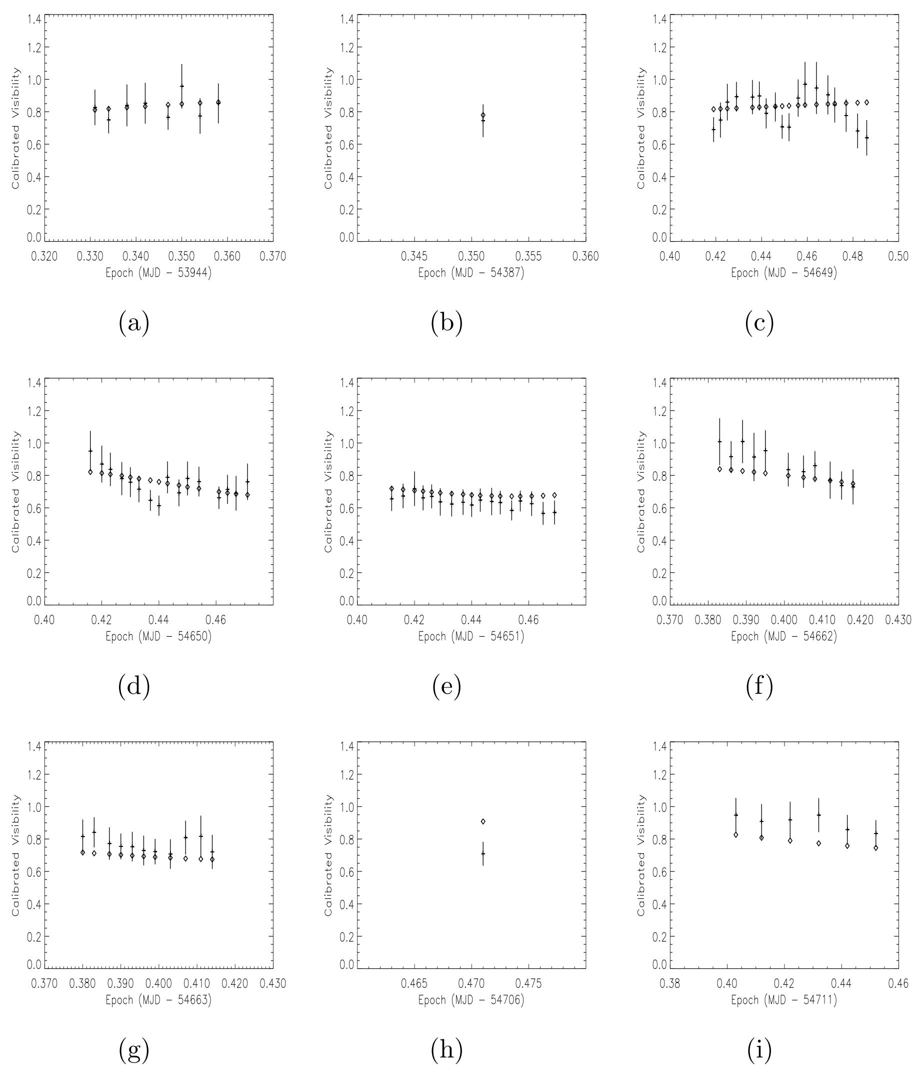

Figure. 5.6: Optimal orbit fit for κ Peg B

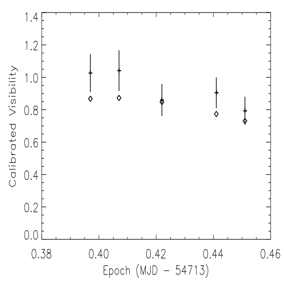

(a)

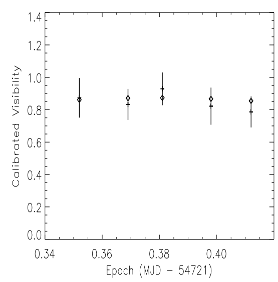

(b)

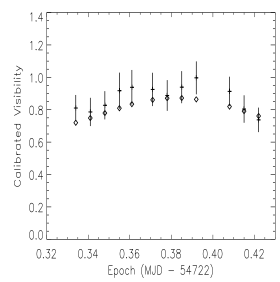

(c)

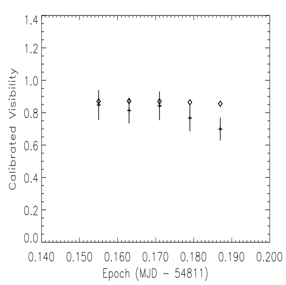

(d)

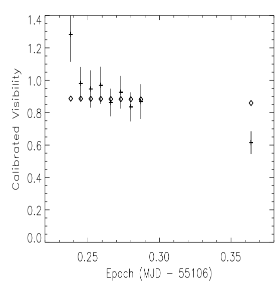

(e)

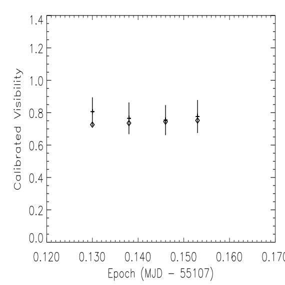

(f)

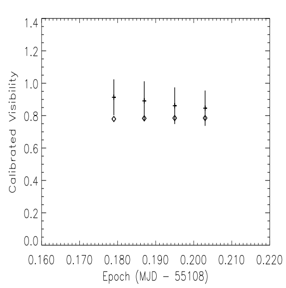

(g)

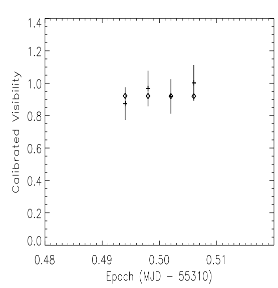

(h)

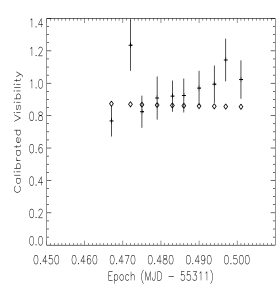

(i)

Figure. 5.7: Optimal orbit fit for κ Peg B (cont'd)

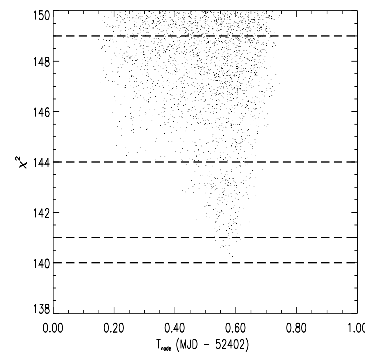

(a)

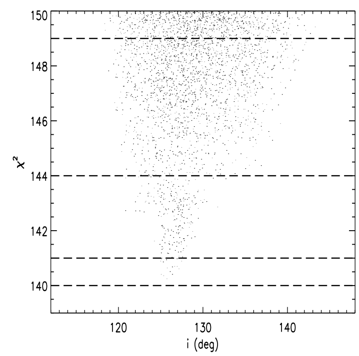

(b)

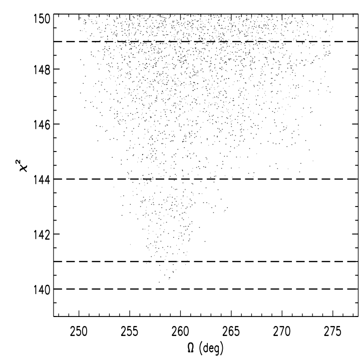

(c)

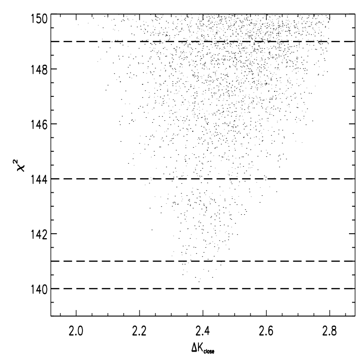

(d)

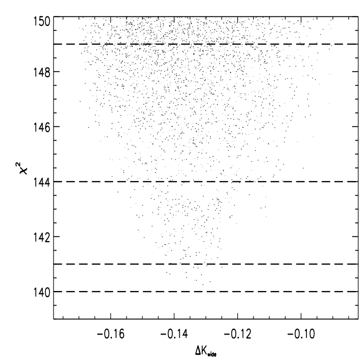

(e)

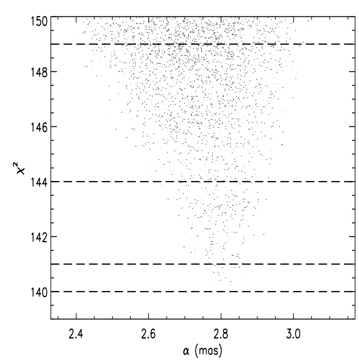

(f)

Figure. 5.8: χ^2 plots for κ Peg B

Table 5.10. κ Peg Mutual Inclination

Element	Value (degrees)	
$i_{\rm wide}$	108.8 ± 0.6	
$i_{\rm close}$	124.9 ± 3.7	
$\Omega_{\rm wide}$	288.0 ± 0.5	
Ambiguous values:		
$\Omega_{\rm close}$	258.2 ± 2.8	78.2 ± 2.8
Φ	30.9 ± 2.6	119.3 ± 3.4

Table 5.11. κ Peg Masses

Element	Value	Muterspaugh et al. (2008)
π (mas)	28.34 ± 0.88	28.93 ± 0.18
α (mas)	2.812 ± 0.082	2.520 ± 0.006
a (AU)	0.09922 ± 0.00438	0.08710 ± 0.00091
P (days)	5.97164 ± 0.00006	$5.9714971 \pm 1.3 \times 10^{-6}$
i	$124.9^\circ \pm 3.7^\circ$	$125.7^\circ \pm 5.1^\circ$
e	0	0.0073 ± 0.0013
$K_{\rm Ba}$ (km/s)	42.1 ± 0.3	
f(M)	0.0462 ± 0.0010	
$M_{\rm Ba}$ ($M_\odot$)	2.617 ± 0.260	1.646 ± 0.074
$M_{\rm Bb}$ ($M_\odot$)	1.038 ± 0.103	0.825 ± 0.059

Table 5.12. Magnitudes of κ Peg components

	AB	B	A	Ba	Bb
V			4.74 ± 0.18	5.00 ± 0.18	
K	2.92 ± 0.33	3.74 ± 0.33	3.61 ± 0.33	3.85 ± 0.33	6.24 ± 0.35
$V-K$			1.13 ± 0.37	1.15 ± 0.38	
$M_{\rm V}$			2.00 ± 0.18	2.26 ± 0.18	

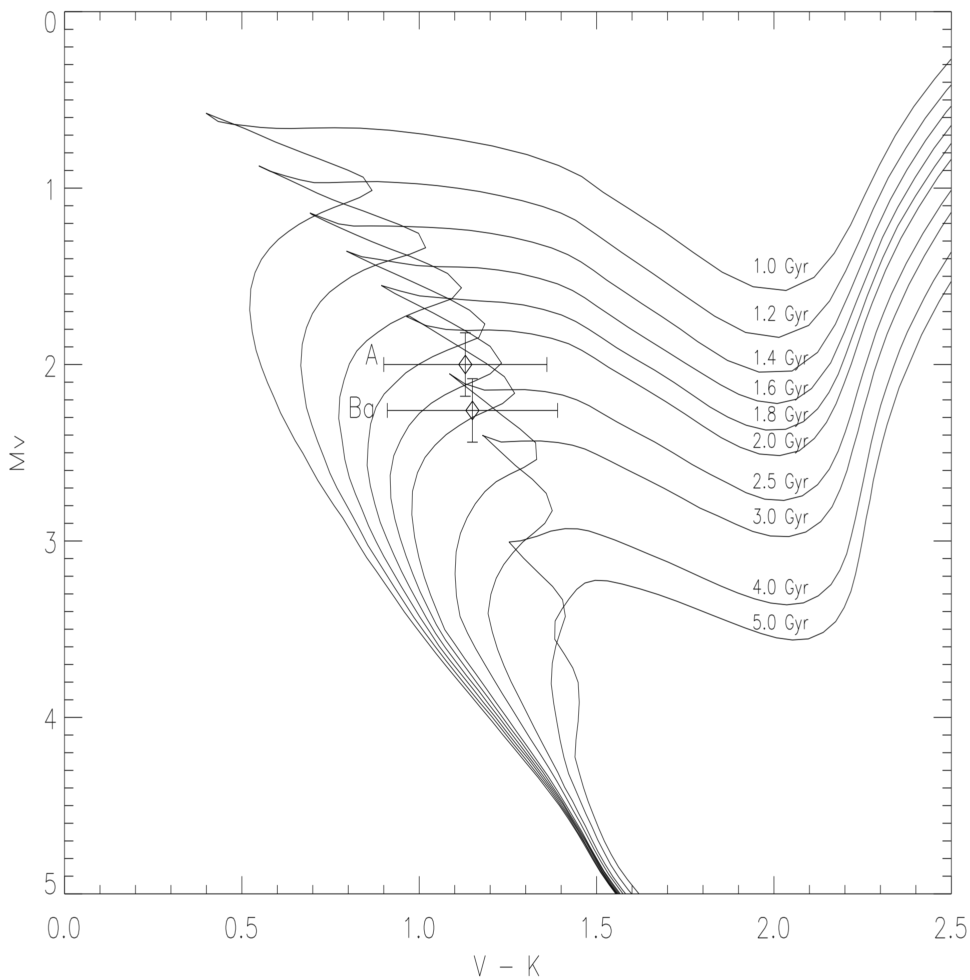

Figure. 5.9: κ Peg Age. M_{V} vs. $V-K$ for κ Peg components along with Y^2 isochrones for $K_{\mathrm{AB}} = 2.92$

5.2.3 η Virginis (HD 107259)

η Virginis is the third and final system for which there is a previously published orbit. This system was previously studied by Hummel et al. (2003) using six-telescope interferometry at the Navy Prototype Optical Interferometer. The A component system contains a pair of A stars (components Aa and Ab are, respectively, A2IV + A4V) orbiting the wide B component of unknown spectral type. The B component is known to be fainter than component Ab, a dwarf, so it is likely to be unevolved (Hartkopf et al. 1992). The wide orbit is a 134-mas, 13.1-year orbit, while the close orbit is about 7.4 mas and 72 days. Because the orbital period is relatively long compared to others in this study, this target does not have complete phase coverage. Other factors contributing to the poorer phase coverage are the amount of time η Vir is available for observation, and weather and technical issues that arose while trying to observe this target. The close binary semi-major axis is also much larger than that for the other targets, such that with certain CHARA configurations, the two stars of the close binary are actually resolvable into SSFPs. This situation was witnessed on 2009 April 13 & 14, making this possibly the first triple fringe packet ever observed at CHARA! The separation of the components of the wide orbit were too far apart to make simultaneous observations of both, and as such the bracketing technique was used here. Unfortunately, data on triple fringe packets where the two packets representing the close binary components are so close together is not useful for the purposes of this project because of the large amount of side-lobe interference.

Visibility information on the two packets of the close binary would only serve to give the diameters of the components, and the separation of the packets would be too affected by side-lobe interference to give any useful information. However, this can serve as a check to the orbit derived. The close orbit should show a large separation between Aa and Ab on the particular CHARA configuration used on 2009 April 13 & 14.

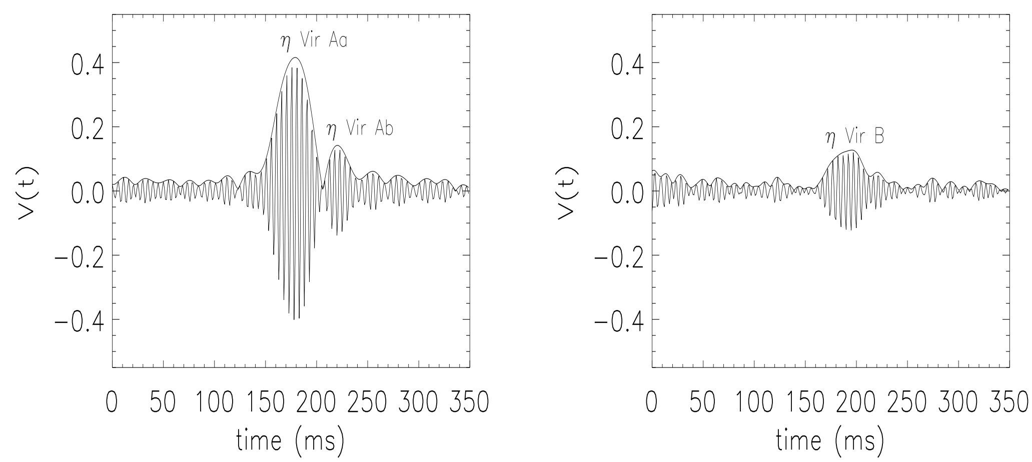

(a) (b)

Figure. 5.10: η Vir triple fringe packet observation. The A component was relatively far away from the B component in delay space ($\sim$400 μm), so bracketing observations were conducted. Each plot represents a single scan. Data are from 2009 April 13.

Using the HIPPARCOS parallax of 13.06 ± 0.84 mas (Perryman et al. 1997) and the spectral types (a very rough estimate in the case of B), the angular diameters in are calculated to be $\Theta_{\mathrm{Aa}} = 0.375 \pm 0.078$ mas, $\Theta_{\mathrm{Ab}} = 0.110 \pm 0.029$ mas, and $\Theta_{\mathrm{B}} = 0.091 \pm 0.027$ mas.

Initial fitting involved letting all the parameters float except for the period. This produced an orbit that was completely dissimilar to the orbit of Hummel et al. (2003). This is understandable, with only 39 data points from only 8 nights (Table 5.13). With such poor phase coverage and so many floating variables, it is believed that many different sets of orbital parameters could fit the data reasonably well. For this reason, it was decided that the solution should be guided by fixing the elements of the spectroscopic orbit with the values of Hartkopf et al. (1992). This includes the e and ω, which are non-zero because of this non-circular orbit, as well as P and T. This produced favorable results. The minimum χ^2 orbital parameters are presented in Table 5.14 along with the orbit by Hummel et al. (2003). The semi-major axis, inclination, and magnitude differences are all very close to the Hummel orbit. Similar to the case with κ Peg, the only parameter that is a trouble spot is Ω_{close}, for which the result here is about 13° less than the Hummel's value. The fit is shown in Figure 5.11, and the χ^2 plots are shown in Figure 5.12. It may be noticed that some of the χ^2 plots have hard edges on the left and/or right side of the χ^2 distribution. In some cases, it is necessary to narrow the search space in order to fill out the plot and display the general shape of the distribution.

The mutual inclination of the system is given in Table 5.15. The Hummel et al. (2003) orbit resolves the ambiguity and suggests that the value $\Phi = 40.1°$ is the correct mutual inclination. Masses are calculated for this double-line system and given in Table 5.16. These masses are reasonable for the proposed spectral types of the two stars. Finally, the individual magnitudes are given in Table 5.17. The value for the overall K magnitude of the system is taken from 2MASS (Skrutskie et al. 2006). Two different sets of possible V magnitudes are given here to show that the individual V magnitudes of the system are very uncertain. The two sources (Hummel et al. (2003) and Hartkopf et al. (1992)) do not agree on which component is the fainter companion and do not give any uncertainties on their magnitudes. The resulting M_V and $V - K$ values are very different, such that an age determination from these values would be challenging even with an evolved component in the system.

Table. 5.13: η Vir Data

t (MJD)	B (m)	ψ (degrees)	$V_{\mathrm{A,obs}}$	$\sigma V_{\mathrm{A,obs}}$	$V_{\mathrm{B,obs}}$	$\sigma V_{\mathrm{B,obs}}$
53083.35892	247.9866	78.7999	0.1663	0.0142	0.0514	0.0045
53083.38542	238.0298	78.4389	0.1518	0.0121	0.0461	0.0017
53084.33732	251.0443	78.8592	0.2658	0.0126	0.0542	0.0027
53084.37063	243.3687	78.6458	0.2458	0.0106	0.0614	0.0055
53085.33445	251.0546	78.8591	0.2158	0.0083	0.0488	0.0014
53085.34953	248.9032	78.8252	0.1981	0.0078	0.0462	0.0026
53085.38012	237.9481	78.4355	0.1625	0.0171	0.0480	0.0035
53108.36691	277.6192	128.4275	0.1267	0.0089	0.0487	0.0033
53108.37890	278.4383	128.3442	0.1377	0.0119	0.0440	0.0018
53108.39970	277.5443	128.5781	0.1419	0.0682	0.0476	0.0048
54567.15584	329.2388	40.7868	0.2674	0.0247	0.1005	0.0131
54567.17579	325.6703	40.1382	0.2563	0.0341	0.1332	0.0204
55337.22111	160.5596	147.9508	0.2712	0.0209	0.0555	0.0054
55337.22750	162.1662	147.0817	0.2592	0.0317	0.0542	0.0055
55337.23337	163.5836	146.3467	0.2569	0.0366	0.0581	0.0073
55337.26794	170.9588	142.9336	0.3215	0.0507	0.0560	0.0108
55353.17301	159.6470	148.4625	0.5145	0.0215	0.1171	0.0082
55353.17680	160.6106	147.9224	0.5125	0.0255	0.1095	0.0112
55353.18065	161.5775	147.3955	0.4875	0.0306	0.1031	0.0117
55353.18438	162.4946	146.9088	0.4785	0.0290	0.0967	0.0043
55353.18825	163.4398	146.4199	0.4298	0.0213	0.0793	0.0058
55353.19199	164.3305	145.9705	0.4323	0.0403	0.0809	0.0091
55353.19571	165.2003	145.5418	0.4301	0.0246	0.0832	0.0060
55353.20305	166.8548	144.7527	0.3541	0.0253	0.0711	0.0053
55353.20678	167.6579	144.3816	0.3371	0.0227	0.0650	0.0039
55353.21052	168.4457	144.0249	0.3129	0.0238	0.0657	0.0070
55353.21429	169.2111	143.6851	0.2992	0.0212	0.0674	0.0049
55353.21810	169.9560	143.3607	0.2903	0.0229	0.0672	0.0061
55353.22183	170.6578	143.0606	0.2743	0.0229	0.0691	0.0038
55353.22549	171.3153	142.7843	0.2729	0.0274	0.0733	0.0080
55353.22932	171.9757	142.5116	0.2752	0.0109	0.0798	0.0055
55354.22601	171.8734	142.5536	0.2622	0.0261	0.1033	0.0050
55354.22998	172.5262	142.2880	0.2875	0.0279	0.0998	0.0072
55354.23399	173.1506	142.0384	0.2764	0.0193	0.1013	0.0099
55354.23781	173.7070	141.8197	0.2774	0.0193	0.1029	0.0066
55354.24172	174.2355	141.6155	0.2903	0.0262	0.1163	0.0084
55354.24574	174.7435	141.4225	0.2578	0.0209	0.1105	0.0097
55354.25003	175.2307	141.2409	0.2692	0.0281	0.1100	0.0128
55354.25498	175.7520	141.0507	0.2933	0.0281	0.1228	0.0095

Table 5.14. Orbital Elements for η Vir A derived from minimum χ^2 fit

Element	Value	Hummel et al. (2003)
Fixed Elements:		
P (days)	71.7919 ± 0.0009	71.7916 ± 0.0006
e	0.272 ± 0.009	0.244 ± 0.007
ω	$200.9° \pm 1.5°$	$196.9° \pm 1.8°$
T (MJD)	52321.7 ± 0.3	52321.4 ± 0.3
$\Theta_{\rm Aa}$ (mas)	0.375 ± 0.078	
$\Theta_{\rm Ab}$ (mas)	0.110 ± 0.029	
Varied elements:		
α (mas)	7.59 ± 0.08	7.36 ± 0.08
i	$45.0° \pm 0.7°$	$45.5° \pm 0.9°$
Ω	$116.5° \pm 0.3°$	$129.5° \pm 0.9°$
$\Delta K_{\rm close}$	1.29 ± 0.08	
$\Delta K_{\rm wide}$	1.72 ± 0.03	
Reduced χ^2	1.00	
Wide orbit:		
$P_{\rm wide}$ (days)	4791.9 ± 18.0	
$T_{\rm wide}$ (BY)	1963.80 ± 0.02	
$e_{\rm wide}$	0.079 ± 0.014	
$\omega_{\rm wide}$	$1.4° \pm 2.4°$	
$\alpha_{\rm wide}$ (mas)	136 ± 12	
$i_{\rm wide}$	$51.1° \pm 0.2°$	
$\Omega_{\rm wide}$	$170.8° \pm 2.4°$	

Note. — Hummel et al. (2003) orbital elements are presented for comparison. The wide orbit and the spectroscopic elements of the close orbit are taken from Hartkopf et al. (1992).

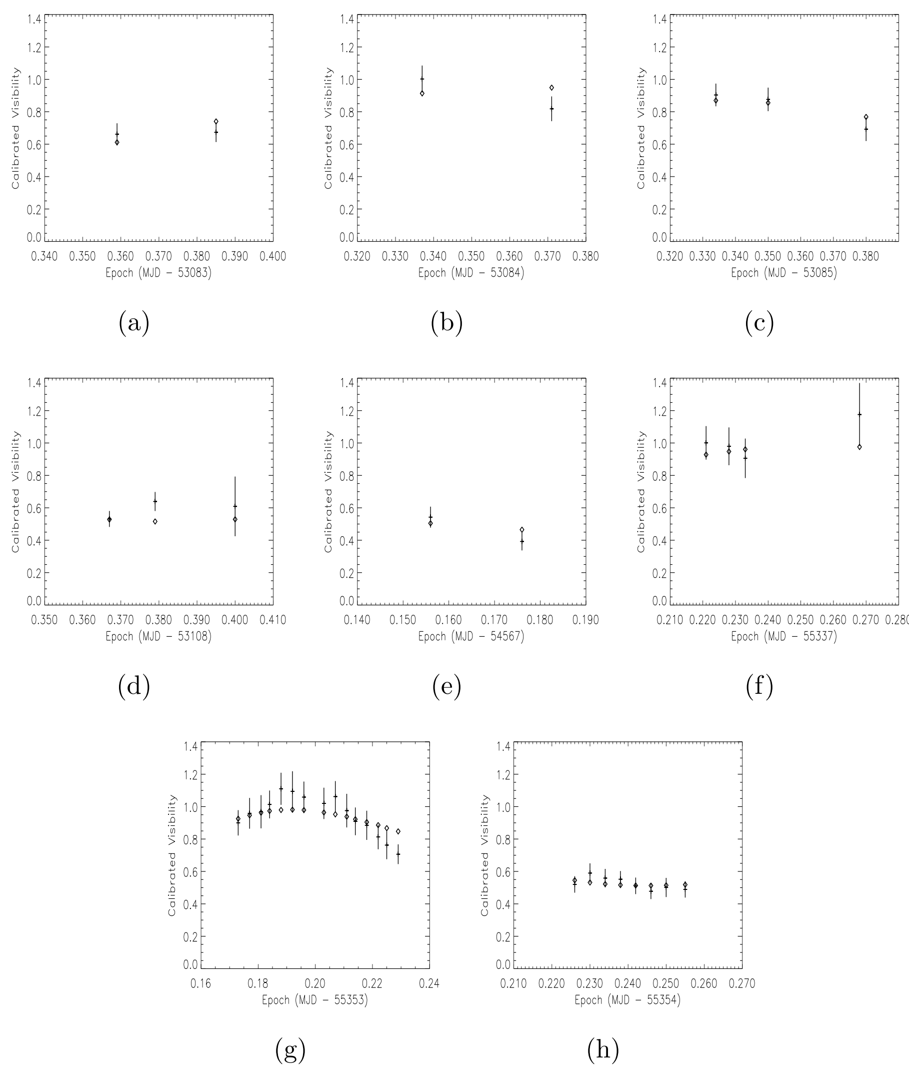

Figure. 5.11: Optimal orbit fit for η Vir A

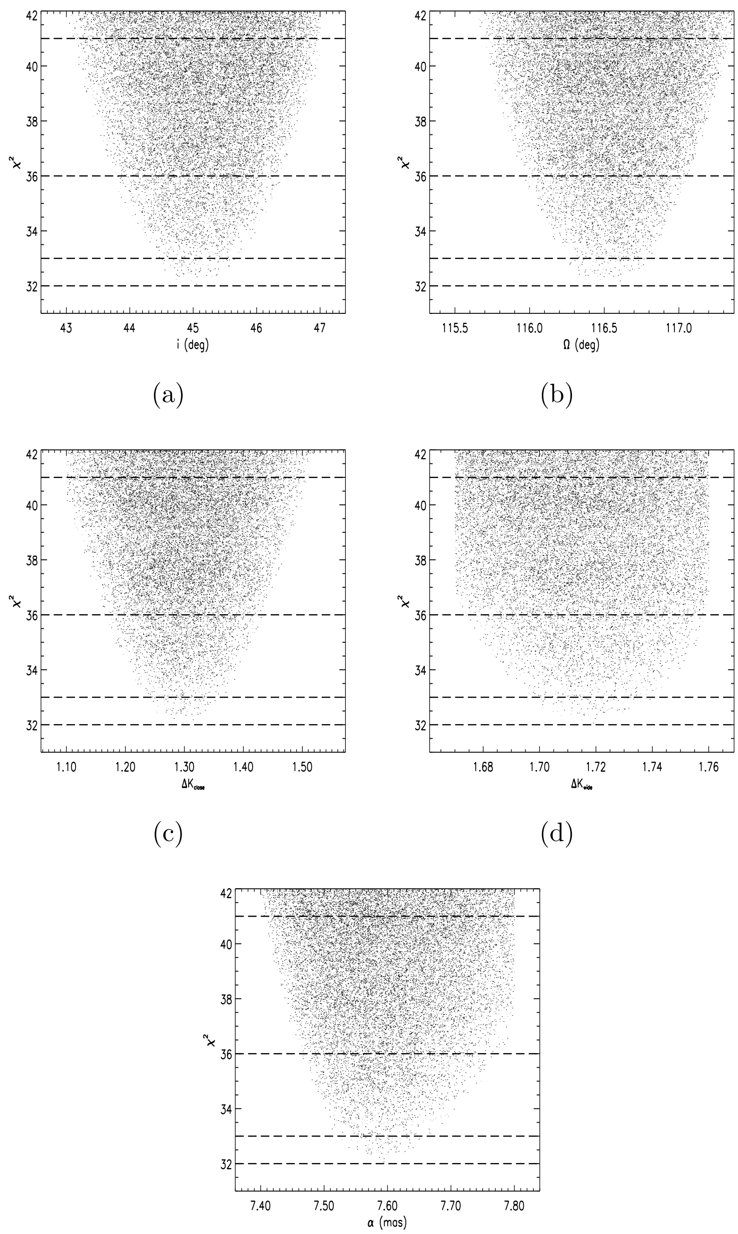

(a) (b) (c) (d) (e)

Figure. 5.12: χ^2 plots for η Vir A.

Table 5.15. η Vir Mutual Inclination

Element	Value (degrees)	
i_{wide}	51.1 ± 0.2	
i_{close}	45.0 ± 0.7	
Ω_{wide}	170.8 ± 2.4	
Ambiguous values:		
Ω_{close}	116.5 ± 0.3	296.5 ± 0.3
Φ	40.1 ± 1.7	82.9 ± 1.2

Table 5.16. η Vir Masses

Element	Value	Hummel et al. (2003)
π (mas)	13.06 ± 0.84	13.0 ± 0.5
α (mas)	7.59 ± 0.08	7.36 ± 0.08
a (AU)	0.581 ± 0.041	
P (days)	71.7919 ± 0.0009	79.7916 ± 0.0006
K_{Aa} (km/s)	26.3 ± 0.2	
K_{Ab} (km/s)	35.6 ± 0.3	
M_{Aa} ($M_{\odot}$)	2.92 ± 0.62	2.68 ± 0.15
M_{Ab} ($M_{\odot}$)	2.16 ± 0.47	2.04 ± 0.10

Table 5.17. Magnitudes of η Vir components

	AB	A	Aa	Ab	B
K	3.789 ± 0.033	3.99 ± 0.03	4.28 ± 0.04	5.57 ± 0.04	5.71 ± 0.09
V			4.2	6.0	6.5
$V - K$			-0.08	0.43	0.79
M_{V}			-0.22	1.58	2.08
V		4.32	4.60	5.90	5.12
$V - K$			0.32	0.33	-0.59
M_{V}			0.18	1.48	0.70

Note. — First set of magnitudes is from Hummel et al. (2003). The second set is from Hartkopf et al. (1992).

5.2.4 η Orionis (HD 35411)

η Ori was the original prototype system for this study. It is the first system presented here with a completely new orbit for the close binary. This is a known quadruple system with a very wide B component at 1.7 arcseconds that is of no interest here. The inner triple consists of a B dwarf (component Ac - B3V) orbiting a pair of B dwarfs (components Aa - B1V and Ab - B3V) in a 9.4-year, 44.1-mas orbit (Balega et al. 1999). In retrospect, the wide orbit here is smaller than ideal, as there will be a period of several years where it is difficult to get a large enough separation between the packets to avoid side-lobe interference. The close binary is an 8.0-day, 0.7-mas orbit (Zizka & Beardsley 1981). The close binary is also an eclipsing system that has been characterized photometrically by Waelkens & Lampens (1988). The combination of the spectroscopy and photometry of η Ori can provide most of the orbital elements of the system, but the orbit presented here provides the first determination of Ω_{close} and thus, the mutual inclination. The orbit solution is given in Table 5.19, while the plot of the data vs. model visibilities is shown in Figures 5.13 and 5.14. The associated χ^2 plots are given in Figure 5.15.

The parallax of this system has been a consistently large source of error. The original HIPPARCOS catalog gives $\pi = 3.62 \pm 0.88$ mas (Perryman et al. 1997), while the revised catalog gives $\pi = 3.26 \pm 1.10$ mas (van Leeuwen 2007). This makes it difficult to come up with an expected value for the semi-major axis of the close binary. One limiting factor on the distance is that the system is part of the Orion

OB-1 association. The Perryman et al. (1997) is preferred here because of the smaller error.

Several nights of data on η Ori are affected by side-lobe interference. These are the nights shown in Figures 4.11 and 4.12. For the epochs on which this occurred, only the corrected data are presented in Table 5.18. The corrected data are given in the form of the original $V_{\rm obs}$ for Aab, but a corrected $V_{\rm obs}$ for Ac. $V_{\rm Ac,obs}$ is calculated by determining the corrected visibility ratio from those figures and dividing the $V_{\rm Aab,obs}$ by the corrected ratio.

The mutual inclination of the system is either $\Phi = 117.4°$ or $\Phi = 65.1°$ (Table 5.20). There is no way to resolve the ambiguity in this case, so a definitive value cannot be determined, but in either case, this system is definitely not coplanar. Mass estimation (Table 5.21) is difficult in this case because of the difference between the expected and derived semi-major axis of the close binary. The expected semi-major axis from the wide orbit is $\alpha = 0.784$ mas, while the value derived here is $\alpha = 0.691$ mas. Also, the large error in the parallax contributes to uncertainties on the masses of nearly 82%.

Magnitudes have been calculated (Table 5.22) for the system based on an overall magnitude of $K_{\rm A} = 3.900 \pm 0.036$ from 2MASS. No age determination is made because there is no evolved component. Even if there had been, calculation of the absolute magnitude, $M_{\rm V}$, would have a high level of error because of the parallax error. It is also likely that the 2MASS magnitude includes the B component (there are no other

2MASS measurements for this system), which would prevent the correct calculation of the individual magnitudes.

Even with the apparent problems in the mass calculations, the orbit still matches previous observations very well. The time of nodal passage, T_{node}, calculated here is 55202.348 MJD. The value for the spectroscopic orbit of Zizka & Beardsley (1981), when brought into the current epoch, is 55202.280 MJD. This is a difference of about 1.6 hours, or 0.8% of the period. The inclination of the system is 85.0°, consistent with an eclipsing system. No inclination is given by the photometric study by Waelkens & Lampens (1988), so no direct comparison can be made, but the fact that an inclination near 90° was derived enhances confidence in this orbit. The semi-major axis, which has already been discussed, is different enough from the expected value to cause large differences in masses, but it is still relatively close. The magnitude differences are satisfactory for stars of this spectral type. If one looks at the ΔV magnitudes and considers the $V-K$ values for stars of these spectral types (given in Table 5.22), the ΔK values make sense. Overall, this first original orbit of the self-calibration method looks to be reasonably good.

Table. 5.18: η Ori Data

t (MJD)	B (m)	ψ (degrees)	$V_{\mathrm{Aab,obs}}$	$\sigma V_{\mathrm{Aab,obs}}$	$V_{\mathrm{Ac,obs}}$	$\sigma V_{\mathrm{Ac,obs}}$
53319.37368	312.2774	75.5245	0.3060	0.0164	0.0948	0.0035
53319.37697	312.7711	75.5975	0.3169	0.0225	0.0986	0.0065
53319.38012	313.1263	75.6616	0.3153	0.0137	0.1043	0.0036
53319.38287	313.3424	75.7133	0.3159	0.0200	0.1091	0.0048
53319.38564	313.4710	75.7612	0.3144	0.0106	0.0977	0.0086
53319.38843	313.5097	75.8050	0.3321	0.0194	0.0984	0.0059
53319.39122	313.4575	75.8448	0.3113	0.0264	0.0953	0.0088
53319.39395	313.3186	75.8796	0.2937	0.0124	0.0906	0.0056
53319.39675	313.0862	75.9111	0.2785	0.0126	0.0903	0.0031
53319.39970	312.7414	75.9399	0.2840	0.0224	0.0916	0.0057

Table. 5.18 – Continued

t (MJD)	B (m)	ψ (degrees)	$V_{\rm A,obs}$	$\sigma V_{\rm A,obs}$	$V_{\rm B,obs}$	$\sigma V_{\rm B,obs}$
53325.37229	313.5088	75.8086	0.2478	0.0615	0.0970	0.0224
53325.37512	313.4473	75.8485	0.2459	0.0106	0.0888	0.0063
53325.37797	313.2906	75.8844	0.2585	0.0132	0.0954	0.0077
53325.38111	313.0086	75.9188	0.2693	0.0263	0.0926	0.0071
53325.38410	312.6323	75.9467	0.2102	0.0092	0.0846	0.0053
53325.38685	312.1956	75.9681	0.1760	0.0134	0.0847	0.0041
53328.33024	307.0348	74.9839	0.1650	0.0140	0.0555	0.0021
53328.33331	308.1665	75.0867	0.1858	0.0134	0.0572	0.0023
53328.33606	309.0852	75.1734	0.1951	0.0198	0.0625	0.0038
53328.33886	309.9348	75.2572	0.1742	0.0108	0.0612	0.0059
53328.34184	310.7425	75.3415	0.1910	0.0135	0.0672	0.0055
53328.34463	311.4027	75.4152	0.1851	0.0175	0.0590	0.0058
53328.34743	311.9771	75.4850	0.1900	0.0080	0.0657	0.0097
53328.35036	312.4803	75.5531	0.1827	0.0128	0.0578	0.0036
53328.35307	312.8567	75.6117	0.1895	0.0069	0.0604	0.0062
53328.35586	313.1554	75.6677	0.1801	0.0118	0.0612	0.0023
53328.35904	313.3859	75.7266	0.1823	0.0146	0.0561	0.0061
53328.36178	313.4895	75.7728	0.1858	0.0180	0.0594	0.0049
53328.36470	313.5036	75.8175	0.1709	0.0109	0.0543	0.0032
53328.36900	313.3432	75.8750	0.1600	0.0163	0.0545	0.0032
53328.37185	313.1179	75.9076	0.1575	0.0156	0.0506	0.0025
53328.37454	312.8176	75.9345	0.1461	0.0141	0.0500	0.0039
53328.37734	312.4159	75.9584	0.1448	0.0110	0.0580	0.0039
53339.29307	304.0008	74.7222	0.2137	0.0134	0.0702	0.0062
53339.29622	305.4119	74.8420	0.2224	0.0120	0.0674	0.0052
53339.29920	306.6438	74.9492	0.2182	0.0146	0.0619	0.0059
53339.30230	307.8166	75.0545	0.2177	0.0186	0.0622	0.0060
53339.30506	308.7730	75.1436	0.2215	0.0138	0.0635	0.0060
53339.30799	309.6908	75.2327	0.2015	0.0174	0.0643	0.0063
53339.31403	311.2765	75.4007	0.1890	0.0129	0.0618	0.0048
53339.31677	311.8558	75.4697	0.1826	0.0171	0.0652	0.0033
53339.31947	312.3439	75.5337	0.1728	0.0103	0.0610	0.0057
53339.32225	312.7560	75.5950	0.1718	0.0132	0.0555	0.0044
53339.32531	313.1071	75.6577	0.1676	0.0148	0.0570	0.0040
53339.32859	313.3622	75.7191	0.1554	0.0098	0.0572	0.0021
53339.33132	313.4791	75.7658	0.1614	0.0163	0.0541	0.0067
53339.33411	313.5085	75.8094	0.1599	0.0131	0.0555	0.0033
53339.33685	313.4488	75.8480	0.1718	0.0131	0.0574	0.0029
53339.33976	313.2900	75.8845	0.1640	0.0115	0.0588	0.0042
53339.34249	313.0499	75.9148	0.1589	0.0201	0.0573	0.0036
53339.34523	312.7226	75.9411	0.1457	0.0102	0.0605	0.0057
53340.31539	312.1102	75.5022	0.1829	0.0179	0.0640	0.0056
53340.31837	312.5964	75.5702	0.1879	0.0082	0.0591	0.0060
53340.32114	312.9559	75.6290	0.1964	0.0166	0.0604	0.0060
53340.32388	313.2234	75.6828	0.1848	0.0191	0.0552	0.0055
53340.32787	313.4569	75.7540	0.1739	0.0133	0.0559	0.0044
53340.33063	313.5096	75.7980	0.1756	0.0102	0.0545	0.0025
53340.33347	313.4710	75.8392	0.1946	0.0120	0.0583	0.0042
53340.33652	313.3244	75.8785	0.1843	0.0106	0.0585	0.0063
53340.33935	313.0918	75.9105	0.1586	0.0176	0.0555	0.0076
53340.34206	312.7805	75.9372	0.1635	0.0075	0.0559	0.0048
53340.34522	312.3114	75.9632	0.1424	0.0037	0.0541	0.0041
53341.32757	313.5079	75.7929	0.1944	0.0209	0.0617	0.0069
53341.33036	313.4816	75.8339	0.2052	0.0237	0.0724	0.0034
53341.33311	313.3670	75.8701	0.1901	0.0216	0.0628	0.0071
53341.33604	313.1467	75.9043	0.1998	0.0369	0.0634	0.0038
53341.33893	312.8325	75.9334	0.1863	0.0120	0.0636	0.0060
53341.34164	312.4489	75.9567	0.1941	0.0146	0.0623	0.0045
53342.31939	313.2970	75.7009	0.1463	0.0199	0.0484	0.0044
53342.32214	313.4470	75.7495	0.1509	0.0167	0.0510	0.0050
53342.32494	313.5086	75.7945	0.1646	0.0163	0.0489	0.0032

Table. 5.18 – Continued

t (MJD)	B (m)	ψ (degrees)	$V_{\mathrm{A,obs}}$	$\sigma V_{\mathrm{A,obs}}$	$V_{\mathrm{B,obs}}$	$\sigma V_{\mathrm{B,obs}}$
53342.32768	313.4802	75.8347	0.1435	0.0121	0.0517	0.0033
53342.33045	313.3626	75.8710	0.1385	0.0102	0.0526	0.0022
53342.33317	313.1597	75.9028	0.1667	0.0128	0.0512	0.0036
53342.33597	312.8608	75.9313	0.1681	0.0075	0.0542	0.0052
53342.33874	312.4754	75.9554	0.1563	0.0078	0.0497	0.0042
53349.29383	312.6017	75.5710	0.2168	0.0149	0.0759	0.0059
53349.29680	312.9825	75.6338	0.2164	0.0166	0.0695	0.0054
53349.29955	313.2433	75.6875	0.2070	0.0157	0.0655	0.0063
53349.30244	313.4223	75.7394	0.2213	0.0106	0.0693	0.0056
53349.30522	313.5030	75.7851	0.2024	0.0142	0.0665	0.0047
53349.30795	313.4943	75.8259	0.2072	0.0214	0.0710	0.0062
53349.31069	313.3979	75.8629	0.2088	0.0262	0.0752	0.0054
53349.31357	313.2027	75.8973	0.2113	0.0166	0.0748	0.0047
53349.31634	312.9228	75.9264	0.1983	0.0143	0.0719	0.0034
53349.31945	312.5018	75.9540	0.2117	0.0144	0.0710	0.0125
53353.24424	298.4431	74.2687	0.2401	0.0098	0.0934	0.0056
53353.24745	300.2559	74.4144	0.2762	0.0156	0.0955	0.0076
53353.25038	301.8136	74.5411	0.2508	0.0310	0.0902	0.0134
53353.25506	304.0990	74.7305	0.2615	0.0245	0.0850	0.0056
53353.25843	305.5954	74.8578	0.2271	0.0178	0.0831	0.0079
53353.26122	306.7413	74.9579	0.2319	0.0171	0.0898	0.0055
53353.26406	307.8139	75.0543	0.2274	0.0135	0.0893	0.0046
53353.26734	308.9400	75.1595	0.2527	0.0184	0.0924	0.0096
53353.27017	309.8111	75.2447	0.2476	0.0218	0.0822	0.0051
53353.27321	310.6474	75.3312	0.2338	0.0155	0.0789	0.0041
53353.27882	311.9107	75.4765	0.1985	0.0149	0.0763	0.0040
53353.28182	312.4368	75.5468	0.2178	0.0139	0.0769	0.0065
53353.28469	312.8423	75.6092	0.2107	0.0114	0.0794	0.0074
53353.28745	313.1419	75.6649	0.1897	0.0225	0.0765	0.0059
53353.29014	313.3491	75.7152	0.2252	0.0116	0.0753	0.0045
53353.29319	313.4817	75.7674	0.1805	0.0066	0.0731	0.0039
53353.29602	313.5077	75.8113	0.2075	0.0243	0.0725	0.0075
53717.36427	265.3854	129.6779	0.1912	0.0193	0.0658	0.0090
53717.37750	270.2451	129.0235	0.1818	0.0172	0.0613	0.0061
53720.33151	253.7076	131.5209	0.1470	0.0191	0.0635	0.0065
53720.34482	260.4400	130.4159	0.1401	0.0130	0.0600	0.0080
54388.40230	163.3136	146.9655	0.2582	0.0148	0.1046	0.0038
54388.40614	165.8257	145.7100	0.2583	0.0117	0.1054	0.0087
54388.41109	169.1326	144.1723	0.2652	0.0124	0.0987	0.0056
54388.41503	171.8078	143.0123	0.2764	0.0148	0.0976	0.0070
54388.41891	174.6224	141.8646	0.2492	0.0093	0.0858	0.0045
54388.42328	177.5169	140.7499	0.2688	0.0150	0.0917	0.0068
54388.42730	180.3496	139.7210	0.2648	0.0139	0.0910	0.0084
54388.43123	183.0855	138.7783	0.2626	0.0116	0.0884	0.0092
54388.43511	185.8098	137.8858	0.2894	0.0093	0.1024	0.0068
54388.43897	188.5194	137.0399	0.2811	0.0168	0.1004	0.0057
54388.44286	191.2598	136.2237	0.2754	0.0266	0.1004	0.0055
54388.44682	194.0589	135.4279	0.1850	0.0331	0.0683	0.0086
54388.45103	196.9129	134.6523	0.2357	0.0411	0.0874	0.0120
54388.45512	199.7014	133.9280	0.2250	0.0267	0.0896	0.0052
54388.45911	202.4062	133.2549	0.2191	0.0258	0.0825	0.0096
54713.49076	323.4983	40.2307	0.2136	0.0257	0.0756	0.0080
54713.49574	322.0478	40.0004	0.1985	0.0189	0.0667	0.0067
54713.50130	320.4059	39.7279	0.1766	0.0166	0.0660	0.0080
54713.50718	318.2852	39.3605	0.1692	0.0144	0.0643	0.0048
54713.51243	316.3761	39.0156	0.1691	0.0118	0.0624	0.0058
54713.51652	314.7334	38.7091	0.1578	0.0152	0.0580	0.0035
54713.52141	312.7239	38.3221	0.1662	0.0143	0.0600	0.0082
54713.52619	310.6815	37.9156	0.1440	0.0140	0.0564	0.0045
54713.53203	308.1198	37.3868	0.1244	0.0138	0.0503	0.0075
54713.53618	306.1335	36.9626	0.1350	0.0138	0.0466	0.0043

Table. 5.18 – Continued

t (MJD)	B (m)	ψ (degrees)	$V_{\rm A,obs}$	$\sigma V_{\rm A,obs}$	$V_{\rm B,obs}$	$\sigma V_{\rm B,obs}$
54713.54096	303.8282	36.4542	0.1273	0.0098	0.0505	0.0048
54721.46828	323.7620	40.2712	0.1811	0.0161	0.0688	0.0062
54721.47467	321.8935	39.9752	0.1910	0.0250	0.0683	0.0081
54721.48104	319.8124	39.6269	0.1837	0.0177	0.0683	0.0050
54721.48662	317.8817	39.2886	0.1880	0.0158	0.0721	0.0073
54721.49233	315.7505	38.8998	0.1902	0.0223	0.0723	0.0054
54721.49820	313.3567	38.4453	0.1907	0.0237	0.0693	0.0103
54721.50391	310.9475	37.9691	0.1921	0.0179	0.0747	0.0103
54722.45899	325.1953	40.4855	0.1644	0.0089	0.0964	0.0070
54722.46226	324.3662	40.3632	0.1592	0.0127	0.0971	0.0123
54722.46553	323.4855	40.2287	0.1535	0.0062	0.0969	0.0087
54722.46873	322.5724	40.0849	0.1561	0.0074	0.0921	0.0091
54722.47195	321.5894	39.9255	0.1519	0.0044	0.0855	0.0049
54722.47611	320.2572	39.7029	0.1499	0.0147	0.0839	0.0037
54722.47943	319.1329	39.5095	0.1480	0.0097	0.0902	0.0047
54722.48320	317.7946	39.2731	0.1675	0.0081	0.1011	0.0075
54722.48651	316.5680	39.0509	0.1855	0.0123	0.1022	0.0034
54722.48972	315.3249	38.8206	0.1718	0.0093	0.0997	0.0098
54722.49293	314.0483	38.5787	0.1615	0.0145	0.0936	0.0060
54722.49622	312.6814	38.3138	0.1746	0.0181	0.0946	0.0112
54722.49967	311.2136	38.0228	0.1394	0.0087	0.0779	0.0085
54723.45802	299.2024	42.7039	0.0763	0.0051	0.0463	0.0050
54723.46163	298.4908	42.6111	0.0826	0.0057	0.0483	0.0042
54723.46508	297.7611	42.5100	0.0827	0.0069	0.0528	0.0028
54723.46866	296.9291	42.3889	0.0915	0.0076	0.0522	0.0060
54723.47224	296.0292	42.2521	0.0911	0.0112	0.0527	0.0051
54723.47605	295.0045	42.0902	0.0964	0.0099	0.0550	0.0023
54723.47972	293.9499	41.9177	0.1042	0.0050	0.0632	0.0056
54723.48312	292.9045	41.7413	0.1016	0.0081	0.0611	0.0043
54723.48651	291.8114	41.5517	0.1007	0.0048	0.0570	0.0042
54723.48982	290.6936	41.3527	0.0997	0.0105	0.0547	0.0049
54723.49314	289.5218	41.1389	0.0997	0.0058	0.0573	0.0032
54723.49656	288.2624	40.9034	0.1011	0.0053	0.0569	0.0021
54723.49986	287.0015	40.6620	0.0911	0.0072	0.0533	0.0058
54723.50356	285.5389	40.3750	0.0963	0.0069	0.0502	0.0044
54723.50688	284.1558	40.0969	0.0915	0.0060	0.0497	0.0049
54723.51030	282.7189	39.8011	0.1137	0.0078	0.0590	0.0045
54723.51374	281.2064	39.4823	0.1043	0.0104	0.0608	0.0050
54723.51762	279.4466	39.1016	0.1168	0.0081	0.0641	0.0024
55109.40963	322.4985	40.0730	0.1659	0.0213	0.0783	0.0102
55109.41360	321.2789	39.8742	0.1681	0.0292	0.0804	0.0070
55109.41754	320.0006	39.6591	0.1603	0.0196	0.0762	0.0073
55109.42152	318.6369	39.4225	0.1840	0.0254	0.0842	0.0061
55109.42565	317.1426	39.1555	0.1997	0.0238	0.0904	0.0116
55109.42968	315.5956	38.8710	0.2124	0.0191	0.0961	0.0075
55186.26446	214.8983	140.3792	0.3509	0.0153	0.1515	0.0099
55186.26849	217.7697	139.5351	0.3411	0.0381	0.1445	0.0176
55186.27202	220.2941	138.8242	0.3684	0.0133	0.1649	0.0105
55186.27546	222.7079	138.1703	0.3464	0.0116	0.1494	0.0067
55186.27882	225.0626	137.5549	0.3640	0.0166	0.1551	0.0124
55186.28225	227.4400	136.9552	0.3257	0.0214	0.1363	0.0099
55186.28561	229.7659	136.3883	0.3357	0.0217	0.1341	0.0082
55186.28899	232.0331	135.8536	0.3219	0.0095	0.1335	0.0067
55186.29246	234.3502	135.3247	0.3281	0.0246	0.1271	0.0068
55186.29612	236.7758	134.7889	0.3061	0.0192	0.1311	0.0132
55186.29972	239.1023	134.2917	0.2949	0.0147	0.1242	0.0080
55186.30362	241.5511	133.7854	0.2836	0.0136	0.1154	0.0117
55186.30753	244.0211	133.2911	0.3084	0.0148	0.1321	0.0098
55186.31100	246.1658	132.8754	0.3215	0.0123	0.1408	0.0045
55186.31451	248.2446	132.4839	0.3136	0.0141	0.1345	0.0066
55186.31789	250.1985	132.1261	0.3149	0.0133	0.1257	0.0062

Table. 5.18 – Continued

t (MJD)	B (m)	ψ (degrees)	$V_{\mathrm{A,obs}}$	$\sigma V_{\mathrm{A,obs}}$	$V_{\mathrm{B,obs}}$	$\sigma V_{\mathrm{B,obs}}$
55186.32127	252.1066	131.7858	0.3128	0.0095	0.1284	0.0037
55186.32454	253.8893	131.4761	0.3208	0.0186	0.1282	0.0080
55186.32792	255.6812	131.1727	0.2953	0.0211	0.1228	0.0047
55186.33480	259.1645	130.6054	0.2945	0.0223	0.1210	0.0063
55186.33789	260.6851	130.3671	0.3134	0.0190	0.1364	0.0057
55186.34128	262.2108	130.1341	0.3059	0.0096	0.1231	0.0069

Table 5.19. Orbital Elements for η Ori Aab derived from minimum χ^2 fit

Element	Value	Spectroscopic Orbit
Fixed Elements:		
P (days)	$7.989255 \pm 4 \times 10^{-6}$	$7.989255 \pm 4 \times 10^{-6}$
e	0	0
ω	0	0
Θ_{Aa} (mas)	0.210 ± 0.093	
Θ_{Ab} (mas)	0.170 ± 0.070	
Varied elements:		
T_{node} (MJD)	55202.348 ± 0.045	55202.280 ± 0.788
α (mas)	0.691 ± 0.060	
i	$85.0° \pm 2.3°$	
Ω	$3.4° \pm 0.8°$	
$\Delta K_{\mathrm{close}}$	0.90 ± 0.38	
ΔK_{wide}	1.217 ± 0.018	
Reduced χ^2	1.00	
Wide orbit:		
P_{wide} (years)	9.442 ± 0.012	
T_{wide} (BY)	1991.02 ± 0.11	
e_{wide}	0.45 ± 0.02	
ω_{wide}	$150.0° \pm 1.6°$	
α_{wide} (mas)	44.1 ± 1.5	
i_{wide}	$102.8° \pm 1.8°$	
Ω_{wide}	$120.4° \pm 1.5°$	

Note. — Wide orbit taken from Balega et al. (1999). Spectroscopic close orbit taken from Zizka & Beardsley (1981)

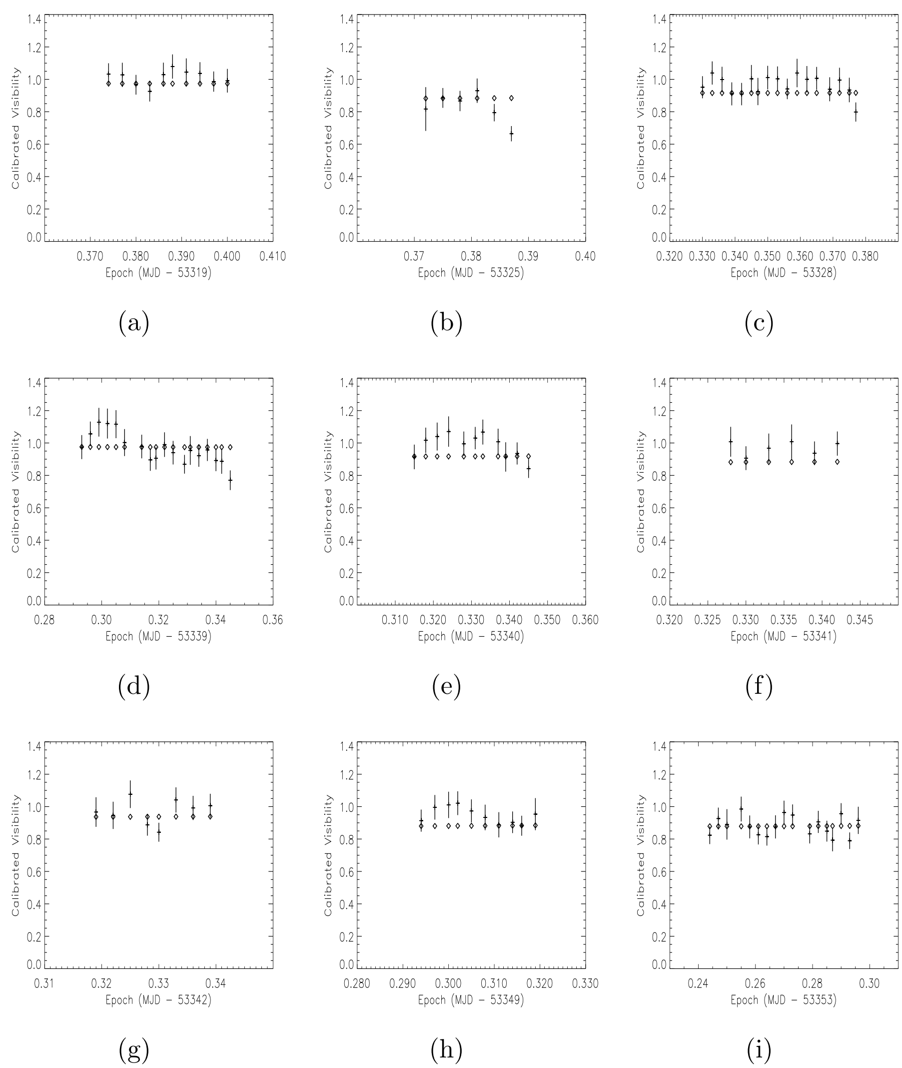

Figure. 5.13: Optimal orbit fit for η Ori Aab

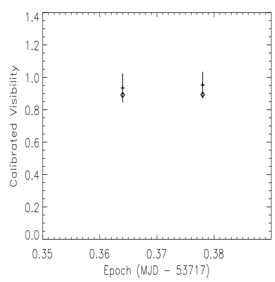

(a)

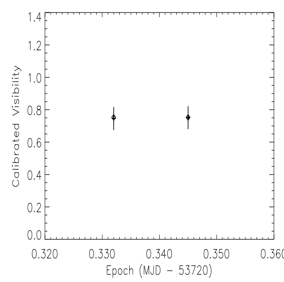

(b)

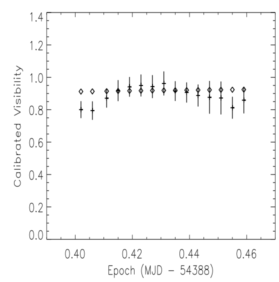

(c)

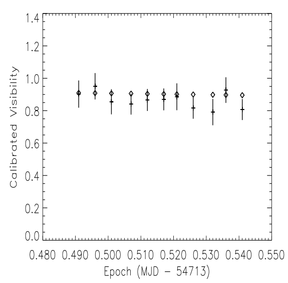

(d)

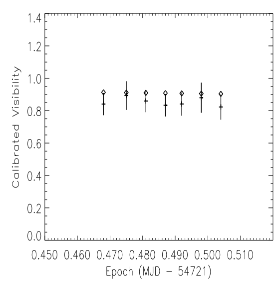

(e)

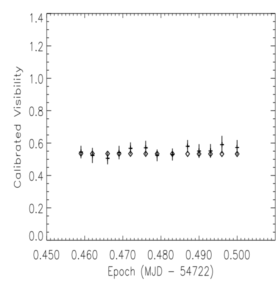

(f)

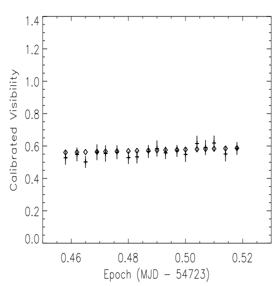

(g)

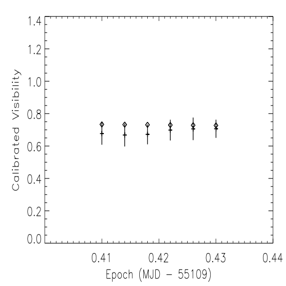

(h)

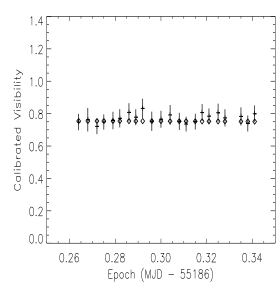

(i)

Figure. 5.14: Optimal orbit fit for η Ori Aab (cont'd)

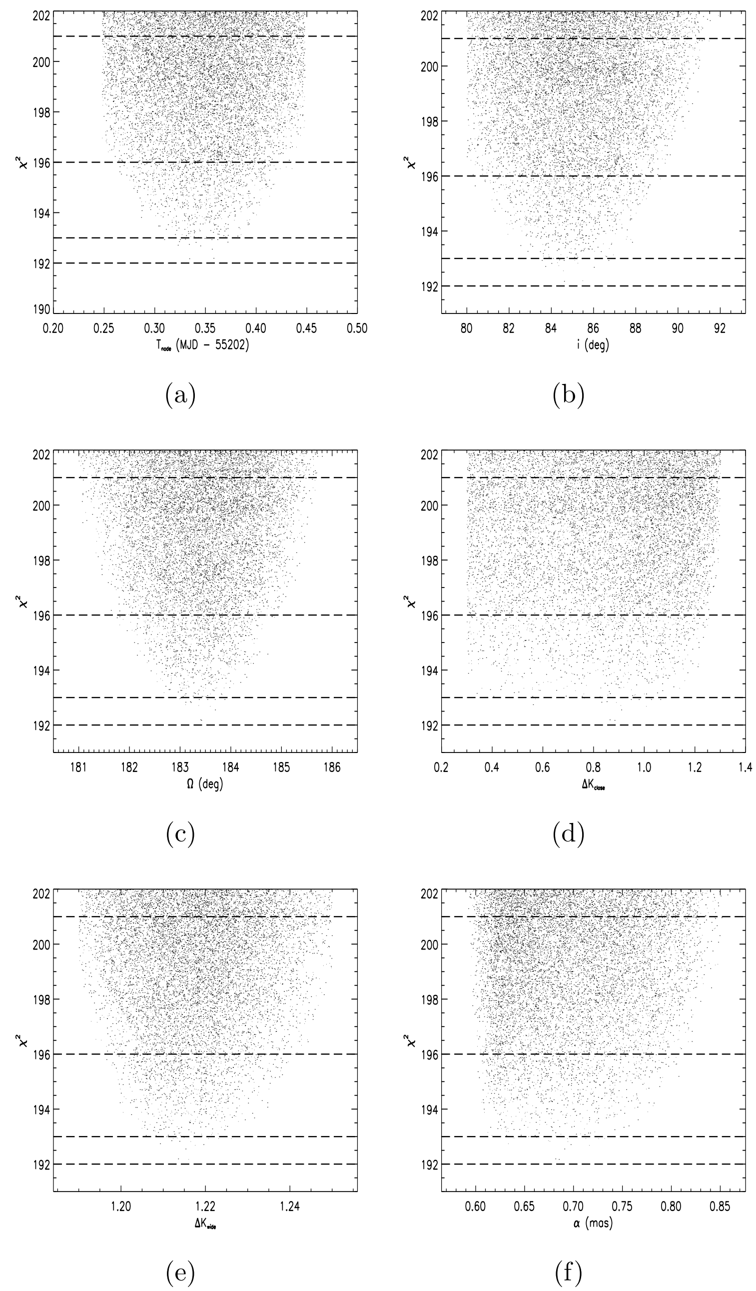

Figure. 5.15: χ^2 plots for η Ori A

Table 5.20. η Ori Mutual Inclination

Element	Value (degrees)	
i_{wide}	102.8 ± 1.8	
i_{close}	85.0 ± 2.3	
Ω_{wide}	120.4 ± 1.5	
Ambiguous values:		
Ω_{close}	3.4 ± 0.8	183.4 ± 0.8
Φ	117.4 ± 1.7	65.1 ± 1.8

Table 5.21. η Ori Masses

Element	Value
π (mas)	3.62 ± 0.88
α (mas)	0.691 ± 0.060
a (AU)	0.191 ± 0.052
P (days)	$7.989255 \pm 4 \times 10^{-6}$
K_{Aa} (km/s)	144.8 ± 0.4
K_{Ab} (km/s)	175.8 ± 3.6
M_{Aa} ($M_{\odot}$)	7.97 ± 6.54
M_{Ab} ($M_{\odot}$)	6.57 ± 5.40

Table 5.22. Magnitudes of η Ori components

	A	Aab	Aa	Ab	Ac
K	3.900 ± 0.036	4.21 ± 0.04	4.60 ± 0.12	5.50 ± 0.40	5.42 ± 0.04
V	3.64	4.24	4.50	5.90	5.65

5.2.5 55 UMa (HD 98353)

55 UMa is the second system in this study for which there is no previously published visual orbit. The wide orbit was derived by speckle interferometry at Mount Wilson by Liu et al. (1997), who also conducted a spectroscopic study of the close orbit using the Multiple Telescope Telescope at Georgia State University's Hard Labor Creek Observatory. The system consists of a close pair of A dwarfs (components A - A1V and Ab - A2V) orbiting a third A dwarf (component B - A1V) in a 5.1-year, 91.3-mas orbit. From the previous source and the spectroscopy of Horn et al. (1996), the close pair has a 2.5-day orbit that is somewhat eccentric (e = 0.3 - 0.4). This makes the system particularly interesting, as most close binaries with periods less than four days have circular orbits and the time-scale for circularization of a system like this is around 5 x 10^6 years (Lloyd 1981). The HIPPARCOS parallax of the system is 17.82 $\pm$ 0.75 mas (Perryman et al. 1997). Combining the parallax and spectral types gives angular diameters of $\Theta_{\mathrm{Aa}} = 0.187 \pm 0.036$ mas, $\Theta_{\mathrm{Ab}} = 0.176 \pm 0.035$ mas, and $\Theta_{\mathrm{B}} = 0.187 \pm 0.036$ mas.

Data for this object (Table 5.23) consist of 97 points taken on seven nights. The orbital solution (Table 5.23) fits the data beautifully in Figure 5.16. There are a few errant data points in nights 5 and 6 that were caused by clouds. The χ^2 plots are given in 5.17. As this is a non-circular orbit, e and ω are left as adjustable elements of the fit. The only fixed orbital element in this case is the period of the close binary.

Information on the mutual inclination is given in in Table 5.25. Although there is no way to resolve the ambiguity, it should be noted that the two derived values of Φ differ by only 11.6°, so the mutual inclination is somewhat well-constrained. The masses of the stars are low for their spectral types when compared with the values of Cox (2000) (Table 5.26). The derived value of the semi-major axis is 0.927 mas, about 7% lower than the expected value of 0.999 mas. This leads to masses that are about 20% lower than the expected values of $M_{\mathrm{Aa}} = 1.91\ M_{\odot}$ and $M_{\mathrm{Ab}} = 1.69\ M_{\odot}$.

Several factors contribute to the confidence placed in this result. The main factor is the similarity of the three non-fixed spectroscopic elements to the work of Horn et al. (1996) and Liu et al. (1997). The epoch of periastron given by those sources, when converted to a current epoch, is 55202.348 MJD, which differs from the value derived by 0.063 days, which is only 2.4% of the orbital period. The eccentricity derived here is $e = 0.340$, compared to 0.329 and 0.323 from the respective sources. Finally, the longitude of periastron derived here is $\omega = 306.7°$, while Horn et al. (1996) and Liu et al. (1997) find 119.1° and 116.8° respectively. After taking into account the 180° difference between the spectroscopic and visual value of ω, the difference between the value derived here and that of Liu et al. (1997) is 9.9°. This may be an effect of apsidal motion, which causes the precession of periastron in a binary system. The magnitudes are also pretty close to what is expected. As the stars in this system are early A stars, one would expect their colors, including $V - K$, to be close to zero. While the $V - K$ values given in Table 5.27 are not exactly zero, they are small enough to confirm that they are A stars. The K magnitudes also confirm what is known from the V magnitudes: A is the brighter component of the wide orbit, but component B is brighter than either of the individual components of A.

Table. 5.23: 55 UMa Data

t (MJD)	B (m)	ψ (degrees)	$V_{\mathrm{A,obs}}$	$\sigma V_{\mathrm{A,obs}}$	$V_{\mathrm{B,obs}}$	$\sigma V_{\mathrm{B,obs}}$
53481.29505	266.1504	125.7080	0.1261	0.0237	0.1066	0.0501
53481.30292	263.5682	124.4447	0.1530	0.0197	0.1192	0.0119
53481.30586	262.4650	123.9514	0.1580	0.0177	0.1215	0.0126
53481.30922	261.1512	123.3937	0.1464	0.0107	0.1145	0.0069
53481.31286	259.6586	122.7944	0.1498	0.0169	0.1167	0.0142
53481.31625	258.2088	122.2432	0.1409	0.0172	0.1103	0.0108
53481.32252	255.3635	121.2365	0.1282	0.0164	0.1052	0.0074
53481.32560	253.8906	120.7492	0.1338	0.0124	0.1009	0.0080
54567.27346	330.6591	16.2260	0.2184	0.0099	0.2249	0.0139
54567.28298	330.6346	14.0372	0.1769	0.0010	0.1981	0.0024
54567.29054	330.5896	12.3663	0.1712	0.0109	0.2118	0.0092
54567.29563	330.5504	11.2008	0.1485	0.0113	0.1838	0.0083
54567.30111	330.5040	9.9317	0.1545	0.0089	0.1984	0.0099
54567.31004	330.4271	7.8545	0.1187	0.0080	0.1739	0.0114
54567.31498	330.3875	6.7087	0.1158	0.0084	0.1813	0.0089
54567.32002	330.3515	5.5505	0.1013	0.0045	0.1660	0.0123
54567.32504	330.3194	4.3400	0.0929	0.0061	0.1686	0.0107
54567.33053	330.2928	3.0515	0.0780	0.0059	0.1728	0.0087
54567.33546	330.2762	1.8767	0.0725	0.0031	0.1610	0.0098
54934.17055	274.9178	157.9783	0.1518	0.0163	0.1711	0.0174
54934.17456	275.2521	156.9070	0.1679	0.0213	0.1953	0.0193
54934.17838	275.5634	155.9114	0.1436	0.0171	0.1696	0.0201
54934.18201	275.8572	154.9673	0.1545	0.0136	0.1727	0.0194
54934.18591	276.1644	153.9686	0.1622	0.0094	0.1820	0.0152
54934.18992	276.4723	152.9474	0.1371	0.0193	0.1620	0.0180
54934.19412	276.7840	151.8820	0.1566	0.0225	0.1727	0.0187
54934.19798	277.0541	150.9206	0.1448	0.0145	0.1510	0.0176
54934.20186	277.3117	149.9557	0.1585	0.0190	0.1756	0.0131
54934.20574	277.5472	149.0144	0.1410	0.0199	0.1596	0.0250
54934.20955	277.7631	148.0800	0.1595	0.0179	0.1559	0.0229
54934.21355	277.9612	147.1281	0.1397	0.0203	0.1601	0.0218
54934.21755	278.1303	146.1968	0.1433	0.0150	0.1536	0.0132
54934.22177	278.2833	145.1864	0.1424	0.0257	0.1727	0.0200
54934.22543	278.3833	144.3374	0.1609	0.0215	0.1796	0.0148
54934.22921	278.4552	143.4749	0.1643	0.0316	0.1848	0.0238
54934.23296	278.4935	142.6311	0.2075	0.0301	0.2136	0.0310
54934.23632	278.4984	141.8782	0.1884	0.0250	0.2077	0.0303
54934.23969	278.4732	141.1263	0.2126	0.0273	0.2228	0.0166
54934.24319	278.4146	140.3665	0.2166	0.0219	0.2072	0.0224
54934.24706	278.3087	139.5319	0.2085	0.0260	0.2140	0.0245
54934.25081	278.1625	138.7268	0.2025	0.0250	0.2042	0.0197
54934.25516	277.9371	137.8072	0.2062	0.0230	0.1822	0.0160
54934.25872	277.7063	137.0638	0.2143	0.0211	0.2023	0.0151
54934.26215	277.4436	136.3583	0.2073	0.0112	0.2028	0.0173
54934.26562	277.1332	135.6473	0.2211	0.0148	0.2085	0.0241
54934.26915	276.7744	134.9362	0.2347	0.0263	0.2025	0.0167
54934.27292	276.3353	134.1794	0.2216	0.0229	0.1968	0.0249
54935.33618	330.2661	179.7654	0.1458	0.0091	0.2258	0.0220
54935.33988	330.2696	178.8735	0.1704	0.0092	0.2541	0.0101
54935.34353	330.2773	178.0255	0.1681	0.0120	0.2477	0.0219
54935.34757	330.2911	177.0497	0.1685	0.0175	0.2552	0.0192
54935.35106	330.3065	176.2331	0.1567	0.0109	0.2620	0.0094
54935.35460	330.3256	175.4077	0.1711	0.0083	0.2373	0.0154

Table. 5.23 – Continued

t (MJD)	B (m)	ψ (degrees)	$V_{\mathrm{A,obs}}$	$\sigma V_{\mathrm{A,obs}}$	$V_{\mathrm{B,obs}}$	$\sigma V_{\mathrm{B,obs}}$
54935.35833	330.3495	174.5174	0.1571	0.0184	0.2334	0.0121
54935.36223	330.3770	173.6144	0.1610	0.0188	0.2117	0.0103
54935.36664	330.4120	172.5715	0.1695	0.0103	0.2114	0.0240
54935.37279	330.4636	171.1488	0.1716	0.0148	0.2189	0.0199
54935.38034	330.5288	169.3974	0.1686	0.0152	0.2142	0.0268
54935.38450	330.5634	168.4276	0.1865	0.0198	0.1902	0.0141
54935.38876	330.5947	167.4664	0.1867	0.0155	0.2178	0.0232
54935.39347	330.6243	166.3998	0.1770	0.0166	0.2078	0.0219
55185.38691	271.0837	4.9859	0.1648	0.0155	0.2508	0.0386
55185.39413	270.9255	2.8885	0.2066	0.0209	0.2857	0.0378
55185.39736	270.8820	1.9522	0.2769	0.0406	0.3000	0.0446
55185.40330	270.8473	0.2238	0.1499	0.0195	0.2414	0.0223
55185.41056	270.8801	178.1107	0.1822	0.0253	0.2689	0.0279
55186.42051	271.1298	174.5476	0.2177	0.0291	0.2891	0.0228
55186.42458	271.2656	173.3569	0.2250	0.0461	0.2463	0.0456
55186.43020	271.4911	171.7413	0.1421	0.0193	0.2255	0.0382
55186.43397	271.6668	170.6613	0.1487	0.0143	0.2479	0.0145
55186.43718	271.8369	169.7144	0.1773	0.0185	0.2616	0.0167
55186.44042	272.0127	168.8131	0.1651	0.0292	0.2314	0.0306
55186.44837	272.5034	166.5702	0.2095	0.0315	0.2292	0.0348
55186.45207	272.7560	165.5265	0.2145	0.0179	0.2490	0.0143
55186.45625	273.0503	164.3778	0.2434	0.0273	0.2493	0.0224
55186.46269	273.5362	162.5960	0.2152	0.0178	0.2154	0.0355
55186.46665	273.8518	161.4958	0.2334	0.0252	0.2215	0.0230
55186.47051	274.1623	160.4462	0.2413	0.0396	0.2232	0.0221
55186.47460	274.4947	159.3485	0.2255	0.0367	0.2392	0.0174
55186.47841	274.8118	158.3194	0.2819	0.0417	0.2622	0.0101
55186.48228	275.1288	157.3014	0.2803	0.0295	0.2765	0.0266
55186.48629	275.4561	156.2546	0.3430	0.0381	0.3125	0.0511
55311.18421	247.0615	22.7410	0.0834	0.0072	0.1531	0.0189
55311.18911	247.2614	21.7658	0.0763	0.0035	0.1327	0.0102
55311.19286	247.3960	21.0095	0.0692	0.0049	0.1298	0.0070
55311.19652	247.5131	20.2610	0.0925	0.0068	0.1407	0.0175
55311.20065	247.6287	19.4104	0.0727	0.0053	0.1330	0.0096
55311.20442	247.7193	18.6354	0.0767	0.0037	0.1193	0.0137
55311.20835	247.8012	17.8186	0.0931	0.0077	0.1346	0.0126
55311.21258	247.8758	16.9322	0.0922	0.0175	0.1346	0.0177
55311.21654	247.9347	16.0876	0.0869	0.0085	0.1329	0.0237
55311.22128	247.9907	15.0928	0.0870	0.0092	0.1346	0.0103
55311.22590	248.0350	14.0836	0.0841	0.0073	0.1297	0.0159
55311.27183	248.1200	3.9145	0.0611	0.0029	0.1168	0.0151
55311.27568	248.1175	3.0491	0.0601	0.0048	0.1251	0.0105
55311.27998	248.1152	2.0739	0.0658	0.0065	0.0976	0.0280

Table 5.24. Orbital Elements for 55 UMa A derived from minimum χ^2 fit

Element	Value	Spectroscopic Orbit
Fixed Elements:		
P (days)	$2.553799 \pm 7.1 \times 10^{-6}$	$2.553799 \pm 7.1 \times 10^{-6}$
$\Theta_{\rm Aa}$ (mas)	0.187 ± 0.036	
$\Theta_{\rm Ab}$ (mas)	0.176 ± 0.035	
Varied elements:		
T (MJD)	55202.411 ± 0.026	55202.348 ± 0.016
e	0.340 ± 0.015	0.323 ± 0.014
ω	$306.7^\circ \pm 6.3^\circ$	$116.8^\circ \pm 2.6^\circ$
α (mas)	0.927 ± 0.026	
i	$47.8^\circ \pm 2.0^\circ$	
Ω	$48.3^\circ \pm 6.6^\circ$	
$\Delta K_{\rm close}$	0.72 ± 0.05	
$\Delta K_{\rm wide}$	0.259 ± 0.014	
Reduced χ^2	1.00	
Wide Orbit:		
$P_{\rm wide}$ (years)	5.127 ± 0.020	
$T_{\rm wide}$ (BY)	1992.503 ± 0.051	
$e_{\rm wide}$	0.126 ± 0.008	
$\omega_{\rm wide}$	$223.9^\circ \pm 3.7^\circ$	
$\alpha_{\rm wide}$ (mas)	91.3 ± 0.9	
$i_{\rm wide}$	$64.8^\circ \pm 0.8^\circ$	
$\Omega_{\rm wide}$	$130.0^\circ \pm 0.8^\circ$	

Note. — Wide orbit and close spectroscopic orbit taken from Liu et al. (1997).

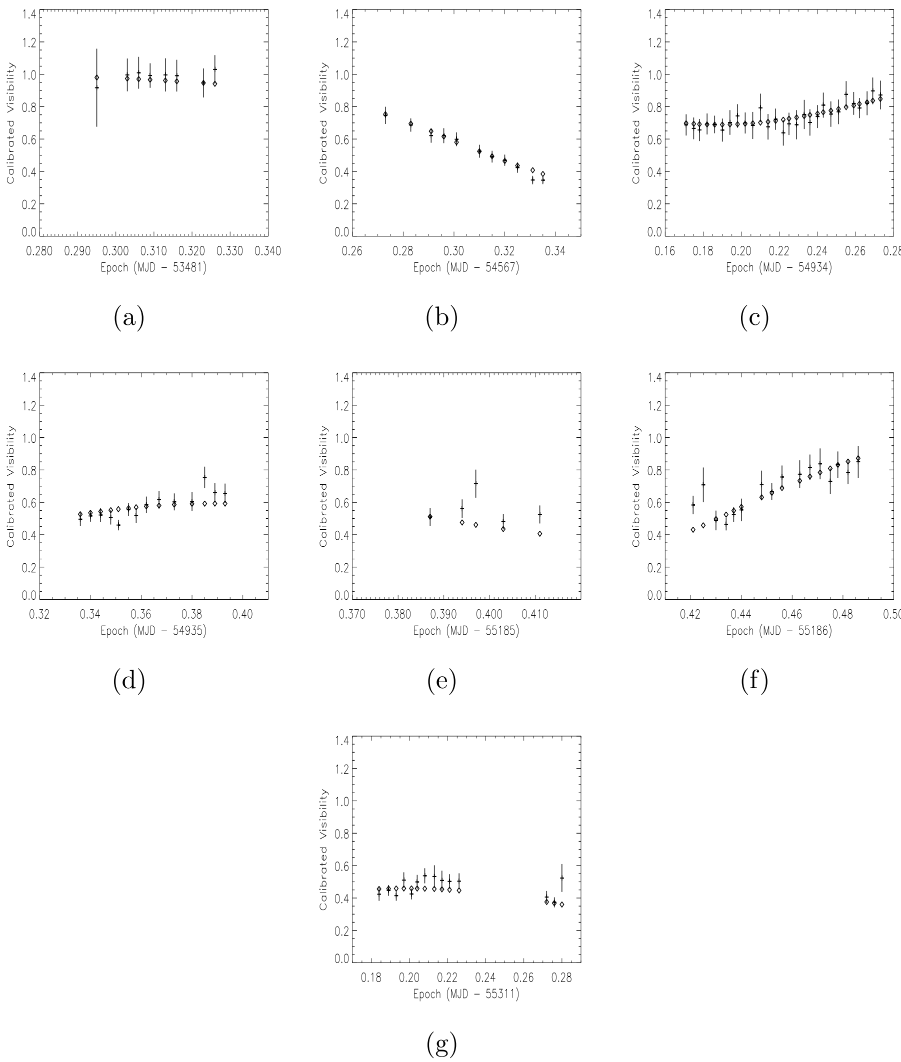

Figure. 5.16: Optimal orbit fit for 55 UMa A

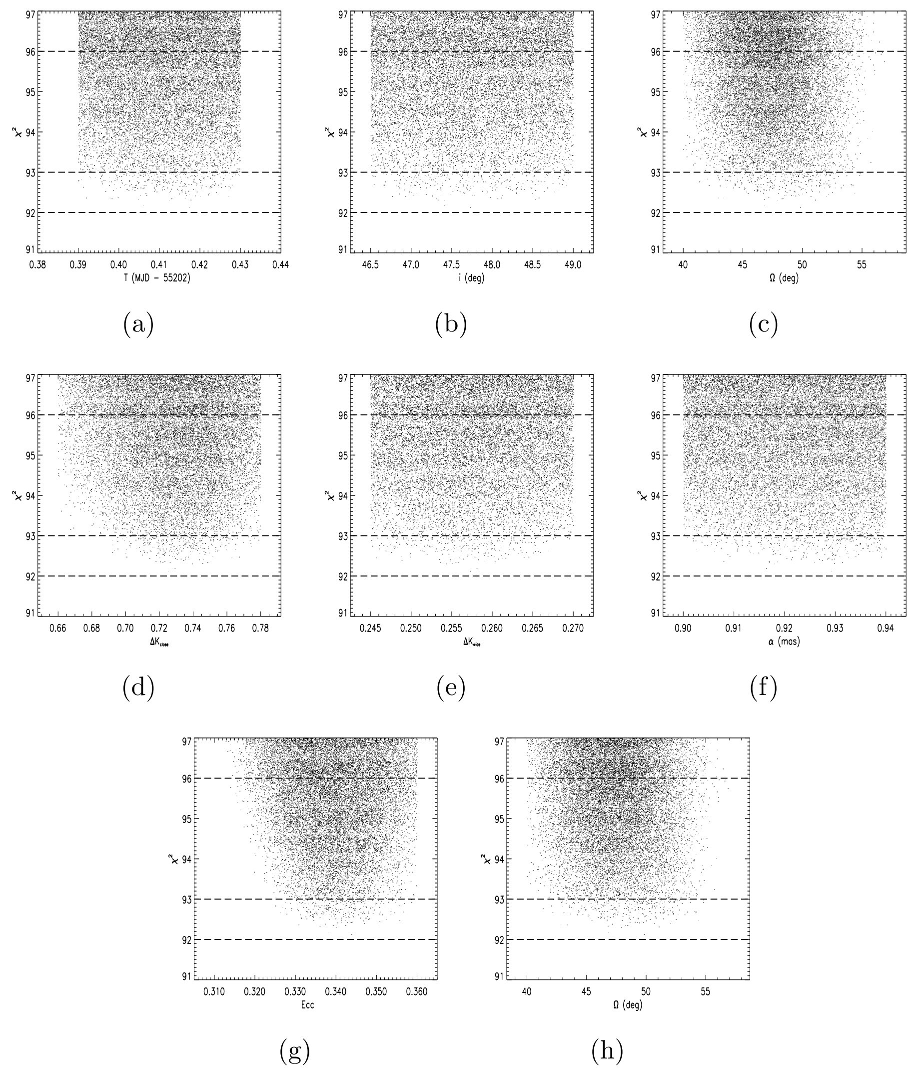

Figure. 5.17: χ^2 plots for 55 UMa A

Table 5.25. 55 UMa Mutual Inclination

Element	Value (degrees)	
i_{wide}	64.8 ± 0.8	
i_{close}	47.8 ± 2.0	
Ω_{wide}	130.0 ± 0.8	
Ambiguous values:		
Ω_{close}	48.3 ± 6.6	183.4 ± 0.8
Φ	67.5 ± 4.8	79.1 ± 4.6

Table 5.26. 55 UMa Masses

Element	Value
π (mas)	17.82 ± 0.75
α (mas)	0.927 ± 0.026
a (AU)	0.052 ± 0.003
P (days)	$2.5537985 \pm 7.1 \times 10^{-6}$
K_{Aa} (km/s)	79.1 ± 1.1
K_{Ab} (km/s)	89.1 ± 1.3
M_{Aa} ($M_{\odot}$)	1.53 ± 0.26
M_{Ab} ($M_{\odot}$)	1.35 ± 0.25

Table 5.27. Magnitudes of 55 UMa components

	AB	A	Aa	Ab	B
K	4.460 ± 0.033	5.09 ± 0.03	5.54 ± 0.04	6.26 ± 0.06	5.35 ± 0.04
V	4.78	5.39	5.89	6.47	5.69
$V - K$			0.45	0.21	0.34

5.2.6 13 Ceti (HD 3196)

13 Ceti is one of the more troublesome targets in this study. The wide orbit of the system (6.89-yr, 241-mas) was presented in the seminal multiplicity study by Duquennoy & Mayor (1991) and later revised in 2005 with new speckle data in IAU Circular 156. Duquennoy & Mayor (1991) also provide the spectroscopic orbit of the 2.1-day close system. The system consists of a close binary (Aa,Ab) of spectral type F8V orbiting with a wide component (B) of type G0V. The fainter component of the close binary is undetected in the spectrum.

The HIPPARCOS parallax is 47.51 $\pm$ 1.15 mas (Perryman et al. 1997), making this system the nearest of all the stars in this study. The parallax and spectral types of the two stars detected in the spectrum combine to give angular diamteters of $\Theta_{\rm Aa}$ = 0.265 $\pm$ 0.040 mas and $\Theta_{\rm B}$ = 0.243 $\pm$ 0.036 mas. Based on the minimum mass estimate from the single-line spectroscopic orbit, and assuming that it is on the main sequence, the angular diameter of the unseen component is $\Theta_{\rm Ab} = 0.088 \pm 0.035$ mas.

The reason that this system is troublesome is because there are two possible minimum χ^2 solutions to the data in Table 5.28. The expected semi-major axis of the close binary is $\alpha = 1.784$ mas. The overall minimum χ^2 fit gives a semi-major axis of $\alpha = 2.81$ mas, with a reduced $\chi^2 = 0.26$. A local minimum χ^2 solution is located at α = 1.73 mas, with a reduced χ^2 = 0.29. The epoch of nodal passage from Duquennoy & Mayor (1991), when converted to the current epoch, is 55201.207 MJD. This value agrees more with the $T_{\rm node}$ value for the 1.73-mas fit than the other. Because of the discrepancy in T_{node} and the fact that the 2.81-mas solution would lead to a mass sum of 6.4 $M_{\odot}$ for an F8V star and a possible M3V star, which should have a mass sum of roughly 1.5 $M_{\odot}$ according to Cox (2000) and a mass sum of 1.5 $M_{\odot}$ from the wide orbit, the 1.73-mas solution has been adopted as the best solution. Both solutions are presented in Table 5.29, but only the one labeled solution 1 was used to determine the fundamental parameters of the system. For both solutions, the errors on the visibilities were scaled until a reduced χ^2 of 1.00 was achieved. The plot of data vs. model visibilities is given in Figure 5.18 and the χ^2 plots are given in Figure 5.19.

The mutual inclination of the system is either 144.4° or 50.9° (Table 5.30). No errors on i_{wide} and Ω_{wide} are given in IAU Circular 156, so a conservative error of 5.0° has been assumed. The masses for this single-line system are given in Table 5.31. These are very close to the minimum mass estimates in Tokovinin (1997), which makes sense given the proximity of the inclination to 90° and the proximity of the derived semi-major axis to the expected one. The component not seen in the spectrum is a low mass star at $M_{\mathrm{Ab}} = 0.348 \pm 0.059$ $M_{\odot}$. It should be noted that although the inclination is close to 90°, eclipses have not been reported for this system.

The magnitudes of the system are also somewhat troubling. One would expect $\Delta K_{\mathrm{close}}$ to be larger (as is the case with κ Peg) than the derived value of 1.16 for stars of these masses. This situation is probably impossible given the proposed spectral types of the stars. Low-mass stars are much brighter in K than they are in V, but this star is not bright enough to give $\Delta K_{\mathrm{close}} = 1.16$. If the distance modulus ($K - M_{\mathrm{K}} = 1.62$) is used to calculate the absolute magnitudes of the stars in K, then $V-K$ values for stars of the suspected spectral types from Cox (2000) can be used to calculate the absolute V magnitudes (Table 5.32). The mass of component Ab suggests a spectral type of M3V, so $V - K = 4.65$ is used. The resulting absolute V magnitude is 8.8, which is more in line with an M0V star. This is another major discrepancy in this system.

Table. 5.28: 13 Ceti Data

t (MJD)	B (m)	ψ (degrees)	$V_{\mathrm{A,obs}}$	$\sigma V_{\mathrm{A,obs}}$	$V_{\mathrm{B,obs}}$	$\sigma V_{\mathrm{B,obs}}$
54326.34733	322.1060	40.3652	0.2281	0.0094	0.1092	0.0068
54326.48732	252.1472	20.1663	0.1913	0.0071	0.0806	0.0102
54370.25195	229.8557	35.1988	0.3370	0.0109	0.1773	0.0138
54385.20491	257.4739	33.3151	0.1459	0.0173	0.0826	0.0109
54385.20917	255.7756	32.8353	0.1420	0.0124	0.0833	0.0064
54385.21415	253.9830	32.3110	0.1473	0.0131	0.0845	0.0068
54385.21819	252.4065	31.8332	0.1371	0.0177	0.0795	0.0082
54385.22233	250.7879	31.3262	0.1345	0.0054	0.0757	0.0056
54385.22650	249.1173	30.7846	0.1393	0.0126	0.0725	0.0097
54385.23051	247.4952	30.2402	0.1331	0.0079	0.0745	0.0095
54385.23472	245.7805	29.6437	0.1426	0.0111	0.0739	0.0043
54385.23872	244.1123	29.0413	0.1277	0.0104	0.0733	0.0059
54711.32295	229.9110	35.2198	0.1747	0.0173	0.0786	0.0037
54721.28715	315.7777	39.4163	0.1620	0.0201	0.0982	0.0105
54721.30152	309.7813	38.3762	0.2093	0.0250	0.0964	0.0112
54721.31736	302.2612	36.9051	0.1966	0.0211	0.1065	0.0096
54722.27668	318.3503	39.8231	0.2126	0.0087	0.1143	0.0057
54722.28307	315.9463	39.4439	0.2282	0.0143	0.1151	0.0069
54722.29001	313.1343	38.9731	0.2591	0.0148	0.1151	0.0091
54722.29696	310.1170	38.4379	0.2491	0.0206	0.1172	0.0063
54722.30405	306.8329	37.8215	0.2431	0.0212	0.1176	0.0069
54722.31134	303.2843	37.1166	0.2327	0.0078	0.1175	0.0082
54722.31853	299.6062	36.3426	0.2503	0.0096	0.1168	0.0079
54723.27154	319.1917	39.9504	0.2718	0.0131	0.1368	0.0084
54723.30878	303.1919	37.0977	0.2704	0.0120	0.1220	0.0056
54723.31552	299.7660	36.3771	0.2369	0.0082	0.1132	0.0043
55107.23904	297.2799	73.7410	0.1890	0.0182	0.1153	0.0142
55107.24662	301.5269	74.1465	0.1693	0.0145	0.1165	0.0115
55107.25541	305.6697	74.5645	0.1839	0.0196	0.1146	0.0108
55107.26824	310.1688	75.0825	0.1972	0.0210	0.1092	0.0101
55107.27568	311.9118	75.3352	0.1708	0.0139	0.1067	0.0094
55107.28498	313.1977	75.6062	0.1833	0.0144	0.1056	0.0098
55107.29275	313.5086	75.7970	0.1982	0.0161	0.1081	0.0117
55107.30077	313.0901	75.9582	0.2075	0.0146	0.1091	0.0098
55186.15546	267.3660	128.9944	0.2828	0.0415	0.1139	0.0179
55186.17419	273.3869	128.3959	0.2400	0.0352	0.1346	0.0157
55186.18290	275.4269	128.2573	0.2133	0.0238	0.1209	0.0224

Table. 5.28 – Continued

t (MJD)	B (m)	ψ (degrees)	$V_{\mathrm{A,obs}}$	$\sigma V_{\mathrm{A,obs}}$	$V_{\mathrm{B,obs}}$	$\sigma V_{\mathrm{B,obs}}$
55186.18719	276.2309	128.2219	0.2442	0.0444	0.1259	0.0095
55186.19098	276.8545	128.2071	0.2154	0.0236	0.1004	0.0125
55460.32331	64.2753	64.8282	0.4369	0.0422	0.2014	0.0215
55460.32637	64.0156	64.7879	0.4411	0.0224	0.2064	0.0251
55460.33097	63.5863	64.7103	0.4052	0.0348	0.1675	0.0162
55460.33372	63.3088	64.6541	0.3870	0.0162	0.1468	0.0166
55460.33699	62.9605	64.5778	0.4056	0.0192	0.1803	0.0147
55460.33972	62.6542	64.5062	0.4333	0.0365	0.1834	0.0258
55460.34273	62.2963	64.4177	0.3875	0.0359	0.1715	0.0186
55460.34553	61.9477	64.3269	0.4105	0.0382	0.1518	0.0193
55460.34956	61.4188	64.1813	0.4338	0.0302	0.1633	0.0118
55460.35239	61.0296	64.0687	0.4175	0.0269	0.1689	0.0206
55460.35552	60.5815	63.9335	0.4163	0.0326	0.1447	0.0078
55461.24099	64.1409	62.9304	0.3275	0.0419	0.1784	0.0161
55461.24393	64.3782	63.1042	0.3837	0.0503	0.1995	0.0355
55461.24675	64.5911	63.2636	0.4047	0.0180	0.1910	0.0256
55461.24963	64.7931	63.4189	0.3638	0.0541	0.1697	0.0259
55461.25239	64.9695	63.5588	0.3922	0.0133	0.1695	0.0250

Table 5.29. Orbital Elements for 13 Ceti A derived from minimum χ^2 fit

Element	Solution 1	Solution 2	Spectroscopic Orbit
Fixed Elements:			
P (days)	$2.081891 \pm 5 \times 10^{-6}$	$2.081891 \pm 5 \times 10^{-6}$	$2.081891 \pm 5 \times 10^{-6}$
e	0	0	0
ω	0	0	0
$\Theta_{\rm Aa}$ (mas)	0.265 ± 0.040	0.265 ± 0.040	
$\Theta_{\rm Ab}$ (mas)	0.088 ± 0.035	0.088 ± 0.035	
Varied elements:			
$T_{\rm node}$ (MJD)	55201.550 ± 0.026	52402.040 ± 0.040	55201.207 ± 0.003
α (mas)	1.727 ± 0.142	2.805 ± 0.171	
i	$98.1° \pm 1.6°$	$81.0° \pm 3.1°$	
Ω	$133.0° \pm 2.2°$	$149.0° \pm 0.9°$	
$\Delta K_{\rm close}$	1.16 ± 0.27	2.04 ± 0.16	
$\Delta K_{\rm wide}$	0.887 ± 0.022	0.905 ± 0.025	
Reduced χ^2	1.00	1.00	
Wide orbit:			
$P_{\rm wide}$ (years)	6.89		
$T_{\rm wide}$ (BY)	2000.98		
$e_{\rm wide}$	0.773		
$\omega_{\rm wide}$	283.8°		
$\alpha_{\rm wide}$ (mas)	241		
$i_{\rm wide}$	49.4°		
$\Omega_{\rm wide}$	329.2°		

Note. — Wide orbit from IAU Circular 156, no uncertainties given. Spectroscopic orbit taken from Duquennoy & Mayor (1991).

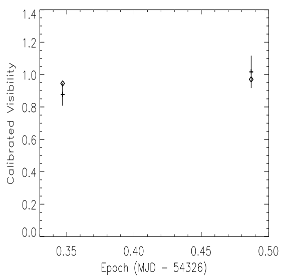

(a)

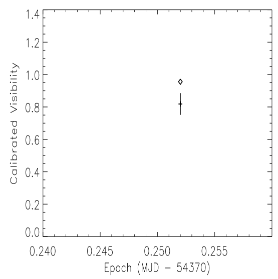

(b)

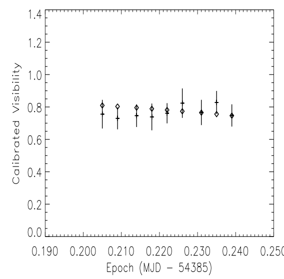

(c)

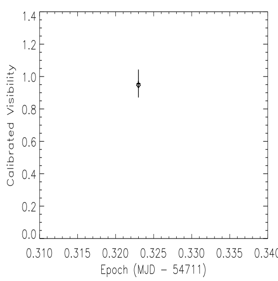

(d)

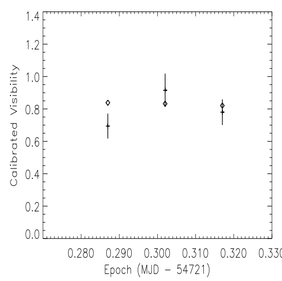

(e)

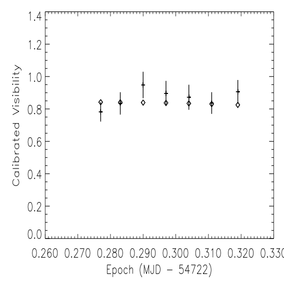

(f)

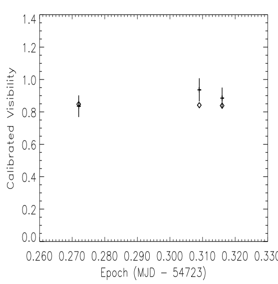

(g)

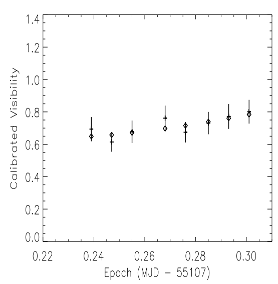

(h)

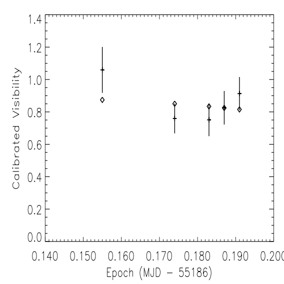

(i)

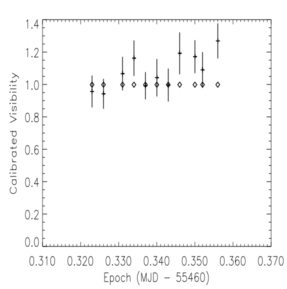

(j)

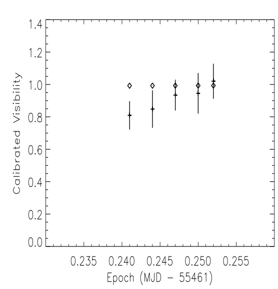

(k)

Figure. 5.18: Optimal orbit fit for 13 Ceti A

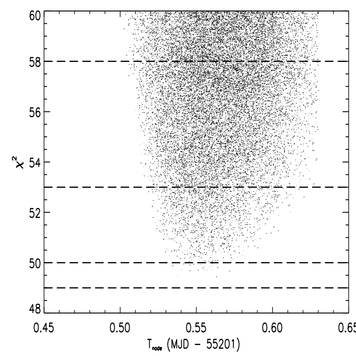

(a)

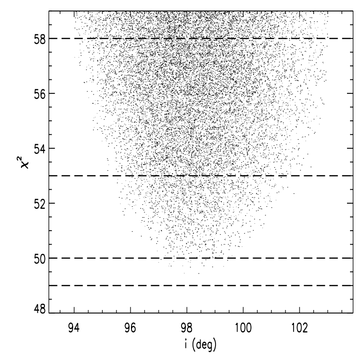

(b)

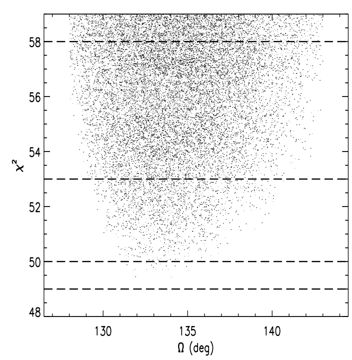

(c)

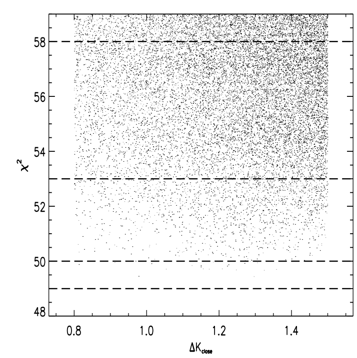

(d)

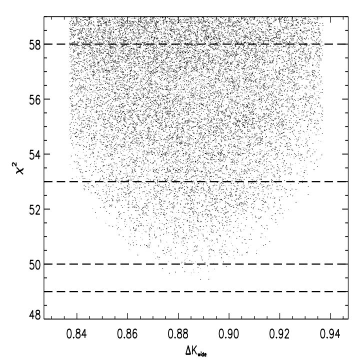

(e)

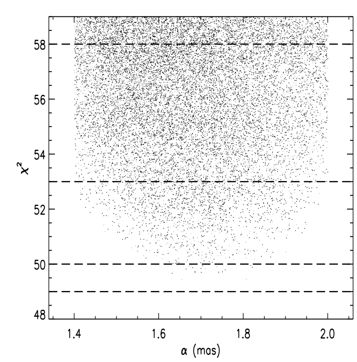

(f)

Figure. 5.19: χ^2 plots for 13 Ceti A

Table 5.30. 13 Ceti Mutual Inclination

Element	Value (degrees)	
$i_{\rm wide}$	49.4 ± 5.0	
$i_{\rm close}$	98.1 ± 1.6	
$\Omega_{\rm wide}$	329.2 ± 5.0	
Ambiguous values:		
$\Omega_{\rm close}$	133.0 ± 2.2	313.0 ± 2.2
Φ	144.4 ± 5.0	50.9 ± 5.1

Table 5.31. 13 Ceti Masses

Element	Value
π (mas)	47.51 ± 1.15
α (mas)	1.727 ± 0.142
a (AU)	0.03635 ± 0.00310
P (days)	$2.081891 \pm 5 \times 10^{-6}$
i	$98.1^\circ \pm 1.6^\circ$
e	0
$K_{\rm Aa}$ (km/s)	43.98 ± 0.39
f(M)	0.0183 ± 0.0005
$M_{\rm Aa}$ ($M_\odot$)	1.133 ± 0.193
$M_{\rm Ab}$ ($M_\odot$)	0.348 ± 0.059

Table 5.32. Magnitudes of 13 Ceti components

	AB	A	Aa	Ab	B
K	3.900 ± 0.230	4.30 ± 0.230	4.62 ± 0.240	5.77 ± 0.361	5.18 ± 0.231
$M_{\rm K}$			3.00 ± 0.261	4.15 ± 0.375	3.56 ± 0.253
$V-K$			1.35	4.65	1.41
$M_{\rm V}$			4.35 ± 0.261	8.80 ± 0.375	4.97 ± 0.253

Note. — $V-K$ values taken from Cox (2000) using spectral types of the components.

5.2.7 CHARA 96 (HD 193322)

CHARA 96 is an anomalous object in this study, because although this target falls within the parameters of the target list, it had been part of the CHARA queue long before this project began. Along with η Orionis, this object was a prototype for this study, but ultimately the short period of the close binary of η Orionis (7.9 days) compared to that of CHARA 96 (312.4 days) was deemed more suitable for study, so all of the above targets bear a greater resemblance to η Orionis than to CHARA 96. All interferometric observations were taken and reduced by Dr. Theo ten Brummelaar using different data reduction software. New spectroscopic observations of the system were conducted by Dr. Douglas Gies in 2010 at Kitt Peak National Observatory and Lowell Observatory. This study's participation in the examination of this object was limited to simply applying the orbit-fitting procedure to the CHARA visibility data. What will be presented here is a summary of results derived by others.

The system itself is a large collection of massive stars, containing at least four and at most six stars of spectral types O and B (ten Brummelaar et al. 2011). The core of the system is a spectroscopic triple where the wide system (Aa,Ab) has a 31-year, 67-mas orbit, and the close binary (Ab1,Ab2) was later discovered to have a 311-day orbit (McKibben et al. 1998). These naming conventions are very different than those in the MSC because it was discovered by ten Brummelaar et al. (2011) that the wide component is actually brighter than the close binary.

Like 13 Ceti, the χ^2 fitting of the data in Table 5.33 is troubling. The spectroscopic elements P, e, ω, and T have been derived in ten Brummelaar et al. (2011) and are fixed in the orbit-fitting of the visibilities. The overall minimum χ^2 solution gives masses ($\sim 20\ M_\odot$) that are far too small for the spectral types ($\sim 30\ M_\odot$), but there are a few other local χ^2 minima that are worth examining. Figure 5.20 (adapted from Figure 3 of ten Brummelaar et al. (2011)) shows χ^2 in the (i, α) plane for a grid in steps of 2° in i and 0.05 mas in α. Within the grid, the minimum is $\chi^2 = 167$ (black) and the maximum is χ^2 is 529 (white). The strong minima are located at (i, α) = (38°, 3.3 mas, $\chi^2 = 167$), (66°, 4.6 mas, $\chi^2 = 210$), and (118°, 4.7 mas, $\chi^2 = 215$). The first minimum gives masses that are too small ($\sim 20\ M_\odot$) and the other two give masses that are too large ($\sim 55\ M_\odot$). Notice, however, that a minimum χ^2 valley exists for $i < 90°$. It is reasoned by ten Brummelaar et al. (2011) that this valley represents the best family of solutions and that since the because between $\alpha = 2.7$ and 5.0 mas in the valley never rises above reduced $\chi^2 = 1.18$, it is premature to rule out any of this solution space.

The lines on Figure 5.20 represent loci of constant mass for stars Ab1 (solid lines) and Ab2 (dashed lines) (ten Brummelaar et al. 2011), and are governed by the following equations:

$$M_{\mathrm{Ab2}} = \frac{a^2}{P \sin i} \frac{K(1-e^2)^{1/2}}{29.8\ \mathrm{km\ s^{-1}}} = 0.455 M_\odot\ \frac{a^2}{\sin i}\ \left(\frac{d}{741\ \mathrm{pc}}\right)^2 \tag{5.6}$$

$$\frac{M_{\mathrm{Ab1}}}{M_{\mathrm{Ab2}}} = \frac{29.8\ \mathrm{km\ s^{-1}}}{K} \frac{a d \sin i}{P\sqrt{1-e^2}} - 1 = \frac{a \sin i}{0.819\ \mathrm{mas}}\ \left(\frac{d}{741\ \mathrm{pc}}\right) - 1. \tag{5.7}$$

Along with these lines, the new estimate of the wide orbit by ten Brummelaar et al. (2011) and the distance by Roberts et al. (2010) put a constraint on the mass of the close binary. By looking at how the observed flux ratios (given by the ΔKs in the orbit-fitting) compare with the expected flux ratios for main sequence stars of these spectral types, a best-fit semi-major axis of 3.85 mas can be derived (Figure 11 of ten Brummelaar et al. (2011)). Applying this in the orbit-fitting, a new solution is derived and presented in Table 5.34. This solution is indicated by a plus sign on Figure 5.20. The plot of data vs. model visibilities is shown in Figures 5.21 and 5.22.

The results here are still very preliminary. It is suspected that because the data were reduced elsewhere, side-lobe interference may be a strong factor in the reason that the χ^2 plane has so many strong local minima. The first night of data used here have been perused (JD = 53982), and it seems that the fringe packets are very close and would have to be corrected or dropped in the method used for the first several targets mentioned here. Also, it is unclear if the packets are correctly identified. The magnitude difference in the wide orbit is very small according to findings from both ten Brummelaar et al. (2011) ($\Delta K_{\mathrm{wide}} = 0.086$) and lucky imaging observations by Maíz Apellániz (2010) ($\Delta K_{\mathrm{wide}} = 0.04 \pm 0.19$). Therefore, it is virtually impossible to determine which packet represents each component by magnitudes alone. The method mentioned in Chapter 3 by Theo ten Brummelaar was used to determine the identities of the packets by astrometry, but due the inability of this method to correctly identify packets whose identities are obvious by magnitide, it is unclear if this method is actually working. On a related note, there are 24 nights of data for this system, so there are many chances to misidentify the fringe packets.

It would be interesting to reduce these data with different software to see if a similar result is obtained. For the current orbit, however, the masses are determined from the lines of constant mass on Figure 5.20 to be $M_{\rm Ab1} = 23\ M_\odot$ and $M_{\rm Ab2} = 9\ M_\odot$. The mutual inclination is either $\Phi = 85^{+16}_{-45}$ or $\Phi = 37^{+13}_{-34}$ degrees, but judging from the uncertainties, nothing definitive can be said about whether or not the system is coplanar.

Table. 5.33: CHARA 96 Data

t (MJD)	B (m)	ψ (degrees)	$V_{\rm Ab,obs}$	$\sigma V_{\rm Ab,obs}$	$V_{\rm Aa,obs}$	$\sigma V_{\rm Aa,obs}$
53591.21766	98.7625	118.8	0.1789	0.0102	0.1596	0.0160
53591.25327	104.3067	109.0	0.2275	0.0171	0.2172	0.0096
53591.28170	107.0294	101.9	0.2072	0.0090	0.2098	0.0080
53591.31540	107.8767	93.9	0.1959	0.0071	0.2229	0.0069
53591.33852	106.8617	88.5	0.1404	0.0057	0.1861	0.0075
53591.35191	105.6798	85.3	0.1722	0.0052	0.2149	0.0065
53591.38451	101.0800	77.2	0.1458	0.0071	0.1984	0.0066
53591.40902	96.2000	70.6	0.1382	0.0054	0.1914	0.0048
53638.23864	170.6224	324.4	0.1368	0.0249	0.1415	0.0223
53638.24415	169.8468	323.5	0.1139	0.0112	0.1498	0.0088
53638.25069	168.8501	322.4	0.1361	0.0085	0.1473	0.0167
53638.25465	168.2040	321.7	0.1239	0.0093	0.1436	0.0173
53638.26272	166.7880	320.4	0.1503	0.0131	0.1917	0.0181
53638.26644	166.0866	319.8	0.1525	0.0088	0.1688	0.0227
53638.27231	164.9191	318.9	0.1281	0.0157	0.1475	0.0176
53638.27654	164.0319	318.9	0.1382	0.0239	0.1641	0.0106
53638.28002	163.2686	317.8	0.1468	0.0110	0.1442	0.0154
53638.28454	162.2380	317.1	0.1571	0.0083	0.1418	0.0063
53638.28871	161.2424	316.5	0.1672	0.0194	0.1679	0.0138
53638.29117	160.6356	316.1	0.1414	0.0112	0.1675	0.0247
53638.29607	159.3854	315.4	0.1351	0.0172	0.1411	0.0083
53638.30121	158.0098	314.7	0.1507	0.0170	0.1704	0.0224
53638.30645	156.5400	314.0	0.1875	0.0105	0.1846	0.0173
53638.31027	155.4253	313.5	0.1671	0.0301	0.1658	0.0137
53639.19320	107.6426	91.8	0.1423	0.0068	0.1581	0.0078
53639.19847	107.4121	90.6	0.1338	0.0097	0.1588	0.0080
53639.20251	107.1891	89.6	0.1260	0.0077	0.1424	0.0070
53639.21022	106.6530	87.8	0.1395	0.0086	0.1430	0.0101
53639.21431	106.3100	86.8	0.1321	0.0064	0.1575	0.0084
53639.22092	105.6723	85.3	0.1430	0.0111	0.1726	0.0085
53639.22687	105.0099	83.8	0.1173	0.0065	0.1825	0.0098
53639.22986	104.6451	83.1	0.1375	0.0110	0.1758	0.0143
53639.23362	104.1591	82.2	0.1277	0.0074	0.1612	0.0075
53639.23647	103.7684	81.5	0.1318	0.0155	0.1468	0.0129

Table. 5.33 – Continued

t (MJD)	B (m)	ψ (degrees)	$V_{\mathrm{Ab,obs}}$	$\sigma V_{\mathrm{Ab,obs}}$	$V_{\mathrm{Aa,obs}}$	$\sigma V_{\mathrm{Aa,obs}}$
53639.24042	103.1978	80.5	0.1406	0.0082	0.1654	0.0092
53639.24405	102.6433	79.6	0.1487	0.0159	0.1546	0.0163
53639.24802	102.0048	78.6	0.1404	0.0142	0.1555	0.0103
53639.25175	101.3755	77.6	0.1156	0.0079	0.1674	0.0094
53639.25466	100.8656	76.9	0.1392	0.0092	0.1752	0.0094
53639.26435	99.0444	74.3	0.1257	0.0092	0.1467	0.0175
53639.26708	98.4993	73.6	0.1486	0.0156	0.1883	0.0122
53639.27170	97.5457	72.3	0.1259	0.0170	0.1371	0.0199
53639.27554	96.7274	71.3	0.1219	0.0126	0.1842	0.0182
53639.27896	95.9781	70.3	0.1402	0.0136	0.1946	0.0126
53639.28290	95.0923	69.2	0.1608	0.0151	0.1786	0.0235
53639.28599	94.3803	68.3	0.1575	0.0093	0.1586	0.0130
53639.29057	93.3045	66.9	0.1419	0.0209	0.1397	0.0120
53639.29481	92.2815	65.7	0.1665	0.0190	0.1211	0.0111
53639.29726	91.6822	64.9	0.1929	0.0241	0.1292	0.0149
53639.30533	89.6630	62.4	0.2040	0.0228	0.1878	0.0321
53639.30931	88.6430	61.1	0.1570	0.0100	0.1869	0.0280
53639.31399	87.4317	59.5	0.1700	0.0234	0.1703	0.0258
53639.31945	86.0030	57.7	0.1669	0.0258	0.1483	0.0117
53893.37538	315.4826	39.3	0.2292	0.0124	0.1832	0.0074
53893.38452	318.0574	37.7	0.2241	0.0135	0.2091	0.0097
53893.38817	318.9963	37.1	0.2246	0.0117	0.2320	0.0105
53893.39694	321.0558	35.5	0.2304	0.0186	0.2535	0.0115
53893.41075	323.7701	33.0	0.2162	0.0108	0.1878	0.0061
53893.41369	324.2705	32.4	0.2316	0.0119	0.1965	0.0088
53893.42206	325.5546	30.8	0.2575	0.0098	0.2014	0.0080
53893.42479	325.9311	30.3	0.2438	0.0081	0.2182	0.0068
53893.43358	327.0100	28.6	0.2305	0.0114	0.2285	0.0094
53914.30366	93.0140	128.0	0.2693	0.0086	0.2437	0.0069
53914.31253	94.8205	125.1	0.2432	0.0150	0.2151	0.0141
53914.32213	96.7182	122.1	0.2928	0.0091	0.2524	0.0078
53914.32665	97.5849	120.7	0.2613	0.0085	0.2345	0.0084
53914.33538	99.1935	118.1	0.2431	0.0104	0.2152	0.0091
53914.33953	99.9241	117.0	0.2547	0.0100	0.2502	0.0066
53914.34811	101.3603	114.5	0.2232	0.0088	0.2230	0.0077
53914.35684	102.7053	112.2	0.2462	0.0086	0.2427	0.0064
53914.36327	103.6110	110.4	0.2299	0.0132	0.2435	0.0097
53950.18226	88.2269	136.2	0.2168	0.0089	0.2236	0.0096
53950.19186	90.2122	132.7	0.1921	0.0065	0.2521	0.0074
53950.19817	91.5253	130.5	0.2080	0.0077	0.2487	0.0075
53950.20463	92.8620	128.3	0.1929	0.0061	0.2314	0.0082
53950.21257	94.4841	125.7	0.1771	0.0056	0.2365	0.0057
53950.22048	96.0645	123.1	0.2147	0.0070	0.2612	0.0076
53950.22711	97.3483	121.1	0.2013	0.0065	0.2705	0.0089
53950.23303	98.4558	119.3	0.1866	0.0066	0.2583	0.0090
53950.24141	99.9543	116.9	0.2075	0.0060	0.2615	0.0074
53950.25203	101.7144	113.9	0.2052	0.0078	0.2494	0.0065
53950.26073	103.0205	111.6	0.1915	0.0073	0.2610	0.0075
53950.27783	105.1904	107.1	0.1844	0.0060	0.2136	0.0059
53950.28493	105.9209	105.3	0.1777	0.0068	0.2110	0.0062
53950.29950	107.0779	101.7	0.2084	0.0103	0.2268	0.0122
53950.31133	107.6624	98.9	0.1607	0.0081	0.1798	0.0106
53950.31549	107.7898	97.9	0.1440	0.0087	0.1825	0.0077
53950.32667	107.9256	95.3	0.1566	0.0091	0.2012	0.0083
53950.33537	107.8206	93.2	0.1930	0.0068	0.2304	0.0072
53950.33978	107.6966	92.2	0.1883	0.0101	0.2099	0.0059
53950.34862	107.3039	90.1	0.1709	0.0111	0.1953	0.0086
53950.35755	106.7132	88.0	0.1387	0.0049	0.1779	0.0064
53950.36332	106.2289	86.6	0.1478	0.0064	0.1628	0.0059
53950.37239	105.3074	84.5	0.1410	0.0070	0.1659	0.0070
53950.38463	103.7612	81.5	0.1402	0.0060	0.1725	0.0079

Table. 5.33 – Continued

t (MJD)	B (m)	ψ (degrees)	$V_{\mathrm{Ab,obs}}$	$\sigma V_{\mathrm{Ab,obs}}$	$V_{\mathrm{Aa,obs}}$	$\sigma V_{\mathrm{Aa,obs}}$
53950.39703	101.8547	78.4	0.1604	0.0061	0.1772	0.0062
53950.40049	101.2659	77.5	0.1519	0.0056	0.1983	0.0076
53982.26200	174.5000	331.3	0.2940	0.0118	0.2595	0.0117
53982.26577	173.9674	330.0	0.2940	0.0118	0.2543	0.0115
53982.27433	173.1971	328.4	0.2900	0.0094	0.2504	0.0085
53982.27954	172.6723	327.4	0.3315	0.0079	0.2813	0.0079
53982.28767	171.7616	326.0	0.3035	0.0105	0.2757	0.0095
53982.29385	170.9925	324.9	0.3154	0.0112	0.2865	0.0094
53982.30232	169.8217	323.5	0.3327	0.0108	0.3049	0.0114
53982.31058	168.5465	322.1	0.3067	0.0134	0.2906	0.0128
53982.31529	167.7561	321.3	0.3336	0.0081	0.3027	0.0126
53982.32436	166.1017	319.9	0.3591	0.0102	0.3151	0.0096
53982.34620	161.3658	316.6	0.2132	0.0177	0.2910	0.0186
53982.35107	160.1568	315.9	0.3947	0.0116	0.3462	0.0105
53982.36042	157.6760	314.6	0.3936	0.0146	0.3497	0.0122
54273.39677	105.5738	106.2	0.1172	0.0069	0.1449	0.0089
54273.40771	106.5706	103.5	0.1342	0.0081	0.1767	0.0086
54273.41250	106.9238	102.3	0.1596	0.0062	0.1855	0.0086
54273.42819	107.7139	98.5	0.1471	0.0047	0.1702	0.0060
54273.43625	107.8935	96.6	0.1443	0.0049	0.1689	0.0048
54273.44577	107.9030	94.4	0.1647	0.0057	0.1928	0.0059
54273.45620	107.6590	91.9	0.1918	0.0050	0.2016	0.0056
54273.46114	107.4501	90.8	0.1694	0.0050	0.1972	0.0053
54273.47754	106.3298	86.9	0.1664	0.0043	0.1815	0.0046
54273.48498	105.6079	85.1	0.1638	0.0043	0.1928	0.0044
54273.49493	104.4390	82.7	0.1511	0.0041	0.1941	0.0042
54285.43607	247.8701	8.0	0.1312	0.0189	0.1591	0.0183
54288.43691	247.9256	6.0	0.1175	0.0066	0.1012	0.0071
54288.48363	247.9524	355.4	0.1232	0.0069	0.1323	0.0122
54289.46863	247.9810	358.2	0.1671	0.0110	0.2042	0.0122
54289.47288	247.9742	357.3	0.1265	0.0261	0.1669	0.0510
54318.38743	330.6577	2.5	0.2314	0.0058	0.1952	0.0068
54412.18986	89.5060	62.2	0.1581	0.0147	0.1333	0.0181
54412.20222	86.3023	58.1	0.0774	0.0063	0.1497	0.0109
54412.21498	82.9294	53.5	0.1217	0.0117	0.1340	0.0079
54412.22642	79.9097	49.1	0.1085	0.0084	0.1400	0.0092
54412.23833	76.8424	44.2	0.1409	0.0118	0.1624	0.0105
54605.50486	278.4416	143.2	0.1325	0.0249	0.1671	0.0221
54657.44123	267.3300	127.0	0.1325	0.0159	0.1674	0.0210
54657.45654	262.0605	124.1	0.2389	0.0329	0.2236	0.0126
54657.46542	258.6102	122.5	0.2696	0.0215	0.2232	0.0152
54692.32654	272.2269	130.7	0.1831	0.0101	0.2470	0.0093
54692.33384	270.5676	129.3	0.2156	0.0070	0.2737	0.0083
54692.38609	330.6578	177.4	0.1840	0.0084	0.1685	0.0100
54692.39369	330.6593	175.6	0.2052	0.0076	0.1773	0.0067
54692.40164	330.6586	173.9	0.1704	0.0090	0.2066	0.0120
54692.40908	330.6517	172.0	0.1426	0.0176	0.1873	0.0083
54692.44310	330.3934	164.3	0.1026	0.0196	0.1349	0.0217
54692.45686	330.0748	161.2	0.1208	0.0146	0.1923	0.0266
54759.12729	275.1597	134.0	0.1980	0.0192	0.1859	0.0123
54759.16600	330.6584	186.2	0.1483	0.0142	0.1372	0.0107
54759.17574	330.6590	183.9	0.1791	0.0086	0.1300	0.0071
54759.18554	330.6569	181.6	0.1789	0.0207	0.1511	0.0113
54759.19445	330.6564	179.5	0.2038	0.0123	0.1363	0.0098
54759.22688	238.0344	115.8	0.1751	0.0189	0.1486	0.0140
54759.26316	330.3363	163.6	0.2210	0.0205	0.2521	0.0137
54759.28859	329.4867	158.0	0.2671	0.0257	0.3021	0.0134
54983.50148	276.7188	136.6	0.2507	0.0081	0.3021	0.0083
54984.36391	262.3922	100.2	0.2828	0.0087	0.2169	0.0079
54984.37002	267.0895	98.6	0.2912	0.0089	0.2267	0.0072
54984.37552	270.8526	97.3	0.2882	0.0112	0.2264	0.0109

Table. 5.33 – Continued

t (MJD)	B (m)	ψ (degrees)	$V_{\mathrm{Ab,obs}}$	$\sigma V_{\mathrm{Ab,obs}}$	$V_{\mathrm{Aa,obs}}$	$\sigma V_{\mathrm{Aa,obs}}$
54984.38063	274.5292	96.1	0.2411	0.0086	0.2403	0.0086
54984.38597	278.0991	94.8	0.2268	0.0066	0.2260	0.0066
54984.39146	281.4216	93.6	0.2170	0.0080	0.2553	0.0087
54984.40340	276.2129	159.5	0.3388	0.0098	0.2731	0.0090
54984.40634	276.4945	158.2	0.3067	0.0084	0.2462	0.0083
54984.41539	276.9390	156.2	0.3437	0.0111	0.3135	0.0151
54984.41976	277.2256	154.9	0.3907	0.0178	0.3344	0.0151
55014.43569	330.5295	193.5	0.2299	0.0071	0.1843	0.0058
55014.44073	330.5737	192.3	0.2265	0.0078	0.2116	0.0070
55014.44568	330.6040	191.3	0.2186	0.0074	0.1971	0.0073
55014.44952	330.6286	190.1	0.2251	0.0091	0.2106	0.0073
55014.45496	330.6444	188.9	0.2054	0.0100	0.1879	0.0100
55014.46076	330.6547	187.4	0.1531	0.0107	0.1724	0.0177
55014.46700	330.6588	186.0	0.2035	0.0256	0.2066	0.0283
55014.47300	330.6594	184.6	0.2007	0.0072	0.2343	0.0081
55014.47879	330.6586	183.4	0.2068	0.0092	0.2617	0.0122
55014.48404	330.6573	182.0	0.2037	0.0104	0.2581	0.0060
55014.48937	330.6565	181.0	0.2242	0.0098	0.2704	0.0080
55054.37561	247.9802	178.1	0.1336	0.0062	0.1209	0.0075
55054.38026	247.9722	177.0	0.1560	0.0059	0.1157	0.0078
55054.38534	247.9600	176.0	0.1269	0.0093	0.1125	0.0084
55054.38862	247.9427	174.9	0.1257	0.0080	0.1372	0.0069
55055.35162	247.9745	182.7	0.1413	0.0090	0.1140	0.0067
55055.35628	247.9803	181.9	0.1346	0.0113	0.1156	0.0047
55055.36141	247.9848	180.9	0.1387	0.0155	0.1254	0.0060
55055.39189	247.9266	174.0	0.1067	0.0142	0.1634	0.0101
55055.39431	247.9025	173.1	0.1150	0.0130	0.1684	0.0100
55055.39966	247.8721	172.0	0.1098	0.0098	0.1307	0.0072
55056.32439	247.8492	188.6	0.1809	0.0110	0.1249	0.0039
55056.33191	247.9036	186.9	0.1757	0.0243	0.1384	0.0209
55056.33809	247.9382	185.4	0.2004	0.0247	0.1184	0.0120
55056.34393	247.9574	184.2	0.1919	0.0195	0.1561	0.0109
55056.34995	247.9718	183.0	0.1944	0.0119	0.1364	0.0107
55056.35486	247.9810	181.8	0.1813	0.0113	0.1468	0.0091
55056.36381	247.9852	179.3	0.1832	0.0128	0.1560	0.0094
55056.36999	247.9805	178.1	0.1909	0.0124	0.1708	0.0098
55056.38137	247.9553	175.6	0.1890	0.0140	0.1852	0.0119
55516.14109	245.7120	117.9	0.2181	0.0157	0.1883	0.0111
55516.15049	330.6593	172.7	0.2637	0.0112	0.1863	0.0093

Table 5.34. Orbital Elements for CHARA 96

Element	Value
Fixed Elements:	
P (days)	312.40 ± 0.10
e	0
ω	0
T (MJD)	50123.0 ± 1.5
$\Theta_{\rm Ab1}$ (mas)	0.047 ± 0.002
$\Theta_{\rm Ab2}$ (mas)	0.041 ± 0.002
Varied elements:	
α (mas)	$3.9^{+1.1}_{-1.2}$
i (degrees)	51^{+17}_{-51}
Ω (degrees)	25^{+3}_{-35}
$\Delta K_{\rm close}$	2.11 ± 0.06
$\Delta K_{\rm wide}$	0.086 ± 0.012
Reduced χ^2	1.18
Wide orbit:	
$P_{\rm wide}$ (years)	34.39 ± 1.01
$T_{\rm wide}$ (BY)	1996.27 ± 1.49
$e_{\rm wide}$	0.3974 ± 0.0412
$\omega_{\rm wide}$	$59.86^\circ \pm 7.25^\circ$
$\alpha_{\rm wide}$ (mas)	55.41 ± 2.97
$i_{\rm wide}$	$44.41^\circ \pm 7.43^\circ$
$\Omega_{\rm wide}$	$273.03^\circ \pm 7.42^\circ$

Note. — Wide orbit taken from ten Brummelaar et al. (2011).

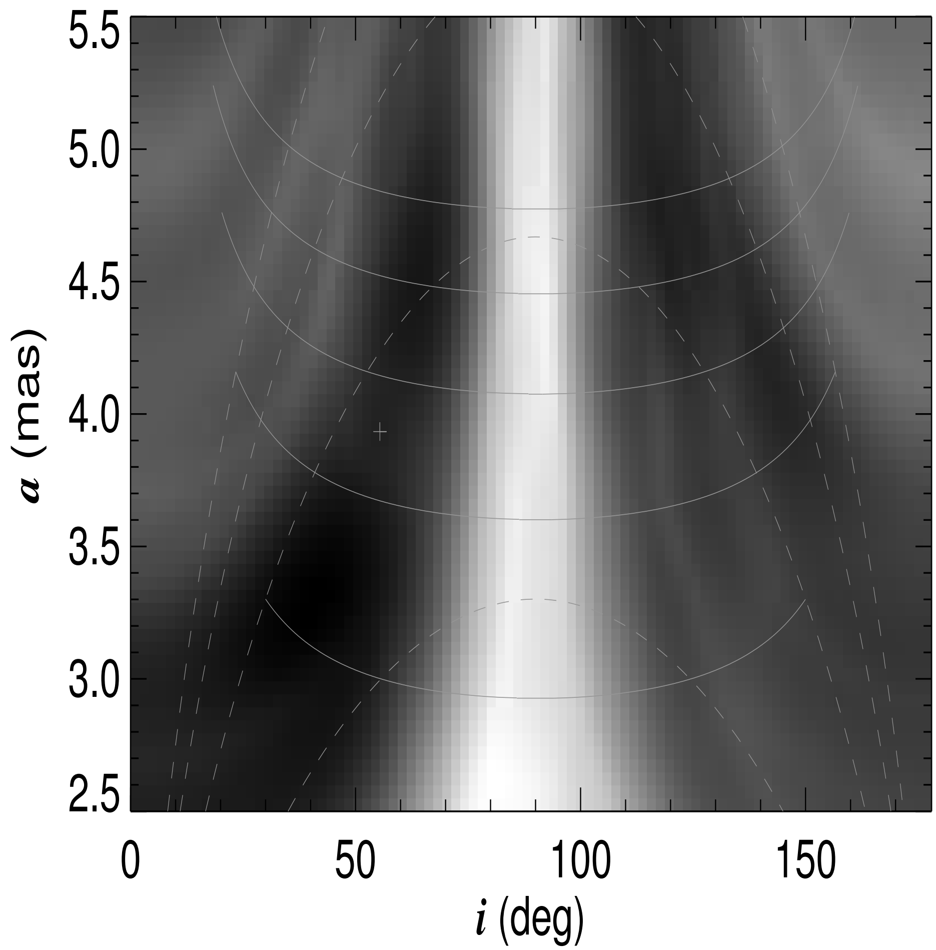

Figure. 5.20: χ^2 as a function of i and α. In this plane, the minimum χ^2 is 167 (black) and the maximum is χ^2 is 529 (white). The solid lines are lines of constant mass for component Ab1 (10, 20, 30, 40, and 50 $M_\odot$ from bottom to top, while the dashed lines are lines of constant mass of component Ab2 (5, 10, 15, and 20 $M_\odot$ from bottom to top). The location of the adopted solution is marked by a plus sign. Strong minima are located at $(i, \alpha) = (38°, 3.3$ mas), (66°, 4.6 mas), and (118°, 4.7 mas). This figure is taken from ten Brummelaar et al. (2011).

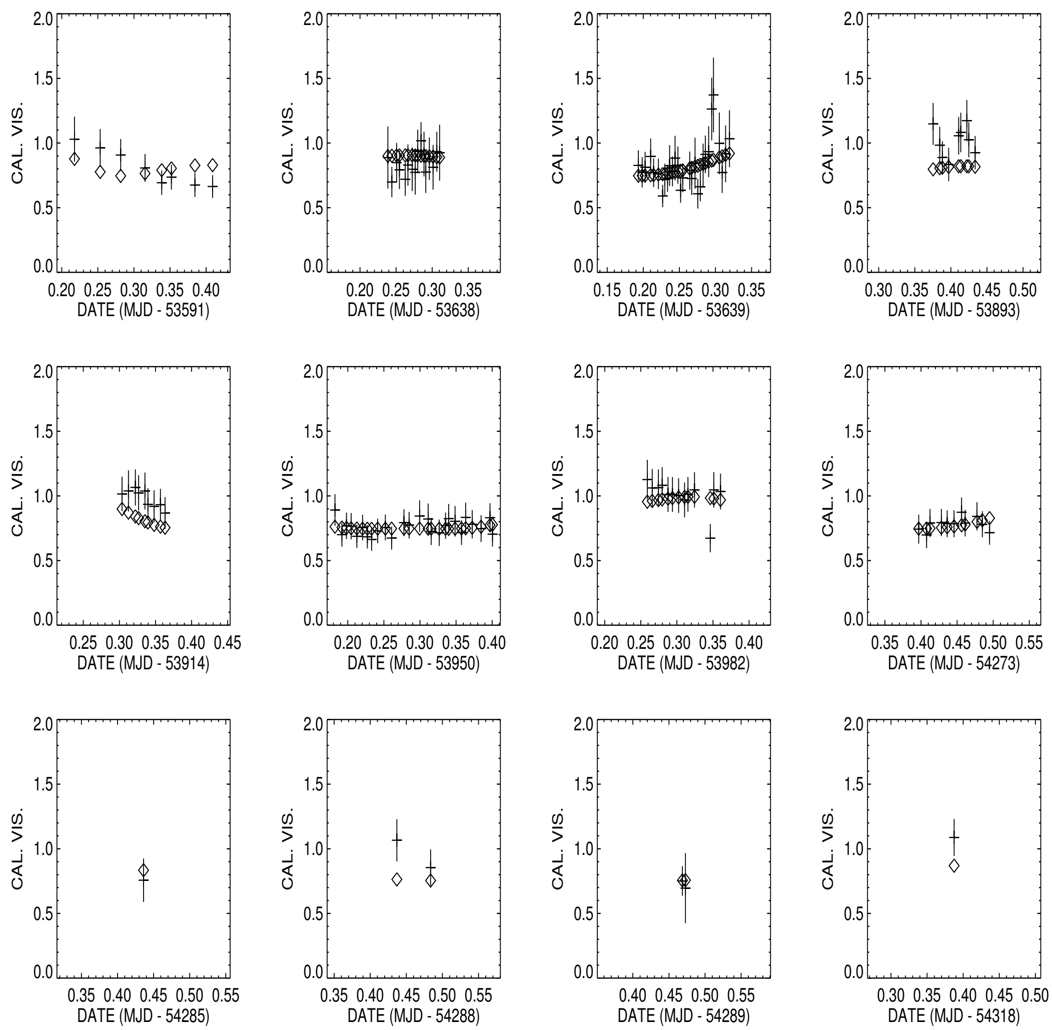

Figure. 5.21: Orbit fit for CHARA 96 Ab

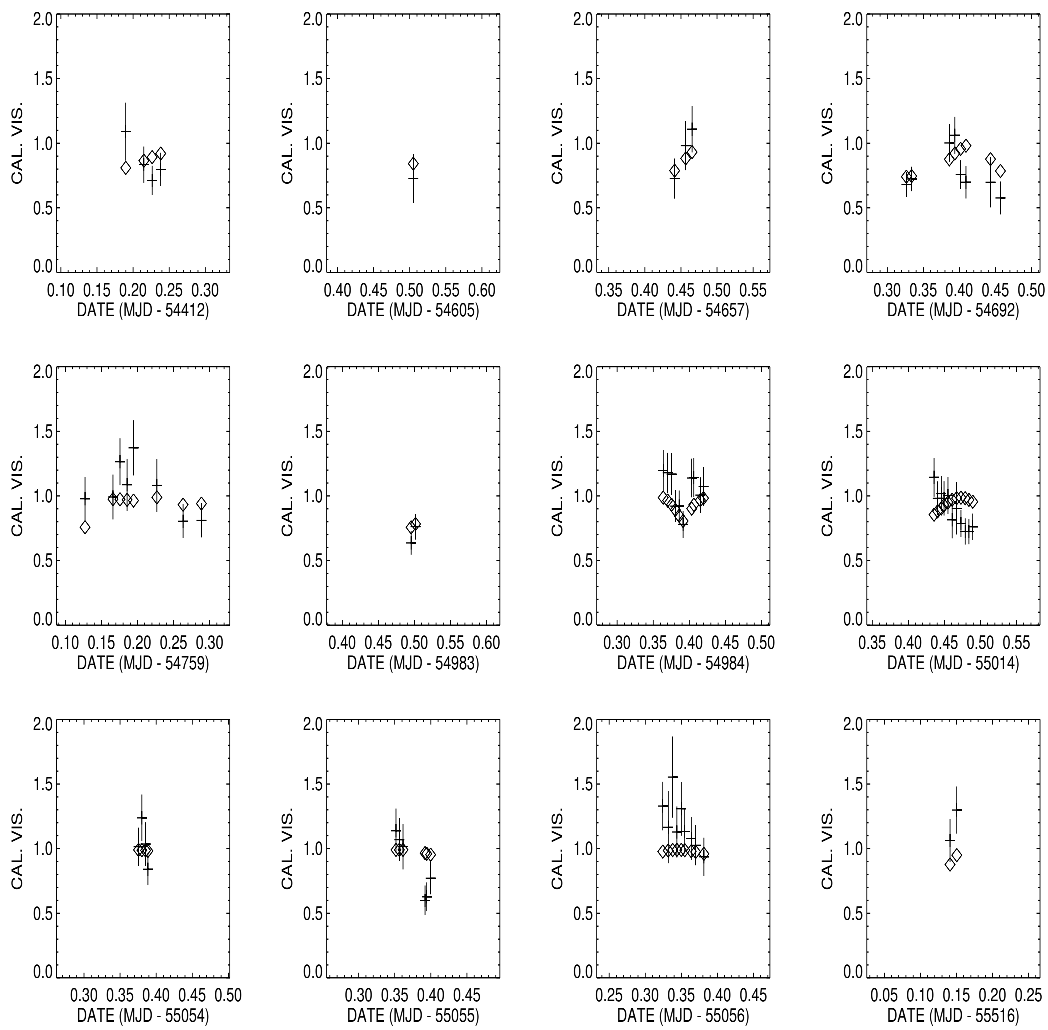

Figure. 5.22: Orbit Fit for CHARA 96 Ab (cont'd)

5.2.8 HD 129132

HD 129132 is the final member of the target list on which SFPs were actually observed. It is also the most disappointing target of this study so far. Although it was observed on 14 different nights, only 3 of the nights had the desired separation between the fringe packets. On the other 11 nights, the separation was below the 45-μm threshold used to determine when SFPs need to be corrected for side-lobe interference. On those nights, an observation baseline was selected to maximize the separation on several of the above targets, but the baseline did not work as well for HD 129132. The side-lobe interference is not as bad as it could be, as the separations for all these nights lie between 24 and 41 μm. Unfortunately, there was not enough data on any of these nights to correct the data by sinusoid fitting. Although this was not the ideal circumstance, an attempt at orbit-fitting with the uncorrected data in Table 5.35 was undertaken.

A speckle wide orbit of 9.3 years and 74 mas and a spectroscopic close orbit of 101 days are given by Barlow & Scarfe (1991). One unique aspect of this system compared to the other targets is that only one component of the system is seen in the composite spectrum. This primary component of the close binary (designated Aa1) is thought to be a F4III star Barlow & Scarfe (1991). Without a mass ratio for the wide orbit, Barlow & Scarfe (1991) were forced to come up with plausible models for the makeup of the system involving the inclination for the close pair $i_{\rm close}$, which must be plugged into the equation for the mass function of the close pair, and q, the mass ratio of the close pair. The conclusion was that the most plausible parameters of the stars are $i_{\rm close} = 45°$, $q = 0.56$, $M_{\rm Aa1} = 1.97\ M_\odot$, $M_{\rm Aa2} = 1.29\ M_\odot$, and $M_{\rm Ab} = 1.82\ M_\odot$. These masses respectively correspond to stars of spectral type F4III, F5V, and A7V (Barlow & Scarfe 1991). The spectral types, along with a parallax of 9.47 $\pm$ 0.71 mas (Perryman et al. 1997), give a way to calculate angular diameters for the system of $\Theta_{\rm Aa1} = 0.242 \pm 0.063$ mas, $\Theta_{\rm Aa2} = 0.057 \pm 0.019$ mas, and $\Theta_{\rm Ab} = 0.071 \pm 0.022$ mas. Also, with a suggested mass total for the close binary ($M_{\rm Aa1} + M_{\rm Aa2} = 3.26\ M_\odot$) and the period for the system, a suggested semi-major axis for the close system can be derived ($\alpha = 6.00$ mas).

This is a non-circular system, so the orbital period is the only fixed parameter in the fitting. The minimum χ^2 fit to the data (Figures 5.23 and 5.24) of component Aa does not show great agreement with the spectroscopic elements of Barlow & Scarfe (1991), although the elements are not in complete disagreement, as seen in Table 5.36. There is close agreement between the eccentricities, but the epochs of periastron are nearly 20 days apart in this 101-day orbit and the longitudes of periastron are nearly 30° apart. The results are also in slight disagreement with the most plausible scenario given by Barlow & Scarfe (1991). The semi-major axis and inclination are both larger than expected for the models used to calculate angular diameters. The disagreement here is not completely unexpected, because the majority of the data is known to be uncorrected, and perhaps with further observations of fringe packets without side-lobe interference, these elements will be in greater agreement. The noticeable disagreement between the model and the data on JD 55380 can be attributed to strong side-lobe interference. The associated χ^2 plots are given in Figure 5.25.

If the derived orbital elements are to be believed, the fundamental parameters of the system are given in Tables 5.37, 5.38, and 5.39. The mutual inclination is well-constrained by this orbit because the two ambiguous values are within 7° of each other. Both values suggest that the plane of the close orbit is nearly perpendicular to the plane of the wide orbit. The masses calculated from this single-line spectroscopic system ($4.56 M_\odot$) are a bit larger than expected from the wide orbit ($3.26\ M_\odot$) of Barlow & Scarfe (1991). Unfortunately, there are no individual V magnitude estimates, so comparison with the K magnitudes cannot be used to find an age estimate even though there is an evolved component.

Table. 5.35: HD 129132 Data

t (MJD)	B (m)	ψ (degrees)	$V_{\rm Aa,obs}$	$\sigma V_{\rm Aa,obs}$	$V_{\rm Ab,obs}$	$\sigma V_{\rm Ab,obs}$
53885.17194	330.6379	35.7890	0.2562	0.0251	0.1073	0.0124
53885.17789	330.6226	34.9959	0.2926	0.0212	0.1044	0.0097
53885.18337	330.4919	34.2171	0.2435	0.0234	0.1058	0.0135
53885.18897	330.2506	33.3937	0.2549	0.0278	0.0966	0.0085
53885.19481	329.8797	32.4815	0.2124	0.0257	0.0813	0.0114
53885.20090	329.4069	31.5412	0.2293	0.0244	0.1017	0.0188
53885.20900	328.6112	30.2101	0.2085	0.0118	0.1003	0.0081
53885.21481	327.9566	29.2337	0.2272	0.0186	0.0959	0.0111
53885.22276	326.9564	27.8516	0.2658	0.0135	0.0948	0.0090
53885.22899	326.0842	26.7086	0.2609	0.0309	0.0837	0.0120
53885.23473	325.2340	25.6241	0.2307	0.0179	0.0787	0.0035
54287.24099	237.5913	177.3212	0.2866	0.0274	0.1236	0.0071
54287.24747	237.7508	175.8120	0.3119	0.0199	0.1132	0.0103
54288.17809	239.4198	11.3291	0.3265	0.0316	0.1392	0.0120
54288.19552	238.3103	7.3548	0.3267	0.0244	0.1160	0.0111
54567.39307	321.7183	21.1734	0.2326	0.0195	0.0817	0.0080
54567.39842	320.8555	20.0388	0.2436	0.0235	0.0858	0.0078
54567.40368	320.0242	18.9115	0.2565	0.0122	0.0850	0.0063
54567.40917	319.1942	17.7415	0.2456	0.0147	0.0854	0.0083
54567.41434	318.3949	16.5622	0.2366	0.0184	0.0830	0.0084
54567.41995	317.5854	15.2987	0.2407	0.0126	0.0948	0.0095
54567.42574	316.7951	13.9775	0.2418	0.0210	0.0955	0.0043
54567.43162	316.0387	12.6047	0.2417	0.0197	0.0982	0.0090
54567.43788	315.2986	11.1193	0.2359	0.0251	0.0958	0.0082
54567.44409	314.6494	9.6465	0.2248	0.0129	0.0953	0.0085
54567.45079	314.0511	8.0687	0.1970	0.0145	0.0910	0.0072

Table. 5.35 – Continued

t (MJD)	B (m)	ψ (degrees)	$V_{\rm Aa,obs}$	$\sigma V_{\rm Aa,obs}$	$V_{\rm Ab,obs}$	$\sigma V_{\rm Ab,obs}$
54567.45781	313.4998	6.2939	0.2028	0.0205	0.0899	0.0074
54567.46520	313.0855	4.5295	0.1794	0.0168	0.0881	0.0062
54649.21995	314.5766	9.4696	0.2301	0.0215	0.1012	0.0058
54649.22442	314.1591	8.3776	0.2356	0.0209	0.0990	0.0085
54649.22855	313.8166	7.3681	0.2549	0.0240	0.1044	0.0062
54649.23254	313.5251	6.3889	0.2426	0.0220	0.0978	0.0073
54649.23626	313.2870	5.4638	0.2457	0.0193	0.1046	0.0081
54649.24007	313.0816	4.5188	0.2474	0.0212	0.1077	0.0098
54649.24371	312.9214	3.6163	0.2232	0.0205	0.1035	0.0073
54649.24747	312.7929	2.6818	0.2245	0.0246	0.1012	0.0085
54649.25185	312.6901	1.5830	0.2192	0.0171	0.1023	0.0084
54649.25550	312.6452	0.6730	0.2297	0.0200	0.1037	0.0055
54649.26077	312.6444	179.3680	0.2253	0.0210	0.1029	0.0071
54649.26449	312.6896	178.4261	0.2066	0.0180	0.1005	0.0059
54649.26894	312.7922	177.3282	0.2071	0.0171	0.1054	0.0103
54649.27262	312.9190	176.4032	0.1986	0.0130	0.0940	0.0082
54649.27709	313.1191	175.2986	0.2064	0.0156	0.0994	0.0090
54649.28287	313.4482	173.9061	0.2158	0.0172	0.1034	0.0082
54649.28925	313.9181	172.3250	0.2040	0.0150	0.1156	0.0071
54649.29508	314.4256	170.9178	0.2136	0.0151	0.1169	0.0089
54649.30088	315.0077	169.5213	0.2268	0.0238	0.1274	0.0105
54649.30644	315.6400	168.1771	0.2440	0.0191	0.1388	0.0079
54650.18019	319.4158	18.0592	0.2046	0.0128	0.0803	0.0077
54650.18374	318.8711	17.2722	0.1968	0.0117	0.0806	0.0054
54650.18732	318.3307	16.4650	0.1910	0.0152	0.0779	0.0062
54650.19117	317.7742	15.6004	0.1813	0.0120	0.0876	0.0050
54650.19430	317.3291	14.8811	0.1751	0.0153	0.0870	0.0028
54650.19790	316.8336	14.0448	0.1769	0.0104	0.0847	0.0068
54650.20144	316.3712	13.2244	0.1908	0.0094	0.0922	0.0056
54650.20505	315.9153	12.3691	0.1833	0.0149	0.0896	0.0057
54650.20877	315.4777	11.4952	0.1852	0.0169	0.0872	0.0065
54650.21240	315.0674	10.6179	0.2060	0.0149	0.0913	0.0071
54650.21580	314.7140	9.8045	0.2052	0.0129	0.0934	0.0046
54650.21929	314.3764	8.9619	0.1887	0.0116	0.0882	0.0065
54650.22314	314.0328	8.0204	0.1989	0.0106	0.0871	0.0053
54650.22661	313.7529	7.1658	0.2321	0.0160	0.0954	0.0051
54650.23002	313.5083	6.3290	0.2340	0.0066	0.1013	0.0068
54650.23337	313.2938	5.4934	0.2525	0.0145	0.1074	0.0039
54650.23672	313.1103	4.6641	0.2516	0.0165	0.1141	0.0063
54650.23999	312.9600	3.8556	0.2591	0.0074	0.1145	0.0054
54650.24344	312.8326	3.0030	0.2607	0.0259	0.1156	0.0071
54650.24700	312.7318	2.1049	0.2694	0.0059	0.1170	0.0092
54650.25032	312.6704	1.2756	0.2745	0.0112	0.1166	0.0056
54650.25373	312.6389	0.4229	0.2602	0.0091	0.1179	0.0090
54650.25718	312.6391	179.5586	0.2727	0.0143	0.1138	0.0070
54650.26065	312.6726	178.6933	0.2457	0.0155	0.1141	0.0098
54650.26360	312.7265	177.9550	0.2429	0.0078	0.1125	0.0058
54650.26711	312.8217	177.0816	0.2140	0.0136	0.1058	0.0058
54650.27072	312.9533	176.1875	0.2134	0.0139	0.1049	0.0054
54651.19215	317.2761	14.7914	0.2179	0.0197	0.1031	0.0134
54651.19948	316.3007	13.0923	0.1810	0.0466	0.0858	0.0193
54651.23174	313.2386	5.2522	0.1993	0.0190	0.0984	0.0085
54651.23633	313.0106	4.1323	0.2072	0.0260	0.1028	0.0090
54651.24138	312.8188	2.8791	0.1740	0.0176	0.0955	0.0047
54651.24857	312.6631	1.0842	0.1934	0.0175	0.1029	0.0083
54651.25369	312.6383	179.8056	0.1857	0.0189	0.1039	0.0053
54651.25995	312.7056	178.2397	0.1842	0.0120	0.1038	0.0085
54663.19975	313.1892	5.0370	0.3421	0.0158	0.1479	0.0096
54663.20311	313.0206	4.1996	0.3301	0.0135	0.1433	0.0136
54663.20640	312.8860	3.3863	0.3203	0.0118	0.1390	0.0087
54663.20981	312.7755	2.5339	0.3199	0.0191	0.1227	0.0057

Table. 5.35 – Continued

t (MJD)	B (m)	ψ (degrees)	$V_{\rm Aa,obs}$	$\sigma V_{\rm Aa,obs}$	$V_{\rm Ab,obs}$	$\sigma V_{\rm Ab,obs}$
54663.21322	312.6966	1.6788	0.3087	0.0081	0.1275	0.0106
54663.21653	312.6506	0.8448	0.2928	0.0123	0.1222	0.0020
54663.22005	312.6353	179.9843	0.2592	0.0162	0.1177	0.0106
54663.22365	312.6541	179.0726	0.2814	0.0209	0.1288	0.0095
54663.22713	312.7058	178.2038	0.2680	0.0168	0.1294	0.0064
54663.23069	312.7925	177.3195	0.2803	0.0137	0.1354	0.0089
54663.23498	312.9429	176.2506	0.2729	0.0180	0.1350	0.0100
54663.23922	313.1407	175.1921	0.2619	0.0165	0.1320	0.0088
54663.24313	313.3620	174.2313	0.2564	0.0287	0.1343	0.0077
54663.24733	313.6423	173.2024	0.2557	0.0286	0.1340	0.0100
54663.25157	313.9719	172.1600	0.2590	0.0226	0.1405	0.0131
54663.25580	314.3425	171.1284	0.2601	0.0245	0.1349	0.0097
54692.15384	268.0945	125.5570	0.3631	0.0300	0.1496	0.0147
54692.22565	320.8042	160.0299	0.3705	0.0230	0.1261	0.0056
54692.23098	321.6690	158.8906	0.3638	0.0276	0.1211	0.0116
54692.23685	322.5736	157.7278	0.3302	0.0248	0.1272	0.0101
54698.16726	240.2132	166.4620	0.1856	0.0193	0.0713	0.0074
54698.17266	240.6830	165.2905	0.1598	0.0114	0.0692	0.0043
54698.17858	241.2205	164.0312	0.1725	0.0169	0.0681	0.0032
54698.18504	241.8278	162.6869	0.1720	0.0163	0.0792	0.0083
54698.19129	242.4376	161.3976	0.1753	0.0163	0.0789	0.0061
54698.19728	243.0292	160.1881	0.1754	0.0137	0.0811	0.0064
54699.18015	241.6358	163.1040	0.2099	0.0232	0.0910	0.0059
54699.18547	242.1484	162.0022	0.1978	0.0233	0.0846	0.0079
54699.19103	242.6839	160.8899	0.1788	0.0188	0.0845	0.0072
54699.19698	243.2705	159.7033	0.1668	0.0125	0.0835	0.0075
55311.29420	247.0301	28.1273	0.2343	0.0107	0.0909	0.0015
55311.29833	246.7537	27.4505	0.2232	0.0181	0.0857	0.0026
55311.30217	246.4724	26.8012	0.2410	0.0149	0.1004	0.0071
55311.30581	246.1918	26.1818	0.2197	0.0157	0.0851	0.0021
55311.33062	243.9604	21.6665	0.1997	0.0125	0.0993	0.0055
55311.33503	243.5163	20.7872	0.1917	0.0113	0.0894	0.0059
55311.33912	243.1147	19.9841	0.2100	0.0128	0.1001	0.0063
55311.34418	242.6115	18.9617	0.2126	0.0117	0.1032	0.0064
55311.34820	242.2137	18.1354	0.2340	0.0155	0.1063	0.0079
55311.35210	241.8329	17.3246	0.2404	0.0167	0.1170	0.0101
55311.35594	241.4655	16.5202	0.2480	0.0163	0.1118	0.0069
55353.38332	170.6721	138.6344	0.2817	0.0176	0.1231	0.0090
55353.38739	169.8789	138.3816	0.3085	0.0116	0.1266	0.0064
55353.39139	169.0666	138.1530	0.3348	0.0247	0.1388	0.0087
55379.28400	174.9948	140.9112	0.2963	0.0185	0.1385	0.0114
55379.29181	174.0592	140.2187	0.3180	0.0268	0.1385	0.0137
55379.29780	173.2341	139.7296	0.3262	0.0252	0.1333	0.0067
55379.30364	172.3287	139.2825	0.3340	0.0121	0.1427	0.0095
55379.30937	171.3828	138.8903	0.3582	0.0182	0.1508	0.0125
55379.31501	170.3214	138.5188	0.3807	0.0213	0.1756	0.0140
55379.32072	169.1657	138.1794	0.4006	0.0339	0.1882	0.0195
55379.32611	167.9921	137.8899	0.3791	0.0225	0.2074	0.0111
55380.27526	175.5012	141.3756	0.4754	0.0136	0.1927	0.0082
55380.27852	175.1769	141.0682	0.4667	0.0185	0.1884	0.0133
55380.28184	174.8177	140.7645	0.4795	0.0128	0.1837	0.0093
55380.28520	174.4280	140.4700	0.5002	0.0174	0.1701	0.0082
55380.28867	173.9878	140.1717	0.4900	0.0168	0.1478	0.0042
55380.29188	173.5577	139.9099	0.4824	0.0090	0.1419	0.0063
55380.29520	173.0783	139.6461	0.4578	0.0198	0.1296	0.0041
55380.29844	172.5843	139.4003	0.4541	0.0135	0.1305	0.0042
55380.30169	172.0624	139.1649	0.4730	0.0219	0.1291	0.0056
55380.30496	171.5053	138.9369	0.4322	0.0173	0.1384	0.0064

Table 5.36. Orbital Elements for HD 129132 Aa derived from minimum χ^2 fit

Element	Value	Spectroscopic Orbit
Fixed Elements:		
P (days)	101.606 ± 0.003	101.606 ± 0.003
Θ_{Aa1} (mas)	0.242 ± 0.063	
Θ_{Aa2} (mas)	0.057 ± 0.019	
Varied elements:		
T (MJD)	55197.32 ± 1.62	55179 ± 0.8
e	0.101 ± 0.004	0.117 ± 0.007
ω	$176^\circ \pm 4^\circ$	$140.7^\circ \pm 2.9^\circ$
α (mas)	6.69 ± 0.05	
i	$56.3^\circ \pm 1.3^\circ$	
Ω	$172.2^\circ \pm 1.0^\circ$	
$\Delta K_{\mathrm{close}}$	2.10 ± 0.08	
ΔK_{wide}	1.098 ± 0.015	
Reduced χ^2	1.00	
Wide orbit:		
P_{wide} (days)	3385 ± 7	
T_{wide} (MJD)	42879.5 ± 40	
e_{wide}	0.073 ± 0.010	
ω_{wide}	$91.4^\circ \pm 4.1^\circ$	
α_{wide} (mas)	74 ± 1	
i_{wide}	$104.6^\circ \pm 0.5^\circ$	
Ω_{wide}	$78.2^\circ \pm 0.7^\circ$	

Note. — Wide orbit and spectroscopic close orbit taken from Barlow & Scarfe (1991).

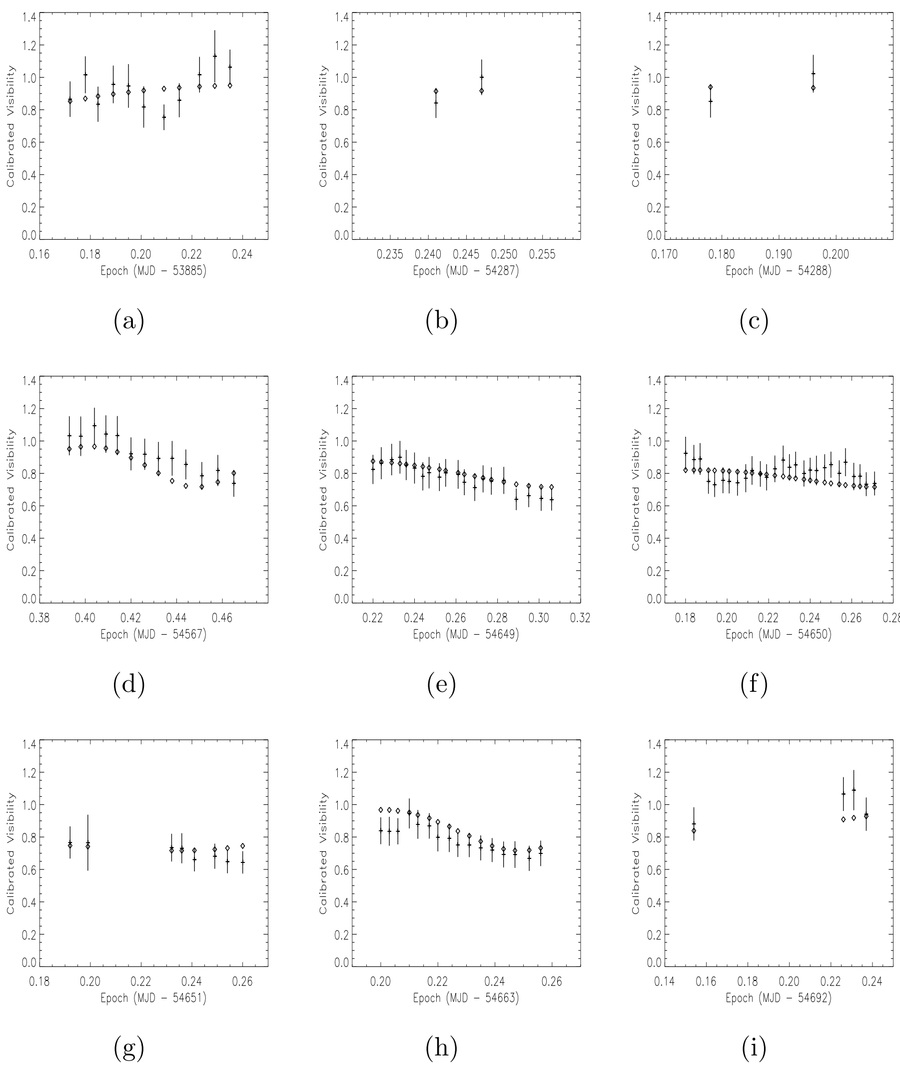

Figure. 5.23: Optimal orbit fit for HD 129132 Aa

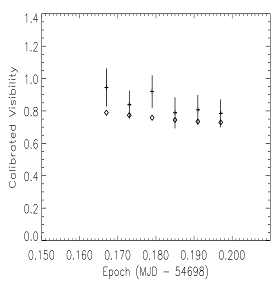

(a)

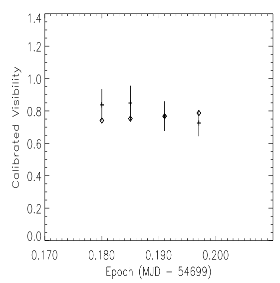

(b)

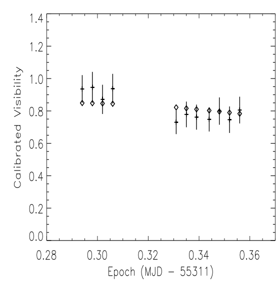

(c)

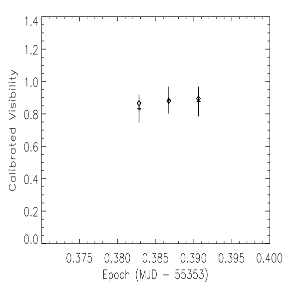

(d)

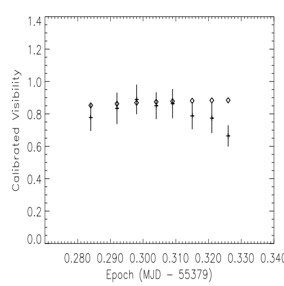

(e)

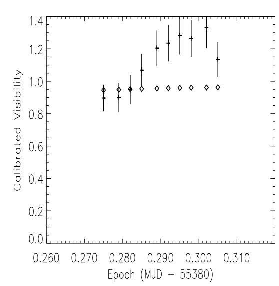

(f)

Figure. 5.24: Optimal orbit fit for HD 129132 Aa (cont'd)

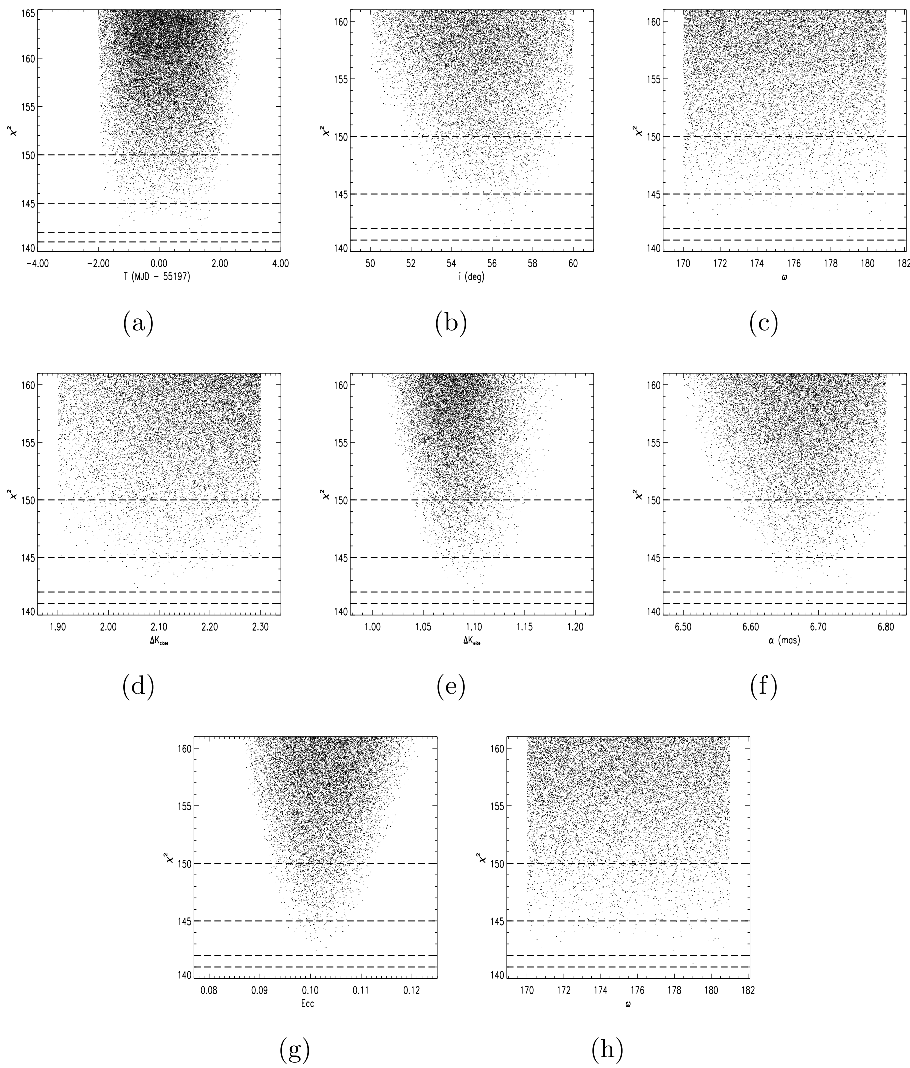

Figure. 5.25: χ^2 plots for HD 129132 Aa

Table 5.37. HD 129132 Mutual Inclination

Element	Value (degrees)	
i_{wide}	104.6 ± 0.5	
i_{close}	56.3 ± 1.3	
Ω_{wide}	78.2 ± 0.7	
Ambiguous values:		
Ω_{close}	172.2 ± 1.0	352.2 ± 1.0
Φ	101.4 ± 1.1	94.8 ± 1.1

Table 5.38. HD 129132 Masses

Element	Value
π (mas)	9.47 ± 0.71
α (mas)	6.69 ± 0.05
a (AU)	0.706 ± 0.063
P (days)	101.606 ± 0.003
i	$56.3° \pm 1.3°$
e	0.101 ± 0.004
K_{Aa1} (km/s)	19.0 ± 0.1
f(M)	0.0711 ± 0.0011
M_{Aa1} ($M_{\odot}$)	3.19 ± 0.572
M_{Aa2} ($M_{\odot}$)	1.37 ± 0.245

Table 5.39. Magnitudes of HD 129132 components

	A	Aa	Aa1	Aa2	Ab
K	5.073 ± 0.015	5.41 ± 0.016	5.56 ± 0.019	7.65 ± 0.082	6.50 ± 0.022

5.3 Other targets

Besides the main targets listed in the previous section, many more hierarchical triple systems from the main and marginal target lists have been observed through the years. The seven targets (all besides CHARA 96) listed above are the ones for which SFPs were found at an early stage of the project. It is reasonable to assume that other objects observed in the early stages that did not show SFPs may have been observed with configurations that were unfavorable for producing SFPs. For this reason, there are a few dozen objects that were placed in the SCAM Queue. If there was any free time during observations during which the seven main targets were unavailable, observations of the Queue targets would be attempted. To maximize the number of Queue targets that could be observed, individual targets were observed only briefly, unless they showed strong SFPs. In those cases, a little more time was allotted to observing the system. By observing Queue targets, a few more SFPs systems were found and many more have been ruled out.

The earliest Queue targets that successfully produced SFPs were HD 163151 and HD 115955. Initially, there was a great deal of excitement surrounding these targets, because, in each system, one of the fringe packets showed strong modulation over the course of observation. However, it was later discovered that the close binaries in these two triple system are contact binaries and, looking at their light curves, are in a constant state of semi-eclipse. It was reasoned that the visibility modulation observed was due to the photometric fluctuation of the close binary relative to the wide component rather than the orbital movement.

Table 5.40 gives the statistics of all Queue targets that were observed. The second column gives the number of nights each target was observed. The third column notes whether SFPs were seen for a target on any of the nights for which it was observed. “Y” indicates that SFPs were definitely observed, “N” indicates that SFPs were definitely not observed, and “M” indicates that SFPs may have been present, but the quality of the data was not good enough to definitively determine one way or another. The last column gives an estimate of the quality of the data by labeling it either good, fair, or poor. Generally, poor data quality is associated with an “M”.

As one can see from the Table 5.40, there are three new hierarchical triple systems (HD 1976, 26961, 41116) that produce SFPs and many that could possibly produce SFPs if observed under good conditions. These would make good future targets for observation with the SCAM. HD 115955 and HD 163151 have been disqualified as candidates for the reason listed above.

Table 5.40. SCAM Queue Observing

Target HD No.	Nights	SFPs	Quality
1976	1	Y	good
5408	1	N	fair
19356	3	N	good
23302	14	N	good
23630	4	N	good
24760	1	N	good
26961	2	Y	fair
28217	1	N	good
28363	1	M	poor
28485	1	N	poor
29763	1	M	fair
37043	7	N	good
36486	1	M	fair
41040	1	M	poor
41116	1	Y	good
58728	1	M	poor
83808	1	M	poor
115955	4	Y	good
132742	1	M	poor
153808	3	N	fair
156283	1	N	good
163151	7	Y	good
166181	1	M	fair
173654	2	N	good
174343	1	M	poor
176155	6	N	good
183344	2	N	good
187949	2	M	poor
202908	1	N	poor
206058	1	N	poor
206267	4	M	fair
203156	13	N	good
207330	1	M	poor
216608	1	M	fair

– 6 –
Discussion

6.1 Mutual Inclination

One important result from this study is the mutual inclinations (Φ) that have been calculated from the orientations of the wide and close orbits. The mutual inclination of a system is defined as the angle between the planes of the wide and close orbits and is given by equation 5.4. The quantity Φ has long been an item of astronomical interest because of its relation to the conditions under which triple systems form (Sterzik & Tokovinin 2002). Initial understanding of the mutual inclination suggested that all triple systems should be coplanar ($\Phi = 0°$), but more recent results have shown that this is not the case.

6.1.1 Formation scenarios

The two methods of binary and multiple system formation considered here are the fragmentation of an initial gas cloud and the capture of a star by energy dissipation. Fragmentation involves the collapse of a gas cloud into a few individual gravitationally bound sub-condensations (Bodenheimer (1978), Bonnell & Bate (1994)). Multiple systems formed by fragmentation cannot account for close binaries in which the semi-major axis is smaller than a few astronomical units (AU) (Clarke 1995). Also, multiple systems formed by fragmentation are expected to be coplanar (small mutual inclination) (Bodenheimer (1978), Bonnell & Bate (1994)).

The capture scenario for binary star formation involves two stars that form as single stars and lose a large fraction of their energies of relative motion to become gravitationally bound (Clarke 1995). In order to lose that energy, it is either transferred to the kinetic energy of a third body, deposited in the tidally excited modes of the atmosphere of one of the stars, or dissipated in the circumstellar disk of one of the stars (Clarke 1995). In small N-body systems, the first of these three capture methods, known as dynamical capture, is a viable method of binary formation (Clarke 1995). The star-disk interaction method of formation is found to substantially increase the number of multiple systems formed McDonald & Clarke (1995). More importantly for the purposes of this study, modeling of dynamical decay in small N-body systems by Sterzik & Tokovinin (2002) produces noncoplanar systems.

Bodenheimer (1978) attempted to model the formation of multiple systems by the fragmentation process through several stages of development, starting with the collapse of a massive rotating gas cloud. The 2D and 3D hydrodynamical calculations of the collapsing cloud lead to the formation of a toroid in the cloud's center. This ring then fragments into smaller subcondensations which may form either binaries or multiple systems. An important result from this modeling is the prediction of coplanarity at all stages of development.

Another major fragmentation modeling attempt by Bonnell & Bate (1994) involves the collapse of a gas cloud into two protostellar cores with either a circumstellar disk around each core or a circumbinary disc around both cores. In these hydrodynamical simulations, the interaction of the two components of the protobinary causes the disk(s) to fragment and form another component (or multiple components). The formation scenarios presented in Bonnell & Bate (1994) can account for multiple systems of any size. Like Bodenheimer (1978), the scenarios of Bonnell & Bate (1994) can only account for coplanar multiple systems.

A major step in modeling the capture scenario was performed by Sterzik & Tokovinin (2002), who conducted extensive modeling of triple systems following the method of Sterzik & Durisen (1995) and Sterzik & Durisen (1998). This modeling involved following the dynamical decay of N-body collapsing cloud simulations until stable triple system configurations were reached, then performing statistical analysis on the mutual inclinations of the resulting systems. The most important initial conditions are N (the number of bodies), the shape of the initial cloud, its rotational energy, and its virial status. An important factor of the modeling here is the ability to form non-coplanar systems for various sets of initial conditions.

Fekel (1981) conducted a study of many important parameters of multiple systems using the statistics of several observed systems. One of these parameters was the mutual inclination of the observed multiple systems. Fekel (1981) defined coplanarity in this study as:

$$\Phi < 15^\circ \quad \text{or} \quad \Phi > 165^\circ \tag{6.1}$$

a definition that has been adopted for the current work. All systems in the study by Fekel (1981) only had spectroscopic orbits for the close binaries, so Φ could not be calculated directly. However, because the term $\cos(\Omega_{\rm wide} - \Omega_{\rm close})$ in equation 5.4 must be between -1 and 1, a minimum Φ can be calculated based on the orbits' inclinations. An explanation of how to obtain $\Phi_{\rm min}$ is given in Appendix A. Seven of the twenty-one multiple systems considered by Fekel (1981) had a $\Phi_{\rm min}$ that did not satisfy condition 6.1, and thus were deemed non-coplanar. The remaining fourteen systems could not be categorized as either coplanar or non-coplanar without visual orbits. Although the Fekel (1981) study did not directly calculate the mutual inclination for any systems, an important result came from it: a significant number of multiple systems are non-coplanar. This suggests that perhaps the capture method is more relevant to the creation of multiple systems than the fragmentation method.

The study by Sterzik & Tokovinin (2002) further addressed the issue of coplanarity by determining an average value of the mutual inclination using data from the Multiple Star Catalog (Tokovinin 1997). For a sample of 22 triple systems, the calculated average is $<\Phi> = 67° \pm 9°$ (Sterzik & Tokovinin 2002). This suggests a strong tendency against coplanarity. However, this result is preliminary. The sample size of the study is small, and the standard deviation of $<\Phi>$ is large ($\sigma = \pm 64°$). Also, three of the 22 systems meet the requirements for coplanarity according to condition 6.1. Furthermore, for 19 of these 22 systems, the value for either $\Omega_{\rm wide}$ and $\Omega_{\rm close}$ possesses the aforementioned 180° ambiguity, so the mutual inclination included in the average above for each of these 19 systems was randomly chosen from the two possible values of Φ. Clearly, more systems must be added to these statistics to get a better idea of the mutual inclinations in triple systems.

6.1.2 Distribution of Φ

If one considers all orbits to be randomly oriented in space, the corresponding cumulative distribution of the mutual inclinations, when considering both ambiguous values, is (Tokovinin 1993):

$$F(\Phi) = 0.5(1 - \cos\Phi). \tag{6.2}$$

A common analysis followed by Sterzik & Tokovinin (2002), Tokovinin (1993), and Muterspaugh et al. (2006a) is to compare this random distribution to the distribution of observed mutual inclinations. For ambiguous systems, both possible angles of Φ are considered. Examination of the MSC (Tokovinin 1997) has shown that since the study of Sterzik & Tokovinin (2002), the number of systems with two visual orbits at adjacent hierarchy levels has increased from 22 to 42, including five new orbits presented in the current study. Table 6.1 lists all of these systems, starting with the eight orbits derived in this study. Only one value of Φ is listed for the six of these systems in which the ambiguity has been resolved by Heintz (1996), Hummel et al. (2003), Muterspaugh et al. (2008), or Csizmadia et al. (2009). A few systems listed (HD 15089, HD 29140, HD 40932) have more specific designations because of the more complex structures of those systems. HD 15089 is a three-tiered hierarchical system in which all three visual orbits are known, so mutual inclinations can be derived between the widest and middle orbits and the middle and closest orbits. It is unclear whether the mutual inclination between the widest and closest orbit is of any physical significance. HD 29140, HD 40932, and HD 68255/7 are double-double hierarchical systems in which both components of a wide orbit are close binaries. A mutual inclination can be derived between the wide and close orbits for each of the close binaries. It is unclear whether the mutual inclination between the two close binaries is of any physical significance. A quick glance at Table 6.1 should reveal that coplanarity is not an option in most of the known triple systems. In only four of the 42 systems here (HIP 2552, HD 15089 A, HD 68255, HD 198183) is either value of Φ below the 15° threshold. Two more systems (HD 9770, HD 222326) have one Φ value right on the threshold at 15.3° and 17.3°, respectively, and uncertainties may put them below the coplanarity limit. Two systems (HD 209790 and HD 215013) have one possible value of Φ above the 165° of coplanarity for counter-rotating orbits. The current study has produced eight orbits, none of which satisfy the condition for coplanarity. In the remaining 28 systems, coplanarity is not satisfied by either value of Φ. Therefore, it seems that the findings in this study are in line with what is already known: nature shows no tendency towards coplanarity.

Table. 6.1: All Known Mutual Inclinations

HD No.	**log P_{close} (days)**	i_{wide}	Ω_{wide}	i_{close}	Ω_{close}	Φ_1	Φ_2
3196	0.32	49.4	329.2	98.1	133.0	144.4	50.9
35411	0.90	102.8	120.4	85.0	3.4	117.4	65.1
98353	0.41	64.8	130.0	47.8	48.3	67.5	79.1
107259	1.85	51.1	170.8	45.0	116.5	39.9	
129132	2.01	104.6	78.2	56.3	172.2	101.3	94.8
157482	0.35	56.2	143.7	85.9	130.4	32.2	
193322	2.49	46.2	255.2	51	25	85	38

Table. 6.1 – Continued

HD No.	**log $P_{\rm close}$ (days)**	$i_{\rm wide}$	$\Omega_{\rm wide}$	$i_{\rm close}$	$\Omega_{\rm close}$	Φ_1	Φ_2
206901	0.78	108.0	288.8	124.9	258.2	32.0	
HIP 2552	3.76	47.3	174.7	44.6	175.1	2.7	91.9
5408	3.25	54.9	175.0	47.6	329.9	99.2	20.8
9770	3.22	35.2	141.3	22.0	158.0	15.3	56.6
12376	3.67	113.2	168.5	67.0	191.4	51.3	159.0
15089 AB	5.35	87.6	109.8	115.0	0.8	108.2	73.9
15089 A	4.28	115.0	0.8	106.0	175.0	138.6	10.5
19356	0.46	84.0	312.3	82.3	47.0	93.8	
29140 Aa	0.55	69.9	146.7	110.6	287.5	143.3	55.9
29140 Ab	0.90	69.9	146.7	27.2	34.0	82.0	61.9
29316	3.99	133.0	112.5	141.0	20.8	58.9	57.1
40932 A	0.65	96.0	204.9	47.1	50.5	136.7	54.2
40932 B	0.68	96.0	204.9	110.7	111.3	91.2	84.5
68255	3.80	146.0	74.2	142.0	77.0	4.3	72.0
68257	4.34	146.0	74.2	173.9	157.6	33.8	35.2
74956	1.65	105.2	163.6	88.0	27.4	134.8	46.6
74874	3.74	39.0	229.3	50.0	284.8	39.4	
76644	4.16	57.8	4.8	108.0	21.0	52.5	159.6
98230	2.83	121.2	100.9	91.0	318.0	132.3	
98800	2.50	88.3	184.8	66.8	337.6	143.7	34.0
105824	4.44	129.5	122.2	83.1	138.4	48.8	144.3
108500	4.00	143.0	39.0	139.0	164.5	68.1	33.7
131977	2.49	72.5	317.3	110.9	14.1	67.6	126.5
144069	4.22	131.5	47.4	34.5	25.3	98.8	159.9
144217	0.83	87.1	89.5	111.8	294.2	149.5	34.5
170109	5.04	123.0	60.0	108.9	14.4	43.0	112.3
196795	2.96	85.9	128.6	18.2	173.6	73.2	98.8
198183	3.63	133.8	138.6	135.0	150.0	8.2	90.6
199766	4.57	110.9	253.9	92.2	105.2	141.6	35.8
209790	2.91	109.0	85.0	71.9	93.5	38.0	171.9
213051	3.97	141.7	133.2	22.3	20.9	144.6	129.6
215013	4.48	126.9	27.1	42.2	13.8	85.5	165.4
217675	3.48	107.1	32.0	179.9	54.0	72.8	73.0
218658	2.75	30.0	81.0	99.0	107.9	72.2	125.2
222326	3.91	147.5	30.5	150.0	63.8	17.3	59.6

With all the values of Φ in Table 6.1, the observed distribution of mutual inclinations can be compared to the random distribution given by 6.2. With six unambiguous mutual inclinations and 36 ambiguous systems, a total of 78 values can be considered, compared to the 41 values available to Sterzik & Tokovinin (2002). A number of systems have also been updated with new orbital elements since the work by Sterzik & Tokovinin (2002). The distribution of the mutual inclinations has been plotted in Figure 6.1. The new distribution is very similar to the old one, especially at lower values of Φ. A Kolmogorov-Smirnov (K-S) test of the new distribution against the distribution of Sterzik & Tokovinin (2002) gives an agreement probability of P = 0.99. A K-S test for both distributions against the random distribution gives P = 0.09 for the new distribution and P = 0.07 for the Sterzik & Tokovinin (2002) distribution. The agreement with the Sterzik & Tokovinin (2002) distribution signifies that perhaps the true distribution is starting to come into focus. There is strong disagreement with the random distribution of orientations. To that effect, Sterzik & Tokovinin (2002) have calculated many model distributions based on the initial conditions of the gas cloud. As shown in Figure 3 of Sterzik & Tokovinin (2002), the initial conditions that best match observations are an axis ratio of 10:1, a rotational energy of 10% of the overall gravitational energy of the system, and no random kinetic energy. The best-fit model distribution gives an average mutual inclination of $<\Phi> = 73^\circ \pm 5^\circ$. Unfortunately, without access to the modeling routines of Sterzik & Tokovinin (2002), a new $<\Phi>$ cannot be calculated based on the new distribution. However, the similarity between

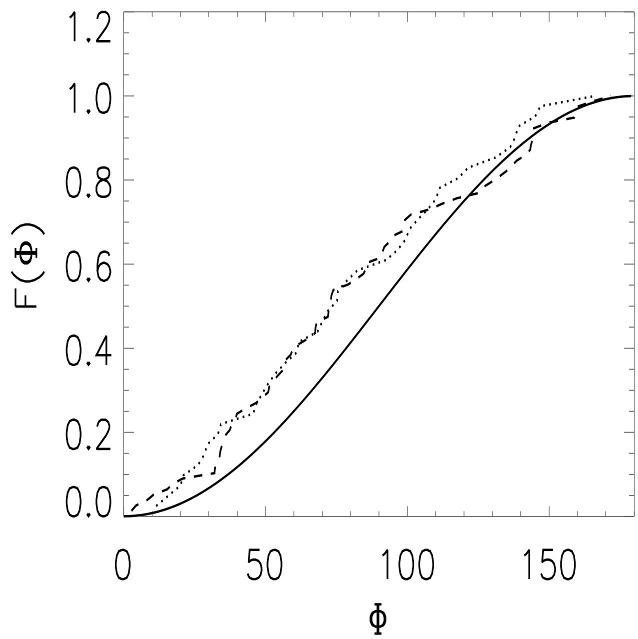

Figure. 6.1: Distributions of mutual inclinations. The solid line represents randomly distributed mutual inclinations. The dashed line represent the distribution calculated in this work, while the distribution of Sterzik & Tokovinin (2002) (dotted line) is presented for comparison.

the new distribution and that of Sterzik & Tokovinin (2002) suggests that the new value of $<\Phi>$ would be similar to $73° \pm 5°$.

Another way to look at the distribution of mutual inclinations is to randomize the value for each system. For each of the 36 ambiguous orbits, one of the two possible values of Φ is randomly chosen as the correct value. These are combined with the six unambiguous values to get an average value of Φ. The minimum possible value of $<\Phi>$ is obtained if the smaller angle is randomly chosen for every system. This value is calculated to be $<\Phi>_{\rm min} = 52°$. In the same way, the maximum value is found to be $<\Phi>_{\rm max} = 106°$. After a few hundred iterations of this randomization, the average value is $<\Phi> = 79° \pm 5°$, a value far from coplanarity. This value should be taken with a note of caution, however. Consider, for instance, two coplanar triple systems, one with $\Phi_1 = 0°$ and the other with $\Phi_2 = 180°$. Although both are coplanar according to the definition of Fekel (1981), the average value of the two-system distribution would be $<\Phi> = 90°$ and would suggest non-coplanarity. For this reason, further analysis was conducted by separating each random set of mutual inclinations into bins of 0° - 90° and 90° - 180° and calculating an average for each. The new minima and maxima of the two bins are $<\Phi_{0-90}>_{\rm min} = 33°$, $<\Phi_{0-90}>_{\rm max} = 64°$, $<\Phi_{90-180}>_{\rm min} = 102°$, and $<\Phi_{0-90}>_{\rm max} = 144°$. The new averages are $<\Phi_{0-90}> = 49° \pm 3°$ and $<\Phi_{90-180}> = 126° \pm 4°$, which still suggest a strong tendency against coplanarity. The results of the randomization are shown in Figure 6.2.

The mutual inclination as a function of the period of the inner orbit is plotted in Figure 6.3. An interesting result from this plot is the lack of possible coplanar systems for inner periods of up to 1000 days. In this region, there is only one system that lies within 30° of either 0° or 180°. This suggests that maybe the capture method is even more important for creating multiple systems with small inner binaries. It has been commented above that the fragmentation method creates large, coplanar systems. The inability of this method to create small coplanar systems makes sense when considering Figure 6.3, as it seems that there are no small coplanar systems in nature. It should be noted that this result is also preliminary because about half of

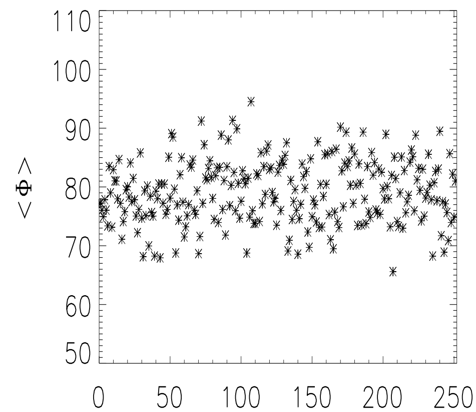

(a)

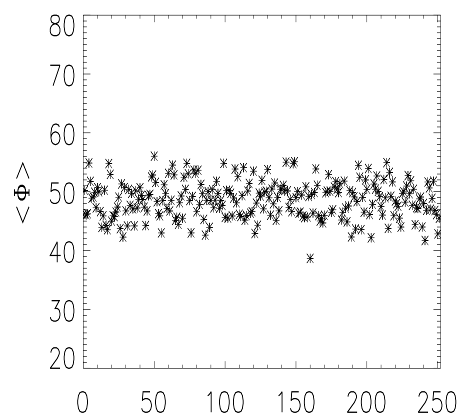

(b)

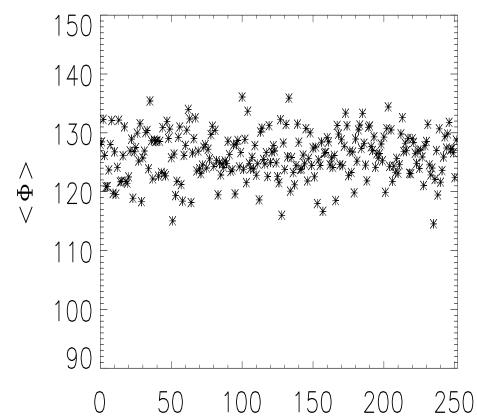

(c)

Figure. 6.2: Mutual inclination randomization. The results of randomizing the mutual inclination for each ambiguous system. Each point represents one iteration of the randomization. The top plot shows the average mutual inclination if all systems are included. The bottom plots show the average mutual inclination of bins of $0° - 90°$ (left) and $90° - 180°$ (right).

the points in Figure 6.3 are false values of Φ from the ambiguity in $\Omega_{\rm close}$. Also, there are still only a small number of systems available.

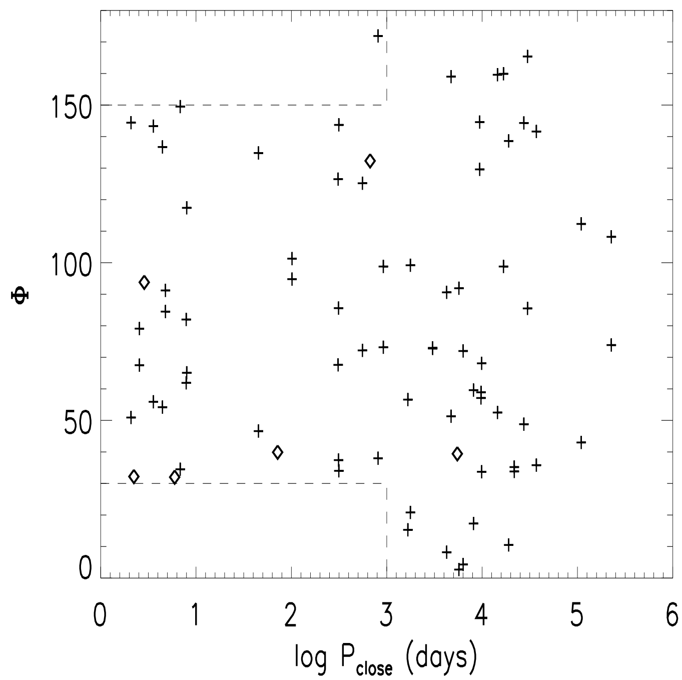

Figure. 6.3: Mutual inclination vs. Period of inner orbit. The diamonds represent the six unambiguous systems, while the crosses represent all ambiguous values of Φ. The dashed line indicates a region between inner binary periods of 0 to 1000 days and within 30° of both $\Phi = 0°$ and $\Phi = 180°$ in which there is a noticeable lack of points.

Another consideration to address is how these systems are affected by Kozai oscillations. According to Kozai (1962), the wide component of a triple system will induce a quadrupolar distortion on the close binary for any system in which the mutual inclination is between a critical angle Φ_c and $180° - \Phi_c$, where Φ_c is found to be 39.2° (Kozai 1962). This effect, explored further by Fabrycky & Tremaine (2007), will cause large oscillations in both the eccentricity and inclination of the close binary on a timescale of:

$$\tau = \frac{2P_{\rm wide}^2}{3\pi P_{\rm close}} \frac{M_{\rm Aa}+M_{\rm Ab}+M_{\rm B}}{M_{\rm B}} (1-e_{\rm wide}^2)^{3/2} \tag{6.3}$$

where P is period, M is mass, and e is eccentricity. As an example, $\tau = 1060$ yr for HD 157482. The oscillation of $i_{\rm close}$ means that Φ also oscillates. The oscillation damps out after a few Gyr (Fabrycky & Tremaine 2007), leaving a circular close binary ($e_{\rm close} = 0$), and a final resting value of $i_{\rm close}$ and Φ. Fabrycky & Tremaine (2007) predict that the resting value of Φ is either $\Phi_{\rm c} = 39.2°$ or $180° - \Phi_{\rm c} = 140.8°$. Fabrycky & Tremaine (2007) also predict that observations should show a buildup of mutual inclinations around 39.2° and 140.8° for systems with 3 days $< P_{\rm close} <$ 10 days. Very few of the systems above satisfy the period constraint, but the ones that do are given in Table 6.2. Of the seven systems, 4 (including 1 of the 2 orbits derived in this work) have at least one value of Φ that is within 10° of either 39.2° or 140.8°. An examination of Figure 6.3 between periods of 3 days (log $P_{\rm close} = 0.48$) and 10 days (log $P_{\rm close} = 1$) shows a possible buildup around 140° and no buildup around 40°, although there are a few points around 30° and 50°. Clearly, more systems are needed to confirm or deny the buildup around the critical angles.

In closing, of the eight systems studied in this project, none can be considered coplanar using either of the ambiguous values of the Φ. Also, the eight mutual inclinations derived in this study have contributed a significant percentage (10%) of the statistics that lead to a distribution function which suggests a highly non-coplanar average mutual inclination. The two systems studied here with a close binary period

Table 6.2. Mutual Inclinations for Selected Close Binaries

HD No.	$P_{\rm close}$ (days)	Φ_1	Φ_2
29140 Aa	3.57	143.3	55.9
29140 Ab	7.89	82.0	61.9
35411	7.99	117.4	65.1
40932 A	4.44	136.7	54.2
40932 B	4.78	91.2	84.5
144217	6.83	149.5	34.5
206901	5.91	32.0	

between three and ten days contribute 28% of the statistics used to test the predictions of Kozai oscillations. These statistics are too preliminary to make an assessment on whether this effect is seen. Finally, the non-coplanar nature of the mutual inclination suggests that the capture method may be more important in the formation of multiple stars than the fragmentation method.

6.2 Evaluation of the Self-Calibration Method

When implementing a new method in any field of study, the first question that must be considered is: Does it work? The most intuitive way to determine whether the SCAM is working is to compare the resulting orbits to previously published work. Luckily, there are three systems for which orbits have already been published. There are also a few cases where the spectroscopic orbital parameters can be compared to the derived visual orbital parameters. Much of the comparison between such parameters was conducted in Chapter 5, and the results were favorable. In almost every case, the visual orbital parameters derived here showed loose agreement (a few σ) with previously published visual and/or spectroscopic parameters. In addition, the most notable case of mismatched parameters was HD 129132, a system for which the data were uncorrected for side-lobe interference. In that case, the failure of the SCAM to match the parameters of the spectroscopic orbit may be a confirmation of the method rather than an indictment. Another way to judge the effectiveness of the method is to examine how well the orbits fit the data. In most cases, the fit is quite pleasing, with very few nights having large residuals. In general, on the first attempt at fitting an orbit, before the errors are scaled to reach a reduced χ^2 of 1.00, the reduced χ^2 is around 0.35. The notable exception in this case is CHARA 96.

The problem with the calculation of the masses is frustrating. The cubic dependence of the masses on the semi-major axis means a measurement of α that is not relatively close to a published value could lead to a large disagreement in the masses. This should not be considered the death-knell of this method, however. There are two ways used to determine if the masses of a system make sense, but there are flaws with each way. First, the semi-major axis of the close binary system can be calculated from the mass sum and mass ratio of the wide orbit. However, this semi-major axis is based on a visual wide orbit that is often a "work in progress" because of the several-year period. Updates on these orbits every few years can significantly change the orbital parameters. A comparison of all the mass sums obtained from orbit fitting with the expected mass sums from the wide orbit is given in Table 6.3. For the three systems with previously published orbits, the mass sum from the previous work is put in the table instead of the expected value. This table shows that the comparison between the two sets of masses is a mixed bag, with some of the masses very similar to the expected value and some very different.

The second way to judge the masses of the system is to compare them with standard masses of stars with the same spectral type. However, the spectra of these systems often do not show all three components, so spectral types given by published sources are guesses. The inconsistency in the masses could also stem from the SCAM itself. An alternative way to judge these masses is to look at the mass-luminosity relation, presented in Figure 6.4, of the stars in the close binaries. These stars span a wide range of spectral types, so it is possible to view the mass-luminosity relation over a large range of masses and magnitudes. Figure 6.4 shows a distinct trend common to the mass-luminosity relation, so perhaps the masses found here are generally reasonable. The only distinct outlier is 13 Ceti Ab, which lies at the bottom right of Figure 6.4. The absolute K-magnitude is lower than expected from the general trend, which further adds to the speculation that $\Delta K_{\rm close}$ for 13 Ceti is underestimated. According to the mass-luminosity relation of Henry & McCarthy (1993) for low-mass stars, a star of this mass should lie at an absolute K-magnitude between 6 and 7.

Side-lobe interference still induces a small amount of error in the visibility amplitude of each packet even at very wide separations. To that effect, it would be useful to know the separation in greater detail, but unfortunately, speckle interferometry cannot provide the precision that is needed to know exactly how much constructive

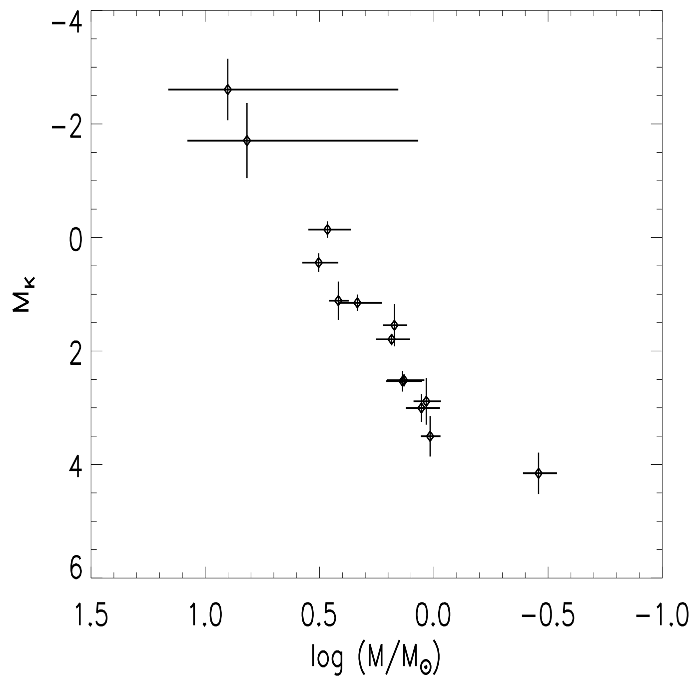

Figure. 6.4: Mass-luminosity relation in K. This is the mass-luminosity for the stars in the close binaries of the targets. The absolute K-magnitudse, M_{K}, are plotted against the logarithmic masses of the components.

or destructive interference is affecting the packets. An observing strategy to help correct this is to devote an entire night to only observing one or two targets and watching the visibilities of the packets change sinusoidally during several hours of observation.

Another source of error that may be contributing to the error on the masses is the inability to definitively identify the two fringe packets. This issue is frustrating, but it will eventually be resolved with future study at the CHARA Array. In the meantime, a strategy that can be used to tackle this problem is to observe a target

Table 6.3. Mass Comparison

System	$P_{\rm close}$ (days)	π (mas)	$\alpha_{\rm close}$ (mas) derived	$\alpha_{\rm close}$ (mas) expected	$M_{\rm sum}$ ($M_\odot$) derived	$M_{\rm sum}$ ($M_\odot$) expected
V819 Her B	2.22	14.7 ± 0.2	0.664 ± 0.0233	0.666 ± 0.0058	2.566 ± 0.274	2.560 ± 0.067
κ Peg B	5.97	28.34 ± 0.88	2.812 ± 0.082	2.520 ± 0.0058	3.655 ± 0.280	2.472 ± 0.078
η Vir A	71.79	13.06 ± 0.84	7.59 ± 0.08	7.36 ± 0.08	5.08 ± 0.78	4.72 ± 0.18
η Ori Aab	7.99	3.62 ± 0.88	0.691 ± 0.060	0.784	14.5 ± 8.5	21.6
55 UMa A	2.55	17.82 ± 0.75	0.927 ± 0.026	0.999	2.88 ± 0.36	3.60
13 Ceti A	2.08	47.51 ± 1.15	1.727 ± 0.142	1.784	1.481 ± 0.202	1.53
HD 129132 Aa	101.61	9.47 ± 0.71	6.69 ± 0.05	6.00	4.56 ± 0.62	3.26

many nights in a row with the exact same setup. Then, at least the relative identities of the packets would be known.

A final problem that may be influencing the results found here is the nature of the magnitude differences. The magnitude difference in the wide orbit tends to shift the calibrated visibilities of the target vertically on plots like Figure 5.1 such that the highest point lies at about $V = 1$. The magnitude difference in the close orbit relies on the difference in visibility between the highest and lowest points of Figure 5.1. Without observing the system constantly for the duration of the close binary orbit, there is no way to know exactly what the highest and lowest visibility points should be, so it the magnitude differences that we have calculated for these systems may represent a lower limit on $\Delta K_{\rm wide}$ and an upper limit on $\Delta K_{\rm close}$ rather than the actual values. In addition, it should be noted that the uncertainties on $\Delta K_{\rm wide}$ are so small that they are below the variability levels of the stars in some cases, so these errors may be underestimated.

Based on the information above, the answer to the question would have to be "yes," the method works reasonably well. Of course, a few problems with the method still exist, but overall, the similarities between the orbits derived here and the previously published information are too strong to be mere coincidence. Even with these problems, the SCAM is a worthwhile venture that can be applied to many more multiple systems.

6.3 Future Work

Re-examination of the MSC (Tokovinin 1997) has provided many more objects that may be feasible targets for the SCAM. If the initial constraint of $\alpha_{\text{wide}} < 250$ mas is relaxed to 1 arcsecond (roughly the field of view of CHARA telescopes), a list of targets with wider separations can be compiled. The separation given by the MSC is a time-specific separation that is often outdated. The Fourth Catalog of Interferometric Measurements of Binary Stars (Hartkopf et al. 2001) can be consulted to find the separation for a more recent epoch. Also, any system with large semi-major axis may be at a point in its orbit where the separation of the components is small enough for application of the SCAM. Table 6.4 gives a list of good targets for which the SCAM may be used in the future. Besides the new constraint on α_{wide}, all of the original criteria from Table 2.1 are used for the targets listed in Table 6.4.

Even if the separation of an orbit is not small enough for simultaneous observation of SFPs, bracketed observation of the two fringe packets can still be conducted without having to move the telescopes. Although it is not the preferred observing strategy, there is nothing inherently wrong with bracketed observing of SFPs.

Table 6.4. Future SCAM Targets by HD No.

1486	28217	61429	184242
1976	29911	70826	185082
2333	33647	71581	185936
3210	34364	82780	187362
7331	36486	83650	193797
8027	37041	100018	198288
10543	38735	142378	203839
12533	41116	151746	205372
16811	42443	153720	208905
21242	43358	165590	210211
23862	45191	178091	214511
23874	54250	179950	216014
26961			

In addition to the objects listed in Table 6.4, about half of the the marginal targets in the original target list (Table 2.2) remain unobserved. These would also be worth observing with the SCAM in the future. It stands to reason that because many of the objects observed already did not produce SFPs, many of the objects in Table 6.4 will also fail to produce SFPs. More importantly, though, is that a handful of them will produce SFPs.

The SCAM will eventually exhaust its usefulness because of the limited number of targets on which it will work. The MSC has been fully examined three times looking for every possible object on which the method can be applied, and the systems in Tables 2.2, 5.40, and 6.4 represent the vast majority of them. However, there are enough targets to keep observers busy for many years. Even if only a handful of the objects in Table 6.4 produce orbits, they will provide important steps in this field of study. After all, at this point only 38 multiple systems (5 new ones from this work) have complementary visual orbits (including the four quadruple systems with two wide/close orbit pairs), even if most of them are ambiguous. The most fertile source for new mutual inclination determinations is the group of multiple systems in which the inner orbit is a close binary. The resolving power of long-baseline interferometry is vital to the study of these systems. CHARA and others are just beginning to unlock the potential of multiple systems with orbit determinations by O'Brien et al. (2011), Muterspaugh et al. (2008), and ten Brummelaar et al. (2011). The more systems CHARA is able to observe with the SCAM, the better we can understand how mutual inclinations are distributed in nature and eventually, how binary and multiple systems form.

References

Bagnuolo, Jr., W. G. et al. 2006, AJ, 131, 2695

Balega, I. I., Balega, Y. Y., Hofmann, K., Tokovinin, A. A., & Weigelt, G. P. 1999, Astronomy Letters, 25, 797

Barlow, D. J., & Scarfe, C. D. 1991, AJ, 102, 2098

Beardsley, W. R., & King, M. W. 1976, PASP, 88, 200

——. 1977, Rev. Mexicana Astron. Astrofis., 3, 85

Benson, J. A., Dyck, H. M., & Howell, R. R. 1995, Appl. Opt., 34, 51

Boden, A. F. 2007, New A Rev., 51, 617

Bodenheimer, P. 1978, ApJ, 224, 488

Bonnell, I. A., & Bate, M. R. 1994, MNRAS, 269, L45

Bowsher, E. 2010, Master's thesis, Georgia State University

Campbell, W. W., & Wright, W. H. 1900, ApJ, 12, 254

Clarke, C. J. 1995, in Evolutionary Processes in Binary Stars, ed. R. A. M. J. Wijers, M. B. Davies, & C. A. Tout (Dordrecht: Kluwer), 31

Cox, A. N., ed. 2000, Allen's Astrophysical Quantities, 4th edn. (Springer-Verlag New York, Inc.)

Csizmadia, S. et al. 2009, ApJ, 705, 436

Demarque, P., Woo, J., Kim, Y., & Yi, S. K. 2004, ApJS, 155, 667

Duquennoy, A., & Mayor, M. 1991, A&A, 248, 485

Dyck, H. M., Benson, J. A., & Schloerb, F. P. 1995, AJ, 110, 1433

Fabrycky, D., & Tremaine, S. 2007, ApJ, 669, 1298

Farrington, C. D. et al. 2010, AJ, 139, 2308

Fekel, Jr., F. C. 1981, ApJ, 246, 879

Hartkopf, W. I., McAlister, H. A., & Franz, O. G. 1989, AJ, 98, 1014

Hartkopf, W. I., McAlister, H. A., & Mason, B. D. 2001, AJ, 122, 3480

Hartkopf, W. I., McAlister, H. A., Yang, X., & Fekel, F. C. 1992, AJ, 103, 1976

Heintz, W. D., ed. 1978, Double Stars (Geophysics and Astrophysics Monographs, Vol. 15, 1st edn. (Dordrecht: Reidel)

Heintz, W. D. 1996, AJ, 111, 408

Henry, T. J., & McCarthy, Jr., D. W. 1993, AJ, 106, 773

Horn, J., Kubat, J., Harmanec, P., Koubsky, P., Hadrava, P., Simon, V., Stefl, S., & Skoda, P. 1996, A&A, 309, 521

Hummel, C. A. et al. 2003, AJ, 125, 2630

Kozai, Y. 1962, AJ, 67, 591

Liu, N. et al. 1997, ApJ, 485, 350

Lloyd, C. 1981, MNRAS, 195, 805

Mayor, M., & Mazeh, T. 1987, A&A, 171, 157

McAlister, H. 2005, Lecture Notes for ASTR 8500: Binary Stars, University Lecture

McDonald, J. M., & Clarke, C. J. 1995, MNRAS, 275, 671

McKibben, W. P. et al. 1998, PASP, 110, 900

Michelson, A. A. 1920, ApJ, 51, 257

Muterspaugh, M. W. et al. 2008, AJ, 135, 766

Muterspaugh, M. W., Lane, B. F., Konacki, M., Burke, B. F., Colavita, M. M., Kulkarni, S. R., & Shao, M. 2006a, A&A, 446, 723

Muterspaugh, M. W., Lane, B. F., Konacki, M., Wiktorowicz, S., Burke, B. F., Colavita, M. M., Kulkarni, S. R., & Shao, M. 2006b, ApJ, 636, 1020

O'Brien, D. P. et al. 2011, ApJ, 728, 111

Perryman, M. A. C. et al. 1997, A&A, 323, L49

Pourbaix, D. et al. 2004, A&A, 424, 727

Press, W. H., Flannery, B. P., Teukolsky, S. A., & Vetterling, W. T. 1986, Numerical Recipes in C: The Art of Scientific Computing

Raghavan, D. et al. 2009, ApJ, 690, 394

Roberts, L. C. et al. 2010, AJ, 140, 744

Scarfe, C. D., Barlow, D. J., Fekel, F. C., Rees, R. F., Lyons, R. W., Bolton, C. T., McAlister, H. A., & Hartkopf, W. I. 1994, AJ, 107, 1529

Skrutskie, M. F. et al. 2006, AJ, 131, 1163

Sterzik, M. F., & Durisen, R. H. 1995, A&A, 304, L9+

——. 1998, A&A, 339, 95

Sterzik, M. F., & Tokovinin, A. A. 2002, A&A, 384, 1030

ten Brummelaar, T. A. 2007, private communication

ten Brummelaar, T. A. et al. 2005, ApJ, 628, 453

——. 2011, submitted

Tokovinin, A. A. 1993, Astronomy Letters, 19, 383

——. 1997, A&AS, 124, 75

van Hamme, W. V. et al. 1994, AJ, 107, 1521

van Leeuwen, F., ed. 2007, Astrophysics and Space Science Library, Vol. 350, Hipparcos, the New Reduction of the Raw Data

Waelkens, C., & Lampens, P. 1988, A&A, 194, 143

Wasson, R. et al. 1994, AJ, 107, 1514

Zizka, E. R., & Beardsley, W. R. 1981, AJ, 86, 1944

Appendices

– A –

Calculations of parameters

A.1 Calculating ρ and θ

In order to find separation (ρ) and position angle (θ) at a specific time for a binary star orbit, it is first necessary to calculate the Thiele-Innes elements, which are better suited to calculating rectangular coordinates than the classical elements α, ω, Ω, i (Heintz 1978):

$$A = \alpha(\cos(\omega)\cos(\Omega) - \sin(\omega)\sin(\Omega)\cos(i)) \tag{A.1}$$

$$B = \alpha(\cos(\omega)\sin(\Omega) + \sin(\omega)\cos(\Omega)\cos(i)) \tag{A.2}$$

$$F = \alpha(-\sin(\omega)\cos(\Omega) - \cos(\omega)\sin(\Omega)\cos(i)) \tag{A.3}$$

$$G = \alpha(-\sin(\omega)\sin(\Omega) + \cos(\omega)\cos(\Omega)\cos(i)) \tag{A.4}$$

The mean angular motion of the orbit μ and the eopch of periastron T can be used to calculate the mean anomaly M, or the mean angular displacement from periastron passage in the orbital plane, at an epoch of t:

$$\mu = \frac{2\pi}{P} \qquad M = \mu(t - T) \tag{A.5}$$

For eccentric orbits, the eccentric anomaly E can be determined from the mean anomaly and the eccentricity e. E is the angle found by drawing a line through the position of the star perpendicular to the semi-major axis of the orbit. This line is then extended to the auxiliary circle that describes the elliptical orbit. E is then the angle between point at which the line intersects the auxiliary circle, the center of the ellipse, and the point at which the line intersects the semi-major axis. E is given by:

$$M = E - \sin E. \tag{A.6}$$

Since E cannot be found directly from M, an iterative method is used until the values of E_{n} converge on the final value of E:

$$E_0 = M + e\sin(M) + 0.5e^2\sin(2M) \tag{A.7}$$

$$M_{\mathrm{n}} = E_{\mathrm{n}} - e\sin(E_{\mathrm{n}}) \tag{A.8}$$

$$E_{\mathrm{n}} = E_{\mathrm{n-1}} + \frac{M - M_{\mathrm{n-1}}}{1 - e\cos(E_{\mathrm{n-1}})}. \tag{A.9}$$

The parameters X and Y can be determined from E and e. X and Y can also be described relative the line drawn to find E. The distance between the point at which that line intersects the orbit ellipse and the point at which the line intersects the semi-major axis is aY, where a is the semi-major axis in astronomical units (AU). The distance between the point at which the line intersects the semi-major axis and the focus at which the more massive star lies is aY. These parameters are given by:

$$X = \cos(E) - e \tag{A.10}$$

$$Y = (1 - e^2)^{0.5}\sin(E) \tag{A.11}$$

In terms of all the parameters described above, the declination x and right ascension y are given by:

$$x = AX + FY \tag{A.12}$$

$$y = BX + GY \tag{A.13}$$

In terms of ρ and θ of the orbit, x and y are:

$$x = \rho \cos \theta \tag{A.14}$$

$$y = \rho \sin \theta \tag{A.15}$$

ρ and θ can then be solved for:

$$\theta = \arctan(\frac{y}{x}) \tag{A.16}$$

$$\rho = \frac{y}{\sin(\theta)} \tag{A.17}$$

The sign of ρ can be used to solve the quadrant error of θ, then the absolute value can be taken to find the final ρ:

$$\theta = \theta + \pi \quad \text{if} \quad \rho < 0 \tag{A.18}$$

$$\rho = |\rho| \tag{A.19}$$

A.2 Calculating B and ψ

The baseline length (B) and position angle (ψ) can be calculated by first finding their spatial frequency value on the (U,V) plane. The (U,V) coordinates can be calculated with knowledge of CHARA's location and the position of the target system for a given epoch.

$$U = B_{\mathrm{E}} \cos(H) - B_{\mathrm{N}} \sin(l) \sin(H) + B_{\mathrm{z}} \cos(l) \sin(H) \tag{A.20}$$

$$\begin{aligned} V = B_{\mathrm{E}} \sin(\delta) \sin(H) - B_{\mathrm{N}}(\sin(l) \sin(\delta) \cos(H) + \cos(l) \cos(\delta)) \\ -B_{\mathrm{z}}(\cos(l) \sin(\delta) \cos(H) - \sin(l) \cos(\delta)) \end{aligned} \tag{A.21}$$

$$H = \mathrm{LST} - \alpha \tag{A.22}$$

where δ and α are the declination and right ascension of the target, $B_{\mathrm{E,N,z}}$ are the three-dimensional geographic coordinates of the baseline at CHARA in the E-W, N-S, and vertical directions (given in Table A.1), l is the latitude of the CHARA Array, H is the hour angle of the target, and LST is the local sidereal time at the epoch of observation. CHARA's latitude is known to be $l = 34.2°$. B and ψ can then be calculated by the following equations:

$$B = (U^2 + V^2)^{0.5} \tag{A.23}$$

and

$$\psi = \arctan(\frac{V}{U}) \ . \tag{A.24}$$

Table A.1. Baseline Coordinates at CHARA

Baseline	$B_{\rm E}$	$B_{\rm N}$	$B_{\rm z}$
W2S1	-69.0845925	199.3424346	0.4706086
W2S2	-63.3361994	165.7610938	-0.1732716
W2E1	-194.4177258	-106.5860627	6.3897083
W2E2	-139.4737376	-70.3722525	3.2731730
W2W1	105.9838176	-16.9848118	11.2681347
W1S1	-175.0684101	216.3272464	-10.7975261
W1S2	-169.3200170	182.7459056	-11.4414063
W1E1	-300.4015434	-89.6012509	-4.8784264
W1E2	-245.4575552	-53.3874407	-7.9949617
E2S1	70.3891451	269.7146871	-2.8025644
E2S2	76.1375382	236.1333463	-3.4464446
E2E1	-54.9439882	-36.2138102	3.1165353
E1S1	125.3331333	305.9284973	-5.9190997
E1S2	131.0815264	272.3471565	-6.5629799
S2S1	-5.7483931	33.5813408	0.6438802

A.3 Normalizing separated fringe packet visibilities

Observing separated fringe packets presents a unique complication in the visiblity calibration process that arises from the magnitude difference between two packets. The resolution of this problem is given by ten Brummelaar (2007). The normalized visibility for a single packet is the fringe amplitude A divided by the mean intensity $<I>$, after dark signal subtraction:

$$V = \frac{A}{< I >}. \tag{A.25}$$

When two packets are observed within the same field of view, what is actually measured involves the mean intensity of both packets:

$$V_1' = \frac{A_1}{< I_1 + I_2 >} = \frac{A_1}{< I_1 > + < I_2 >} \tag{A.26}$$

$$V_2' = \frac{A_2}{< I_1 + I_2 >} = \frac{A_2}{< I_1 > + < I_2 >}. \tag{A.27}$$

An intensity ratio can be defined here:

$$\beta = \frac{< I_2 >}{< I_1 >} = 10^{0.4\Delta m}. \tag{A.28}$$

Substitutions in these equations give:

$$V_1' = \frac{A_1}{< I_1 > +\beta < I_1 >} = \frac{1}{1+\beta}\frac{A_1}{< I_1 >} \tag{A.29}$$

$$V_2' = \frac{A_2}{\frac{<I_2>}{\beta} + < I_2 >} = \frac{\beta}{1+\beta}\frac{A_2}{< I_2 >}. \tag{A.30}$$

Now, the equations can be put in terms of the normalized single-packet visibilities:

$$V_1' = \frac{1}{1+\beta}V_1 \tag{A.31}$$

$$V_2' = \frac{\beta}{1+\beta}V_2. \tag{A.32}$$

Then, the single-packet visibilities can be solved for in terms of the the visibilities that are measured:

$$V_1 = (1+\beta)V_1' \tag{A.33}$$

$$V_2 = \frac{1+\beta}{\beta}V_2'. \tag{A.34}$$

Finally, the ratios of the measured and normalized visibilities can be compared and the formula for correcting data for the effect of the magnitude difference between the packets can be established:

$$\frac{V_1}{V_2} = \beta\frac{V_1'}{V_2'}. \tag{A.35}$$

It should be noted that in this analysis, object 1 is designated as the brighter component.

A.4 Calculating Φ_{min}

This section should start by reproducing equation 5.4:

$$\cos\Phi = \cos i_{\text{wide}}\cos i_{\text{close}} + \sin i_{\text{wide}}\sin i_{\text{close}}\cos(\Omega_{\text{wide}} - \Omega_{\text{close}}) \tag{A.36}$$

When a 180° ambiguity exists for either one or both values of Ω, the + in the above equation become a $\pm$:

$$\cos\Phi = \cos i_{\text{wide}}\cos i_{\text{close}} \pm \sin i_{\text{wide}}\sin i_{\text{close}}\cos(\Omega_{\text{wide}} - \Omega_{\text{close}}) \tag{A.37}$$

The term $\cos(\Omega_{\text{wide}} - \Omega_{\text{close}})$ must be between -1 and 1. Plugging this into equation A.37 gives the following inequalities:

$$\cos\Phi \leq \cos i_{\text{wide}}\cos i_{\text{close}} + \sin i_{\text{wide}}\sin i_{\text{close}} \tag{A.38}$$

$$\cos\Phi \geq \cos i_{\text{wide}}\cos i_{\text{close}} - \sin i_{\text{wide}}\sin i_{\text{close}}. \tag{A.39}$$

A useful trigonometric identity is used to transform the inequalities further:

$$\cos i_{\text{wide}}\cos i_{\text{close}} \pm \sin i_{\text{wide}}\sin i_{\text{close}} = \cos(i_{\text{wide}} \mp i_{\text{close}}) \tag{A.40}$$

$$\cos\Phi \leq \cos(i_{\text{wide}} - i_{\text{close}}) \tag{A.41}$$

$$\cos\Phi \geq \cos(i_{\text{wide}} + i_{\text{close}}) \tag{A.42}$$

Now, applying an arccosine to both sides of inequalities A.41 and A.42 flips the signs of both:

$$\Phi \geq i_{\text{wide}} - i_{\text{close}} \tag{A.43}$$

$$\Phi \leq i_{\text{wide}} + i_{\text{close}} \tag{A.44}$$

Bringing the two inequalities together gives:

$$i_{\text{wide}} - i_{\text{close}} \leq \Phi \leq i_{\text{wide}} + i_{\text{close}} \tag{A.45}$$

From here, the minimum and maximum mutual inclination can be defined:

$$\Phi_{\text{min}} = i_{\text{wide}} - i_{\text{close}} \tag{A.46}$$

$$\Phi_{\text{max}} = i_{\text{wide}} + i_{\text{close}} \tag{A.47}$$

Although both a minimum and maximum can be defined, Fekel (1981) only considered the minimum. No reason is given for this.

– B –
Visibility Curves

For single stars, results are displayed by plotting data points against a curve of visibility versus baseline, where the curve is dependent on the angular diameter of the star. For binary stars, the visibility is dependent not only on the angular diameters and baseline, but also on the separation and magnitude difference between the two stars. Since the separation is continually changing as the stars orbit the barycenter, the binary's visibility cannot be described by a single curve versus baseline. For this reason, we prefer to examine plots of visibility versus epoch like Figure 5.6. However, for another perspective on the quality of the fit, curves of visibility versus baseline have been plotted against our data points in the Figures below. With the best-fit orbital parameters, the separation at a particular epoch can be calculated and combined with the magnitude difference and the angular diameters of the stars to produce these curves. Since the separation changes significantly from one night to the next, there is a plot for each night of data for every target. The separation can even change significantly over the course of the night, so for each plot below, three curves have been generated: one for the first observation epoch, one for the midpoint of the observation epochs, and one for the last epoch. This has been done for the seven of the eight main targets (minus CHARA 96) discussed in Chapter 5.

B.1 V819 Her Revised

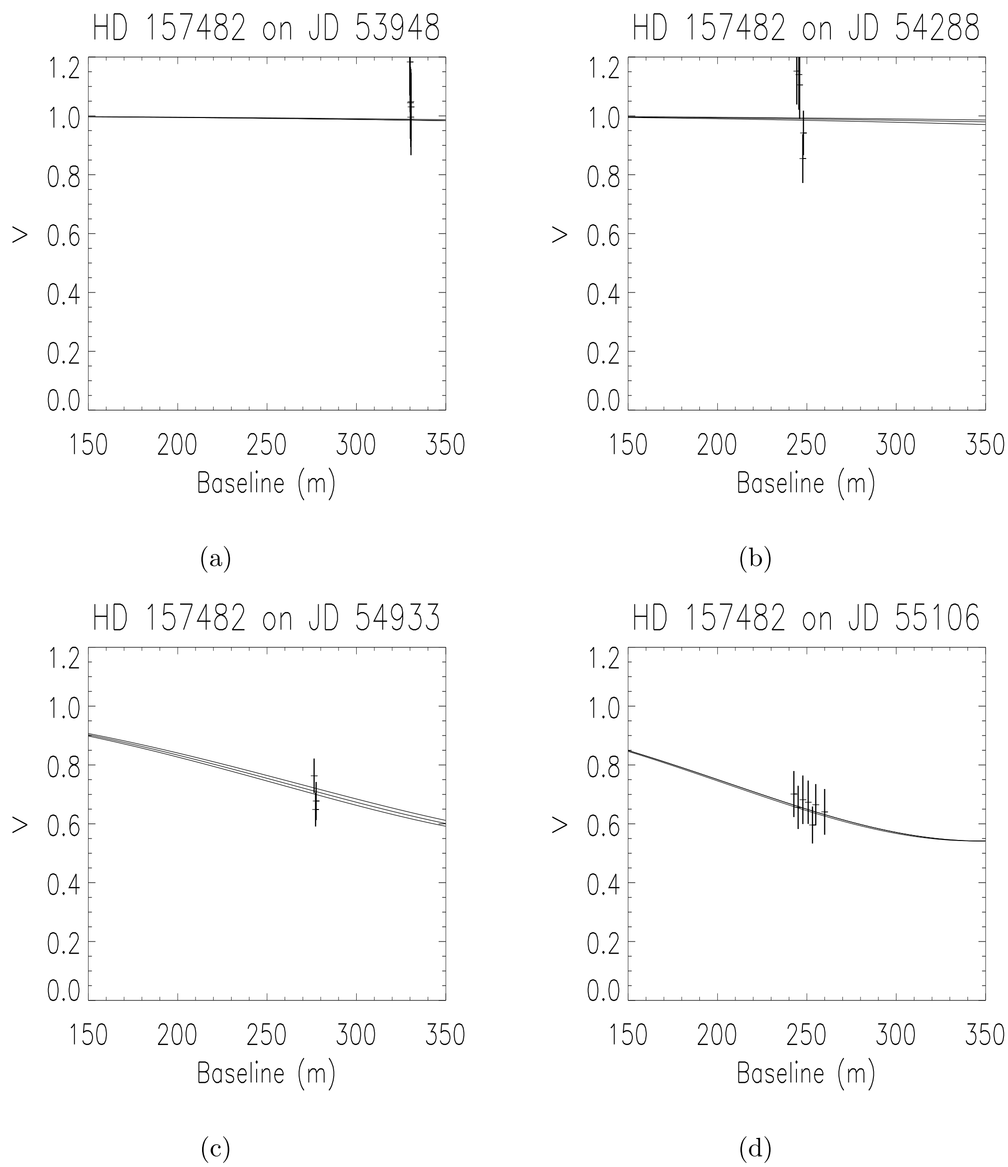

Figure. B.1: Visibility Curves for V819 Her 1

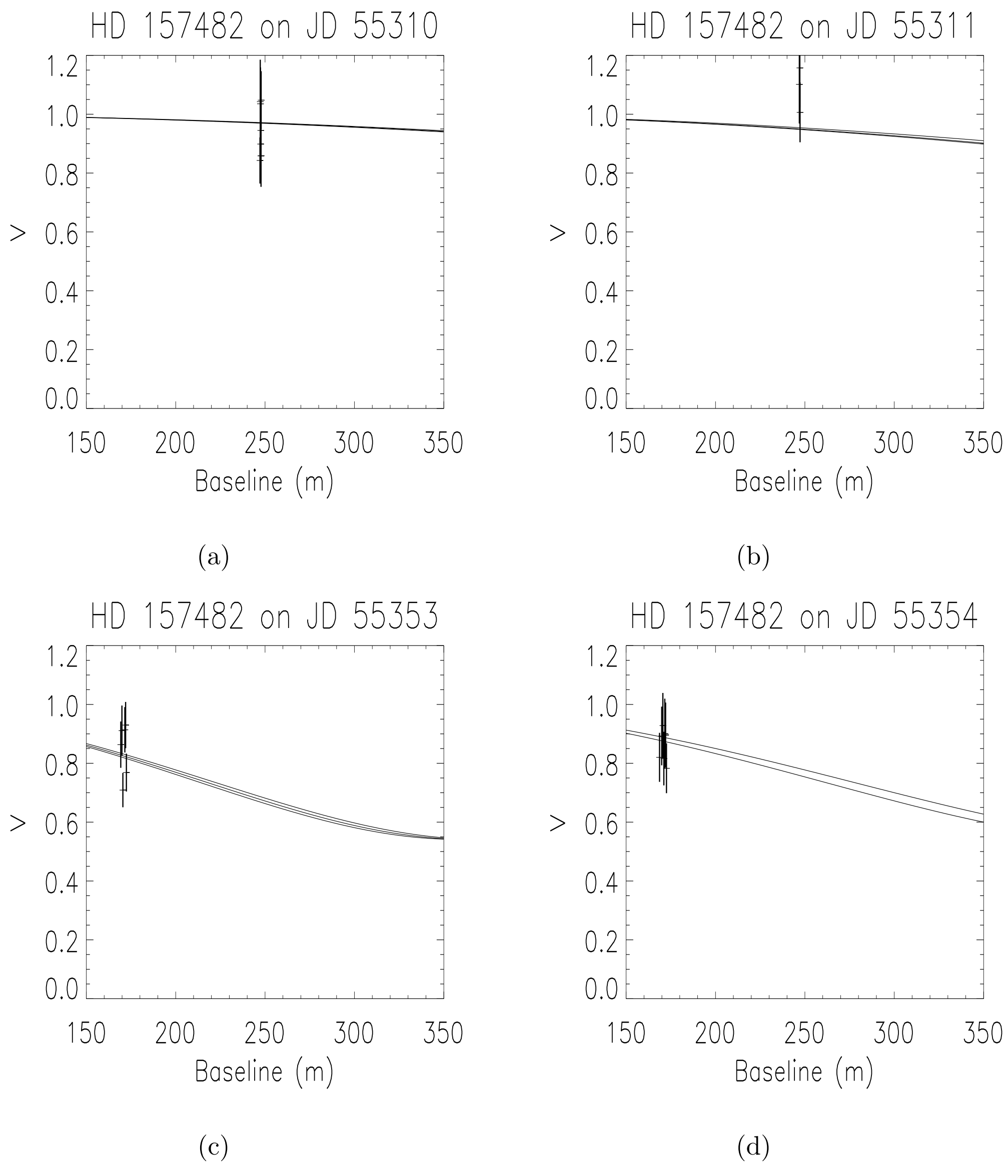

Figure. B.2: Visibility Curves for V819 Her 2

B.2 κ Peg

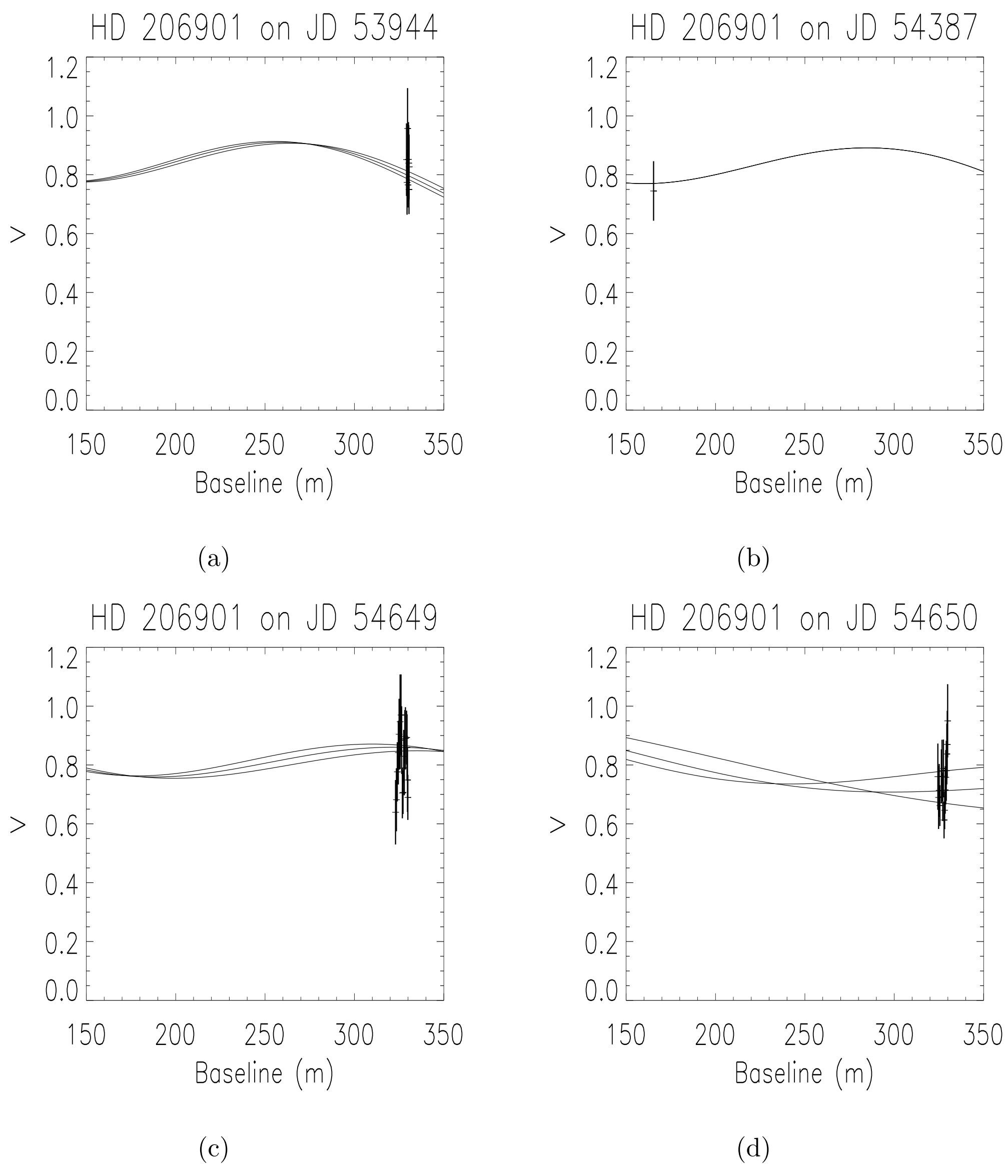

(a) (b) (c) (d)

Figure. B.3: Visibility Curves for κ Peg 1

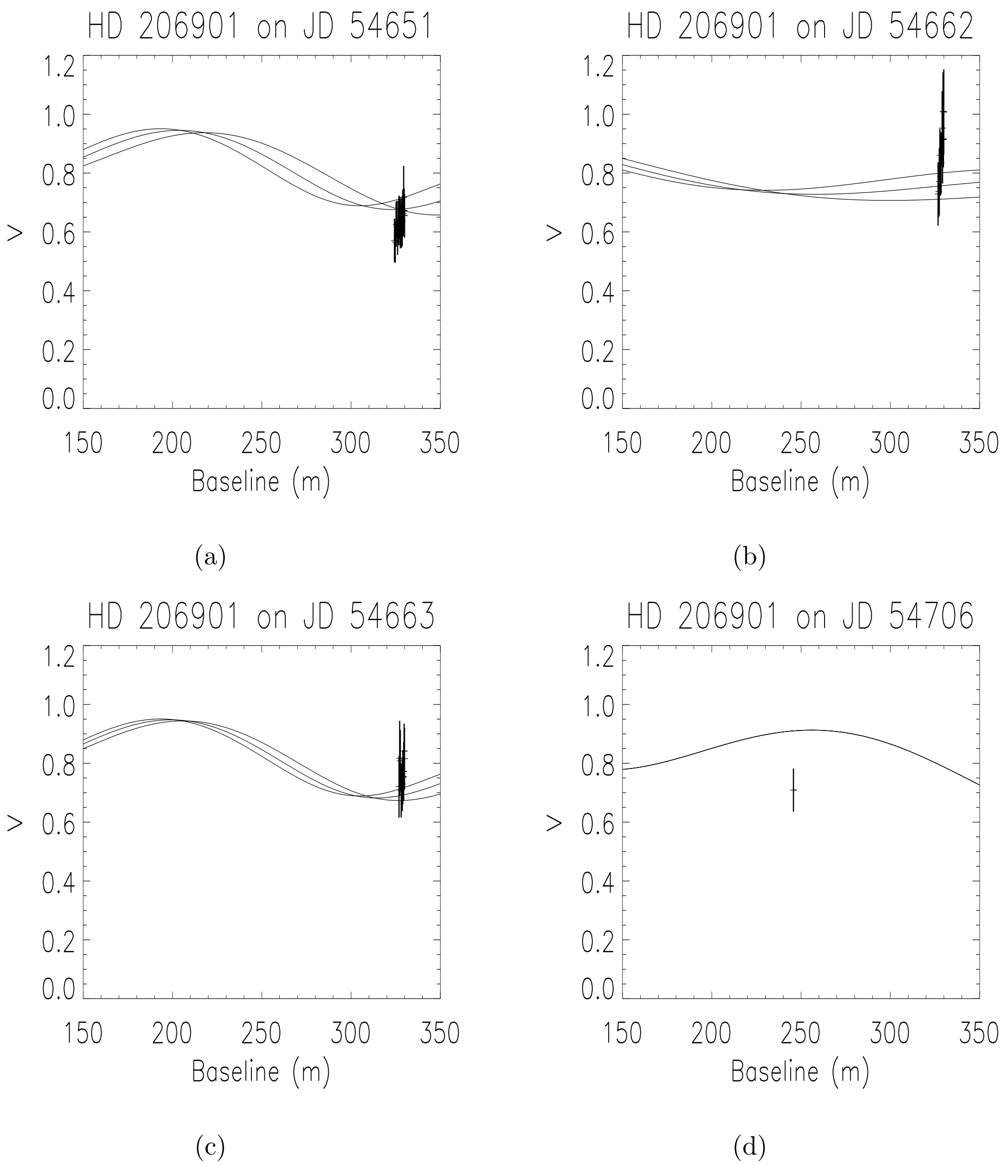

(a) (b) (c) (d)

Figure. B.4: Visibility Curves for κ Peg 2

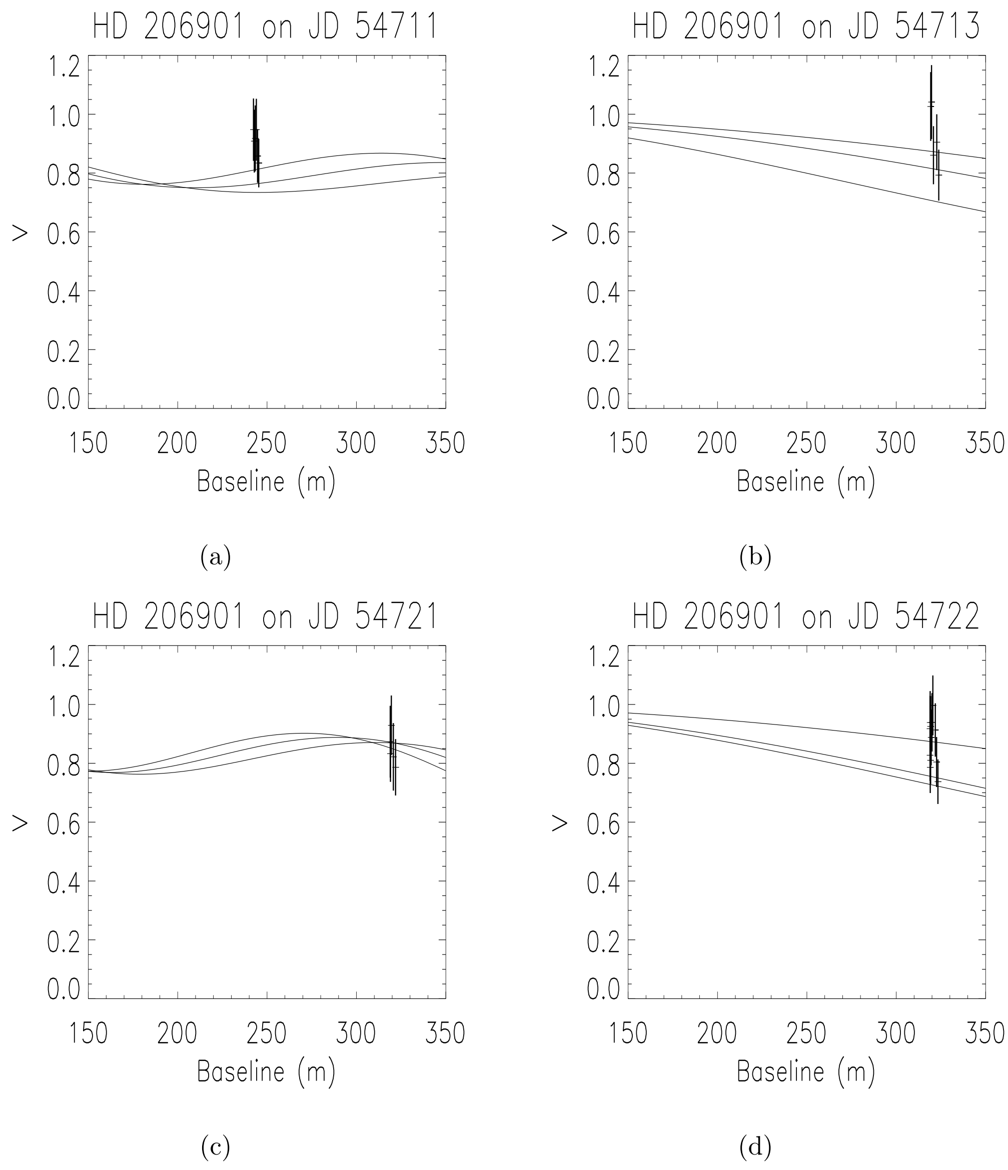

Figure. B.5: Visibility Curves for κ Peg 3

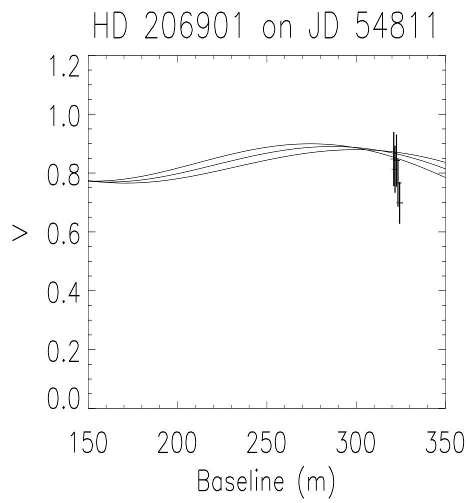

(a)

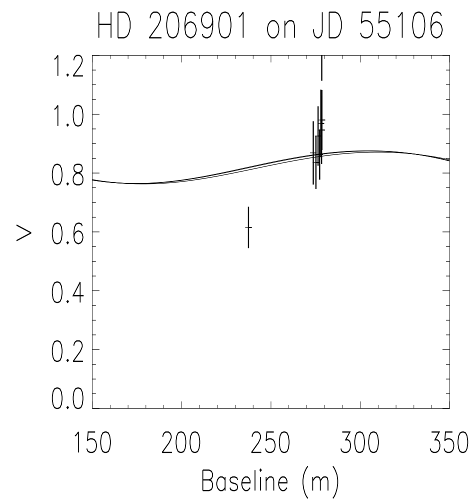

(b)

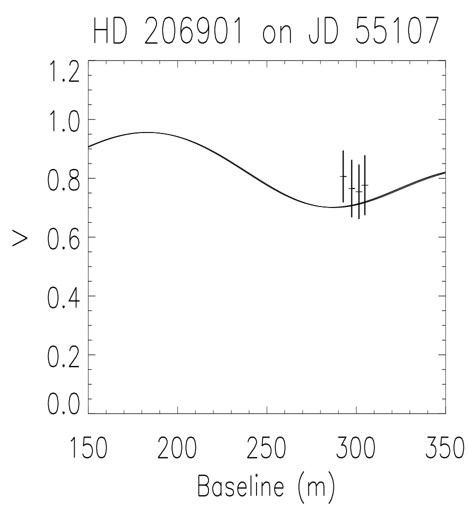

(c)

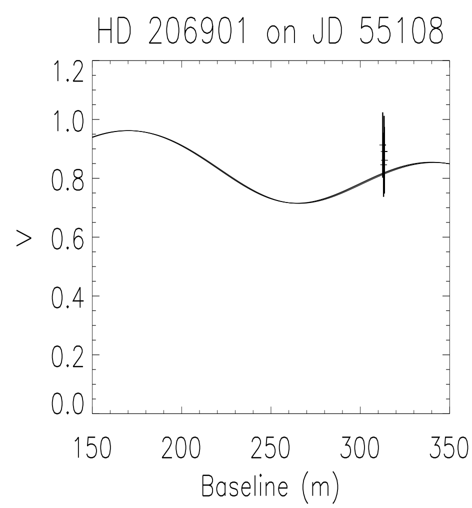

(d)

Figure. B.6: Visibility Curves for κ Peg 4

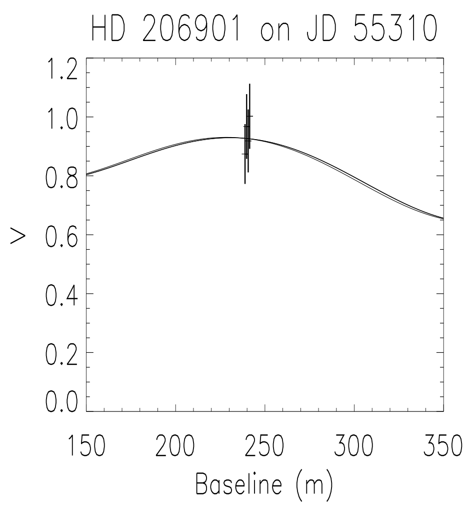

(a)

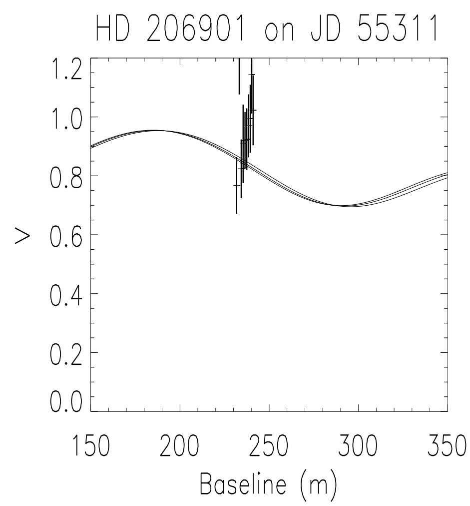

(b)

Figure. B.7: Visibility Curves for κ Peg 5

B.3 η Vir

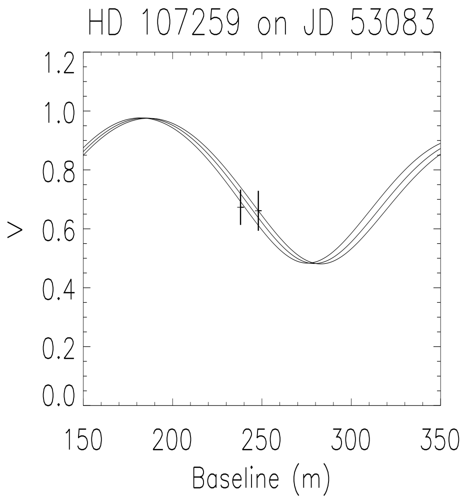

(a)

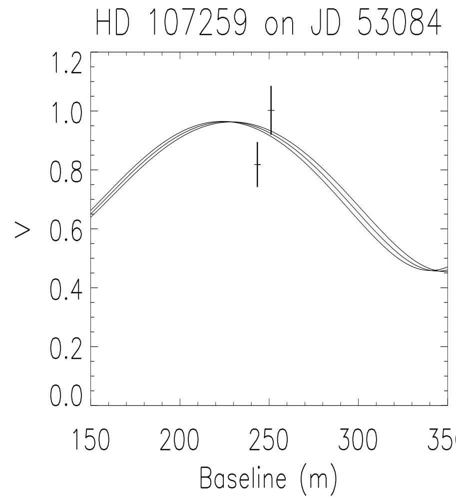

(b)

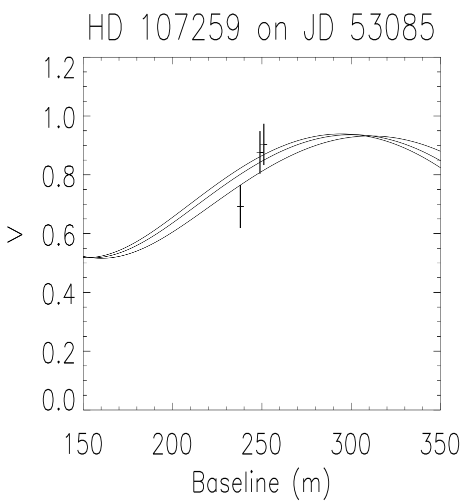

(c)

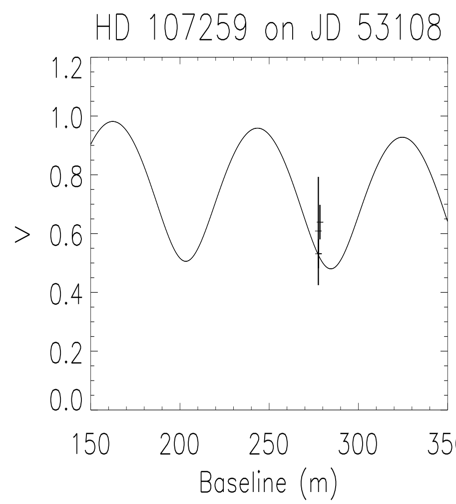

(d)

Figure. B.8: Visibility Curves for η Vir 1

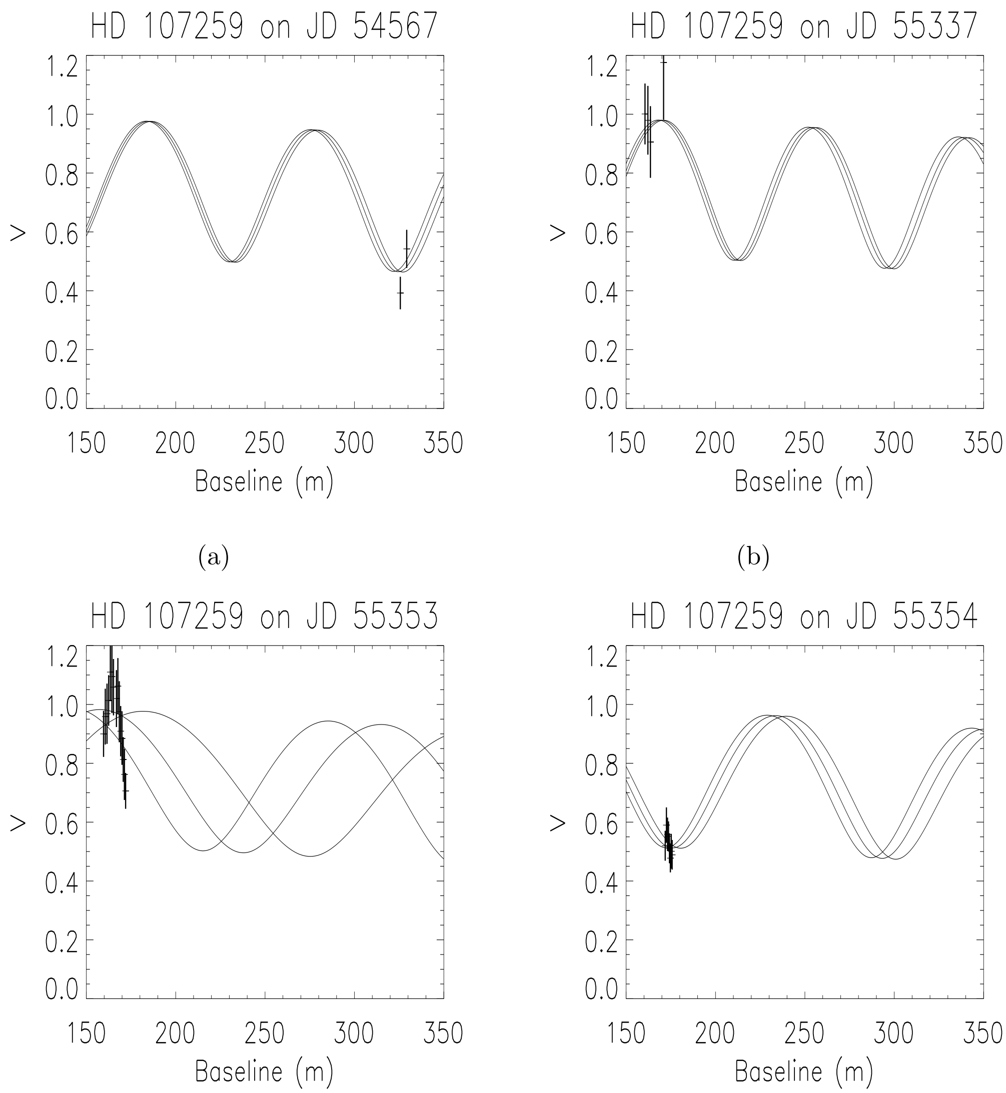

(a) (b) (c) (d)

Figure. B.9: Visibility Curves for η Vir 2

B.4 η Ori

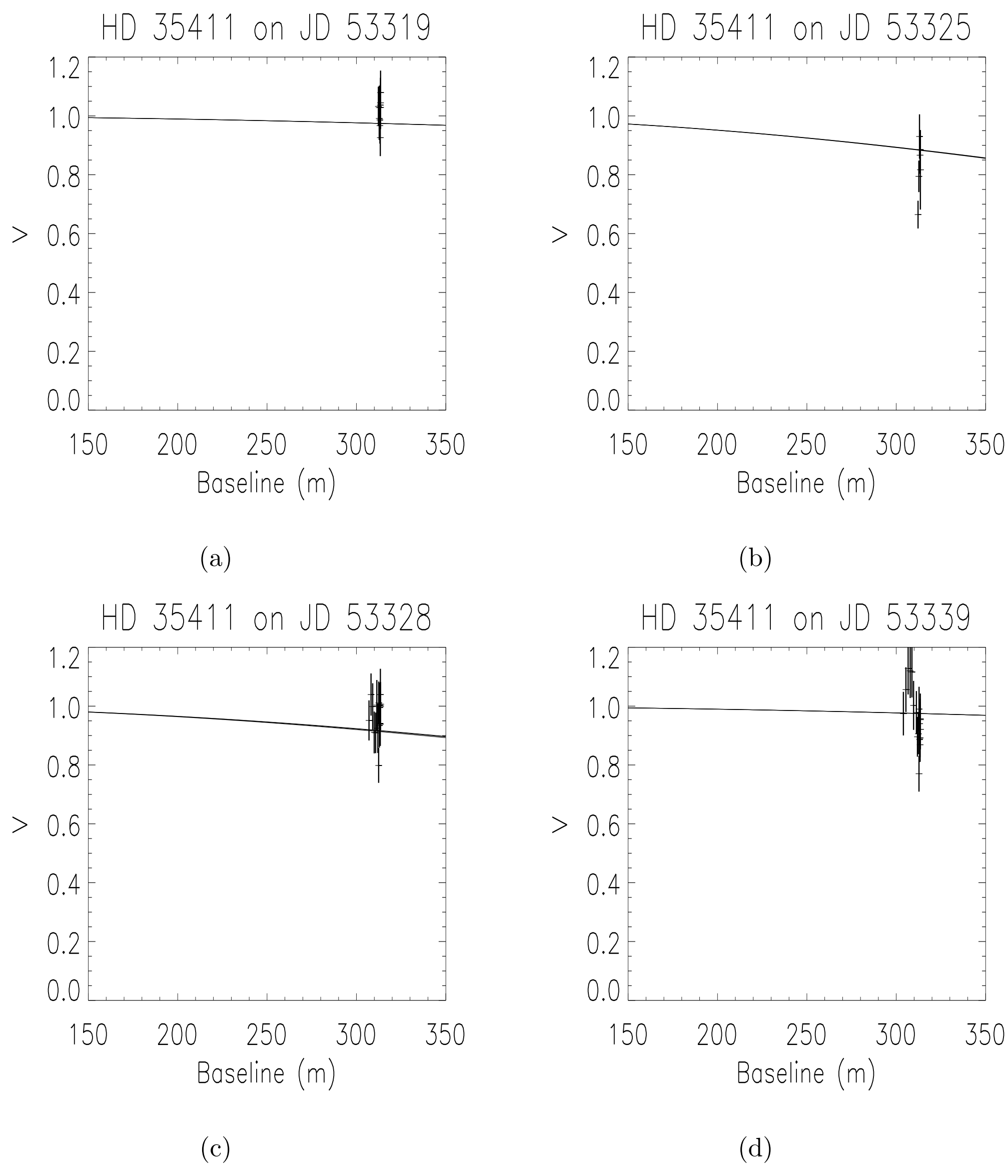

Figure. B.10: Visibility Curves for η Ori 1

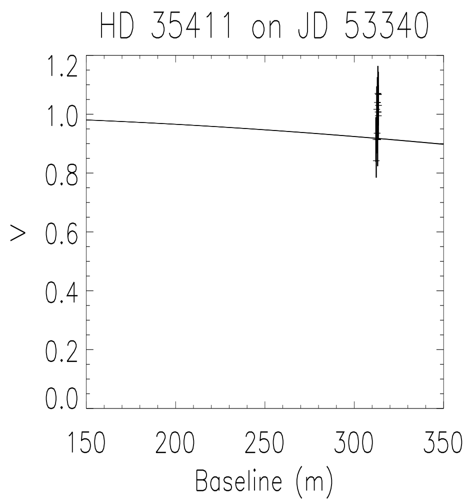

(a)

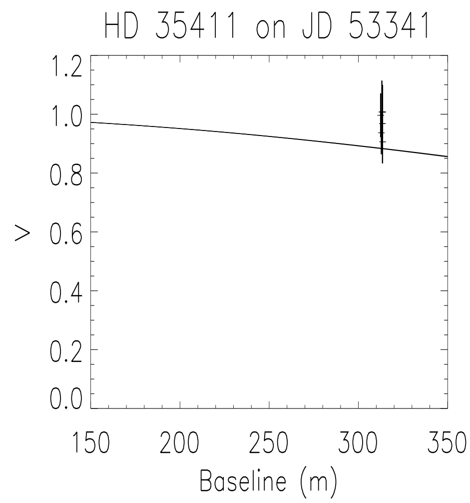

(b)

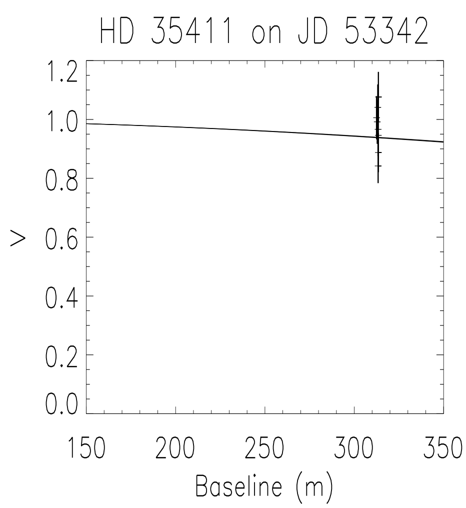

(c)

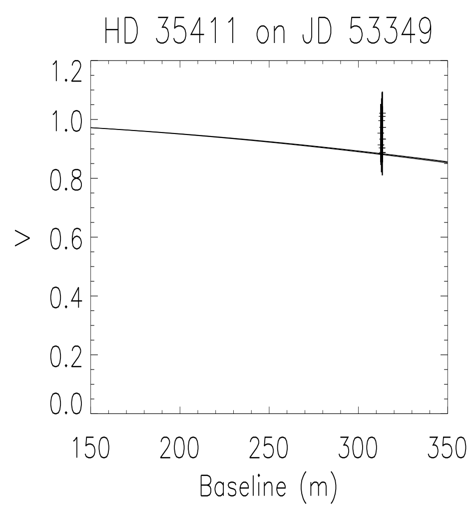

(d)

Figure. B.11: Visibility Curves for η Ori 2

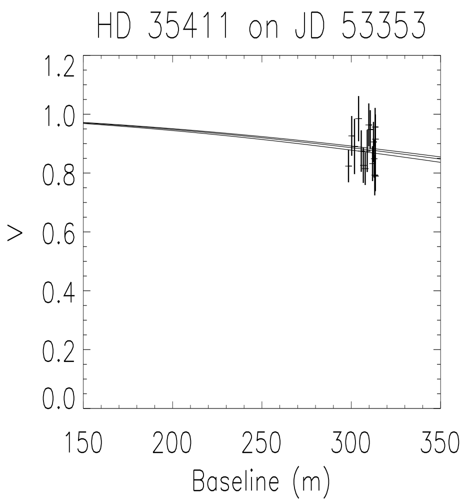

(a)

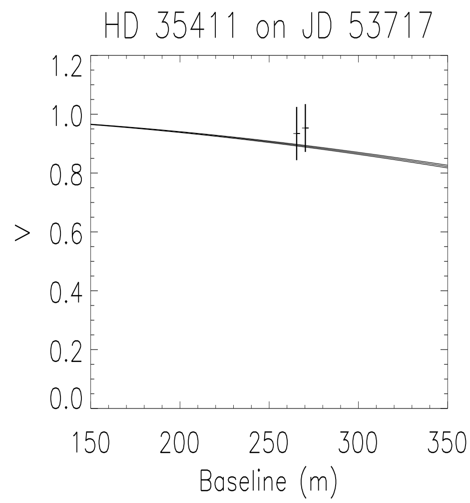

(b)

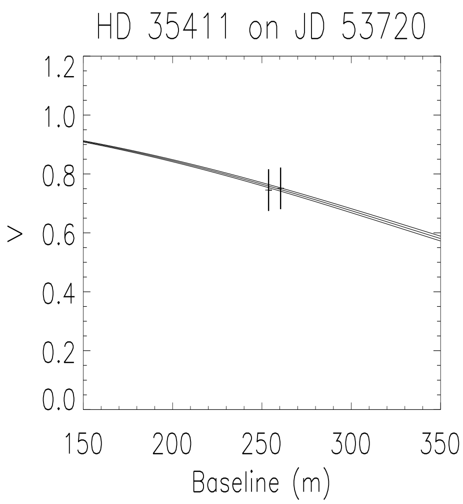

(c)

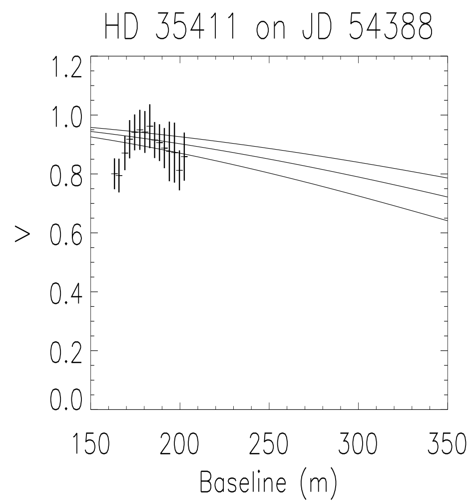

(d)

Figure. B.12: Visibility Curves for η Ori 3

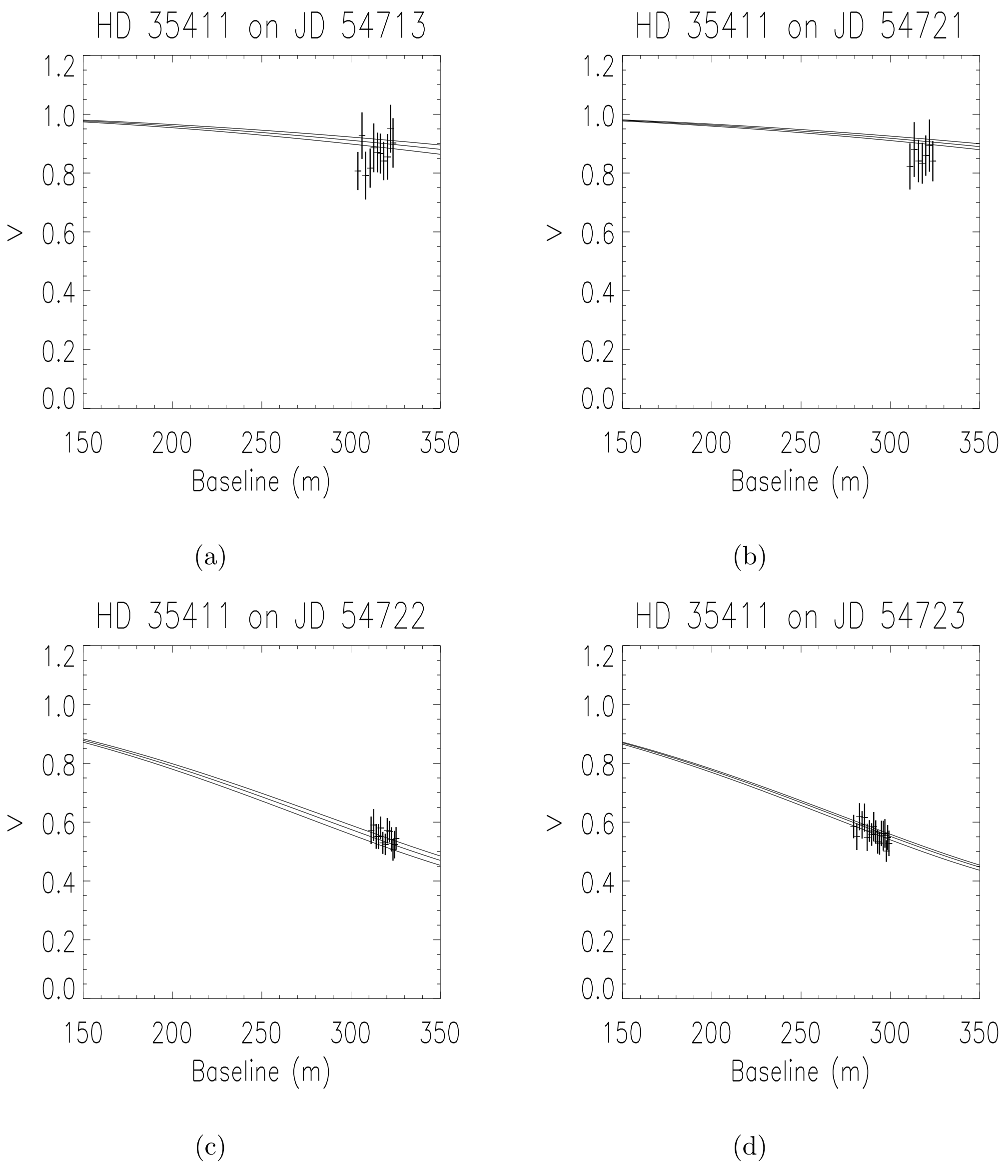

Figure. B.13: Visibility Curves for η Ori 4

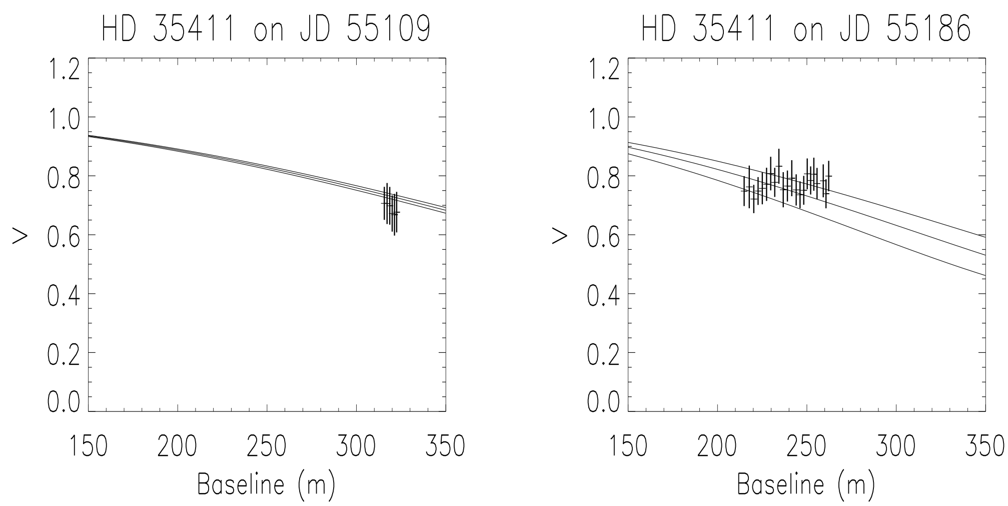

(a) (b)

Figure. B.14: Visibility Curves for η Ori 5

B.5 55 UMa

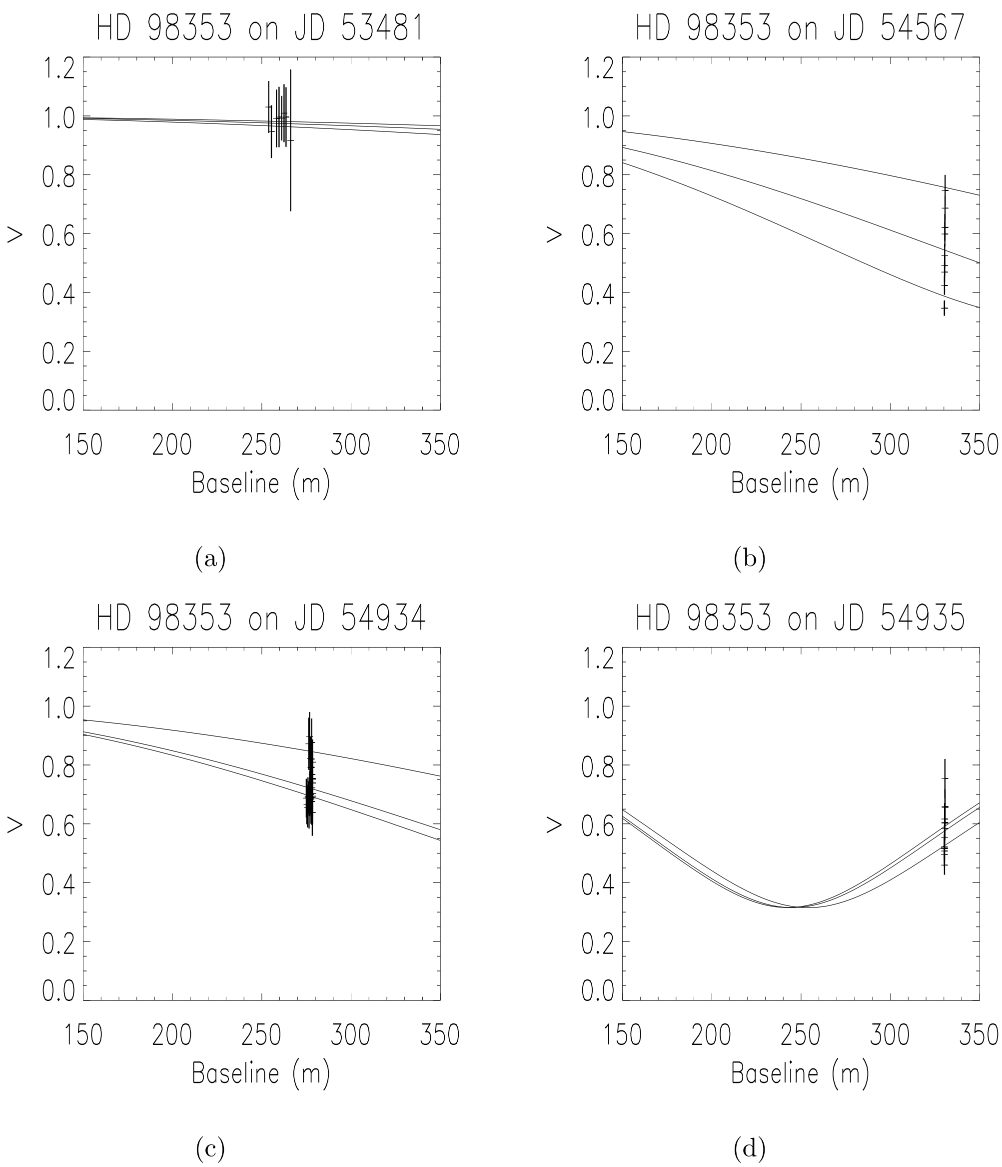

(a) (b)

(c) (d)

Figure. B.15: Visibility Curves for 55 UMa 1

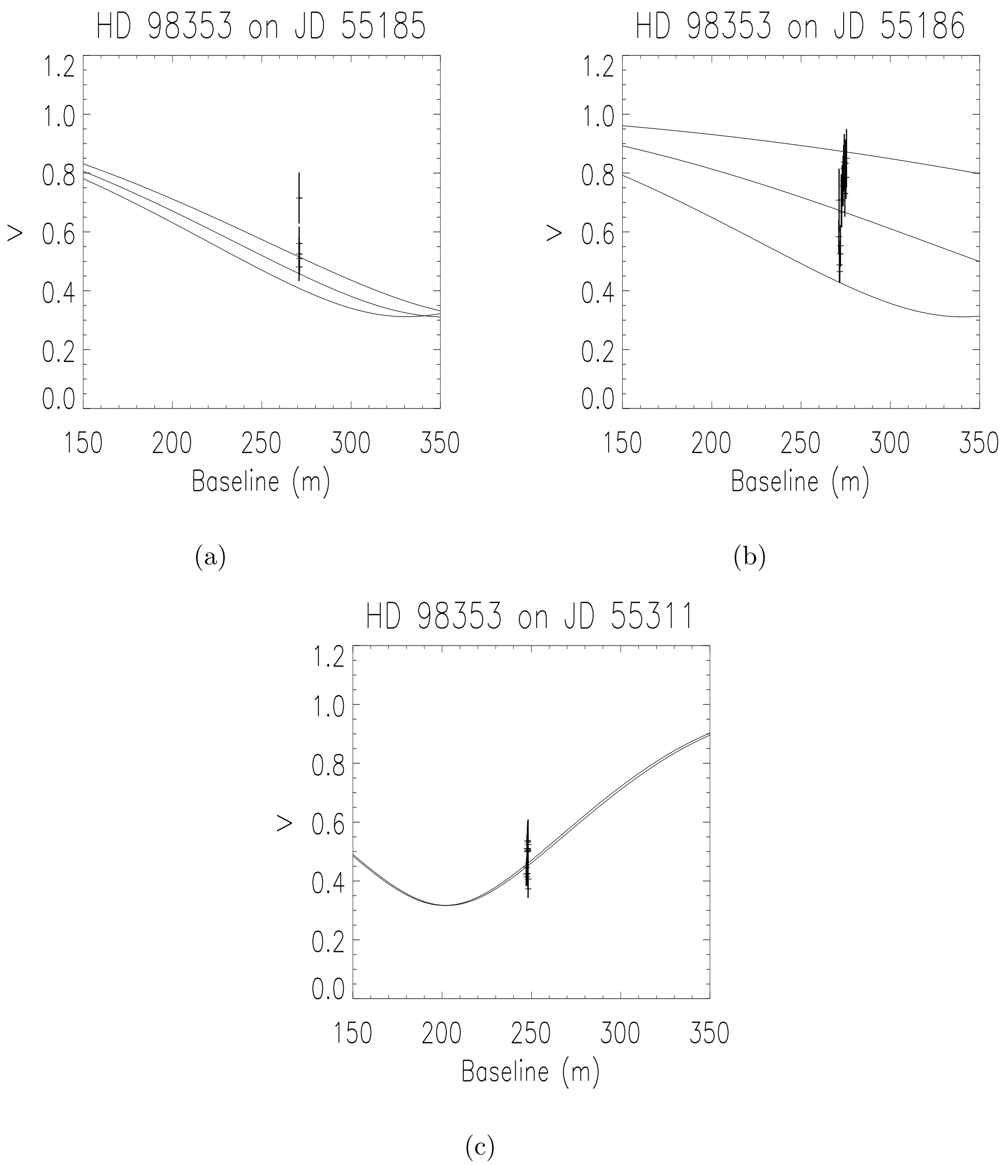

Figure. B.16: Visibility Curves for 55 UMa 2

B.6 13 Ceti

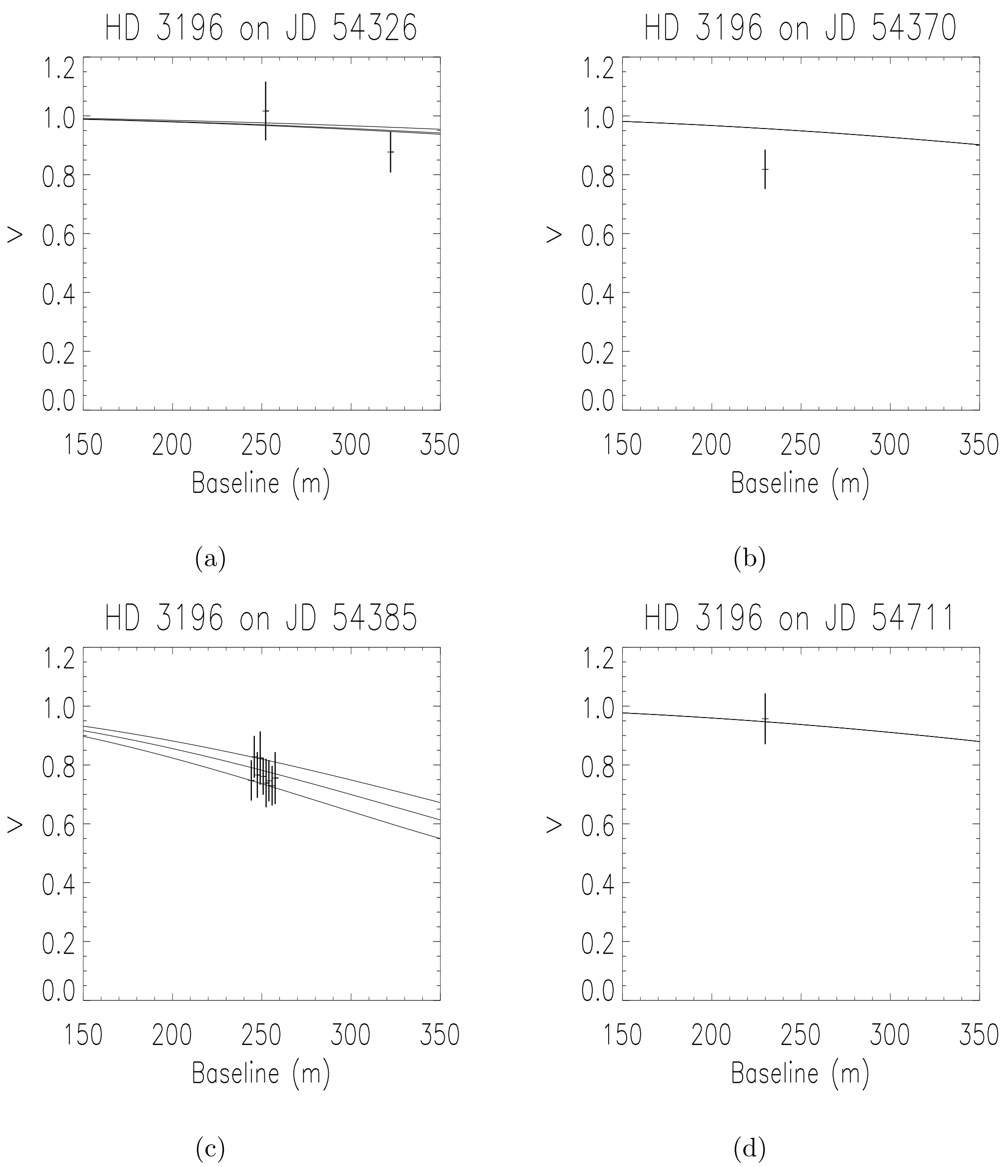

(a) (b) (c) (d)

Figure. B.17: Visibility Curves for 13 Ceti 1

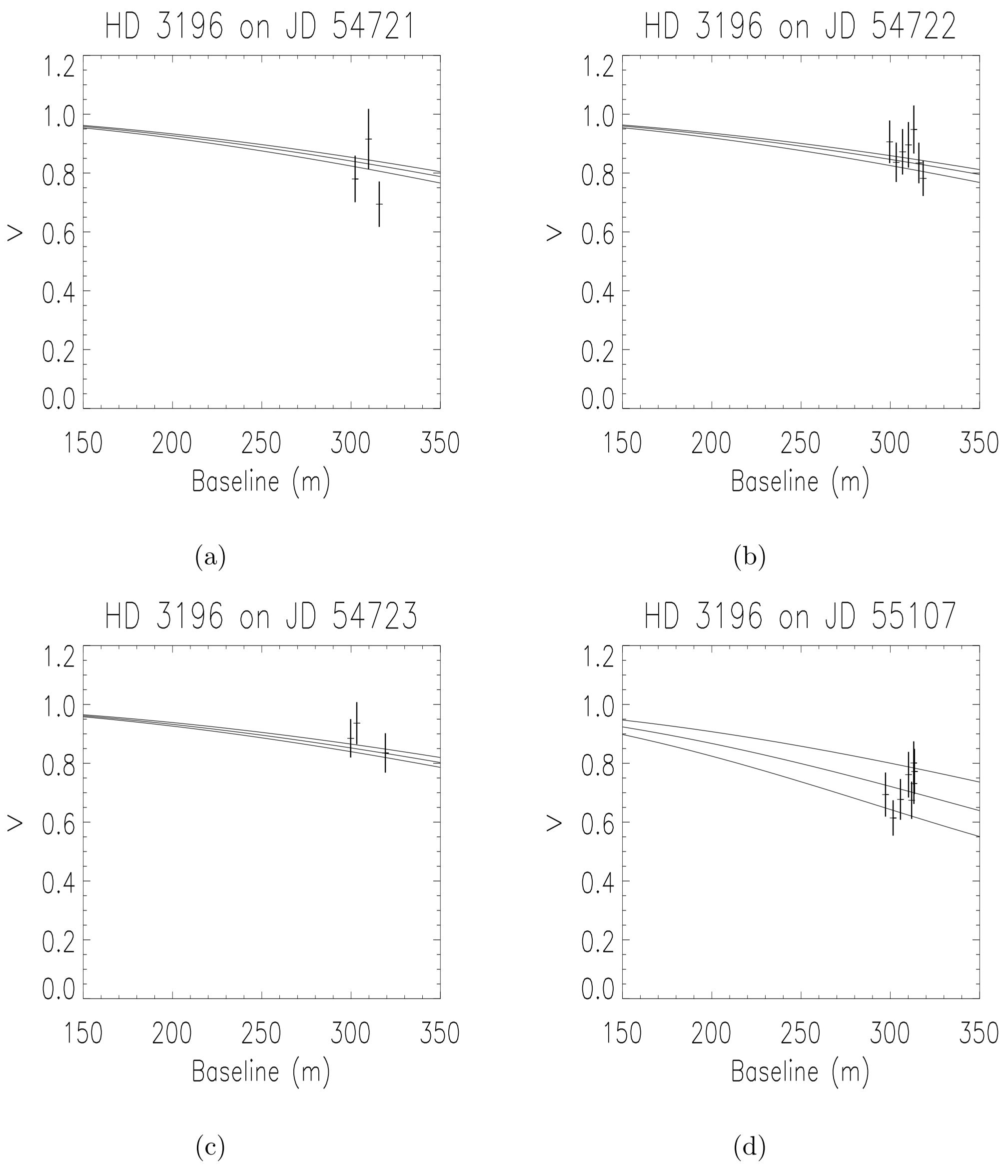

(a) (b) (c) (d)

Figure. B.18: Visibility Curves for 13 Ceti 2

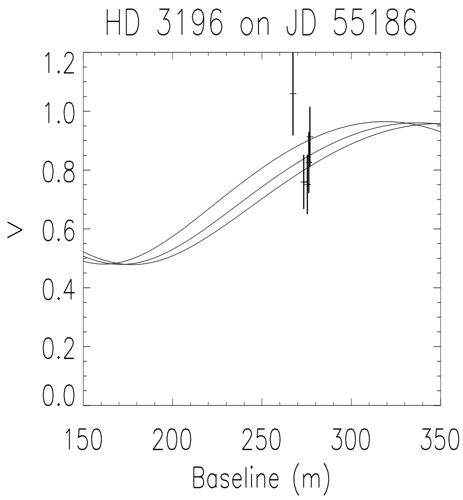

(a)

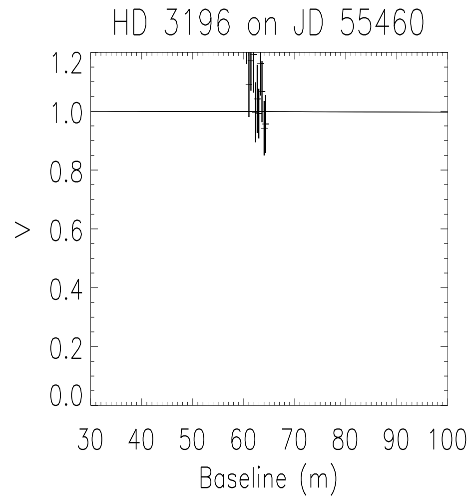

(b)

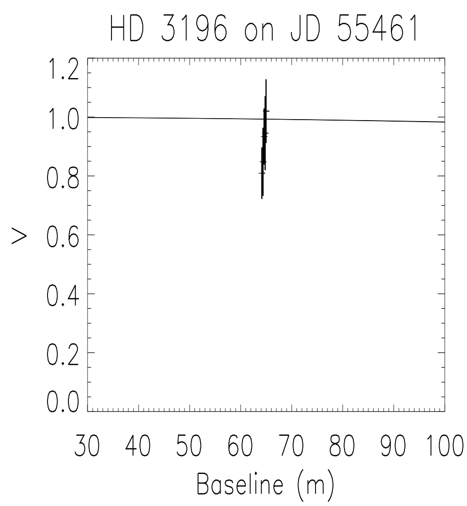

(c)

Figure. B.19: Visibility Curves for 13 Ceti 3

B.7 HD 129132

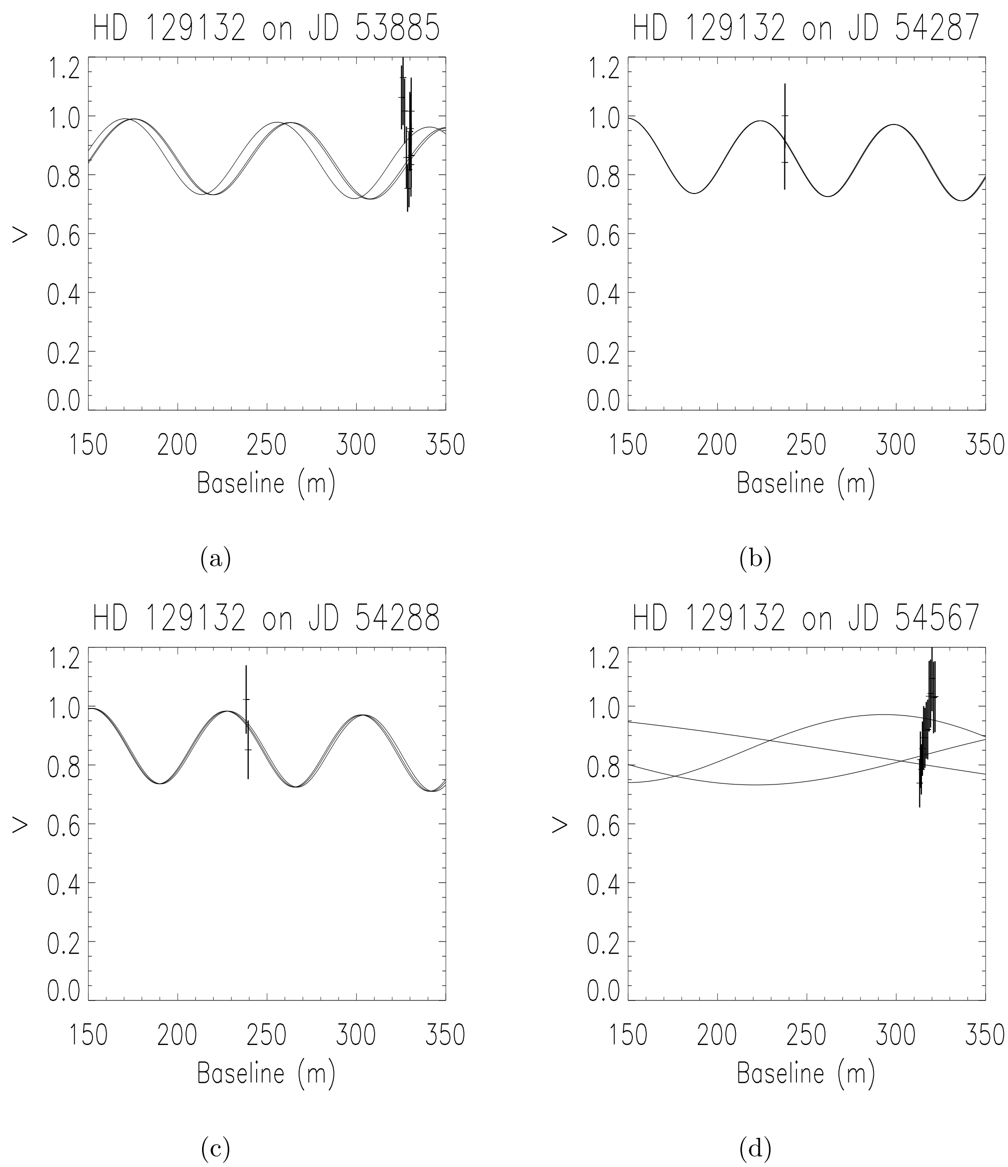

Figure. B.20: Visibility Curves for HD 129132 1

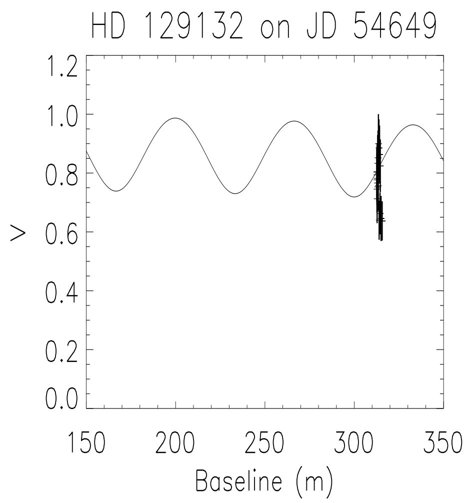

(a)

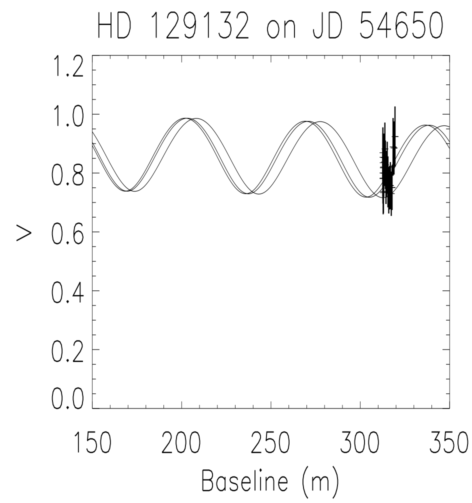

(b)

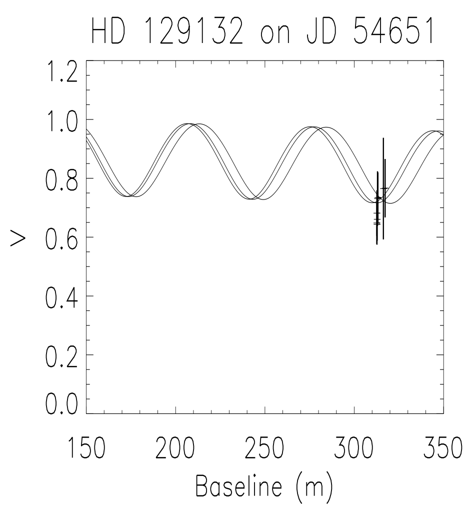

(c)

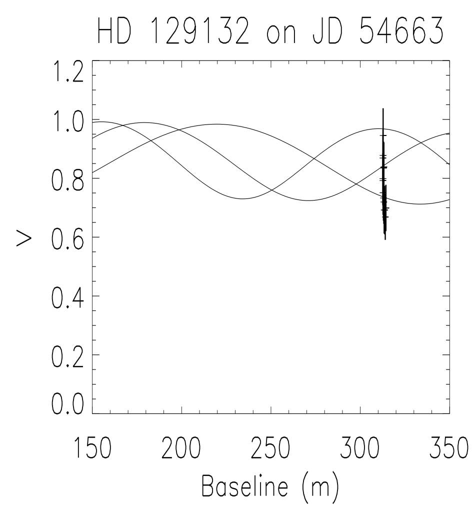

(d)

Figure. B.21: Visibility Curves for HD 129132 2

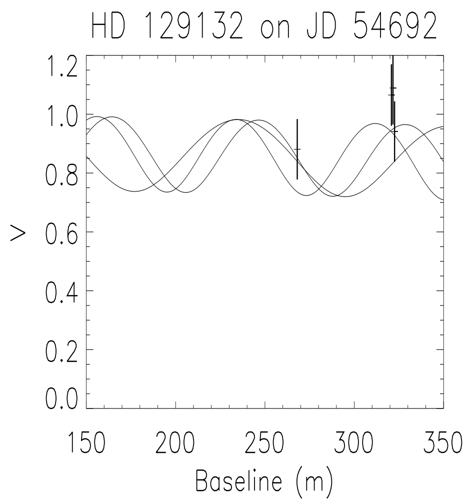

(a)

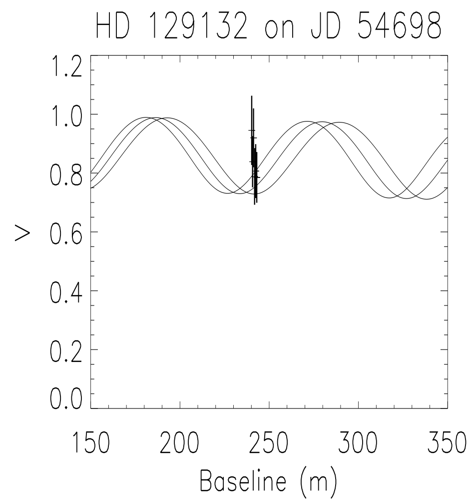

(b)

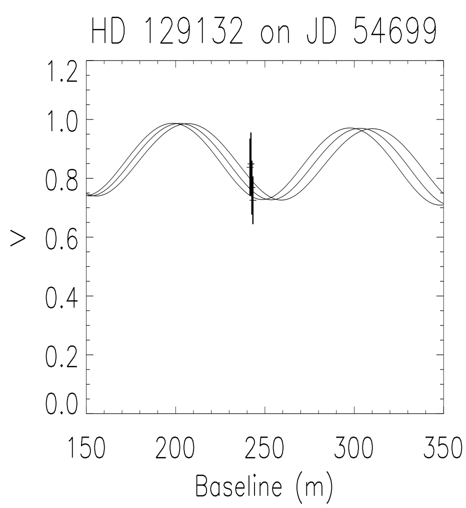

(c)

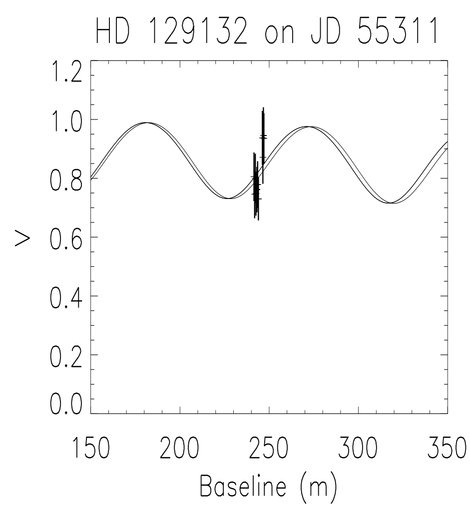

(d)

Figure. B.22: Visibility Curves for HD 129132 3

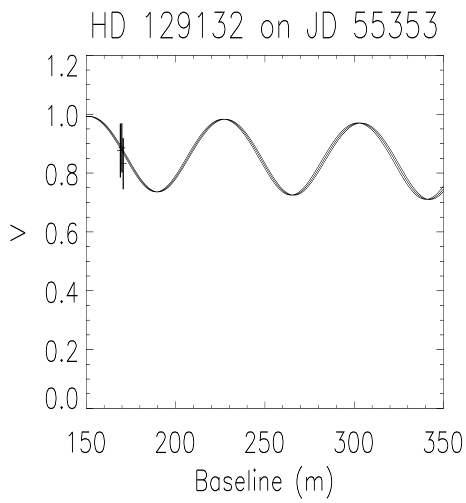

(a)

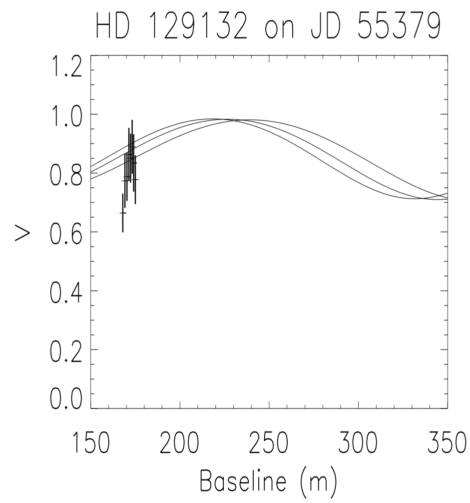

(b)

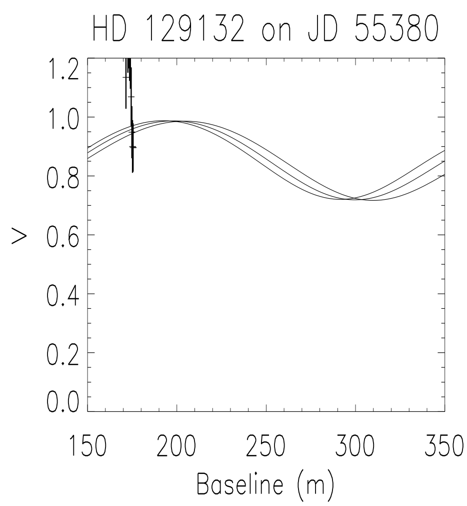

(c)

Figure. B.23: Visibility Curves for HD 129132 4

– C –
Orbit Plots

The following Figures show the orbits of the close binaries of the eight targets. These are presented in order to give an idea of how the orbit looks on the sky and how good the phase coverage is for each orbit.

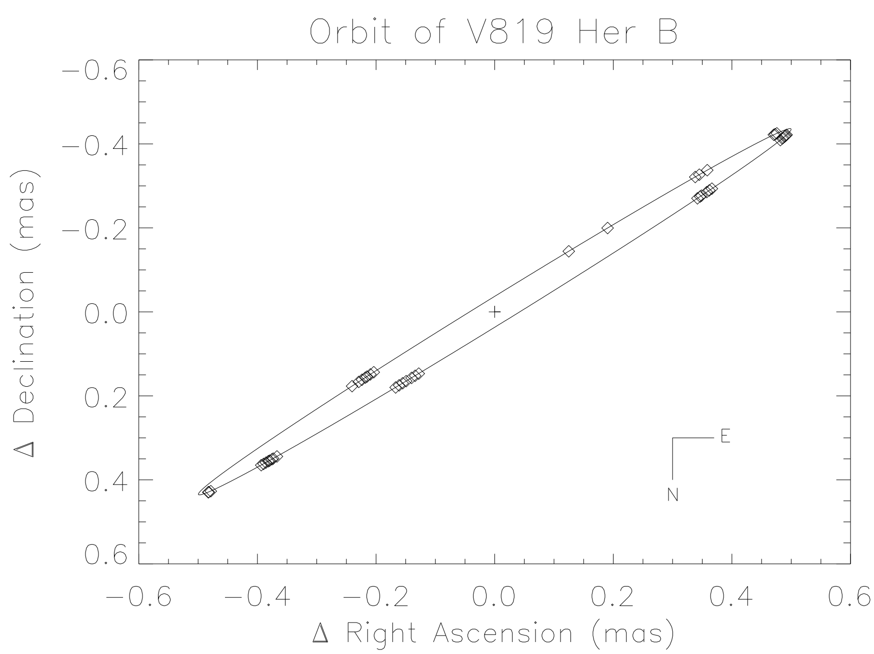

Figure. C.1: V819 Her B orbit. The diamond are the epochs of observation for the target.

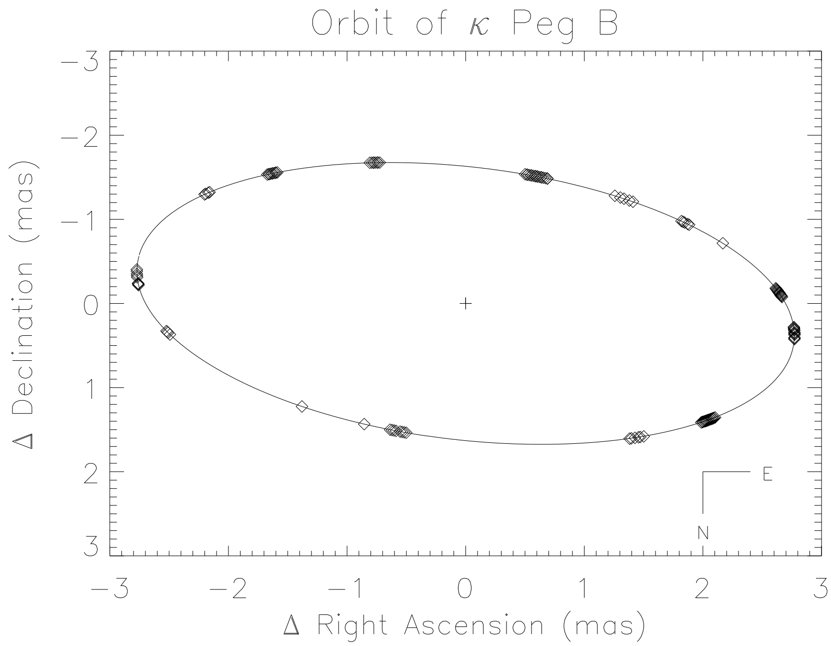

Figure. C.2: κ Peg B orbit

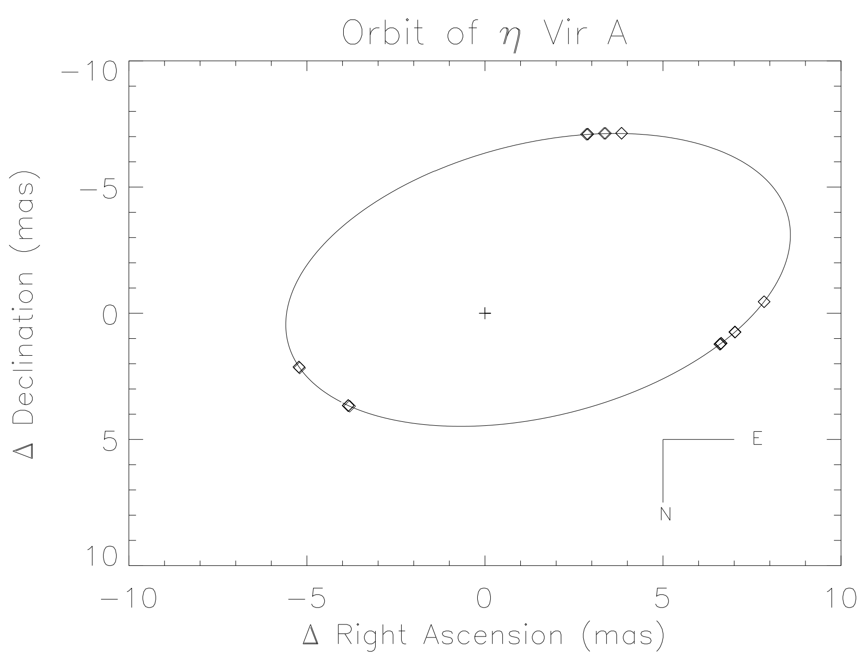

Figure. C.3: η Vir A orbit

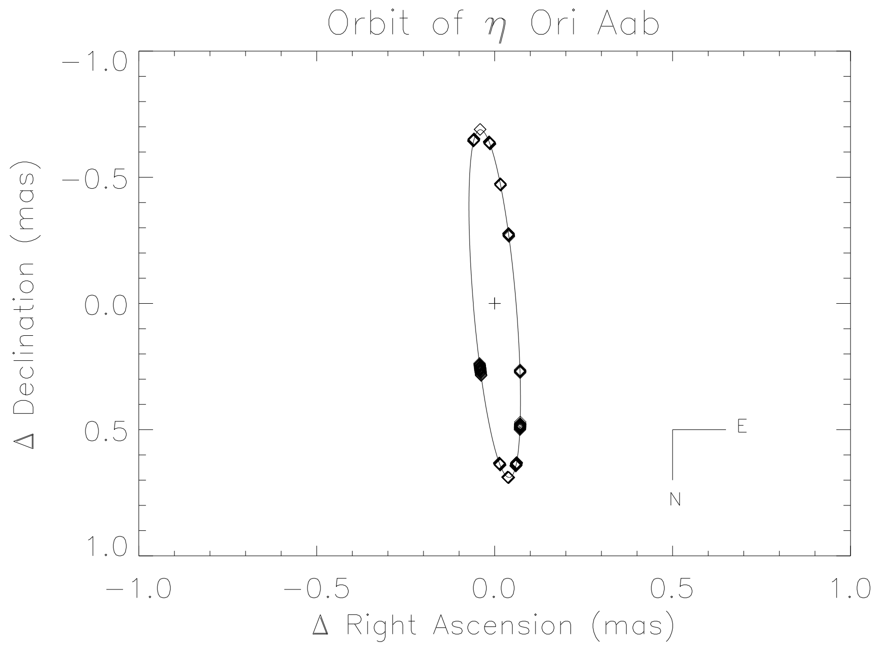

Figure. C.4: η Ori Aab orbit

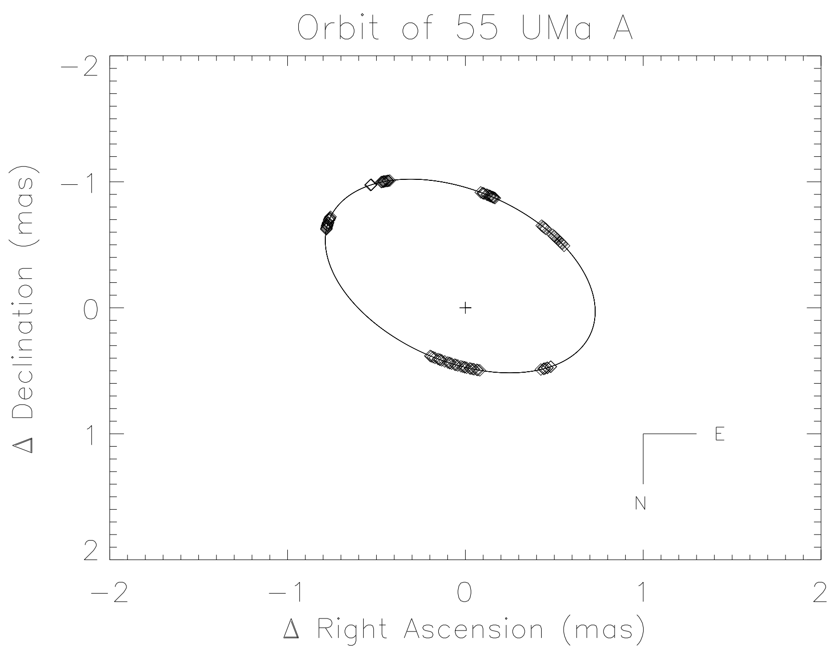

Figure. C.5: 55 UMa A orbit

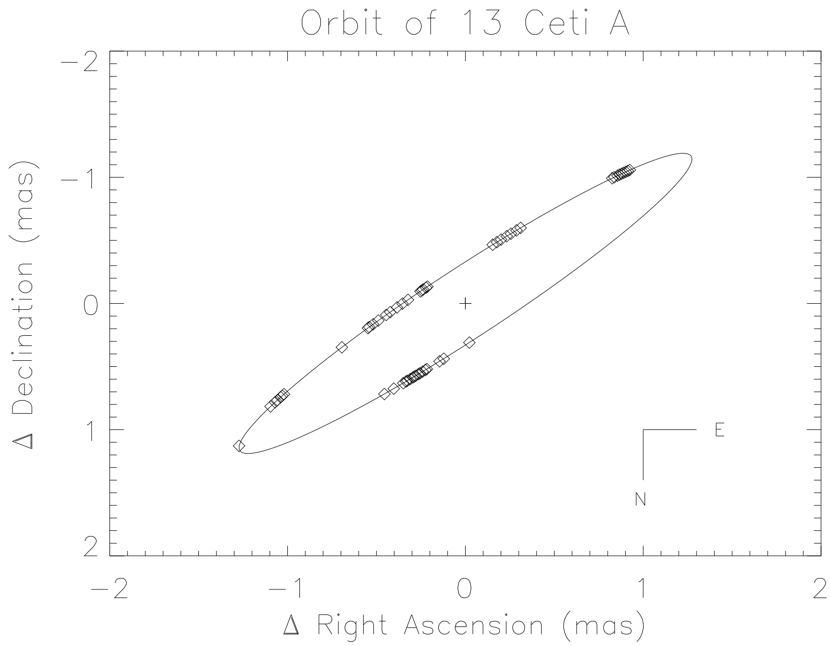

Figure. C.6: 13 Ceti A orbit

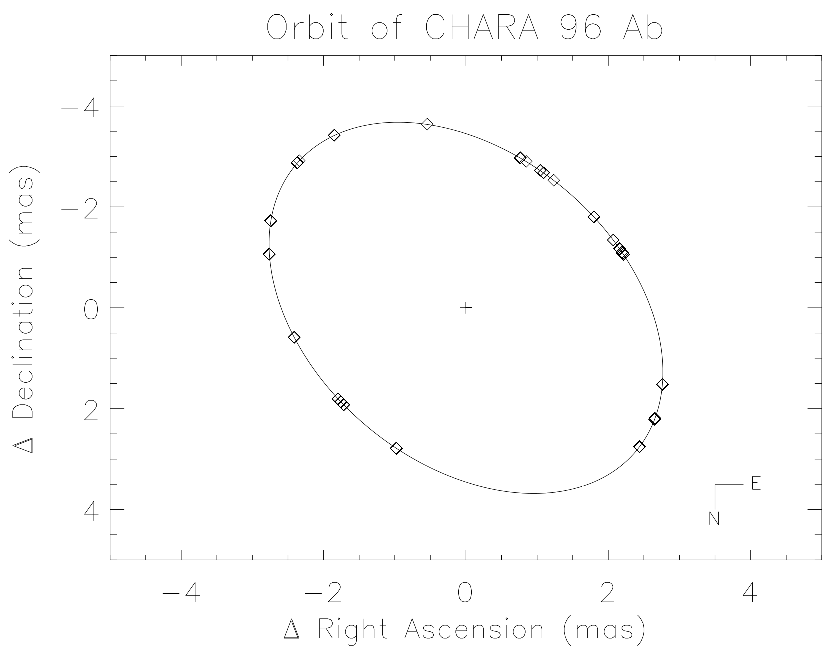

Figure. C.7: CHARA 96 Ab orbit

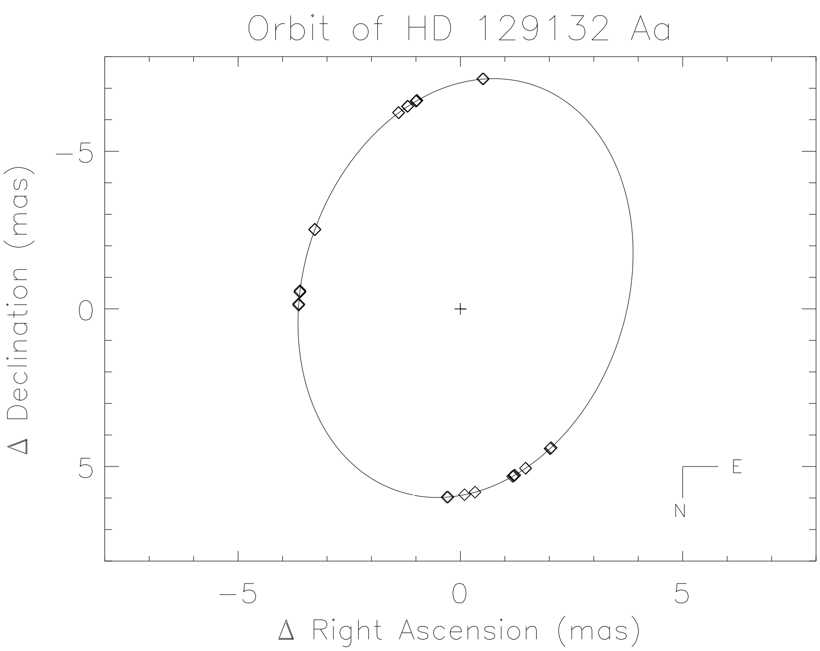

Figure. C.8: HD 129132 Aa orbit